Tunable High-Field / High-Frequency ESR and High-Field Magnetization on Single-Molecule Clusters

Dissertation

zur Erlangung des akademischen Grades

Doctor rerum naturalium
(Dr. rer. nat.)

vorgelegt

der Fakultät für Mathematik und Naturwissenschaften
der Technischen Universität Dresden

von

Diplom-Physiker
Christian Golze

Gutachter: Prof. Dr. B. Büchner
Prof. Dr. H.-H. Klauß
Prof. Dr. J. Schnack

Tag der Einreichung: 30.08.2007
Tag der Disputation: 06.12.2007

Contents

Introduction

For more than half a century, chemical researchers have synthesized magnetic materials from *organic* and *metal-organic* precursors. In doing so, significant extensions of the physical properties have been realized when compared to the atomic *organic-free* magnets which are based on ferrites or rare-earth compounds (e.g. hematite, magnetite, SmCo, or NdFeB). Though the prevalence of the latter conventional magnets is tremendous, there is demand for magnetic materials with novel properties which are not within the scope of the traditional magnetic materials. Examples include compounds which combine magnetism with physical properties such as optical transparency, true solubility or low dimensions, where the magnetism may be switched by light, temperature or pressure.

In the past, a variety of organic-based magnetic substances have been synthesized. By selective variation of the *inter*-molecular exchange strengths it is nowadays possible to reproduce the classical counterparts of existing topologies on a molecular basis—like three-dimensional network structures (3D), thin magnetic films or layered compounds (2D), chains (1D) or single domain grains (0D). Remarkably, coordination chemistry allows one to influence the topology by rather subtle changes in the synthesis, while the high energy metallurgical creation process of conventional magnets requires more significant efforts to change the structure. *Chemical engineering* enables to go even beyond the conventional prospects by creating structures which lack an analogue of traditional magnets. For instance star-shaped clusters, wheels, butterflies or perfectly identical giant molecules are synthesized by exploiting the precision of self-assembling mechanisms.
Low dimensional systems with small spins have been intensively studied by theorists since they exhibit unusual ground states owing to quantum effects (see, e.g., [1–3]) which are much more pronounced than in the classical limit. Thus, the former examples are highly attractive to verify the theoretical predictions for such systems. A secondary effect of the ability to tailor intra- and inter-molecular exchange strengths is the possibility to shift the properties under study into the scope of the experimental limitations, e.g. in terms of attainable magnetic field strengths. In fact, molecule-based magnets have already evolved to a broad interdisciplinary research area of chemists and physicists.

This thesis is particularly focussed on the magnetic properties of zero-dimensional molecular clusters of iron group elements. Due to the increasing flexibility of synthetic chemistry, a large variety of complex molecular entities have been recently

synthesized. The progress is characterized by the clusters comprising a steadily increasing number of paramagnetic metal ions which are magnetically coupled by a growing variety of diamagnetic bridge ligands. The latter are crucial not only for rendering the intra-molecular magnetic coupling between the spin centers but also for providing the ligand field for the magnetic ions which they are connecting. The most prominent and extensively studied representatives of *single-molecule magnets* are the compounds usually abbreviated with $Mn_{12}Ac$ and Fe_8. Both molecules have an $S = 10$ ground state. By means of crystal field effects, the quantum states with $m_S = \pm 10$ are favored, while the potential energy within this multiplet is highest for $m_S = 0$. This energy barrier enables the storage of data: Once polarized to $m_S = +10$ or $m_S = -10$ (interpreted as quantum bits), a blocking of the magnetization is observed in form of a hysteresis as long as the thermal energy is low compared to the height of the barrier. However, in $Mn_{12}Ac$ and Fe_8 a alternative novel relaxation pathway was discovered which enables the relaxation of the magnetization by quantum mechanical tunneling of the direction of the magnetization vector. This famous effect and the potential barrier are subject of current research. Both are predominantly affected by the total spin and the magnetic anisotropy of the molecule. Therefore, the intra-molecular bridging ligands are crucial components in the synthesis of single-molecule magnets, since they mediate the magnetic spin exchange *and* cause the crystal field of the spin carriers.

In this work several novel multinuclear clusters have been characterized by study of macroscopic and local magnetic properties both in static and pulsed magnetic fields. The experimental methods span measurements of the susceptibility down to 1.8 K (static) and 35 mK (dynamic), respectively, as well as magnetization measurements in pulsed fields up to 52 T. The local properties have been studied with tunable high field/ high frequency electron spin resonance (tHF ESR) in the sub-terahertz regime. This method proved to be a valuable tool to directly probe large zero-field splittings and to obtain the spectrum by systematic excitation of individual spin states.

ESR is a well established technique in chemistry. However, its application in solid state physics was seriously restricted in the past. The reason is the frequency (~ 10 GHz) of standard ESR spectrometers. Paramagnetic centers in solid matrices are appreciably affected by intra-molecular magnetic exchange and the crystal field. Therefore, broad ESR linewidths are expected for low external fields of the order of the fluctuating fields by means of the interaction. For considerable crystal fields, the resulting zero-field gap may even exceed the excitation energy and render the compound ESR silent. However, in the last decades the method found application in the research field of solid state physics mainly thanks to the frequency increase of the applicable radiation. Today, commercial ESR spectrometers are operational at 94 GHz, and non-standard high power tunable sources cover the whole sub-terahertz domain and even reach beyond.

In fact, even nowadays high frequency ESR has its place in the chemists work

environment. Current research in coordination chemistry in the field of molecular magnetic clusters requires the characterization of magnetic anisotropy, the increase of this latter quantity being one of the primary aims of current research.

The thesis is organized in three chapters. In the first chapter, an overview of the ESR method is given. It covers the basic resonance phenomenon and the classical relaxation mechanism, as described by Bloch. The following sections address the spin Hamiltonian formalism, thus, introducing the quantum mechanical description of the many electron Hamiltonian, the Zeeman effect, the spin-orbit coupling and the influence of the ligand field in solids. The aim of this chapter is to obtain a preferably complete and consistent introduction to the phenomenon of magnetic anisotropy caused by the crystal field. The chapter closes with a discussion on the possibilities and the limits of simulating ESR spectra. Objectives of simulation are the determination of the experimental ESR parameters within the framework of a model system. This approach is appropriate in particular for the understanding of powder averaged data of magnetic anisotropic samples.
The second chapter explores the technical issues of modern high frequency ESR equipment. The relevance of tunable high field / high frequency ESR in solid state physics is inspected. Subsequently, the challenges in generation, transmission and detection of sub-terahertz radiation are investigated more closely. Several spectrometers and equipment for magnetization measurements—used to obtain the experimental results in this thesis—are described in detail.
After this technical part, the third chapter is dedicated to the magnetism of single-molecule clusters. Firstly, the development from the conventional organic-free to organic-based molecular magnets is reviewed. Thereafter, a variety of novel recently synthesized polynuclear clusters is investigated. Most of the studied systems are 0D tetranuclear compounds of iron group ions, either homonuclear (Ni_4) or heteronuclear with different motifs of the magnetic core structure (star-shaped: Mn_3Cr, butterfly-shaped: Fe_2Cu_2). With magnetization measurements, the ground state of each systems is characterized. ESR has been used to determine the zero-field splitting due to crystal field effects and g-factors. In addition, the very first system investigated in this chapter is an exception, since it forms—at least from the structural point of view—a homonuclear 2-leg spin-ladder based on Ni. Eventually, even this compound turns out to be a system of downright perfectly isolated Ni-dimers and therefore well classifies as single-molecule dinuclear cluster. Finally, the main results are summarized.

1 Electron Spin Resonance

1.1 Overview

The phenomenon of induced absorption or emission of magnetic dipole radiation with the effect of reorientation of electronic magnetic moments is called Electron Spin Resonance (ESR) [4]. More generally one speaks of Electron Paramagnetic Resonance (EPR), when the orbital moments of the electrons contribute to the magnetic moment in addition to the pure electron spins.

The physics of this well established technique will be reviewed in this chapter, starting with the easiest scenario of an $S = 1/2$ system. The basic phenomena and effects are introduced by the application of this example: the intrinsic magnetic moment due to the electron spin and the gyromagnetic factor which both give rise to the Zeeman effect in external magnetic fields. The possible magnetic transitions are determined by the resonance condition and the quantum mechanical selection rules for electromagnetic dipole radiation.

In this work molecular clusters are investigated which exclusively comprise iron group ions as the source of permanent magnetic moments. Therefore, the coverage is restricted to the physical properties of the 3d-shell which is primarily responsible for the magnetism of the iron group elements.

Embedded into a crystal structure, the magnetic centers are influenced by the surrounding ligands and they may also interact with each other. First, the focus will be on the influence of the ligand field which basically lowers the symmetry of the free ion from a spherical continuous to a finite discrete one. While for free ions the energy of the orbital states is degenerate, it is shown that even in the highest attainable symmetry of a crystal structure—which is the cubic symmetry—this orbital energy degeneracy is lifted. Further symmetry-lowerings have a strong impact on the orbital contribution to the magnetic moment. Together with the spin-orbit coupling, the crystal field accounts for magnetic anisotropy which may manifest itself in splittings of the energy levels even in zero magnetic fields.

Thereafter, the effective spin Hamiltonian $\mathcal{H}_{\text{eff}}$ is introduced in order to ease the quantum mechanical description. It results when Zeeman energy and spin-orbit coupling are treated as a perturbation of the crystal-field-affected eigensystem $\mathcal{H}_0 + \mathcal{H}_{\text{CF}}$. The formalism allows the description of the properties probed by ESR and magnetization experiments in terms of simple parameters.

The final steps of this chapter will describe systems comprising a finite number of exchange coupled magnetic centers with the proper extension of the spin Hamiltonian formalism and aspects for modeling ESR spectra.

1.2 The Resonance Phenomenon

Thinking of the physical properties of an electron, its most evident attribute is that it carries an electrical charge. Electrons are also not mass-less, although their charge-to-mass ratio is quite large in comparison to protons or other elementary charged objects. These two properties are already sufficient for the understanding of numerous effects which can be described with the electrodynamic theory of Maxwell, e.g. the dipole radiation of accelerated electrons.
With the advent of quantum mechanics in the early 20th century the spin as another electronic characteristic was discovered. Though the origin is not clear, it is interpreted as an intrinsic moment of the particle and it manifests itself in the fine-structure of terms, for instance in the anomalous Zeeman effect [5]. The latter was explained in 1925 by Uhlenbeck and Goudsmit [6] with the hypothesis that the electron itself carries a magnetic moment of one Bohr magneton, $1\,\mu_\mathrm{B}$, and a mechanical angular moment of $1/2\,\hbar$. Eventually, in 1922 Stern and Gerlach succeeded to reveal the electron spin with their famous experiment. [7]

Although the spin is not the most obvious property of the electron due to its pure quantum nature, it is quite easy to reveal with ESR. If a system (e.g. a molecule) with a spin of $S = 1/2$ is put in an external homogeneous magnetic field directed along the z-axis, $\mathbf{H} = H_z\mathbf{e}_z$, it will quantize with respect to the field direction. Since the spin is associated with a magnetic moment, its direction influences the energy of the system,

$$E(m_S) \;=\; g\,\mu_\mathrm{B}\,\mathbf{S}\cdot\mathbf{H} \;=\; g\,\mu_\mathrm{B}\,m_S H_z. \qquad \text{Zeeman energy} \tag{1.1}$$

The description of the spin is thereby accomplished by the vector operator $\mathbf{S}$ where its z-component is characterized by the magnetic quantum number m_S with possible integer or half-integer values of $-S \le m_S \le S$, depending on the spin quantum number S. Equation (1.1) is valid for any spin $\mathbf{S}$. More general, it holds even for the total angular momentum $\mathbf{J} = \mathbf{L} + \mathbf{S}$ which is the sum of the orbital angular momentum $\mathbf{L}$ and the spin. In this case, indeed, the proportionality factor g (the gyromagnetic factor, short: g-factor) has to be substituted by the Landé factor, (1.41), owing to different g-values of the individual magnetic moments associated with $\mathbf{L}$ and $\mathbf{S}$. However, the size of the magnetic moment of the free electron,

$$\boldsymbol{\mu} \;=\; g_\mathrm{e}\,\mu_\mathrm{B}\,\mathbf{S}, \qquad \text{electron magnetic moment} \tag{1.2}$$

is not exactly $1\,\mu_\mathrm{B}$ as predicted by Uhlenbeck, Goudsmit and eventually also by Dirac's theory, but slightly larger due to radiative corrections which are subject of quantum electrodynamics. Therefore, in (1.2) the g-factor is not exactly 2, but, e.g., the result of a series expansion about the Sommerfeld fine-structure constant α,

$$g_\mathrm{e} \;=\; 2\left(1 + \frac{\alpha}{2\pi} + O(\alpha^2)\right) \approx 2.00232. \qquad \text{free electron g-value} \tag{1.3}$$

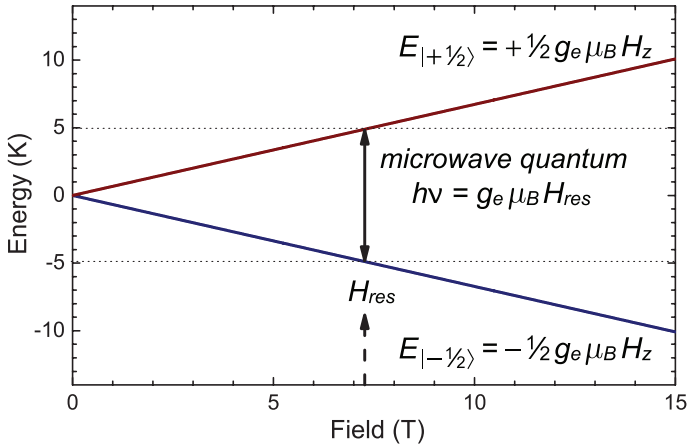

Figure 1.1: *Zeeman effect for an $S = 1/2$ system: The Zeeman levels $E_\uparrow$ and $E_\downarrow$ depend linearly on the external field H. A microwave quantum with energy $h\nu = g_e \mu_B H_{res}$ induces a spin flip at the resonance field H_{res}.*

The splitting of the energy levels in (1.1) is the result of the application of an external field and different values of m_S, and is known as the Zeeman effect (section 1.5). The resulting $2S + 1$ levels are called the Zeeman levels, as shown in Fig. 1.1. A magnetic dipole transition between the levels is possible by absorption or emission of a properly sized electromagnetic quantum $h\nu$, i.e., owing to the conservation of energy the resonance condition,

$$h\nu = g\,\mu_B\,|\Delta m_S|\,H_z, \qquad \text{RESONANCE CONDITION} \tag{1.4}$$

has to be satisfied. In case of the single electron, the only possibility for absorption is the transition $m_S = -1/2 \longrightarrow +1/2$, while the inverse process is associated with the emission of a photon. At a finite temperature and in thermodynamic equilibrium the higher lying energy level of (1.1), $E(m_S = +1/2)$, is less occupied in favor of the lower lying, $E(m_S = -1/2)$. This statement is true also for more than two energy levels and the thermal population is described by Boltzmann statistic, (1.66). Since the transition rates between the spin levels generally depend on their population it can be shown that the net effect of the spin transition processes is always absorption.
For systems with higher spin the emerging possibilities for transitions between the various spin states are restricted by the quantum mechanical selection rules. For magnetic dipole radiation they compute [4] to

$$\Delta L = 0, \qquad \Delta S = 0, \qquad \Delta m_S = \pm 1. \qquad \text{SELECTION RULES} \tag{1.5}$$

For a single electron the selection rules are trivial, because the electron spin is constant $S = 1/2$ and both mentioned transitions correspond to $|\Delta m_S| = 1$.

In the classical picture the spin precesses like a gyroscope about the axis of the external field, as shown in Fig 1.2a. In the experimental setup the magnetic component $\mathbf{H}_1$ of the linearly polarized radiation is perpendicular to the external field $\mathbf{H}$, see Fig 1.2b. Linear polarization can be interpreted as the superposition of two circularly polarized waves where in the resonance case one component

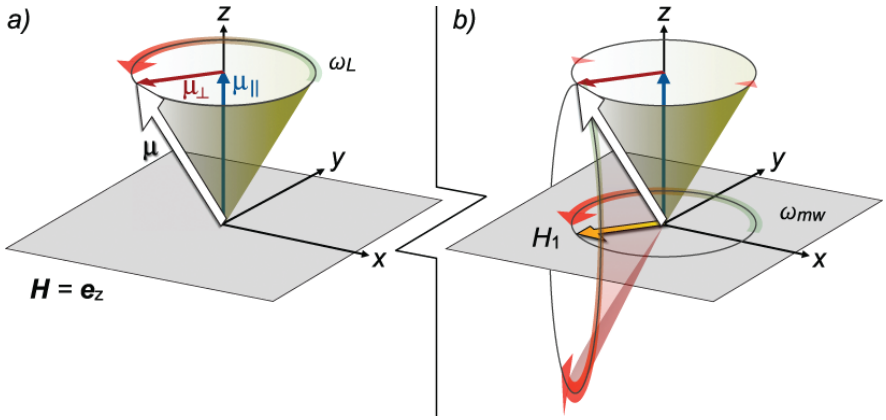

Figure 1.2: *Classical idea of the spin-flip. a) The magnetic moment* $\boldsymbol{\mu}$ *precesses with* ω_L *about the external field axis. b) Circular polarized radiation of the frequency* ω_{mw} *and its magnetic field vector* $\mathbf{H}_1$ *precessing in the xy-plane. At resonance the magnetic moment* $\boldsymbol{\mu}$ *starts precessing about the* $\mathbf{H}_1$ *direction.*

rotates in the same direction and with equal frequency as the gyroscopic motion of the spin takes place. In the rotating frame of the spin the torsional moment $-\boldsymbol{\mu} \cdot \mathbf{H}_1$ turns the magnetic moment to the opposite direction over a period of rotations and, therefore, *flips the spin*. By measuring the transmitted power of the irradiated microwave the spin flip is recognized as absorption in the case of resonance.

1.3 Relaxation and Lineshape

The graph of the detected microwave power P plotted versus an independent physical quantity is referred to as *ESR spectrum*. In this section and throughout this thesis the independent variable is assumed to be the external magnetic field H. For further details of measurements in the frequency domain refer to section 2.4.

Accepting the resonance condition (1.4) for the lineshape a sharp peak is expected to occur in the spectrum at the resonance field, $f(H) \propto \delta(H - H_{\text{res}})$, were it not for some additional effects. Instead the measured lines have always a finite width. It typically ranges from a fraction of 1 Gauss for free radicals in solution to widths of the order of Tesla for solid matrices of strongly interacting spin centers. The linewidth is finite owing to the *spin relaxation* including fundamental aspects as well as a variety of system specific effects which further broaden the line in a homogeneous or inhomogeneous manner.

Spin relaxation

An excited spin system which is embedded in a matrix of ligands will sooner or later relax due to the interaction with other spins or the lattice itself into a thermal equilibrium state. The equilibrium is thereby characterized by the Boltzmann statistic for the entire occupation and non-coherence of the individual states. Although there are plenty of mechanisms for a spin to relax, it is straightforward to give a lower limit for the linewidth of an ESR line. This universal linewidth is basically caused by a finite lifetime τ of the occupied spin state which after Heisenberg's relation [8] is necessarily associated with an uncertainty for the transition energy $\Delta E \geq \hbar\,\tau^{-1}$. Independently from possible additional interactions which commonly further shorten the lifetime, with increasing strength the natural linewidth in field units,

$$\Delta H \;\propto\; \frac{\hbar}{g\mu_\mathrm{B}}\frac{1}{\tau}, \qquad \text{NATURAL LINEWIDTH} \tag{1.6}$$

solely depends on the reciprocal lifetime of the particular occupied state. As a direct result of the quantum nature of the photons it is a principal property of and present—though not always observable—for any resonance technique operating in the quantum limit.

In a rather general treatment the classical description of relaxation processes is given by the Bloch equations of motion [9]. They describe the time evolution of the magnetization density (short: magnetization) $\mathbf{M}(t)$ which is basically the sum of the magnetic moments $\boldsymbol{\mu}$ of the participating spins. Furthermore, they consider the external field $\mathbf{H}$ and introduce phenomenological terms for the lifetime of the longitudinal and transversal spin polarization formulating its statistical decay by an exponential law:

$$\frac{\partial\mathbf{M}}{\partial t} \;=\; \frac{g_\mathrm{e}\mu_\mathrm{B}}{\hbar}(\mathbf{M}\times\mathbf{H}) \;-\; (\mathbf{M} \;-\; \chi_0\mathbf{H})\left(\frac{1}{T_1}\mathbf{e}_\parallel \;+\; \frac{1}{T_2}(\mathbf{e}_{\perp 1} \;+\; \mathbf{e}_{\perp 2})\right) \tag{1.7}$$

where $\mathbf{e}_\parallel := H^{-1}\,\mathbf{H}$ is the unit vector of the field direction. The directions perpendicular to the field are arbitrarily chosen and denoted as unit vectors $\mathbf{e}_{\perp 1}$ and $\mathbf{e}_{\perp 2}$, respectively, with $\mathbf{e}_{\perp 1} \;\perp\; \mathbf{e}_{\perp 2}$.
Formally, for infinite relaxation times T_1 and T_2 the last part of equation (1.7) vanishes and the change of the magnetization is just directional, whereas the magnitude is constant. This theoretical case corresponds to a gyroscopic motion of $\mathbf{M}$ where the longitudinal magnetization $M_\parallel$ is conserved and the component perpendicular to the field $\mathbf{M}_\perp$ precesses with the Lamor frequency,

$$\omega_\mathrm{L} \;=\; \hbar^{-1}\,g_\mathrm{e}\,\mu_\mathrm{B}\,H \qquad \text{LAMOR FREQUENCY} \tag{1.8}$$

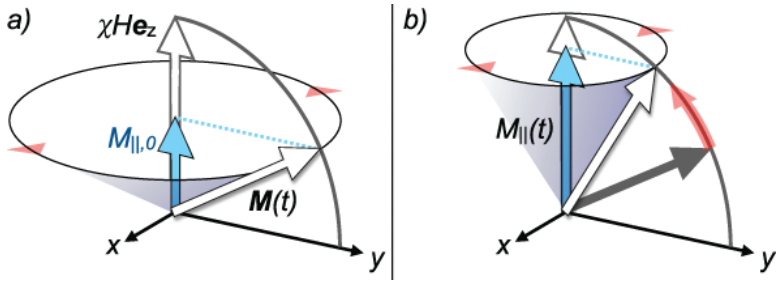

Figure 1.3: *Relaxation of $M_\parallel$ towards the equilibrium, $\chi(T)H$. a) The magnetization, $\mathbf{M}(t)$ precesses with ω_L about the external field axis, $\mathbf{e}_z$. For $t = 0$ its projection on the field axis is $M_{\parallel,0}$. b) $\mathbf{M}(t)$ is gradually aligned to the equilibrium value for $t > 0$, until $M_\parallel = \chi H$ for $t \to \infty$.*

about the field axis, identical to the motion of the single magnetic moment in Fig. 1.2a.
For a finite longitudinal lifetime T_1 the parallel component of the magnetization $M_\parallel(t)$ relaxes to its steady state χH obeying an exponential decay law which is the integral of

$$\frac{\partial M_\parallel}{\partial t} = -\frac{M_\parallel - \chi H}{T_1}. \qquad \text{LONGITUDINAL RELAXATION} \qquad (1.9)$$

Thereby, the static susceptibility[1] $\chi(T)$ is determined by the Boltzmann occupation of the energy levels in equation (1.1). The process is drafted in Fig. 1.3. For relaxation into thermal equilibrium, the spin system needs a reservoir and an interaction mechanism in order to store and transfer the energy.
Possible processes are the spontaneous emission of a microwave quantum (interaction with the radiation field) and spin-lattice relaxation (e.g. direct, Raman, Orbach spin-phonon processes, etc. [10]). The occurrence of spontaneous emission events scales with ν^3 and is thus insignificant for frequencies lower than 1 THz. [11] Therefore, the energy transfer to the lattice is the favored way of relaxation for the spin system. This is why the longitudinal relaxation time T_1 is called the spin-lattice relaxation time.

The transverse magnetization relaxes according to the rate equation

$$\frac{\partial M_\perp}{\partial t} = -\frac{M_\perp}{T_2}. \qquad \text{TRANSVERSE RELAXATION} \qquad (1.10)$$

Fig. 1.4 shows the transverse projections of the individual spins and the resulting magnetization. By spin-spin interaction the phase coherence is lost for $t > 0$ and the transverse polarization of the spins decays as a result of their xy-projections becoming gradually uniformly distributed again. For a mono-exponential time

[1] **Nomenclature:** Static susceptibility: χ, dynamic susceptibility: χ_ω, temperature independent susceptibility, comprising a dia- and a paramagnetic contribution: $\chi_0 = \chi_{\text{dia}} + \chi_{\text{para}}$

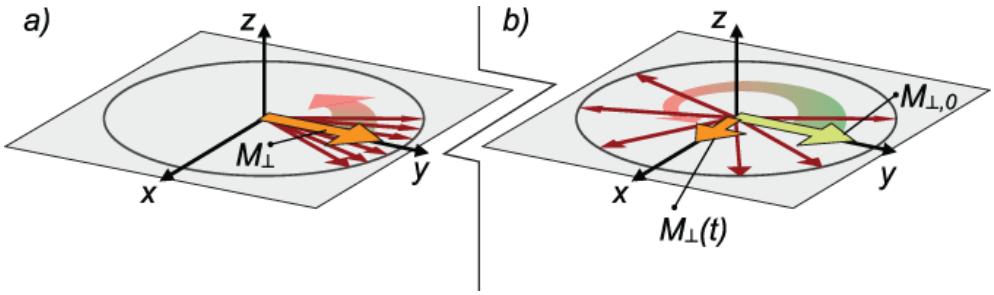

Figure 1.4: *Transverse relaxation. a) In the non-equilibrium state individual projections on the xy-plane of each spin (small red arrows) are precessing coherently about the field axis with the Lamor frequency so that a present preferential direction of these spin components is conserved. In this case, the transverse magnetization $M_\perp$ (orange arrow) is finite and precesses with the mean frequency ω_L in the plane. b) By spin-spin interaction the coherence is destroyed and, therefore, the individual projections of the spins start to average with respect to their direction. Consequently, $M_\perp(t)$ gradually decays to zero which is the equilibrium state.*

evolution of the decay $M_\perp(t > 0)$ is described by equation (1.10) and the timescale T_2 is called the spin-spin relaxation time.

A continuative discussion of the Bloch equations with an additional perturbation term to model a linear polarized microwave of frequency ω_{mw} and amplitude H_1 is given in [11, 12]. The calculation yields the power absorbed in the spin system,

$$P \propto \omega_{\mathrm{mw}} \chi''_\omega H_1^2, \qquad \text{ABSORBED POWER} \tag{1.11}$$

to be proportional to the imaginary part of the dynamic susceptibility χ''_ω which is proportional to the static one, χ. Furthermore, the lineshape of the absorbed power at frequency ν as a function of the applied field H is a Lorentzian,

$$P_\nu(H) \propto \frac{\Delta H}{(H - H_{\mathrm{res}})^2 + (\Delta H)^2}, \qquad \text{LORENTZIAN} \tag{1.12}$$

which is plotted in Fig. 1.5b.

As mentioned before, the longitudinal relaxation is due to the coupling of the spins to the phonons or, e.g., some other spin systems. Therefore, T_1 is generally temperature dependent, while in the first instance the transverse relaxation time is not. At low temperature only a few phonons exist and in particular in conjunction with strong spin-spin interaction the transverse relaxation time is commonly shortened by several orders of magnitude as compared to the spin-lattice relaxation time: $T_2 \ll T_1$. The spin system may then be associated with a spin temperature T_{s} and the energy distribution is denoted as spin diffusion. However, it should be noted that each longitudinal relaxation process destroys the coherence as well and hence accounts for transverse relaxation, too. Consequently, the spin system relaxes at least on the timescale of T_1 which may even

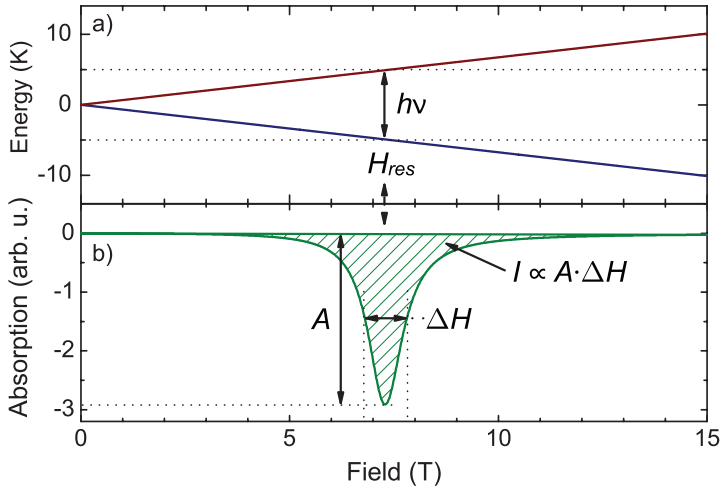

Figure 1.5: *Calculated ESR absorption signal for an $S = 1/2$ system. a) Zeeman levels. b) Lorentzian lineshape with amplitude A at the resonance field H_{res} with linewidth ΔH. The absorbed power P is proportional to the intensity of the line I which corresponds to the area of the shape, $I \propto A\,\Delta H$.*

become the determinant scale of relaxation in systems where the spins are efficiently coupled to the lattice by means of the spin-orbit coupling (section 1.6). While the Bloch equations (1.7) provide only a conception of modeling the spin relaxation phenomenon, it is instructive to study the lineshape itself in order to identify different broadening mechanisms.

Further lineshape properties

After the derivation of the lineshape the measured quantities and their importance for the interpretation of ESR lines are shortly introduced in this paragraph. The object of an ESR experiment is the determination of the spin structure and dynamics of the system investigated. A common approach is to set up a spin Hamiltonian (1.51) and (1.48) which is done in section 1.9, and then to quantify the parameters with the results from the analysis of the measured ESR spectra. For now, the Zeeman energy (1.1) is sufficient to identify some basic lineshape properties.

The resonance field: The g-factor of the measured resonance mode is determined from the resonance field H_{res} and the excitation frequency ν used in the experiment. An application of the resonance condition (1.4) results in the expression

$$g = \frac{h}{\mu_{\mathrm{B}}} \frac{\nu}{H_{\mathrm{res}}} \approx \frac{1}{14} \frac{\nu(\mathrm{GHz})}{H_{\mathrm{res}}(\mathrm{T})} \tag{1.13}$$

for the g-value. It is remarkable that equation (1.13) is generally true for $S = 1/2$, as long as the g-factor is isotropic. If not, the investigated system is magneti-

cally anisotropic, implying an angular dependence of g with respect to the field direction.
In systems with $S \geq 1$ effects of the ligand field have to be considered which may introduce a magnetic anisotropy not necessarily only due to g. In such cases g is not determined by equation (1.13), but by the slope of ν/H_{res} in the high field limit

$$g \;=\; \lim_{H_{\mathrm{res}}\to\infty} \frac{h}{\mu_{\mathrm{B}}} \frac{\partial\,\nu}{\partial H_{\mathrm{res}}}. \tag{1.14}$$

If g is anisotropic, it is substituted by a 3×3 interaction matrix, $\bar{\bar{g}}$ [13]. The modified Zeeman energy (1.1) is then described according to

$$E(m_S) \;=\; \mu_{\mathrm{B}}\, \mathbf{S} \cdot \bar{\bar{g}} \cdot \mathbf{H}. \tag{1.15}$$

In the case of a symmetric $\bar{\bar{g}}$ (i.e. $g_{nm} = g_{mn}$) it gets a tensorial character and is transformed to its principal axis system [12]. From the principal values g_{11}, g_{22}, and g_{33}, an effective g-value is given by the construction

$$g_{\mathrm{eff}} \;=\; \sqrt{g_{11}\sin^2\theta\cos^2\phi + g_{22}\sin^2\theta\sin^2\phi + g_{33}\cos^2\theta} \tag{1.16}$$

which is used to describe angular dependent ESR measurements. The angles θ and ϕ describe the polar coordinates of the magnetic field with respect to the principal axis system of $\bar{\bar{g}}$.

ESR Intensity: The intensity I of an ESR line corresponds to the integral of the lineshape. In cases where the lineshape is defined by a Lorentzian or Gaussian shape-function $f(H, A, \Delta H)$ the intensity is simply related to the product of the amplitude A and the linewidth ΔH introduced by f:

$$I \;\propto\; A\,\Delta H. \tag{1.17}$$

As an example of shape-functions, Fig. 1.5b shows the Lorentzian lineshape. While ESR measures the imaginary part of the dynamic susceptibility the integral of a particular resonance is a measure of the absolute number of resonating spins and hence, I is proportional to the *local static* susceptibility, χ_{loc},

$$I \;\propto\; \chi_{\mathrm{loc}} \int_{-\infty}^{+\infty} f(H)\, dH. \tag{1.18}$$

1.4 Many Electron Hamiltonian

The free-electron scenario of section 1.2 is the simplest example to illustrate the principle of the ESR technique by means of a spin ½ system. However, for the investigation of real systems a more sophisticated approach is required. In real systems the electrons giving rise to an ESR signal are bound to the matter. Therefore, it principally does not matter whether they are strongly localized like in good insulators or itinerant like conduction electrons in metals. Consequently, the investigation of real systems (which, moreover, may exhibit $S \geq 1$,) first and foremost requires to consider entire atoms where some of their electrons give rise to ESR and some do not.

A sufficient approach to meet the consequences of multiple electrons being trapped in the electrostatic potential of the nucleus is the many electron Hamiltonian,

$$\mathcal{H}_0 = \sum_k \left(\frac{\mathbf{p}_k^2}{2m} - \frac{Ze^2}{r_k} + \frac{1}{2} \sum_{l \neq k} \frac{e^2}{|\mathbf{r}_k - \mathbf{r}_l|} \right). \tag{1.19}$$

It represents the classical formulation of N electrons situated in the Coulomb field caused by the nucleus and the other electrons. The sum in (1.19) therefore runs over all N electrons in the atom or ion. The main difficulty in solving the associated static Schrödinger equation,

$$E\,\psi_N = \mathcal{H}_0\,\psi_N, \tag{1.20}$$

is the last term in (1.19) which represents the interaction of the electrons among themselves and significantly complicates the eigenvalue problem.
A common approach to solve (1.20) in the local picture is the Hartree-Fock approximation [14]. The N-particle wavefunction ψ_N is here an $N \times N$ Slater determinant of N single electron spinors ϕ_k. Without going into detail, this ansatz allows each electron to be described with a single-electron Schrödinger equation comprising the potential of the core and an additional effective potential $v_k(\{\phi_l\})$ which depends on the set of wavefunctions of the remaining $N-1$ electrons. Eventually, it is sufficient to treat single electron wavefunctions instead of the unhandy ψ_N in the following.
The approximation of Hartree is the assumption of the effective potential for the kth electron $v_k(\{\phi_l\})$ to be spherically symmetric. Therefore, the single electron spinor can be written as a product of a radial, an angle dependent, and a spin part,

$$\phi_k = R_{nl}(r)\, Y_l^{m_l}(\theta, \varphi)\, \chi(m_s), \quad k = (n, l, m_l, m_s) \tag{1.21}$$

which is similar to the hydrogen solution.
Hamiltonian (1.19) is diagonalized by states (1.21) in terms of the constructed $\psi_N(\{\phi_k\})$. The use of a determinant of spinors thereby ensures the antisymmetry of ψ_N and thus satisfies the Pauli principle by the natural antisymmetry

of determinants. The ground state is determined by minimizing the energy in (1.20) which can be achieved by successively "filling" free electronic states with electrons starting from the lowest energy level.
The single electron wavefunctions (1.21) are characterized by the quantum numbers n, l, m_l, s, and m_s. In this sense states of the same main quantum number n define a shell, while states of the same quantum number of the orbital moment l pertain to one subshell. For a fixed pair of quantum numbers $(n,\, l)$ the subshell is spanned by $2l+1$ orbitals of identical energy, each of them holding at most two electrons with different spin direction m_s. This manifold of $2(2l+1)$ electronic states defines a multiplet.

1.5 The Zeeman Effect

The application of a uniform magnetic field in z-direction is considered in the formalism of the Hamiltonian (1.19) by the transition from the canonical momentum to the kinetic one,

$$\mathcal{H}_0 \rightarrow \mathcal{H}_0' \quad : \quad \mathbf{p}_k \longrightarrow \mathbf{p}_k' = \mathbf{p}_k + \frac{e}{c}\mathbf{A}(\mathbf{r}_k). \tag{1.22}$$

The field is introduced in form of the vector potential $\mathbf{A}$ satisfying the Coulomb gauge $\mathbf{A} = (\mathbf{H} \times \mathbf{r})/2$. By calculating the difference in kinetic energy,

$$\frac{1}{2m}\sum_k \mathbf{p}_k'^2 - \mathbf{p}_k^2 = \frac{e\hbar}{2m}\sum_k \underbrace{\mathbf{l}_k \cdot \mathbf{H}}_{\text{PARA-,}} + \underbrace{\frac{e^2H^2}{8mc^2}\left(x_k^2 + y_k^2\right)}_{\text{DIAMAGNETIC}} \tag{1.23}$$

the field dependent part of the modified Hamiltonian (1.22) is extracted. Equation (1.23) results in a paramagnetic and a diamagnetic contribution. The paramagnetic part corresponds to the Zeeman contribution of the orbital moments which cause a permanent magnetic moment. In contrast, the diamagnetic contribution is purely field-induced owing to its dependence on the square of the field. It is neglected in the following, since it is not responsible for an ESR signal. Moreover, in moderate fields it is usually overcompensated by the permanent moment as long as it exists.
As the electron spins $\mathbf{s}_k$ are not a property of the original Hamiltonian (1.19) but of the spinors ϕ_k (1.21) they are subsequently included in (1.23) by substituting $\mathbf{l}_k \rightarrow \mathbf{l}_k + g_\mathrm{e}\,\mathbf{s}_k$. The factor $e\hbar/2m$ in (1.23) is the Bohr magneton and by the introduction of the total spin and the total orbital momentum,

$$\mathbf{S} = \sum_k^{\substack{\text{incomplete}\\ \text{subshell}}} \mathbf{s}_k, \qquad \text{TOTAL SPIN} \tag{1.24}$$

$$\mathbf{L} = \sum_k^{\substack{\text{incomplete}\\ \text{subshell}}} \mathbf{l}_k \qquad \text{TOTAL ORBITAL MOMENTUM} \tag{1.25}$$

the complete Zeeman term is written in the form

$$\mathcal{H}_{\mathrm{Z}} = \mu_{\mathrm{B}}(\mathbf{L} + g_{\mathrm{e}}\,\mathbf{S}) \cdot \mathbf{H}. \qquad \text{Zeeman Hamiltonian} \tag{1.26}$$

The sums in (1.24) and (1.25) only need to run over electrons in incomplete subshells since the momenta otherwise vanish due to the Pauli principle and Hund's rules (section 1.8),

$$\sum_{m_{s_k}}^{\substack{\text{complete}\\ \text{orbital}}} \mathbf{H} \cdot \mathbf{s}_k \,|m_{s_k}\rangle = 0, \qquad \sum_{m_{l_k}}^{\substack{\text{complete}\\ \text{subshell}}} \mathbf{H} \cdot \mathbf{l}_k \,|m_{l_k}\rangle = 0. \tag{1.27}$$

Certainly, also the ion's nucleus may carry a magnetic moment giving rise to the nuclear-Zeeman effect and thus principally playing a role for the magnetic energy as well. The magnetic moment of the nucleus is three orders of magnitude smaller compared to the electronic contribution. Therefore, the additional splittings which are expected from the coupling of electronic spins with the spin of the nucleus are small in comparison to the linewidth of strongly exchange coupled electronic spins. In other words, the described scenario corresponds to the case where the exchange within the electronic system dominates the hyperfine coupling energy, i.e. $E_{\mathrm{ex}} \gg E_{\mathrm{hc}}$ which is usually the case in solids. If so, the hyperfine-structure is either not observed in the experiment at all or it gives rise to a negligible line broadening and is hence neglected in the following. Nevertheless, the nuclear-Zeeman effect can easily be probed in diluted systems, i.e. radicals in solution and is, therefore, significant in these systems.

The Hamiltonian (1.22) is diagonalized with consideration of the external field strength to get the eigenstates and the energy spectrum. Depending on the actual element of the periodic system it turns out that in the weak-field limit the eigenstates may be determined by the relativistic effect of the spin-orbit coupling, with the Zeeman interaction becoming only a small perturbation. Therefore, it is necessary to consider the corrections to (1.22) by the relativistic approach which is done in the next section.
Ignoring the spin-orbit coupling for now, it is noteworthy that wavefunctions ψ_N which diagonalize the field free Hamiltonian $\mathcal{H}_0$ are eigenfunctions of $\mathcal{H}_{\mathrm{Z}}$ as well, with eigenvalues

$$\mathcal{H}_{\mathrm{Z}}\,\psi_N = \mu_{\mathrm{B}} H_z\,(m_L + g_{\mathrm{e}}\,m_S)\;\psi_N. \tag{1.28}$$

The quantum numbers m_L and m_S in (1.28) are the z-components of the corresponding operators $\mathbf{L}$ and $\mathbf{S}$ acting on incomplete shell electrons.

Nomenclature: The magnetic moment of fully occupied subshells vanishes, (1.27), and in addition a magnetic dipole transition is restrained owing to the selection rules (1.5) so that ESR is restricted to states within non-closed subshells. This remains true also for paramagnetic ions *within* a crystal structure at least

until the concept of shells becomes questionable as for conductors. As is common practice in literature, the ESR-relevant subshells are henceforth referred to as *shells*.
In this sense, single-electron states will be denoted using a truncated bra-ket notation, $|m_l, m_s\rangle$ instead of $|n, l, m_l, m_s\rangle$, if the referred states belong to an incomplete shell. For instance the denotation $|m_l, m_s\rangle$ for ions of the iron group assumes $n = 3$ and $l = 2$.
Furthermore, the notation of the states will be generally shortened by omitting the quantum number of some angular momentum, if the dependence of the z-component is given: $|m_\alpha\rangle \equiv |\alpha, m_\alpha\rangle$.

1.6 The Spin-Orbit Coupling

In the rest frame of a particular electron that is orbiting around the nucleus, a magnetic field is produced at the electron's place which is proportional to the angular momentum of that motion. In general the resulting interaction between this motional nuclear magnetic field and the spin magnetic moment cannot be calculated analytically, because it depends on the unknown electrostatic potential affecting the electron. Thus it is written in the form

$$\mathcal{H}_{\mathrm{SO}}^{k} = \zeta\, \mathbf{l}_k \cdot \mathbf{s}_k \qquad \text{with } \zeta = \frac{\hbar^2}{2m^2c^2} \begin{cases} \partial V/(r\partial r), & \text{universal} \\ Ze^2/r^3, & \text{hydrogen-like} \end{cases} \tag{1.29}$$

addressing the kth electron of an incomplete shell in terms of orbital moment and spin $\mathbf{l}_k$ and $\mathbf{s}_k$, respectively, and ζ expressing the strength of the coupling. However, for hydrogen-like ions with only a single electron in the outermost shell the potential V is solely caused by the core and a closed expression is found for ζ, (1.29). Depending on the charge of the nucleus, Ze, the spin-orbit coupling gains in strength for heavier elements. If more than one electron is considered, the structure of the coupling will basically be the same for each electron, but the amplitude will be influenced by screening effects which lower the coupling for electrons in outer shells.
By comprising the electronic angular momentum $\mathbf{l} = \mathbf{r} \times \mathbf{p}$ the spin-orbit coupling depends on the ratio $v/c = \beta$ and is, therefore, already a relativistic effect which vanishes in the classical limit, $\beta \to 0$. While the introduction of (1.29) is somehow artificial, it is noteworthy that (1.29) is a direct result of the Dirac equation.

In case of the LS- or Russel-Saunders coupling the total spin of an incomplete shell $\mathbf{S}$ is coupled to its total orbital momentum $\mathbf{L}$,

$$\mathcal{H}_{\mathrm{LS}} = \lambda\, \mathbf{L} \cdot \mathbf{S} \qquad \text{with } \lambda = \pm\frac{\zeta}{2S}, \tag{1.30}$$

with the coupling strength of λ which is positive for less than half filled shells and negative otherwise.

To give an example, the spin-orbit coupling has a strong effect on the Lanthanides which comprise a highly charged nucleus in addition to the fact that the magnetically relevant 4f-electrons are localized rather close to the core and, therefore, experience a substantial nuclear magnetic field by means of their orbital motion. For this reason the total angular momentum $\mathbf{J} = \mathbf{L} + \mathbf{S}$ is an integral of the motion and, therefore, the eigenstates $|m_J, S, L\rangle$ of $\mathcal{H}_{\mathrm{LS}}$ depend on J and m_J instead of m_S or m_L for the eigenstates of H_0. Both basis sets can be mapped onto each other [14] by the application of the Clebsch-Gordon coefficients,

$$|m_J, S, L\rangle = \sum_{m_L, m_S} |m_S, m_L\rangle \langle m_S, m_L\, |m_J, S, L\rangle\,, \tag{1.31}$$

$$\text{with} \quad J = |L - S|\,, \ldots, L + S \tag{1.32}$$

$$\text{and} \quad -J < m_J < J, \tag{1.33}$$

which describe how the spin-orbit coupling mixes the unperturbed eigenstates of $\mathcal{H}_0$.
In contrast to the former example, the 3d-transition metals are comparatively light. Their 3d-electrons are effectively screened by the inner shells so that the impact of the LS-coupling is weak and usually treated as small perturbation. Precisely the fact that the 3d-electrons are located in the outermost shell causes quite radical changes for the eigenstates in presence of a crystal electric field (CF) induced by adjacent ligands next to the ion. For the iron group ions, the hierarchy of interactions implies that the spin-orbit coupling in solids cannot be treated apart from the CF (which is subject of the next section) by considering the CF-Hamiltonian $\mathcal{H}_{\mathrm{CF}}$.

$$\mathcal{H}_0 \quad > \quad \mathcal{H}_{\mathrm{CF}} \quad > \quad \mathcal{H}_{\mathrm{Z}} \quad \approx \quad \mathcal{H}_{\mathrm{LS}} \tag{1.34}$$

1.7 Influence of the Ligand Field

Compared to the rare earths, the magnetism of transition metal salts is considerably influenced by the CF. For instance electronic charges from the magnetic shell of the Lanthanides, which is the incomplete 4f shell, are screened by the fully occupied 5s and 5p shells owing to their larger distance from the nucleus, $\langle r \rangle_{5\mathrm{s},\,5\mathrm{p}} > \langle r \rangle_{4\mathrm{f}}$. Therefore, the orbital moments of the 4f shell are comparatively weakly affected by the electrostatic potential of adjacent ligands and at least the susceptibility of rare earth salts can often be calculated in the approximation of free ions [15]. In contrast, the 3d-shell of the iron group ions is the outermost, and, therefore, the movement of the electrons is substantially influenced by the CF.

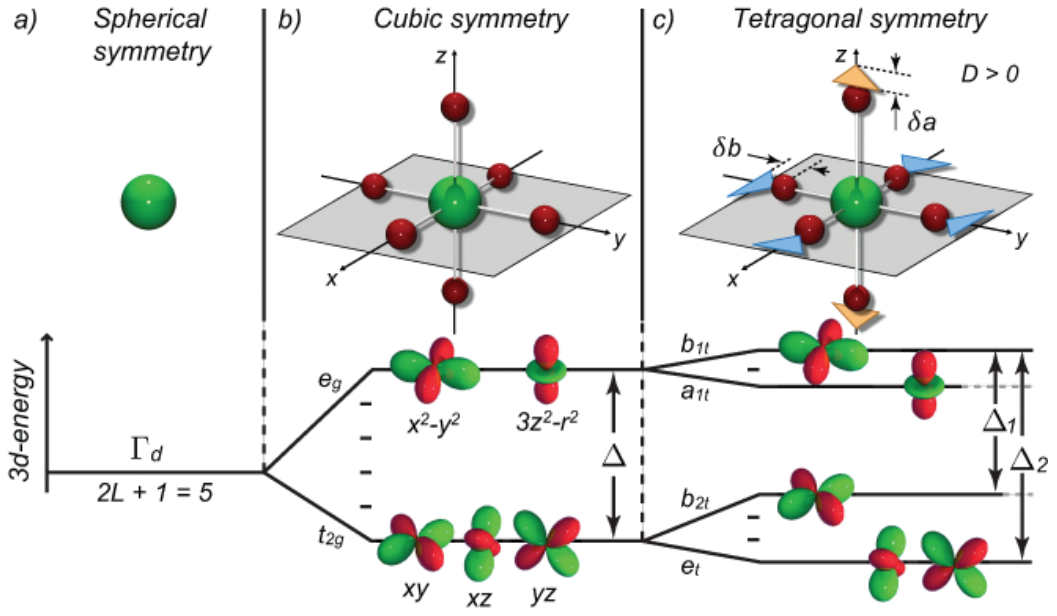

Figure 1.6: *Different symmetries and d-shell energies. a) For the free 3d-ion its five d-shell orbital states are fully degenerate in energy. b) In an octahedral coordination the energy degeneracy is partially lifted. The irreducible representations of the resulting t_{2g} and e_g-levels are given in the standard basis $\{xy, xz, yz\}$ and $\{x^2 - y^2, 3z^2 - r^2\}$, respectively. c) The symmetry of an octahedron is lowered from cubic to tetragonal, e.g. by a small uniaxial distortion of the size δa or by an in-plane distortion described by δb. The irreducible representations b_{1t}, a_{1t}, and b_{2t} are one-dimensional, while e_t is, still, twofold degenerate in this symmetry. See text for details.*

Without exception the samples investigated in this work are insulating crystals of molecules comprising clusters of paramagnetic 3d-transition metal ions. Therefore, the treatment of the ligand effects is focused on the 3d-shell magnetic properties of the iron group elements. Concerning ESR spectroscopy, the ligands do not produce an ESR signal on their own since they are diamagnetic. Nevertheless, they significantly affect the resonance lines due to the embedded paramagnetic centers in the form of shifts of the resonance field as well as they are, at least under certain conditions, responsible for compounds becoming ESR-silent (section 2.2).

The basic effect of the CF is the reduction of the energy degeneracy for d-shell orbital energies owing to their different alignment preferences with respect to the particular symmetry of the electrostatic potential caused by the ligands. The emerging constriction of the orbital degree of freedom in combination with the spin-orbit coupling finally yields a magnetic anisotropy of the crystal. This section discusses the most common symmetry scenarios in terms of qualitative classifications of the orbital energies, while the following section investigates the consequences of the CF for the magnetic properties.

Cubic symmetry

The phenomenon of the decrease of orbital degeneracy is introduced by application of a CF with cubic symmetry. A possible realization is for instance a 3d-ion which is octahedrally coordinated by oxygen ligands. The bonds between the paramagnetic ion and the ligands are assumed to be ionic. The occupied d-states are well localized and the interaction with the ligands can be treated in the point-charge approach. The arrangement of the ligands and the orbitals resulting from the choice of real basis states are illustrated in Fig. 1.6b. They graphically represent the following energy situation: states of the e_{g}-level have their lobes directed towards the negative charged ligands so that they are lifted up in energy due to the repulsive Coulomb interaction of charges with identical sign. With respect to the e_{g}-level the energy of the $t_{2\mathrm{g}}$ orbitals is lowered, because their lobes point to the directions which minimize the Coulomb repulsion.
The tools to actually decompose the fivefold degenerate representation of the free ion into a threefold degenerate $t_{2\mathrm{g}}$ and a twofold degenerate e_{g} level is provided by the study of finite groups [16, 17]. The procedure is only outlined here:
The Hamiltonian of the free ion (1.19) is spherically symmetric and, therefore, its symmetry group, the special rotational group SO_3, comprises all proper rotations in three-dimensional space. Since the rotations are generated by the operator of the angular momentum $\mathbf{L}$ the eigensubspace of $\mathbf{L}$ is the subspace of all rotations, and concerning the d-shell the spherical harmonics $Y_{L=2}^{m_L}$ with $m_L = -2, -1, \ldots, 2$ form a basis of its 5-dimensional irreducible representation Γ_{d}. It is possible to construct a basis of real states by combining spherical harmonics of opposite m_L-signs to the tesseral harmonics $\propto Y_2^{m_L} \pm Y_2^{-m_L}$ which are defined in the appendix.
When placing the 3d-transition metal ion into a CF which is caused by the octahedral environment of O^{2-} ligands, the Hamiltonian acquires an additional term due to the CF,

$$\mathcal{H}_{\mathrm{CF}} \;=\; \mathcal{H}_{\mathrm{oct}} \;=\; \sum_{i=x,y,z} \left(\frac{q}{|\mathbf{r} - a\,\mathbf{e}_i|} \;+\; \frac{q}{|\mathbf{r} + a\,\mathbf{e}_i|} \right), \tag{1.35}$$

comprising the Coulomb potential for each oxygen of point charge q with a bond length of a along the coordinate axes. The symmetry group of $\mathcal{H}_{\mathrm{oct}}$ is the octahedral group O_h which is a finite subset of SO_3 containing only rotations R which preserve the octahedron and, therefore, leave the CF invariant, $R\,\mathcal{H}_{\mathrm{CF}} = \mathcal{H}_{\mathrm{CF}}$. The irreducible representations of the O_h group are calculated by means of group theory and turn out to be 1, 2 and 3 dimensional. They imply a reducibility of the spheric representation Γ_{d} into a 2-dimensional (e_{g}) and a 3-dimensional ($t_{2\mathrm{g}}$) irreducible representation for cubic symmetry [18],

$$\Gamma_{\mathrm{d}} \;=\; e_{\mathrm{g}} \oplus t_{2\mathrm{g}} \qquad \text{CUBIC DECOMPOSITION.} \tag{1.36}$$

The benefit from group theory is thereby to spread the states belonging to Γ_{d} on the representations e_{g} and $t_{2\mathrm{g}}$ and to identify their dimensions. As eigenfunctions

of the spherical Hamiltonian $\mathcal{H}_0$ the wavefunctions $|d_{xy}\rangle$, $|d_{xz}\rangle$, $|d_{yz}\rangle$,$|d_{x^2-y^2}\rangle$, and $|d_{3z^2-r^2}\rangle$, strictly solve the eigenproblem,

$$\mathcal{H}_{\mathrm{CF}}\,\phi \;=\; E_{\mathrm{CF}}\,\phi, \quad \text{with } E_{\mathrm{CF}} \;=\; \begin{cases} E_{\mathrm{e_g}}, & \text{for } \phi \in \{|d_{3z^2-r^2}\rangle\,, |d_{x^2-y^2}\rangle\} \\ E_{\mathrm{t_{2g}}}, & \text{for } \phi \in \{|d_{xy}\rangle\,, |d_{xz}\rangle\,, |d_{yz}\rangle\}, \end{cases} \tag{1.37}$$

justifying this particular selection of basis states to be named *natural*. They are proportional to the former introduced tesseral harmonics, as defined in A.7–A.11. The difference $|E_{e_g} - E_{t_{2g}}| := \Delta$ is referred to as the cubic splitting, whose magnitude is an attribute of both the charge and the bond length of the ligands and which is often given in the unit of $10\,Dq$ from optical spectroscopy [12].

Tetragonal symmetry

The symmetry is lowered from cubic to tetragonal by elongating (contracting) the apex and in-plane oxygen bonds shown in Fig. 1.6c by the amounts δa and $\delta b \neq \delta a$, respectively. The Hamiltonian of the CF (1.35) is then supplemented by a tetragonal contribution,

$$\mathcal{H}_{\mathrm{CF}} \;=\; \mathcal{H}_{\mathrm{oct}} \;+\; \mathcal{H}_{\mathrm{tetra}}. \tag{1.38}$$

The symmetry of $\mathcal{H}_{\mathrm{CF}}$ is by now restrained to the tetragonal group $C_{4\mathrm{h}}$ which is a genuine subset of the octahedral group, $C_{4\mathrm{h}} \subset O_{\mathrm{h}}$. In comparison to the cubic case, the e_{g} level splits into the $a_{1\mathrm{t}}$ and the $b_{1\mathrm{t}}$-level, while $t_{2\mathrm{g}}$ splits further into the, still, twofold degenerate e_{t} and the $b_{2\mathrm{t}}$-level. The eigenvalue problem

$$\mathcal{H}_{\mathrm{CF}}\,\phi \;=\; E_{\mathrm{CF}}\,\phi, \quad \text{with } E_{\mathrm{CF}} \;=\; \begin{cases} E_{\mathrm{b_{1t}}}, & \text{for } \phi \;=\; |d_{x^2-y^2}\rangle \\ E_{\mathrm{a_{1t}}}, & \text{for } \phi \;=\; |d_{3z^2-r^2}\rangle \\ E_{\mathrm{b_{2t}}}, & \text{for } \phi \;=\; |d_{xy}\rangle \\ E_{\mathrm{e_t}}, & \text{for } \phi \;\in\; \{|d_{xz}\rangle\,, |d_{yz}\rangle\}, \end{cases} \tag{1.39}$$

gives rise to four different eigenenergy values as illustrated in Fig. 1.6c. Unlike the perfect octahedral coordination this uniaxial distortion gives rise to magnetic anisotropy which is discussed in the following section.

Further reduction of the symmetry is achieved for instance by an additional in-plane distortion. It can be accomplished by concurrent compression and elongation of the ligands on the x- and y-axis, respectively, by the amount of δc. This distortion then leads to an orthorhombic system and eventually splits the exclusively remaining degeneracy of the twofold e_{t}-level in (1.39). Additionally, and in contrast to the former tetragonal distortion, the eigenstates of $\mathcal{H}_{\mathrm{orth}}$ are not anymore the tesseral harmonics but a mixture of them. Therefore, $\mathcal{H}_{\mathrm{orth}}$ is treated as a perturbation of $\mathcal{H}_{\mathrm{oct}} + \mathcal{H}_{\mathrm{tetra}}$ for small orthorhombic distortions δc.

1.8 Hund's Rules and Quenching of the Orbital Moment

The character of the ground state of a free ion can be calculated by application of the empirical rules of Hund [19]. As they rule the occupation of the orbitals in terms of their quantum numbers, the magnetic moment of the ion is immediately determined. A given electron configuration in the ground state is, therefore, occupied by electrons so that

1. the total spin S is a maximum,
2. the total orbital angular moment L is maximal, by leaving the first rule preserved, and
3. the total angular moment, J, is equal to $|L \pm S|$ for subshells less($-$) or more($+$) than half-filled, respectively.

For example Ni^{2+} has $3d^8$ configuration. The free ion contains a non-magnetic argon configuration with eight additional electrons in the d-shell which then maximize the spin and the orbital moment to $S = 1$ and $L = 3$ with the quantum number of the total angular momentum resulting in $J = 4$, see also Fig. 1.7. The theoretical effective number of Bohr magnetons,

$$p = g\sqrt{J(J+1)}, \qquad \text{EFFECTIVE MAGN. MOMENT} \qquad (1.40)$$

$$g = \frac{3}{2} + \frac{S(S+1) - L(L+1)}{J(J+1)}, \qquad \text{LANDÉ FACTOR} \qquad (1.41)$$

then yields $p_{\text{theo}} = 5/4\sqrt{20} \approx 5.6$, while the experimental value from susceptibility measurements will be just approximately 3, if measured on Ni salts. The reason for the discrepancy is the quenching of the orbital moment of transition metal ions embedded in a crystalline environment. For Ni salts the number of Bohr magnetons is basically determined by the spin, $p_{\text{exp}} \approx 2\sqrt{S(S+1)} \approx 2.8$.

Figure 1.7: *$3d^8$ configuration of a free Ni^{2+} ion, determined by Hund's rules: The five energetically equivalent d-orbitals are each occupied by one electron with their spins aligned parallel (up) while the remaining three electrons have their spins aligned antiparallel (down) due to the Pauli principle. Resulting total spin: $S = 1$. The five parallel spins thereby cancel their total orbital angular momentum and the remaining three maximize it to $L = 2 + 1 + 0 = 3$. The resulting total angular momentum is $J = L + S = 4$.*

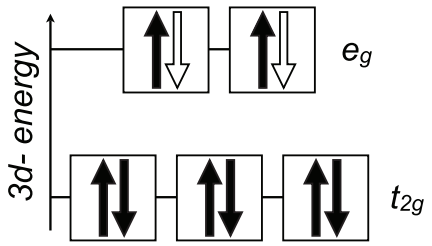

Figure 1.8: *High-spin configuration of the 3d-shell for a Ni^{2+}-ion. See text for details.*

In the following explanation, the spin-orbit coupling is neglected. The symmetry of the crystal hosting the Ni ions is cubic at the most. In the cubic case the d-shell orbitals are lifted in energy by the CF splitting Δ as shown in Fig. 1.6b. Five of eight electrons occupy different orbitals collectively aligning their spins parallel. The remaining three electrons fill the t_{2g}-level completely, and the net total spin of $S = 1$ results, compare Fig. 1.8. The total angular momentum for free ions is $L = 3$ after Hund. In Tab. 1.1 the action of $\mathbf{L}$ on the d-orbitals is shown. Therefore, the expectation value of the L_z-operator in the e_g manifold (the only magnetic one) vanishes,

$$\langle d_{3z^2-r^2}|\, L_z\, |d_{3z^2-r^2}\rangle \;=\; 0\; \langle d_{3z^2-r^2}|\; d_{3z^2-r^2}\rangle = 0 \tag{1.42}$$

$$\langle d_{x^2-y^2}|\, L_z\, |d_{x^2-y^2}\rangle \;=\; 2i\; \langle d_{x^2-y^2}|\; d_{xy}\rangle = 0, \tag{1.43}$$

independently from the actual choice of the e_g basis. The same is true for $\langle L_x\rangle$, $\langle L_y\rangle$ and, therefore, $\langle\, \mathbf{L}^2_{e_g}\,\rangle$. Consequently, the orbital moment is quenched by the CF.

The quenching is not always complete like in the previous case. In a cubic CF the orbital moment of configurations $3d^1$, $3d^2$, $3d^6$, and $3d^7$ is quenched only partially and the system is then said to have a pseudo total angular momentum of $\tilde{L} = -1$. However, if the symmetry is lowered to such a degree that the orbital energy degeneracy is fully lifted (all representations are 1-dimensional), the quenching will lead to $\tilde{L} = 0$ as a result of the basis states then being real functions [18]—the tesseral harmonics.

	$d_{3z^2-r^2}$	$d_{x^2-y^2}$	d_{xy}	d_{yz}	d_{xz}
L_x	$-i\sqrt{3}d_{yz}$	$-id_{yz}$	id_{xz}	$id_{x^2-y^3} + i\sqrt{3}d_{3z^2-r^2}$	id_{xy}
L_y	$i\sqrt{3}d_{xz}$	id_{xz}	$-id_{yz}$	id_{xz}	$id_{x^2-y^3} - i\sqrt{3}d_{3z^2-r^2}$
L_z	0	$2id_{xy}$	$-2id_{x^2-y^2}$	$-id_{xz}$	id_{yz}

Table 1.1: *How the components of the orbital momentum operator $\mathbf{L}$ act on the d-orbitals. The e_g subspace for instance is completely mapped into the orthogonal t_{2g} by $\mathbf{L}$: $L_\alpha\,\{e_g\} \subset \{t_{2g}\}$, $\alpha = x, y, z$. Taken from [20].*

1.9 Effective Spin Hamiltonian and Magnetic Anisotropy

An optical excitation of an atom or ion from the ground state to the first excited state is of the order of eV and in comparison the microwave or mm/sub-mm wave energy used in ESR is rather low (section 2). Hence, for a quantum mechanical description it is reasonable to consider only the ground state and few, if any, nearby states from the infinite number of atomic states [21].

As seen in the former sections, magnetic resonance only occurs within multiplets which are split either initially by the CF (section 1.7) or externally by a magnetic perturbation (section 1.5). An effort to reduce the quantum mechanical description to the scope of ESR [12] hence making it more transparent and easier to handle is the transition from the Hamiltonian which was deduced in the former section,

$$\mathcal{H}_0 \,+\, \mathcal{H}_{\mathrm{CF}} \,+\, \mathcal{H}_{\mathrm{Z}} \,+\, \mathcal{H}_{\mathrm{LS}}, \tag{1.44}$$

to the so called *effective spin Hamiltonian* $\mathcal{H}_{\mathrm{eff}}$. The formalism utilizes the effective spin $\tilde{S}$ which has proven to be sufficient to describe a multiplet of $2\tilde{S}+1$ spin levels. This approach is widely used in various spectroscopic methods in order to find a suitable short-cut which allows to interpret and classify the obtained spectra without using fundamental theories [22].
It should be noted that the effective spin Hamiltonian is usually rather *empirically composed* than *deterministically deduced* from theory. For example the consideration of the technique which is actually used determines already an energy scale, and structural properties of the compound define a certain coordination symmetry. The effective spin Hamiltonian is a form of description which is adapted to the subject and, therefore, highly specific instead of universal.

For ESR on iron group compounds the Zeeman energy (1.26) and the spin-orbit coupling (1.30),

$$\mathcal{H}_{\mathrm{Z}} \,+\, \mathcal{H}_{\mathrm{LS}} \,=\, \mu_{\mathrm{B}}\,\mathbf{H}\cdot(\mathbf{L} \,+\, g_{\mathrm{e}}\,\mathbf{S}) \,+\, \lambda\,\mathbf{L}\cdot\mathbf{S}, \tag{1.45}$$

are both of the same order of $10^{-2}\,\mathrm{eV}$ and, therefore, simultaneously treated as a perturbation of the non-degenerate ground state $|0, m_S\rangle$ (the orbital ground state $|0\rangle$ is here a linear combination of the d-shell orbitals) found by diagonalization of $\mathcal{H}_0 + \mathcal{H}_{\mathrm{CF}}$. The result from the calculation of the perturbation series up to the second order reads

$$\mathcal{H}_{\mathrm{eff}} \,=\, \underbrace{\mu_{\mathrm{B}}\,g_{\mathrm{e}}\,\mathbf{H}\cdot\tilde{\mathbf{S}}}_{1^{\mathrm{st}}\ \mathrm{order}} \underbrace{-\,\mu_{\mathrm{B}}\,\mathbf{H}\cdot(2\lambda\boldsymbol{\Lambda})\cdot\tilde{\mathbf{S}} \,-\, \lambda^2\,\tilde{\mathbf{S}}\cdot\boldsymbol{\Lambda}\cdot\tilde{\mathbf{S}} \,-\, \mu_{\mathrm{B}}^2\,\mathbf{H}\cdot\boldsymbol{\Lambda}\cdot\mathbf{H}}_{2^{\mathrm{nd}}\ \mathrm{order}}. \tag{1.46}$$

The first term in (1.46) gives the Zeeman energy solely caused by the spin, since the orbital contribution vanishes in first order perturbation theory owing

to $\langle 0\,|L_z|\,0\rangle = 0$ for non-degenerate orbital ground states. In this sense, the CF is already a first order effect. The spin-orbit coupling affects only in second order in virtue of the $\mathbf{\Lambda}$ tensor. It results from the admixture of different orbital states $|n\rangle$ to the ground state $|0\rangle$ by the application of the operator of the orbital momentum $\mathbf{L}$,

$$\Lambda_{ij} = \sum_{n\neq 0} \frac{\langle 0\,|L_i|\,n\rangle\,\langle n\,|L_j|\,0\rangle}{E_n - E_0}, \tag{1.47}$$

and, therefore, reflects the symmetry of the CF.

The last term in (1.46) describes the temperature-independent paramagnetism (TIP, Van Vleck term), $-\mu_\mathrm{B}^2\,\mathbf{H}\cdot\mathbf{\Lambda}\cdot\mathbf{H}$. Since the TIP yields a constant contribution to all spin states it is not recognized with ESR and hence excluded from the spin Hamiltonian [21]. Nevertheless, its knowledge is useful for the interpretation of magnetization data which is often used as a starting point for the modeling of ESR spectra.

With introduction of matrices for the g-factor $g_{ij} = g_\mathrm{e}\delta_{ij} - 2\lambda\Lambda_{ij}$ and the so called single ion anisotropy $D_{ij} := -\lambda^2\Lambda_{ij}$ the standard notation of Hamiltonian (1.46) is obtained,

$$\mathcal{H}_\mathrm{eff} = \underbrace{\mu_\mathrm{B}\mathbf{H}\cdot\bar{\bar{g}}\cdot\mathbf{S}}_{\text{Zeeman energy}} + \underbrace{\mathbf{S}\cdot\mathbf{D}\cdot\mathbf{S}}_{\text{eff. CF Ham.}}, \qquad \text{SPIN HAMILTONIAN} \tag{1.48}$$

where the tilde labeling of the effective spin was omitted to keep the notation clear. Operation of (1.48) is restricted to the spin space and the orbital momentum does not need to be considered since it is implicitly contained. The anisotropy is rendered by $\bar{\bar{g}}$ and $\mathbf{D}$: While the energy splitting due to the Zeeman effect depends on both the field strength and its direction as a result of $\bar{\bar{g}}$, the single ion anisotropy $\mathbf{D}$ lifts the degeneracy of different spin orientations already in absence of a magnetic field in the case of $S > 1/2$. For $S = 1/2$ Kramers theorem [23] of spin parity predicts a degeneracy owing to the half-integer spin in spite of the CF.

Magnetic Anisotropy due to Single Ion Anisotropy

In order to clarify the properties of the effective CF Hamiltonian $\mathbf{S}\cdot\mathbf{D}\cdot\mathbf{S}$ in (1.48) the real tensor $\mathbf{D}(\Lambda_{ij})$ is diagonalized with eigenvalues D_{xx}, D_{yy}, and D_{zz}. Introduction of the prevalent parameters (e.g. [22])

$$D = D_{zz} - (D_{xx} + D_{yy})/2 \tag{1.49}$$

$$E = (D_{xx} - D_{yy})/2 \tag{1.50}$$

and subtraction of the constant $D\,S(S+1)/3$ finally yields the more descriptive form,

$$\mathbf{S}\cdot\mathbf{D}\cdot\mathbf{S} \longrightarrow \underbrace{D\left(S_z^2 - \frac{1}{3}S\,(S\,+\,1)\right)}_{\text{axial anisotropy}} + \underbrace{\frac{1}{2}E\left(S_+^2\,+\,S_-^2\right)}_{\text{transverse anisotropy}}, \tag{1.51}$$

which is often found in literature [12]. The shift operators $S_\pm$ are defined in (1.55)–(1.56). The axial anisotropy term in (1.51) primarily depends on S_z^2 and is, therefore, diagonal, when operating on the pure spin states $|m_S\rangle$. The transverse anisotropy gives rise to an admixture of the states in virtue of appearing non-diagonal matrix elements $\langle m_S \pm 2|\, S_\pm^2\, |m_S\rangle$. Thus, it should be remarked that an admixture of pure spin states in zero field requires at least a finite transverse anisotropy *and* a spin of $S \geq 1$. Indeed, with the aid of an external field, a spin state admixture is possible even without a transverse anisotropy for $S > 1/2$ as long as it is not aligned parallel or antiparallel to the anisotropy axis.

It is obvious that in cubic symmetry ($D_{xx} = D_{yy} = D_{zz}$) both D and E vanish and the complex is magnetically isotropic. The more interesting case of an axial symmetry by means of a finite uniaxial anisotropy D with an additional external field aligned to this anisotropy axis is discussed now. The situation and the corresponding spin levels are illustrated in Fig. 1.9 by means of a central ion with $S = 2$ which is coordinated by a uniaxially distorted octahedron of ligands. While the case of $S = 1$ is principally also contained in the figure—and can be easily obtained just by ignoring the spin states $|\pm 2\rangle$ and their implications—the study of a spin 2 system is more conclusive, because it shows more universally how the single ion anisotropy applies to different spin states: subsequent spin levels $|m_S\rangle\,, |m_S - 1\rangle$ are lifted by the energy of $D\,(2|m_S| - 1)$ which results in an overall splitting of DS^2.
In Fig. 1.9a the octahedron is distorted by an elongation of the apex oxygen bonds on the z-axis which is accompanied by a compression of the oxygen bonds in the xy-plane. This scenario corresponds to a positive sign of D. Therefore, the spin precesses in the xy-plane and the ground state is a spin singlet $|0\rangle$ which is clearly non-magnetic, at least in absence of an external field. By applying an external field, the situation is changing. The first excited spin state $|-1\rangle$ has a negative slope and, therefore, it crosses the singlet at the critical field $H_{\mathrm{c}1}$. For similar reasons $|-2\rangle$ undergoes a level-crossing with $|-1\rangle$ at $H_{\mathrm{c}2} > H_{\mathrm{c}1}$. Consequently, for an increasing external field the ground state changes at the critical fields $H_{\mathrm{c}|m_S|}$ from $|m_S + 1\rangle$ to $|m_S\rangle$ for every $m_S \leq -1$.
It is noteworthy that for fields $0 < H < H_{\mathrm{c}1}$ the ground state remains $|0\rangle$ indeed, and, therefore, is non-magnetic as it is for $H = 0$. Nevertheless, in literature these kind of ground states are sometimes referred to as *diamagnetic ground states* which basically emphasizes the—usually dominating, but here—missing paramagnetic moment while accommodating the remaining and always present diamagnetic term in (1.23).

The reverted scenario is shown in Fig. 1.9b. Here, the apex oxygen bonds are shortened while the oxygen-square in the xy-plane is stretched. This arrangement leaves D with a negative sign and results in the z-direction becoming the easy axis of the system. The favored ground state is now magnetic and twofold degenerate in zero field, $|\pm 2\rangle$. It becomes $|-2\rangle$ with the application of a finite external field. (The case of $S = 1$ corresponds to a twofold degenerate ground state $|\pm 1\rangle$ in zero field, and $|-1\rangle$ for a finite field, respectively.)
By an additional in-plane distortion—accomplished by concurrent compression and elongation of the ligands on the x- and y-axis, respectively,—the symmetry is lowered to orthorhombic and also E in (1.51) becomes finite. Therefore, this distortion corresponds to the introduction of a transverse anisotropy. For systems with integer spin the degeneracy is then completely lifted, while for half-integer spins degenerate pairs of $|\pm m_S\rangle$ remain. These Kramers doublets are a consequence of the time reversal symmetry of the Hamiltonian [12, 23].

For even lower symmetries the CF Hamiltonian (1.48) is not anymore sufficient for

Figure 1.9: *Zero field splittings and field dependent spin state energies for $H \perp z$. a) The ground state is non-magnetic, $|0\rangle$, for a positive D-value which means that the spin precesses in the xy-plane. With increasing external field the state $|-1\rangle$ crosses $|0\rangle$ at the critical field H_{c1}, and, therefore, becomes the ground state for $H_{c1} < H < H_{c2}$ until finally $|-2\rangle$ becomes the favored spin orientation for $H > H_{c2}$ (not shown). b) Negative values of D cause the spin to precess parallel to the symmetry axis. In zero field the ground state is twofold degenerate. For details see text. Calculation: $|D| = 1\,K$, $g = 2$.*

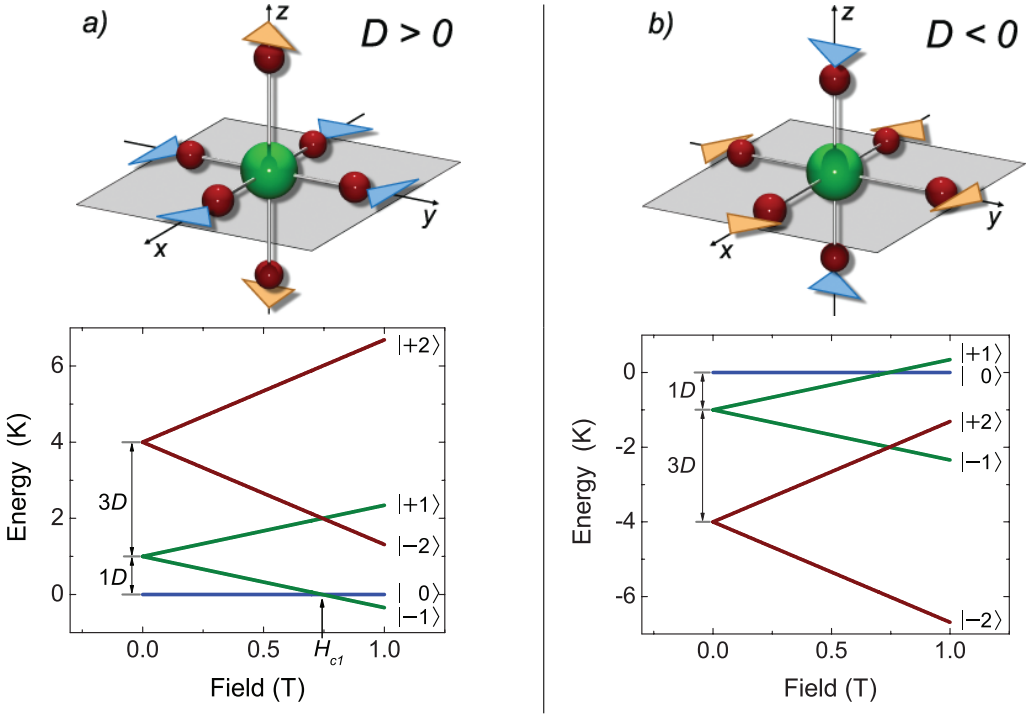

the description. A more general approach considers higher order spin operators $\mathbf{S}^k$ where k is an even integer. Similar to the description of vibrational modes for molecules it is possible to find a formulation to describe more complex distortions as they are given by low symmetry crystal fields. In this picture, a distortion is interpreted as an operation of a function of spin operators. As the space of distortions is finite, an irreducible representation of the finite set of operators can be found for a particular symmetry. The space of distortions is then spanned by a set of irreducible tensor operators (ITO) which basically reflect the symmetry of the actual CF. The treatment is subject of the tensor algebra of ITOs [12, 24–27].

As a matter of fact, higher order distortions (refer e.g. [28]) must be calculated in some situations. However, for the majority of the cases the consideration of the basic lowest order distortions leads often to a sufficient characterization of the experimental data and they remain the leading terms of the description. Another point is that in particular in the field of molecular magnetism, the samples are often available only in poly-crystalline form. This fact renders even a basic description possible only by paying high computational costs (section 1.11).

Anisotropic Gyromagnetic Value

The total angular momentum may be quenched to an increasing degree as the orbital degree of freedom disappears. As the spin-orbit coupling tends to mix the d-states again, it turns out as a mechanism to restore at least some of the angular momentum (section 1.8).

A real $\bar{\bar{g}}$-matrix in (1.48) is diagonal with principal values parallel and perpendicular to the field: $g_\parallel$, $g_{\perp 1}$, and $g_{\perp 2}$. Similar to the single ion anisotropy, the g-values of all principal directions are identical in cubic symmetry, but with a possible deviation from the spin only value, g_e. In general, an axial symmetry gives rise to anisotropy of the g-factor, $g_\parallel \neq g_{\perp 1} = g_{\perp 2}$. As an example, the $3d^3$, $3d^8$ and $3d^9$ configurations give the following corrections $\Delta g_{\parallel,\perp} = g_{\parallel,\perp} - g_\mathrm{e}$ for a tetragonal symmetry (e.g. [12]):

$\Delta\bar{\bar{g}}_{ij}$	$3d^3$	$3d^8$	$3d^9$
$\parallel$	$-8\lambda\Delta_0^{-1}$	$-8\lambda\Delta_0^{-1}$	$-8\lambda\Delta_0^{-1}$
$\perp$	$-8\lambda\Delta_1^{-1}$	$-8\lambda\Delta_1^{-1}$	$-2\lambda\Delta_1^{-1}$

(1.52)

The energies $\Delta_{0,1}$ represent the splittings between the levels $e_\mathrm{t}, b_{1\mathrm{t}}$ and $b_{2\mathrm{t}}, b_{1\mathrm{t}}$, respectively, illustrated in Fig. 1.6. Note the sign of λ in equ. (1.30).

Table 1.52 reveals that the anisotropy of the g-factor is a result of the cooperation of the spin-orbit coupling (λ) and the CF ($\Delta_{0,1}$), and once more shows the close relation of both phenomena in solids.

1.10 Exchange Coupled Spins

It is straightforward to expand the formalism of the effective spin Hamiltonian (1.48) to multiple not necessarily interacting spin centers just by adding the dedicated Zeeman energies and single ion anisotropies of the individual spins. By doing so, the main inconveniences arise from the increasing dimension of the Hilbert space which indeed creates a remarkable impact yet on the manageability in concrete computations. In fact, the dimension of the spin space for five coupled spin centers can already grow to the impressive dimension of $6^5 = 7776$ (e.g. Mn_5^{II}) complicating even pretended easy calculations by the pure amount of data for the matrix operators (see also section 1.11).

In the following sections, the sum of two spin operators $\mathbf{S}_1$ and $\mathbf{S}_2$ with dimensions $\dim_{1,2} = 2S_{1,2} + 1$ is associated with the result of the operation

$$\mathbf{S}_{\text{tot}} = \sum_{i=x,y,z} \left[S_{1k} \otimes \mathbf{1}_{\dim_2} + \mathbf{1}_{\dim_1} \otimes S_{2k} \right] \cdot \mathbf{e}_k, \tag{1.53}$$

where S_{ik} is the kth component of the ith spin operator, $\mathbf{1}_{\dim_j}$ is the j-dimensional unity matrix and $\mathbf{e}_k$ the unity vector of the k-direction.
Also the spin states are calculated by the outer product of the individual states,

$$|m_{S_1}, m_{S_2}\rangle = \left\{ \mathbf{1}_{\dim_1} |m_{S_1}\rangle \right\} \otimes \mathbf{1}_{\dim_2} + \mathbf{1}_{\dim_1} \otimes \left\{ \mathbf{1}_{\dim_2} |m_{S_2}\rangle \right\}. \tag{1.54}$$

As a result of this construction, spin operators associated with different spins commute, $S_{i\alpha} \cdot S_{j\beta} = S_{j\beta} \cdot S_{i\alpha}$ for $i \neq j$, i.e. each operator "acts" in its own subspace without interfering with alien spin states. With (1.53) and (1.54) the generalized spin operators act on a given spin state $|m_{S_1}, m_{S_2}\rangle$ in the following manner,

$$S_{ix} |m_{S_1}, m_{S_2}\rangle = \frac{1}{2} \left(S_{i+} + iS_{i-} \right) |m_{S_1}, m_{S_2}\rangle \tag{1.55}$$

$$S_{iy} |m_{S_1}, m_{S_2}\rangle = \frac{1}{2i} \left(S_{i+} - iS_{i-} \right) |m_{S_1}, m_{S_2}\rangle \tag{1.56}$$

$$S_{iz} |m_{S_1}, m_{S_2}\rangle = m_{S_i} |m_{S_1}, m_{S_2}\rangle \tag{1.57}$$

$$S_{i\pm} |m_{S_1}, m_{S_2}\rangle = \sqrt{S_i(S_i+1) - m_{S_i}(m_{S_i} \pm 1)} \, |m_{S_1} \pm \delta_{1i}, m_{S_2} \pm \delta_{2i}\rangle. \tag{1.58}$$

More complex spin systems comprising $n > 2$ spins are composed by the subsequent application of (1.53) and (1.54), respectively.

Exchange coupling

The simplest form of interaction between two spins is given by the bilinear form

$$\mathcal{H}_{\text{ex}} = \mathbf{S}_1 \cdot \mathbf{J}_{12} \cdot \mathbf{S}_2, \tag{1.59}$$

with the exchange matrix $\mathbf{J}_{12}$ admixing the spins. A well-defined decomposition of $\mathbf{J}_{12}$ is given e.g. by Moriya [29],

$$\mathcal{H}_{\text{ex}} = \underbrace{J_{12}\,\mathbf{S}_1 \cdot \mathbf{S}_2}_{\text{isotropic}} + \underbrace{\mathbf{S}_1 \cdot \mathbf{D}_{12} \cdot \mathbf{S}_2}_{\text{symmetric}} + \underbrace{\mathbf{d}_{12} \cdot (\mathbf{S}_1 \times \mathbf{S}_2)}_{\text{antisymmetric}}. \tag{1.60}$$

In the so called strong exchange limit the isotropic or Heisenberg-term [30] J_{12} is predominant and the total spin (1.53) remains a good quantum number with values according to

$$|S_1 - S_2| \leq S \leq S_1 + S_2. \tag{1.61}$$

Every allowed quantum number for the total spin S represents a spin-multiplet. The multiplet energies are defined by

$$E_{\text{iso}} = \frac{1}{2} J_{12} \left[S(S+1) - S_1(S_1+1) - S_2(S_2+1) \right], \quad J_{12} < 0 \rightarrow \text{FM}. \tag{1.62}$$

As in literature different denotations for E_{iso} are in use, it should be noted that $J_{12} < 0$ corresponds to a ferromagnetic (FM) exchange in (1.61), while a positive sign of the exchange parameter is associated with an antiferromagnetic (AFM) exchange coupling.

1.11 Modeling

The description of the magnetic properties of 0D molecular clusters has an essential convenience, when compared to systems of higher dimensionality: the dimension of the Hilbert space will be finite, at least, if excited electronic states can be neglected in favor of the well separated ground state. This very fact enables to define a very compact and to a great extend transparent spin Hamiltonian $\mathcal{H}$. The main objective in the analysis of ESR data is to find a model system which principally describes the appearing

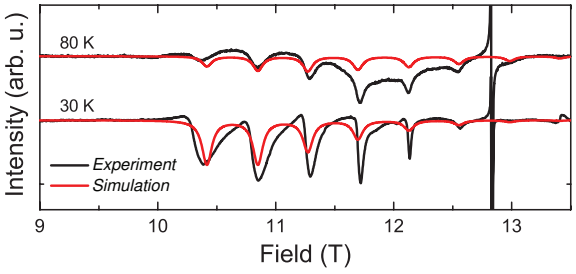

Figure 1.10: *Experimental (black) and simulated (red) ESR spectra of NiBiAz, see section 3.5 for details.*

resonance signals by means of the spectra's properties. Due to the ESR method being a local probe a proper spin Hamiltonian should principally reproduce a bunch of spectrum features at the same time—a fact which raises complex requirements to fit procedures and renders them a time-consuming undertaking in consideration of the numerous fit parameters and the often high dimensionality of the spin space. A small selection of characteristics commonly taken into consideration for the analysis of a set of ESR spectra is given e.g. by the number of resonance lines, the position of their resonance fields among each other and with respect to the external magnetic field, the lineshape in terms of the line intensities, their ratios among multiple lines and the temperature dependence. Further important points are of course frequency and angular dependences. Generally, the number of items clearly increases with the rising comprehensiveness of the considered system. Additionally, a potential fit procedure is complicated by admixtures of dispersion and absorption portions of each single resonance, the overlap of resonance lines and, finally, the potential presence of non-linear backgrounds. Almost any of the mentioned issues can be found in the example shown in Fig. 1.10. After all, fit procedures for ESR spectra are definitely possible to develop, but will be successful only in special cases under subset conditions.
However, in order to check the quality of the considered model and for improving the accuracy of the determined parameters it is desired to have at least the possibility to simulate magnetic resonance spectra where the comparison of experimental and calculated spectra may give important conclusions for the refinement of the model parameters.

Although this task is difficult in general, it remains practicable in cases of not too large quantum numbers for the total spin and a sufficiently high symmetry for the ligand field. In particular for single crystals the situation is quite comfortable even in the case of overlapping resonance lines.
On the other hand, the analysis becomes far more challenging for anisotropic poly-crystalline samples which exhibit no discrete ESR lines, but *powder averaged* absorption signals.

Scope of the Simulation Program

In the framework of this thesis a program was developed for the computation of ESR powder spectra and a fit algorithm for magnetization curves of poly-crystalline samples. In order to keep the code simple and transparent for easy adaptions to individual problems it is written in the script based language of MATHEMATICA™ [31] from Wolfram Research, Inc. The effort was to gain an instrument for the determination of exchange coupling parameters from susceptibility data and to control the results from the ESR analysis by computing a spectrum and comparing it with the experimental data. The program provides the calculation of

- arbitrary single spin operators $\mathbf{S}$ by declaration of S
- products of spin operators, e.g. $\mathbf{S}_1 \cdot \mathbf{S}_2$, $\mathbf{S}^4$ etc.
- equivalent Steven operators O_2^0, O_2^2, O_4^0, O_4^2, ...
- the complete spin Hamiltonians (magnetic exchange plus magnetic energy)
- the field dependences of the spin levels by a full matrix diagonalization for a given frequency
- transition probabilities and intensities
- the powder averaged ESR spectrum based on Lorentzian or Gaussian (or arbitrary) lineshapes
- the temperature dependence of the ESR spectrum.

Furthermore, the program includes an algorithm for the extraction of the energy of dedicated spin states into a score table in order to gain access to the numerical energy eigenfunctions $E_m(H)$ of the eigen(spin)states. Such a capability is useful for picking e.g. the n lowest lying energy levels out of a spectrum with hundreds of crossing levels.
Generally, the listed features are rather a foundation of classes than an integrated program which makes the code easily extensible for future necessities.

Simulation Procedure

Independently from the complexity of the spin structure the starting point for the simulation of an ESR spectrum is always one and the same. Assuming the existence of an appropriate spin Hamiltonian which describes the interacting spins of the zero-dimensional magnet, the procedure is to basically calculate the $2\,S\,+\,1$ eigen(spin)states $|\chi_1\rangle, |\chi_2\rangle, \ldots, |\chi_{2S+1}\rangle$ and their associated eigen(energy)values $E_1, E_2, \ldots, E_{2S+1}$ by a matrix diagonalization as a function of the external field H. For a certain excitation frequency ν the resonance fields are then calculated by application of the resonance condition, (1.4). Therefore, the equation

$$[E_m(H)\,-\,E_n(H)]\,-\,h\nu\,=\,0 \qquad 1\,\leq\,n\,<\,m\,\leq\,2\,S\,+\,1 \tag{1.63}$$

is solved for the roots $H\,=\,H_\alpha^{m,n}$ within the desired field range $[H_{\mathrm{start}}, H_{\mathrm{end}}]$. The indices m and n thereby specify the participating spin-levels and $\alpha = 1, 2, ...$ distinguishes multiple resonances between the same spin-levels in the case there is more than one. This step requires a maximum of $S\,(2\,S+1)$ equations to solve. The intensity of the spin transition at the resonance field $H_\alpha^{m,n}$,

$$I_\alpha^{m,n}\,\propto\,|\rho_m\,-\,\rho_n|\cdot p_{m\leftrightarrow n}(H_\alpha^{m,n}) \tag{1.64}$$

depends on the polarization and the transition probability $p_{m\leftrightarrow n}$ between the involved spin states $|\chi_m\rangle$ and $|\chi_n\rangle$. The latter is determined by the spin Hamiltonian of the system and calculated by means of the matrix element associated with the transition,

$$p_{m\leftrightarrow n}(H_\alpha^{m,n}) \;=\; \langle\chi_m(H_\alpha^{m,n})|\, S_x\, |\chi_n(H_\alpha^{m,n})\rangle^2 . \tag{1.65}$$

Conveniently, the selection rules for dipole radiation are included implicitly in (1.65) so that an additional test is not necessary: a forbidden transition after (1.5) will just give a vanishing probability for that transition. The polarization density $|\rho_m - \rho_n|$ in (1.64) comprises the occupation densities $\rho_{m,n}$ of the two energy levels concerned to the transition. They are computed by the Boltzmann statistics,

$$\rho_m(T, H_\alpha^{m,n}) \;=\; \frac{\exp(-\frac{E_m}{k_\mathrm{B}\,T})}{\sum_{n\neq m}\,\exp(-\frac{E_m-E_n}{k_\mathrm{B}\,T})}, \tag{1.66}$$

for the system at the temperature T. Finally the single crystal spectrum P_ν^{sc} is generated by the superposition of the individual ESR transition lines

$$P_\nu^{\mathrm{sc}}(H;T) \;\propto\; \sum_{m\neq n,\alpha} I_\alpha^{m,n}\, f(H, H_{0,\alpha}^{m,n}, \Delta H), \tag{1.67}$$

by weighting a shape function (for instance Lorentzian or Gaussian shape) of linewidth ΔH with the intensity $I_\alpha^{m,n}$ for each single recognized transition.

As the outlined procedure includes a full matrix diagonalization its limitations are due to the computational costs. In order to maximize the scope of systems which can be treated in spite of the brute force approach the objective in the implementation of the algorithm is the avoidance of unnecessary computations. The following examination outlines the minimum expenses to be expected. The dimension of the Hilbert space for a system of N coupled spin centers with the spin quantum numbers $S_1, S_2, \ldots, S_N$ is the product of the N spin multiplicities

$$\dim(\mathcal{H}) \;=\; \prod_{n=1}^{N} 2S_n \;+\; 1. \tag{1.68}$$

In the very majority of the cases the diagonalization of the Hamiltonian of such systems can be accomplished only numerically. Hence, the solution of the resonance condition (1.63) is not anymore analytical and, therefore, the energies $E_m(H)$ of the spin states as a function of the field have to be calculated by numerical diagonalization. Therefore, the field interval of the simulation $[H_{\mathrm{start}}, H_{\mathrm{end}}]$ is scanned by a reasonable step-size δH resulting in the number of $|H_{\mathrm{start}} - H_{\mathrm{end}}|/\delta H$ diagonalizations.

	sc	tetra	orth	–
$\delta\theta = \delta\phi = 1°$	1	90	1 800	64 800

Table 1.2: *Relative computation effort for a single crystal spectrum (sc), a powder spectrum of a system with tetragonal (tetra), orthorhombic (orth) or without symmetry.*

Powder Averaging

In case of present magnetic anisotropy the expression for the single crystal spectrum (1.67) becomes angular dependent by means of both the intensity I and the resonance fields H_0. Therefore, for modeling a poly-crystalline sample the distribution of the different orientations of the crystallites with respect to the external field has to be taken into account in the simulation.
A straightforward way for modeling this powder averaging effect is to sum up proper weighted single crystal spectra for diverse orientations of the external field vector $\mathbf{H}(\theta, \phi)$. The angles θ and ϕ represent the spherical coordinates of the unit sphere. Benefitting from the CF symmetry properties it is thereby often sufficient to vary the field orientation only within a suited fraction of the solid angle for a reduction of the calculation efforts. For example a uniaxial symmetry of the CF reduces the computation efforts to varying only the polar angle θ by the step size $\delta\theta$ on the quarter circle within the interval between the hard(easy) axis to the easy(hard) plane of the single crystal. For orthorhombic systems also the azimuth angle ϕ is varied (by $\delta\phi$) but instead of covering the whole unit sphere, one-eighth of it is sufficient to get the full information.
The resulting single crystal spectra for different field orientations are then weighted by the factor $\sin\theta$ to consider the relative frequency of the crystal orientations and are eventually summed up to the poly-crystalline spectrum,

$$P_\nu^{\mathrm{pc}}(H;T) \propto P_\nu^{\mathrm{sc}}(H,\theta,\phi;T)\,\sin\theta. \tag{1.69}$$

The relative computation effort for selected symmetries is shown in Tab. 1.2.

2 Experimental

Energy Scale of ESR

While optical transitions range on the scale of electronvolt (eV), a magnetic transition between spin states costs roughly between two and five orders of magnitude less energy. The actual transition energy depends on the applied external field and the intrinsic properties of the spin system in terms of the spin S, the g-factor or the presence of energy gaps, e.g. owing to lattice distortions.
An illustrative example is given by a hypothetical magnetic transition between two spin levels which are split by the energy of 5×10^{-5} eV (~ 0.5 K). This low energy excitation might be due to the spin transition between states in zero field which are split by incidence of magnetic anisotropy. The same energy is required for the spin flip of the free electron in 0.35 T observable in commercially available X-Band spectrometers operating slightly below 10 GHz. An example for the far energy side is given by an excitation energy of 5×10^{-3} eV corresponding to electron spin resonance of the same electron at 1 THz in a field of 35 T.
Consequently, the typical energy scale for ESR is given by 1–50 K where 1 K corresponds to 8.62×10^{-5} eV. The use of the unit eV for energies is unusual in ESR and, therefore, energies will be always given in Kelvin throughout this thesis. However, the second popular energy unit which is frequently used is given by the reciprocal wavelength, the wavenumber λ^{-1}. The energy of 1 K corresponds thereby to $0.695\,\mathrm{cm}^{-1}$. The conversion to the associated excitation frequency gives 20.8 GHz. This frequency causes magnetic resonance for a free electron at the field of ~ 0.74 T.

$$h\nu \;=\; k_\mathrm{B}T \;=\; \frac{hc}{\lambda} \;\sim\; g_\mathrm{e}\,\mu_\mathrm{B}H \qquad \textsc{Conversion} \tag{2.1}$$

For commonly used constants refer to appendix A.4. The frequency/field relation in (2.1) is due to the resonance condition (1.4). The latter, furthermore, implies resonance fields between 7 and 35 T for high field ESR at typical frequencies between 200 and 1000 GHz. Although, static magnetic fields of ~ 20 T are obtained by the application of superconducting coils at liquid helium temperature, the upper field limit is reached mainly by hybrid magnets[1] or pulsed field methods[2].

The ESR method is classified in the electromagnetic spectrum for different types of spectrometers in Fig. 2.1. The microwave domain starts at about 1 GHz which

[1] e.g. 45 T by combining an 11 T superconducting coil with a 34 T water-cooled resistive insert (National High Magnetic Field Laboratory, Tallahassee, Florida)
[2] e.g. up to ~ 80 T for 10^{-3}-1 s (Los Alamos, Leuven, Osaka)

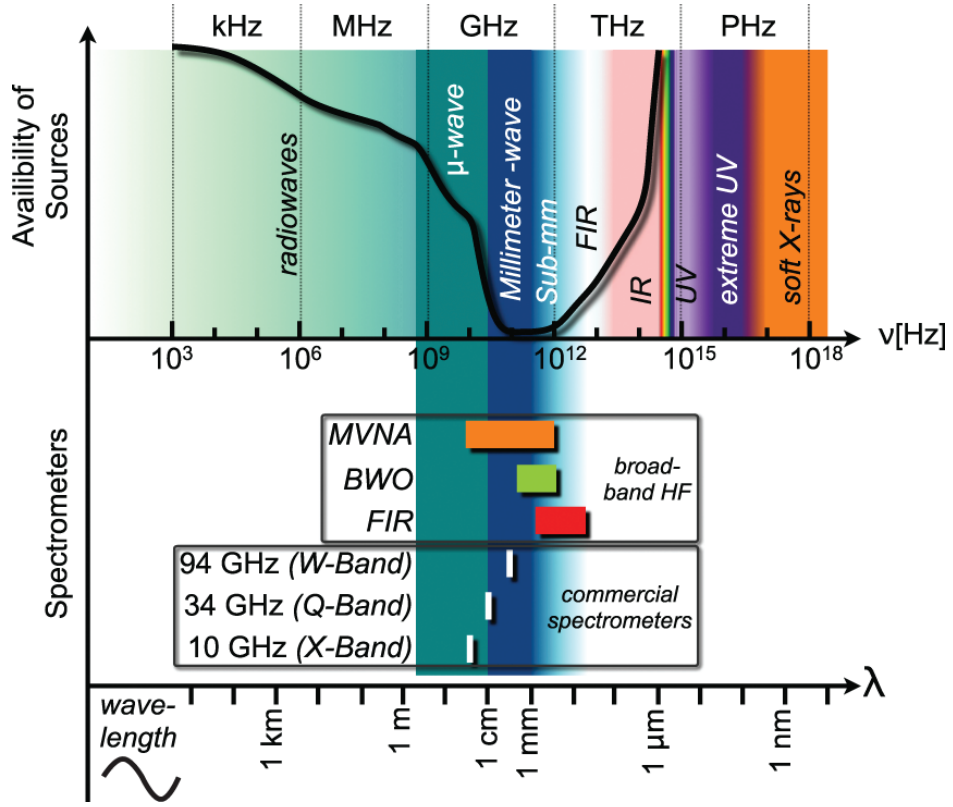

Figure 2.1: *The electromagnetic spectrum. The upper panel shows a representation of the THz-gap, see text for explanation. In the lower panel, diverse versions of commercial and broad-band spectrometers are assigned to their domain of operation in the spectrum.*

lies energetically above the very broad range of the radio frequencies (RF). It runs through the centimeter and millimeter wave intervals and finally merges within the sub-mm domain into the far infrared clearly beyond frequencies of several THz. The upper part of the diagram shows a graph intending to represent the situation of the availability of radiation sources with respect to the generated frequency. While the resources for the generation of radio frequencies are huge, they tend to become less with approaching the μ-wave regime and abruptly fall down for mm-waves. The situation is similar, when starting in the optical regime of visible light and passing the infra- and far infrared intervals. The lack of sources in the mm and sub-mm domain is referred to as the so-called terahertz gap. It is primarily originated by the failure of the usually employed generation and measurement techniques in the two broad areas at lower and higher frequencies. While conventional RF methods work well up to approximately 1 GHz, above this frequency, stray capacitances and effects related to finite cable lengths prevent the precise measurement of the components of the optical conductivity. At the upper side of the frequency spectrum conventional optical methods become progressively ineffective as the frequency is decreased below about 600 GHz, mainly because of

the decreasing source intensity. Another difficulty arises from finite sample size effects, i.e., the wavelength becomes comparable to the sample dimension [32]. In the lower part of Fig. 2.1 some established types of spectrometers are classified with respect to their operation frequencies. Conventional spectrometers thereby start in the lower frequency range. Most commonly used are devices operating in the X-Band at 9.5 GHz at wavelengths of ~ 3 cm. Q- and W-Band spectrometers work at 34 GHz (~ 1 cm) and 94 GHz (~ 3 mm), respectively, and are principally improvements of the X-Band technique. While these facilities operate at a fixed frequency, the frequency of the broad band spectrometers denoted with MVNA and BWO are tunable within orders of magnitude (8 GHz up to ~ 1 THz).

The following section gives the reasons for the recent trend of applying high frequency ESR. Therefore, the differences to the conventional technique are considered as well as the challenges to obtain high power high frequency radiation sources. Thereafter, the spectrometers used to perform ESR on clusters studied in this thesis are described in detail. These are the Millimeter wave Vector Network Analyzer (MVNA), a Backward Wave Oscillator (BWO) based spectrometer and finally a Far Infrared (FIR) laser assisted setup.

2.1 Spectroscopy with mm and sub-mm Waves

Conventional ESR spectrometers utilize Gunn-diodes or klystrons [33, 34] for the generation of a continuous wave radiation field at a single frequency. They commonly employ rectangular single-mode waveguides for the propagation of the radiation and the cavity perturbation technique [35] paired with a lock-in method to get a sufficiently sensitive detection scheme. Thus they are restricted—and, therefore, highly optimized—to a dedicated frequency. Versions of spectrometers working with 10, 34, and 94 GHz (X, Q, and W-Band, respectively) are commercially available. The corresponding wavelengths of these devices are lying in the centimeter and millimeter range. Hence they are perfectly suited for many applications in biology and chemistry where narrow ESR lines are expected in limited field ranges. Indeed, they are often insufficient in solid state physics where large linewidths and considerable zero-field splittings occur, as shown in the following paragraph.

Relevant Probing Energy

Although the technical efforts concerning sources for high magnetic fields and large excitation energies are challenging in all concerns, there are compelling reasons to move to tunable high field/high frequency (tHF) ESR. First and foremost, this technique provides the relevant probing energy for correlated spin systems like they occur in solid state physics. As described in sections 1.7–1.9, symmetry

related splittings of the orbital energies are usual for crystals comprising e.g. 3d-metals. These splittings may cause an anisotropic magnetic behavior by means of the spin-orbit coupling and therefore result in a separation of the individual spin states. Depending on the electron configuration and the CF this separation energy of the spin states may easily exceed some Kelvin. Thus, to give a resonance signal, the ESR excitation frequency has to be sufficiently high to overcome this energy gap—otherwise no resonance will be detected and the compound is said to be ESR-silent. Prominent examples are nickel-based systems. For instance Ni^{II}, if embedded in a matrix of ligands, exhibits a considerable magnetic anisotropy. Although it is just this magnetic anisotropy which attracts great attention to Ni compounds in the research field of molecular magnetism, the very same magnetic property often renders nickel ESR-silent for conventional ESR spectroscopy. In the regime of centimeter wavelengths and even underneath (X-, Q-, or W-Band devices) the excitation energy is often too low to exceed this spin gap[3]. There

[3]In Ni-systems, the gap due to magnetic anisotropy is of the order of 10^2 GHz (4.8 K). See also sections 3.2 and 3.3.

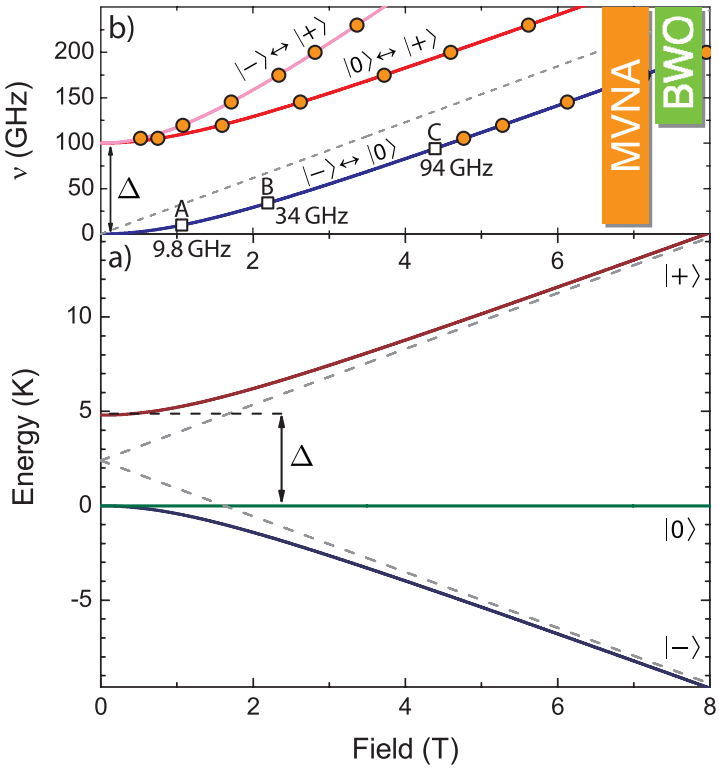

Figure 2.2: *Fictitious spin 1 system, gapped by* $\Delta = 100$ *GHz (4.8 K). a) Spin states* $|+\rangle$, $|-\rangle$, *and* $|0\rangle$, *for H perpendicular to the anisotropy axis. b) Associated resonance branches. Spectrometers operating at 9.8, 34, and 94 GHz and detecting resonances at A, B, C (squares). With tunable HF spectrometers (indicated by the colored labels) each of the three branches is in the scope of the measurement and the gap can be directly determined (circles).*

are exceptions of course (see, e.g., section 3.5). Hence, in particular for the *search* of strongly gapped complexes—like in molecular magnetism—the application of high frequencies is obligatory for a characterization with ESR.

Fig. 2.2a shows an illustrative example of a spin-triplet, $|-\rangle$, $|\,0\rangle$, and $|+\rangle$ which is gapped by the energy of $\Delta = 100\,\mathrm{K}$. The spin state energies in zero field are separated by incidence of the negative axial magnetic anisotropy owing to, e.g., a tetragonal symmetry of the CF. In this example the field dependence of the spin-levels is non-linear, because the symmetry axis is chosen to be the z-axis, with the external magnetic field pointing in a perpendicular direction, $\mathbf{H} \perp \mathbf{e}_z$. If the crystal potential was caused by a pseudo octahedron of ligands stretched in the z-direction, the coordination of the spin center would be identical to the one sketched in Fig. 1.6b. As the energy levels $|+\rangle$ and $|-\rangle$ in Fig. 2.2a are admixtures of the pure spin states, $|-1\rangle$, $|\,0\rangle$, and $|+1\rangle$, transitions between each of them are allowed by the selection rules. The corresponding resonance branches were calculated from the differences of the three possible combinations of the spin state energies and shown in Fig. 2.2b. Clearly, the operation at frequencies 9.8, 34, and 94 GHz limit the scope to the resonance transitions A, B, and C, which are associated merely with the branch $|-\rangle \leftrightarrow |\,0\rangle$. Interestingly, for commonly used X-Band spectrometers which often utilize electromagnets with $H < 1\,\mathrm{T}$, even the plotted resonance A at $\sim$1.065 T is not detectable.

Furthermore, while the application of sufficient high probing energy is generally desired, the *tunability* of the radiation source becomes crucial in this example. This is the case, whenever the frequency dependent evolution of the resonance field is investigated, or if characteristic frequencies (i.e. gap energies) are sought. In the example above, see Fig. 2.2b, a series of spectra at distinct frequencies can trace e.g. the branch $|\,0\rangle \leftrightarrow |+1\rangle$, which can be calculated exactly from the appropriate spin Hamiltonian according to the relation

$$h\nu \;=\; \frac{|\Delta|}{2} \;+\; \frac{1}{2}\,\sqrt{\Delta^2 \;+\; 4\,(g\,\mu_\mathrm{B}\,H)^2}. \tag{2.2}$$

Hence, a tunable source allows to determine the gap Δ directly. Besides the described tracing option, a further convenience of the tunability is clearly the general adaption of the experimental conditions to the relevant energy scales of the investigated system just by tuning the excitation energy to the magnitude of interest.

Spectroscopic Resolution

By the implicit gain of spectroscopic resolution compared to conventional ESR, even the investigation of weakly or non-gapped systems benefits from the application of high frequencies and magnetic fields.

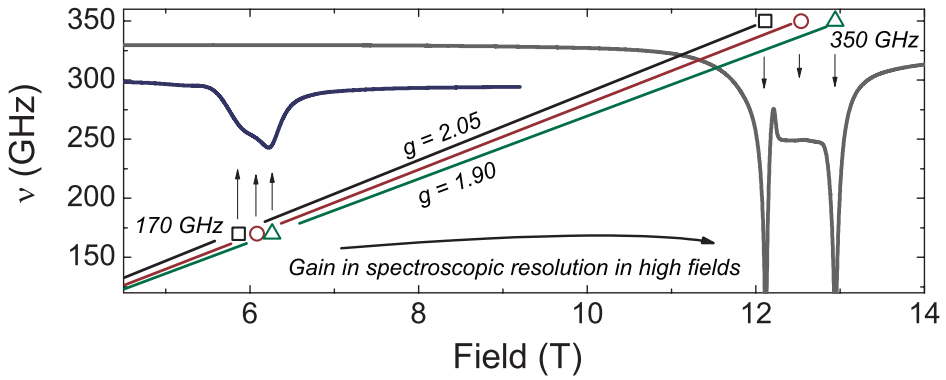

Figure 2.3: *Example resonance branches and absorption signals for the star shaped cluster Mn_3Cr at 170 and 350 GHz measured at 10 K. Low field: Poorly resolved spectrum at low frequency. High field: Two sharp peaks and an additional broad background signal are well developed at 350 GHz. For details see text.*

This predicate is extremely useful for spin-systems exhibiting broad absorption lines in the spectrum which are closely spaced with respect to their linewidth. A concrete example is given in Fig. 2.3, showing two ESR spectra of the same compound which is investigated more detailed in section 3.6. The comparison of the spectra at 170 and 350 GHz demonstrates the gain in spectroscopic resolution: the resonance signals at 170 GHz are resolved rather poor, though it is recognized they are at least two. The same signal at 350 GHz turns out to be originated by two sharp resonance peaks owing to magnetic resonance of spin centers with different g-values. Additionally it is noticed they both share a dome shaped background. The linewidth of the individual ESR lines is of the order of their field interspace ΔH which results in a limited resolution of the resonant absorption signals. On the other hand ΔH grows linearly with ascending fields due to the different g-values $\Delta H \propto \Delta g\, H$. The resonance field, however, can be easily tuned by the frequency ν.

Access to Fast Spin Dynamics

Yet another prospect of tHF ESR is to gain access to fast spin dynamics. As mentioned in section 1.3, the magnetic moment of the "classical" spin is turned over a period of rotations for the Lamor frequency equal to that of the circular polarized component of the wave train. However, if the transverse polarization decays already within the order of a single period due to fast relaxation, the resonance signal will broadened beyond recognition. A solution to the problem is to tune the Lamor frequency (1.8) with high external fields so that the relaxation time becomes long compared to the period of the rotation: $T_2 \gg \omega_{\mathrm{L}}^{-1}$. In order to achieve resonances at higher fields, again, the excitation frequency ν has to be increased.

Challenges of tHF ESR

Concerning high frequency ESR, a serious difficulty is given by the equipment availability of appropriate mm/sub-mm sources and detection systems, not to mention the dilemmas with the handling of the radiation.
Therefore, the establishment of this technique requires a diversity of novel and innovative approaches. They are utilizing configurations which, in general, are not readily available on the commercial market. In the majority of cases the development efforts which lead to such methods proceed hand in hand with advancement on the engineering side, and with applications in various areas of condensed matter physics [32].

Sources: Regarding the sources, a common technique to obtain the mm/sub-mm working frequency is to extend a conventional microwave source with an additional frequency multiplier. Such multipliers are passive non-linear devices, e.g., diodes (see Fig. 2.4). This approach is viable and represents a comparatively straightforward solution. However, the essential disadvantage of this concept is that a growing value of the multiplication factor is delicately at the expense of the output power either (see also section 2.2). Consequently, it is indicated to use a relatively high power source, e.g., a Gunn diode which needs further stabilization efforts.
A widespread example of this approach is to apply a frequency tripler on a Gunn diode operating at 95 GHz to obtain a frequency of 285 GHz. Furthermore, by arranging the diode in a coaxial cavity whose length is mechanically variable, also the base frequency becomes tunable. This method allows already for the generation of a small band of several tens of GHz. The additional utilization of different filters and multipliers allows for the extraction of dedicated multiplication ranks i.e. different frequency bands. In conjunction with the tunable base frequency, a broad-band source is realized in the case of overlapping sub-bands of the multiplication ranks.

Another approach is the construction of genuine mm/sub-mm sources by building classical electrovacuum microwave generators. The Backward Wave Oscillator (BWO) is an example of those. This device (section 2.3) is based on electrons which are emitted from a glowing cathode and accelerated by a high voltage of some kilovolt. By further application of a permanent magnetic field the electron beam passes a chain of resonator-like structures and thereby stimulates an electromagnetic wave. These devices emit a highly monochromatic and polarized radiation up to 1 THz. However, during operation it has to be taken care to cooling issues and due to the high voltage itself. By tuning the voltage U, a quasi continuous frequency spectrum is provided which covers a band of several 100 GHz. A principle difficulty here is the output power which strongly and in a non-linear manner depends on U. [36]

A third example of mm/sub-mm sources is given by Far Infra-Red (FIR) lasers (section 2.5). Here the molecules of an active medium within the optical resonator are excited by a dedicated pumping line of a CO_2 laser which is optically pumped. The geometrical adjustment of this setup is comparatively sophisticated and susceptible to mechanical instabilities. Hence it is requiring a massive construction for installation. FIR lasers are tunable, basically, by selecting different quantum transitions within the spectrum of electronic states of the laser medium or by the exchange of the active medium itself. This fact causes frequency changes to be time consuming concerning the tuning procedure.

Propagation: Commercial ESR spectrometers operate in the X, Q, or W-Band and utilize rectangular shaped single-mode waveguides. These waveguides transport the electromagnetic waves from the source to the resonant cavity comprising the sample to be studied. The dimensions of the resonator are precisely adapted to the wavelength of the radiation. The same is true for the dimensions of the waveguide cross-section in order to minimize the power reducing wave impedance. Thereby, the rectangular shape preserves the polarization of the radiation by construction. By this means, it is ensured that the magnetic component of the microwave field $\mathbf{H}_1$ is perpendicular to the external field $\mathbf{H}$ at the location of the sample. While the impedance Z of such waveguides is real, it is, nevertheless, frequency dependent. When applying higher frequencies, in order to preserve single-mode propagation, the dimensions of the waveguide have to be shrinked proportionally to the wavelength. Consequently, this approach becomes inconvenient for short wavelengths in the mm/sub-mm regime. Power reductions due to the increasing ohmic losses in the conducting waveguide rise drastically with increasing the working frequency. In particular for tunable sources conventional single-mode waveguides with fixed dimensions are hence unfavorable. Instead, simple metallic tubes are used as so-called oversized waveguides, i.e. the dimensions of their cross-section is many times larger compared to the wavelength. A result is the multimode propagation in these "light pipes" causing a complex impedance and, therefore, a loss of control over the plane of polarization. The directions of the microwave fields $\mathbf{E}_1$ and $\mathbf{H}_1$ vary over the tube-length which may be experienced in the detected signal, whenever the setup for the detector is susceptible for that. This is in particular the case for detectors "behind" an additional rectangular shaped waveguide or polarization grid.

Another technical problem has its origin in the monotonic dependence of the resonance field on the applied frequency, (1.4). As a consequence of getting sufficient high magnetic fields, the magnets used for HF ESR utilize superconducting coils which are usually at the bottom part of the magneto-cryostat. In order to get the radiation to the sample in the center of the coil, waveguides with overall lengths of 3–4 m have to be used. These constructions experience not only a good portion of mechanical instabilities due to vibrations. They are also effected by a temperature gradient in the case of non-ambient temperature measurements. While

the gradient itself is insignificant for the measurement, its time dependence—if not in the steady state—causes length variations Δl of the waveguide. Due to the multimode propagation these variations delicately influence the phase of the radiation and, therefore, yield a time depending polarization shift. The shift is proportional to the ratio of the relative length variation to the wavelength, $\Delta l/\lambda$. Therefore, the effect gets stronger for increasing frequency.

Detection: For modern HF ESR spectrometers there are two widespread approaches for detection. In the RF domain, detection is basically realized very similar to the generation of the radiation by the induction of an AC current in a resonant circuit. This is possible for sufficient fast circuits. In conventional ESR spectrometers the direct detection of microwave radiation is realized by Schottky diodes in a homodyne detection scheme. Thereby, the microwave beam is geometrically split into two arms where one is transmitting the sample and one not.

Homodyne detection is indeed also an option for HF spectrometers, but it introduces some inconveniences concerning the power-losses due to the beamsplitter. Moreover, the setup becomes more sophisticated owing to the fact that two beams have to be directed to the detector. Nevertheless, section 2.3 introduces a Mach-Zehnder interferometer as an example of this detection method. As detector, usually a bolometer in form of a Golay cell or a semiconductor (InSb) at liquid helium temperature is used.

In heterodyne detection schemes the reference signal is not anymore a component of the microwave or mm/sub-mm source, but provided by a local oscillator (LO). This oscillator clocks at a considerably lower frequency than the source itself. In order to detect the HF coming from the sample with common RF hardware, the LO signal is used to apply a down-conversion of the HF signal. This conversion is resulting in an intermediate frequency (IF) beat which is either detected directly or further down-converted. The term super-heterodyne detection describes the case where all frequencies in the spectrometer are phase-locked to a single master oscillator. The signal modulation frequency, the sampling frequency, and the intermediate frequency (from the signal down-converter) are all locked to the same clock, so the method is called "time-locked". This method preserves the phase information of the signal and, therefore, enables vector measurements (signal amplitude and phase). The next section starts with a spectrometer applying super-heterodyne detection by application of a network analyzer.

2.2 Millimeter Wave Vector Network Analyzer

The Millimeter wave Vector Network Analyzer (MVNA) is a tunable high frequency spectrometer designed for operation between 8 and 1055 GHz. The generation and detection of the radiation is realized electronically by application of non-linear solid state devices. A phase-sensitive detection of the mm/sub-mm waves is achieved by phase-locked source and detector signals which allows for vector measurements.
The generation of the HF signal is based on the frequency multiplication of a tunable fundamental wave (generated by yttrium iron garnet (YIG) oscillators, 8–18 GHz). The multiplication by passive devices (see Fig. 2.4) thereby implies great power losses for higher harmonics. In order to ensure adequate power also at several hundred GHz, the YIG sources are substituted for frequencies above 68 GHz. They are replaced by the so called ESA extensions which basically consist of tunable Gunn oscillators ($\sim$ 70–110 GHz), other millimeter wave components and assemblies, and the electronics required for the phase-locked loop.
The MVNA-8-350 (ABmm) has been used in combination with a 15–17 T superconducting magneto-cryostat (Oxford Inst.), thus providing a tHF ESR spectrometer with an effective frequency range of $\sim$ 20–475 GHz. The lower limitation of the range is thereby determined on the experimental conditions (available transitions and waveguides, bore hole of the coil) while the upper one is owing to the resonance condition at $g = 2$.

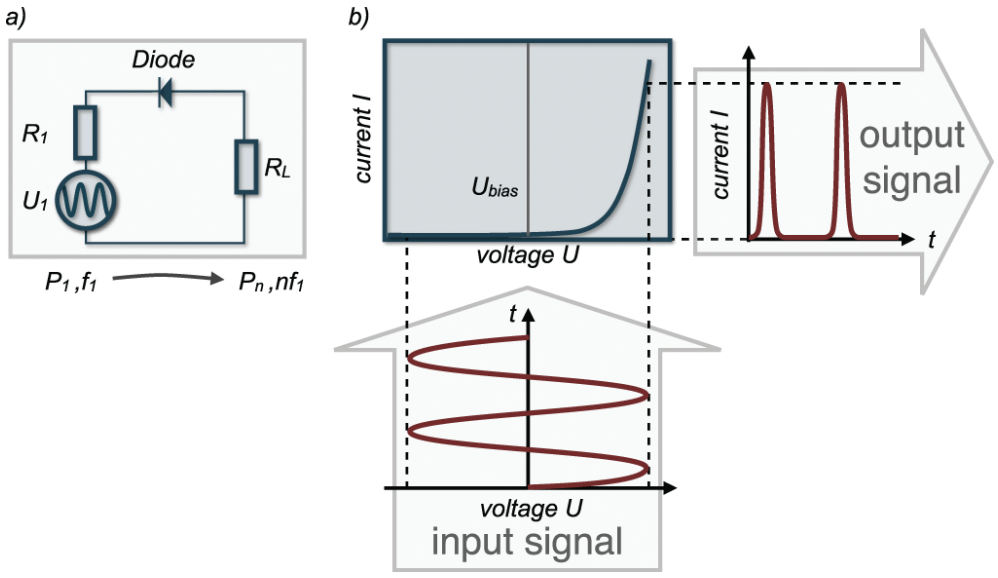

Figure 2.4: *The principle of frequency multiplication. a) Simple frequency multiplier: the fundamental wave U_1 of frequency f_1 and power P_1 is transformed by the diode into a comb of harmonics nf_1 with power P_n. b) The output signal exhibits harmonics of the fundamental input wave due to the non-linear voltage/current characteristic.*

ESA0 Configuration

Fig. 2.5 shows the schematic view of the MVNA as operated without extensions. In this setup—denoted as ESA0 configuration—the spectrometer utilizes two YIG solid state synthesizers which both operate as continuously tunable centimeter-wave sources between 8 and 18 GHz. The actual working frequency of the spectrometer is obtained by the Schottky diodes in the upper part of the figure. They are denoted as Harmonic Generator (HG) and Harmonic Mixer (HM). As a nonlinear device, the generating Schottky HG acts as a frequency multiplier. It is powered by the YIG1 with the frequency F_1 and, therefore, emits a comb of frequencies F_{cm} containing all possible harmonics of F_1. On the detection side, the Schottky HM similarly generates a comb F'_{cm} of harmonics originated by the

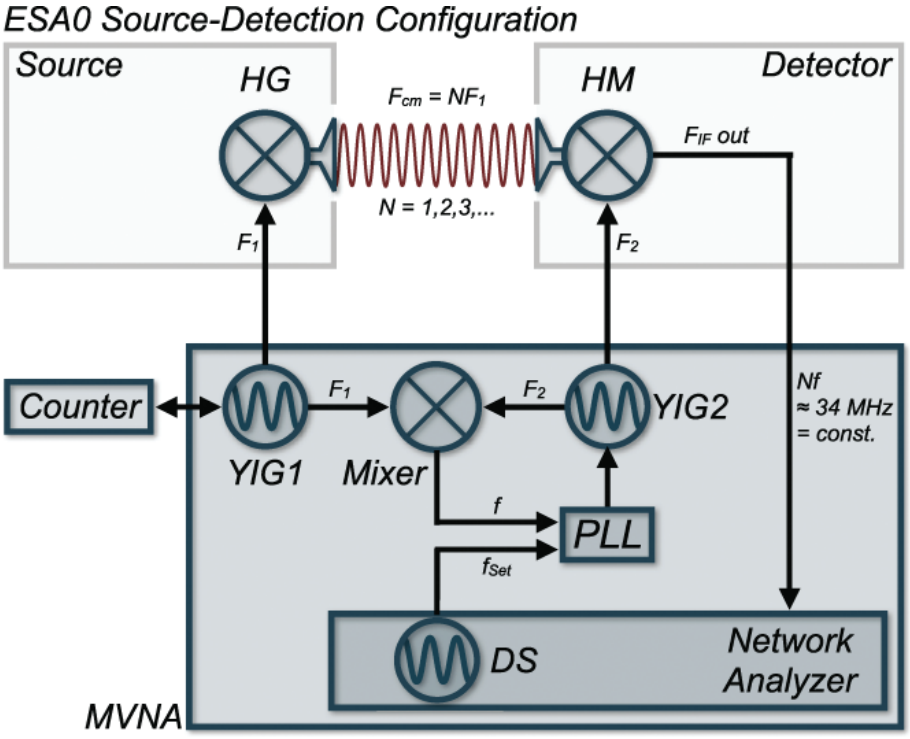

Figure 2.5: *Working principle of the MVNA without extensions. Two Schottky diodes act as harmonic generator (HG) and harmonic mixer (HM) for generation and detection of the centimeter and sub-centimeter waves of frequency F_{cm}. Both diodes are powered by YIG solid state synthesizers. The YIGs are de-tuned by a slight frequency difference $f = F_1 - F_2$ and phase locked by a PLL. The harmonic mixer HM emits a comb of MHz beats where the desired beat N' for detection is found at $f_{lock} = 34.0105$ MHz by tuning f to f_{lock}/N'. For details see text.*

slightly de-tuned base frequency $F_2 = F_1 - f$ of YIG2,

$$F_{\mathrm{cm}} = NF_1, \tag{2.3}$$
$$F'_{\mathrm{cm}} = NF_2, \qquad N \text{ integer.} \tag{2.4}$$

The second function of the Schottky mixer HM is to mix both combs (2.3) and (2.4) to the intermediate frequency beat F_{IF}

$$F_{\mathrm{IF}} = |F_{\mathrm{cm}} - F'_{\mathrm{cm}}| = Nf, \qquad N \text{ integer.} \tag{2.5}$$

The beat frequency (2.5) ranges in the MHz regime and is hence low compared to the signals of the YIGs. The following network analyzer in Fig. 2.5 is set up to a constant locking frequency of $f_{\mathrm{lock}} = 34.0105\,\mathrm{MHz}$. Well directed detuning of the YIG oscillators chooses the N'th harmonic of the comb (2.5) for detection by setting the frequency offset f to the dedicated value of $f_{\mathrm{Set}} = f_{\mathrm{lock}}/N'$. For stabilization the signal of YIG1 is locked to a microwave counter with a negative feedback loop. An additional Schottky diode (Mixer) directly mixes both YIG signals. The resulting offset f is determined by the PLL and corrected to the reference offset f_{Set} which is generated by the software controlled digital synthesizer DS. As result YIG2 is stabilized as a slave of YIG1. To give an example: by choosing the base frequency at YIG1 to $F_1 = 15\,\mathrm{GHz}$ and selecting the harmonic $N' = 3$ by the spectrometer software, the YIG2 is set to a frequency of $F_2 = 15\,\mathrm{GHz} - f_{\mathrm{lock}}/3$ and the vector receiver detects the 3rd harmonic at $34.0105\,\mathrm{GHz}$.

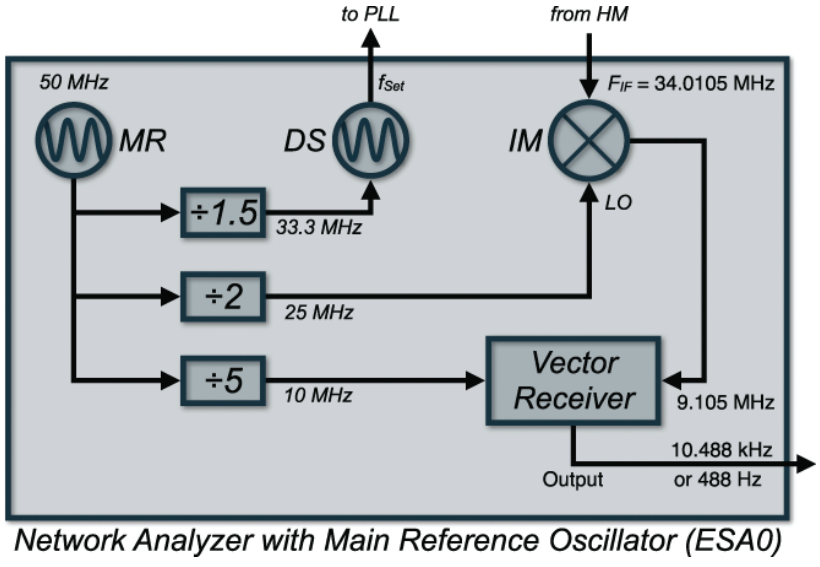

Figure 2.6: *Operation of the network analyzer in the ESA0 configuration (without extensions). The main reference MR clocks at 50 MHz. It cycles the digital synthesizer DS which serves the PLL with the programmable offset frequency f_{Set}. The input mixer down-converts the intermediate frequency beat F_{IF} by the LO frequency 50 MHz/2 to 9.0105 MHz. The vector receiver is also clocked by the MR at 10 MHz. Output is at low frequency.*

Fig. 2.6 shows a more detailed diagram of the Network Analyzer. The main reference oscillator MR clocks at 50 MHz and cycles the digital programmable synthesizer at a ratio of 1.5 (33.3 MHz). The same oscillator operates as the local oscillator LO for the Schottky Input Mixer IM at a ratio of 2.0 (25 MHz) which down-converts the intermediate frequency beat F_{IF} from the output of the detector Schottky HM to 9.0105 MHz. This signal is applied to the vector receiver which is clocked by the 10 MHz signal derived also from the main reference MR. The final output of the receiver is a signal either at 10.488 kHz or 488 Hz which can be conveniently processed by the spectrometer-internal AD hardware or an external lock-in amplifier and is then post-processed by the spectrometer software. The crucial point in the operation of the YIGs is the correlation of their phases, therefore, preserving the *phase information* in the intermediate frequency beat. While usual vector measurements compare signals from the samplewith signals directly from the source, the vector detection in the MVNA is realized with a purely electronic reference [32, 37]. A secondary but important effect of the phase locking method is the actual suppression of phase noise due to the oscillating sources: since YIG2 is a slave to YIG1 through the PLL, it is effectively providing a compensation for the interference signal. Hence, the phase noise of the interference beat is as far as possible decoupled from the phase noise of the sources, but determined by the quality of the phase locking mechanism.

By using various orders of harmonic ranks N the spectrometer provides a broad range of frequencies at a high dynamic range. Indeed, the output power decreases exponentially with increasing N, thus limiting the number of usable harmonics and, therefore, the achievable frequency F_{cm}. However, the frequency range is once more significantly increased by application of the extensions ESA-1 and ESA-2 which in different spectrometer configurations replace either exclusively the harmonic mixer HG or even both Schottky diodes HG and HM. The main strategy in both configurations is to use an external high frequency source which is then locked for conservation of the phase information and noise reduction.

ESA1 Configuration

When operating the spectrometer in ESA1 mode the harmonic mixer HM is replaced by a Gunn oscillator. While the Schottky HM in ESA0 is a passive device driven—and, therefore, also tuned—by the YIG, the Gunn is powered externally and provides a freely tunable frequency range of 68–113.5 GHz at the power of 0–12 dBm (1–16 mW). As the Gunn frequency F_{a} of ESA-1 is associated with wavelengths in the millimeter regime, the spectrometer frequency is denoted as F_{mm} for this configuration.
Fig. 2.7 contains a diagram of the ESA-1-FC source system, when associated with the MVNA-8-350 in the ESA1 configuration. The Gunn oscillator, Gunn A, is powered by the ESA1 supply at a base voltage of 9.3 V and is mechanically tuned to the desired frequency F_{a}. The signal propagates through a Faraday

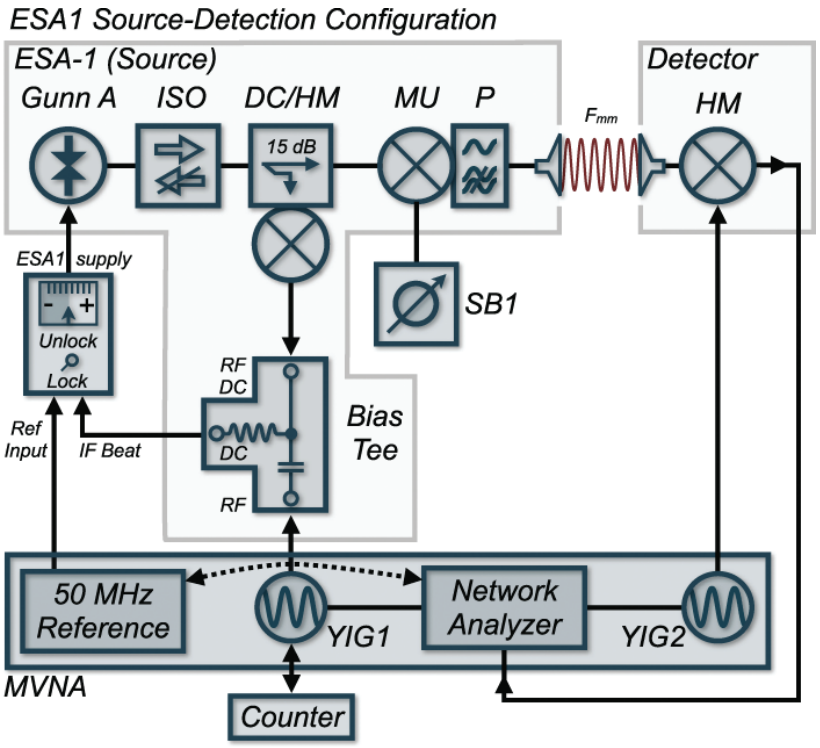

Figure 2.7: *The ESA1 configuration utilizing the ESA-1 high power source extension. The diode Gunn A provides a frequency F_a within the range of 68–113.5 GHz at the power of several mW. The multiharmonic multiplier MU generates a frequency comb $F_{mm} = MF_a$ from the Gunn frequency. Part of the signal F_a is used to stabilize the Gunn by application of a PLL. Therefore, F_a is mixed to a comb of frequencies kF_{cm} where YIG1 is the local oscillator at frequency F_{cm}. The desired beat of harmonic k' is stabilized at 50 MHz for a proper tuned YIG1.*

isolator (ISO, 1.5 dB loss) to avoid a backscattering of microwaves due to standing waves. By the following directional coupler (DC, 1 dB loss) for stabilization and frequency control a good portion of the signal is passed on the special Schottky Multiharmonic Multiplier (MU). This component contains a self-biased Schottky diode which generates a comb of harmonics, $F_{\mathrm{mm}} = MF_{\mathrm{a}}$, with $M = 2, 3, 4, ...$, similar to HM in the configuration ESA0. The 10 kΩ bias resistor in series with a Zener diode and a galvanometer is placed in the external bias-box SB1.
Owing to the alterability of frequencies, the MU further provides additional mechanical tuning options for a better perception of the input frequency F_{a}, as well as for an optimization of the output, depending on the chosen harmonic M'. The output waveguide of the MU is of dimensions which produce a cutoff[4] at 136 GHz. Therefore, it has to be removed in order to operate the extension at the $M = 1$ -band. If the multiplier MU is installed, the signal will pass a removable high-pass filter P providing a cutoff frequency F_{cut}. The filter (attenu-

[4] Only signals with frequencies $f > F_{\mathrm{cut}}$ propagate through the waveguide.

ation $> 75\,\mathrm{dB}$) is adapted to the desired millimeter wave according to $F_{\mathrm{cut}} < F_{\mathrm{mm}}$ and cancels harmonics lower than the harmonic of interest in order to avoid crosstalk effects during the locked Gunn mode, as described below. Finally, for the decoupling of the signal from the waveguide with a minimum of losses removable transitions are used. They are adapted to the filter output dimensions and to the following waveguide—if used—to ensure a guided propagation of the radiation to its destination.

F_{mm} [GHz]	M	ESA
8 – 68	0	0
68 – 113.5	1	1
136 – 227	2	1
227 – 249	3	1
249 – 320	3	2
320 – 420	4	
420 – 525	5	
525 – 618	6	
618 – 735	7	
735 – 900	9	
900 – 1050	10	

Table 2.1: *The harmonics M and ESA configurations for typical F_{mm}-ranges. $M = 1$ corresponds to the MU removed.*

The second output of the directional coupler DC provides the 15 dB Gunn signal of frequency F_{a}. This signal is mixed to the harmonics of the centimeter-wave of the LO YIG1. Therefore, a *Bias Tee* is applied: The LO provides an RF signal between 8 and 18 GHz to the Bias Tee which is multiplied by the harmonic mixer to a comb of frequencies $k \cdot F_{\mathrm{cm}}$ with integer k. The LO is tuned in a manner that a dedicated harmonic k' produces a frequency $k' \cdot F_{\mathrm{cm}}$ close to the Gunn frequency F_{a} with an offset frequency f_{IF} of the order of $10 - 100\,\mathrm{MHz}$, which is small compared to F_{cm}. While the mixer HM mixes all frequencies of the comb to the Gunn frequency F_{a}, it produces a bunch of beats in the RF/DC arm of the Bias Tee[5]. These beats are all RFs in the GHz range, except for the beat signal resulting from the k'th rank which is exactly the offset frequency $f_{\mathrm{IF}} = F_{\mathrm{a}} - k \cdot F_{\mathrm{cm}}$ in the MHz range. Therefore, the MHz beat passes the DC-arm of the Bias Tee which basically works as a low-pass filter.
Finally, in the ESA1 supply, the diplexed IF Beat is amplified and compared by a PLL to the master reference frequency of the MVNA which is 50 MHz in the ESA1 configuration. Therefore, the locking condition for the beat is

$$F_{\mathrm{a}} + \Delta F_{\mathrm{a}} = k' \cdot F_{\mathrm{cm}} - 50\,\mathrm{MHz}. \tag{2.6}$$

When the beat is locked, the PLL stabilizes the Gunn frequency F_{a} by providing a correction to the basis supply of up to $\pm 0.7\,\mathrm{V}$ which depends on the detuning ΔF_{a} of condition (2.6) and is indicated by the ESA1 supply. The maximum correction voltage of 0.7 V thereby accords to a frequency shift of $\Delta F_{\mathrm{a}} \approx \pm 0.25\,\mathrm{GHz}$. With the multiplier MU removed, the frequency range of the spectrometer accords to the range of the Gunn oscillator. Application of the MU allows to work with the harmonic $M = 2$ (136–227 GHz) and $M = 3$ (227–249 GHz). As the

[5] While DC, generally, is the abbreviation for direct current, it is often used to distinguish low or intermediate frequencies from RF signals. In this sense the description is somewhat misleading and should be substituted, when operating Bias Tees in the cm/mm wave regime: DC→IF, RF→HF.

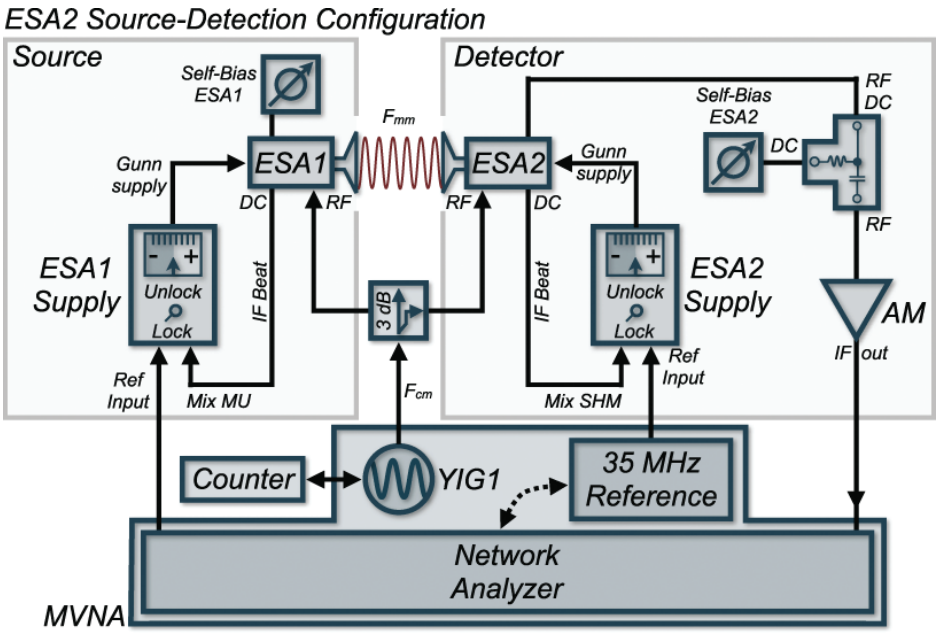

Figure 2.8: *The ESA2 configuration utilizing both extensions ESA-1 and ESA-2. For phase-locking, both Gunns are stabilized by application of the same YIG whose centimeter-wave is split by a 3 dB coupler. The detection signal is diplexed to the amplifier AM.*

detector is, still, a passive YIG powered Schottky Mixer, the detection of higher frequencies makes use of high harmonic ranks ($N > 10$). Therefore, the dynamic range becomes poor and the detection difficult. This problem is solved by application of a second Gunn oscillator which replaces the harmonic mixer in the ESA2 configuration.

ESA2 Configuration

Basically, the ESA-2 module works very similar to ESA-1: the used Gunn oscillator covers a frequency range of 78–114 GHz (80–105 GHz used) for F_b. The oscillator is controlled by a PLL in the ESA2 supply. The PLLs correction voltage depends on the diplexed beat frequency of the k'th LO harmonic and the Gunn frequency. To ensure the phase-lock of both Gunn signals, the extensions ESA-1 and ESA-2 use the same centimeter-wave of YIG1 as LO which is symmetrically split by a 3 dB directional coupler. Unlike extension ESA-1, the detector module ESA-2 utilizes a special Schottky Harmonic Mixer (SHM) instead of an MU. The SHM detects a comb of successive harmonics from ESA-1. An additional Bias Tee is applied to separate the DC self-bias current across the SHM from the detected signal of frequency F_IF. The signal is amplified by the low-noise (1 dB) amplifier AM (1–300 MHz) with a gain of 37 dB and then detected by the vector receiver in the MVNA. The ESA2 configuration is used for generation and detection of har-

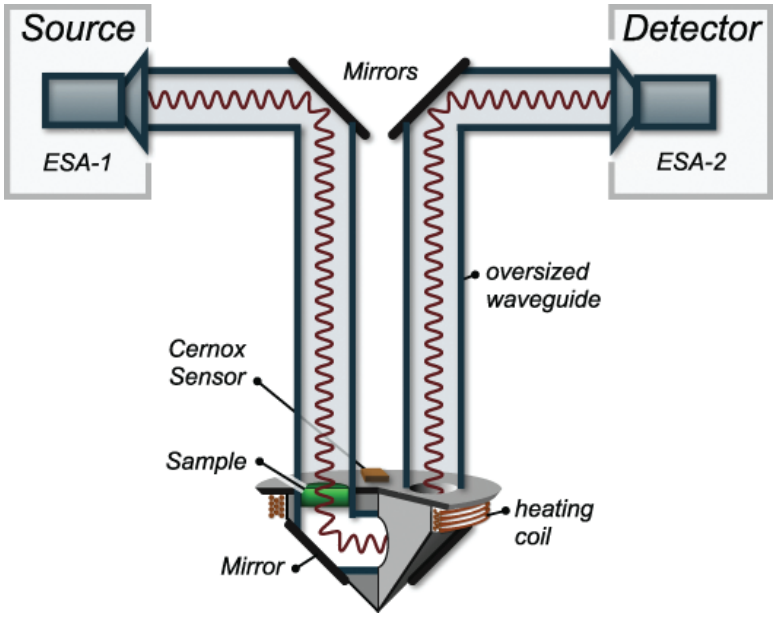

Figure 2.9: *MVNA transmission probehead. The sample holder provides a Cernox sensor and a heating coil for temperature control.*

monic ranks $M \geq 3$, thereby covering a frequency range from 249 up to 1050 GHz.

Tab. 2.1 provides an overview of the configurations ESA0–ESA2 and their associated harmonics and frequency ranges of operation. Due to the large variability of wavelengths, the spectrometer utilizes a variety of filters, waveguides, transitions and isolators which are optimized for their associated frequency bands.
Fig. 2.9 shows the principle of a standard probehead for transmission mode ESR measurements, developed throughout this work. The probehead is designed to fit into the variable temperature insert (VTI) of the utilized magneto-cryostat in order to apply magnetic fields up to 17 T and temperatures between 2–300 K. The radiation from ESA-1 propagates through a brass tube, which acts as an oversized waveguide. The propagation direction is changed by 90° by application of 45° copper-mirrors. At the bottom of the plumb line (> 2 m long) the waveguide is soldered to a prism shaped sample holder made from copper which includes also a Cernox sensor and a heating coil for temperature stabilization. Furthermore, a good portion of the vertical part is enclosed in an additional encapsulation tube (not shown in the figure) in order to avoid vibrations owing to the helium flux in the VTI. For better thermal energy exchange during the experiment, the outer tube is filled with a heat exchange gas (1 atm of helium).

2.3 Backward Wave Oscillators

This section describes a further spectrometer used in this work which is based on tunable monochromatic generators, namely the so called Backward Wave Oscillators (BWO) [38]. BWOs are similar to classical electrovacuum microwave generators like klystrons or magnetrons, but with essential enhancements: depending on their dimensions they generate extremely short wavelengths down to 0.2 mm (1.5 THz) and they are electronically tunable in a broad range. Furthermore, the radiation is of large power (tens of mW), highly monochromatic ($\Delta f/f \approx 10^{-5}$), and exhibits a high degree of polarization (99.99%) [36, 38].
Since BWOs are operating within a magnetic field for the collimation of the electron beam, they are subdivided in packetized and unpacketized BWOs, depending on whether they are built into a permanent magnet or separated from it. Fig. 2.10 shows the principle of an unpacketized BWO. The cathode is warmed by a heater and, therefore, emits electrons which are accelerated to the anode by an electrical potential in the range of some kilovolts. While they travel to the collector, the electrons are collimated by the external magnetic field to form the electron

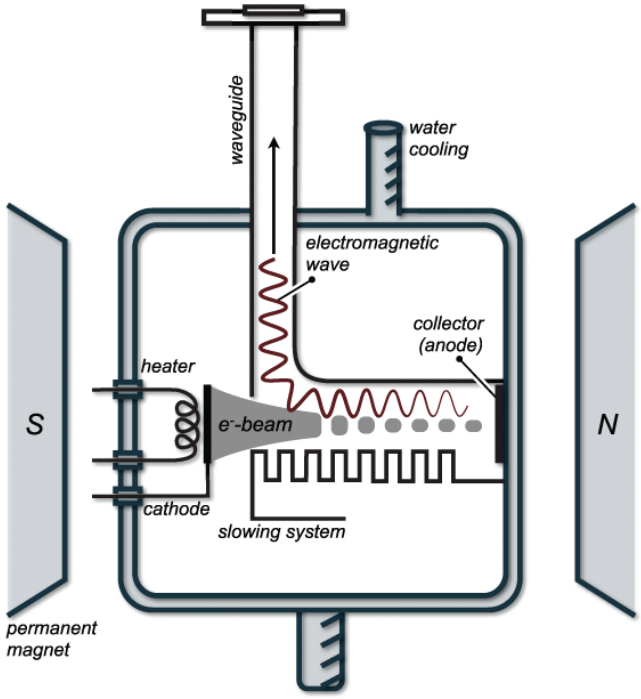

Figure 2.10: *Unpacketized BWO lamp. The electrons emitted by the heated cathode are accelerated to the anode by an electric field. The external magnetic field in acceleration direction as well as the slowing system cause the beam to be subdivided in electron clouds which are drifting to the anode. The electromagnetic wave results from the charge distribution which is periodic in space and time. The whole system is evacuated and encapsulated by a water cooled housing. For details see text.*

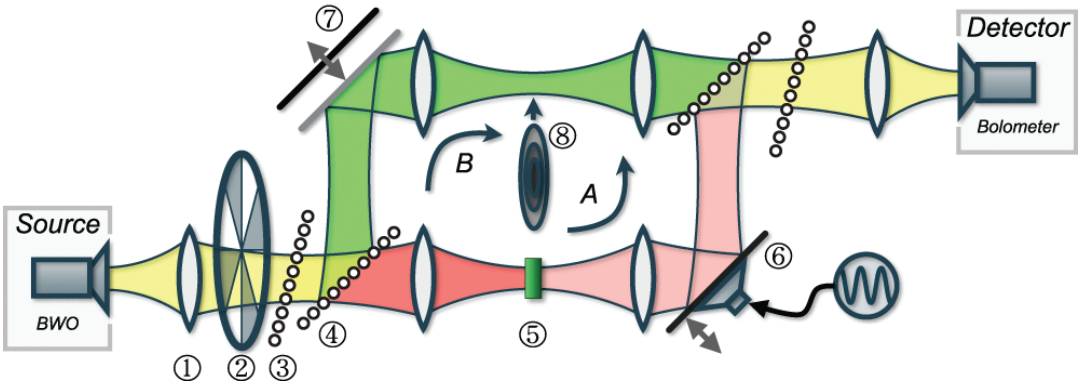

Figure 2.11: *Quasi-optical Mach-Zehnder interferometer. For details see text.*

beam passing a comb-like structure of electrodes. This so called slowing system causes a spacial variable electric potential and, therefore, causes the electrons to group themselves in periodical bunches. As a result of the charge distribution being periodical in space and time, an electromagnetic wave forms, traveling in the opposite direction to the electrons (backward wave). Thereby, the electrical field strength tunes the velocity of the electrons and thus the radiation frequency.

Fig. 2.11 shows a BWO-based spectrometer in Mach-Zehnder geometry for vector measurements. The millimeter wave leaves the oversized waveguide of the BWO in form of a divergent beam. It propagates quasi-optically in free space. After passing the dielectric lens made from teflon/polyethylene for collimation (1), it is amplitude modulated (chopped) (2) with a stabilized frequency of 22.8 Hz and polarized by a grid (3). The following beam splitter (4) divides the optical path into arms A and B with perpendicular polarization $P_\mathrm{A} \perp P_\mathrm{B}$. Beam A is focussed on the sample (5), collimated again, and then redirected by a mirror (6, phase modulator) which vibrates with a constant low (audio) frequency in the direction perpendicular to its plane. Beam B is redirected by an adjustable mirror (7, phase compensator), and then focussed and collimated on another grid which recombines the beams. Finally, the radiation passes an analyzer grid and is focussed on the detector, e.g., a bolometer. The detector signal is amplified by a lock-in amplifier which is triggered by the chopper frequency.

In order to accomplish a vector measurement two individual measurements for the transmission coefficient and the phase-shift are required. For detection of the transmission coefficient, T, a microwave absorber (8) is put in the optical path of beam B. For this configuration the detector signal, I_s, is proportional to the transmitted radiation by the sample. The absolute transmission coefficient is determined by the ratio of the intensity which was observed by a second

measurement without the sample, I_0:

$$T = \frac{I_{\text{sample}}}{I_0}. \qquad \text{TRANSMISSION COEFFICIENT} \tag{2.7}$$

For measurement of the phase shift ϕ the absorber (8) is removed. The measurement quantity here is the position, x_s, of the movable mirror (7) which preserves a minimum of the signal at the detector due to destructive interference. Thereby, the lock-in amplifier is triggered on the frequency of the phase modulation, accomplished by the vibrating mirror (6). With the reference measurement without sample, x_0, the phase shift can be computed according to,

$$\phi = 2\pi\nu\,(x_s - x_0 + d_s). \qquad \text{PHASE SHIFT} \tag{2.8}$$

In (2.8) ν is the frequency of the millimeter wave and d_s is the thickness of the sample.

In fact, magnetic resonance measurements on $Fe_2^{III}Cu_2^{II}$ (section 3.7) have been performed with a setup different from the one shown in Fig. 2.11. In order to apply a magnetic field, and different temperatures to the sample, a probehead for insertion into the VTI of the magneto-cryostat has been constructed. Fig. 2.12 shows the working principle. Similar to the Mach-Zehnder configuration the beam is collimated and chopped. After passing a polarization grid the beam is then focussed into a transition which is mounted to a cross of oversized waveguide tubes. In the center of the cross a polarization grid works as a semi-transparent mirror (1) realized either by a polymeric foil, e.g. mylar, or by a construction of thin conducting wires which are aligned parallel. The orientation of the grid is such that a fraction of the radiation is reflected to the bottom of the probehead. At the end of the tube a cone shaped concentrator (2) reduces the diameter of the waveguide. The radiation then runs through the sample and is eventually

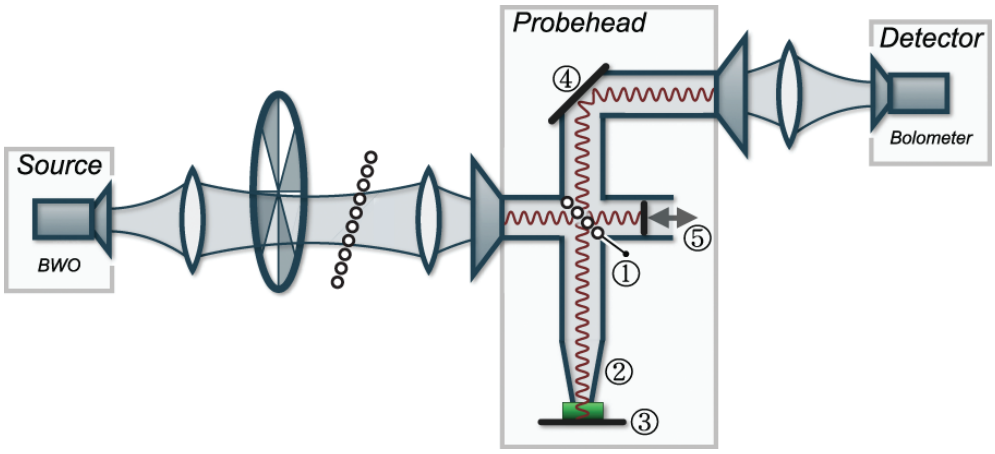

Figure 2.12: *BWO spectrometer in combination with a reflection mode probehead in a homodyne reflection scheme. For details of the setup see text.*

reflected by a copper mirror (3). In case of magnetic resonance the polarization of the reflected millimeter wave is shifted and the component perpendicular to the grid is transmitted by the beam-splitter (1). Finally, the radiation is redirected by a 45° mirror in the upper part of the probehead (4) to a lens which focusses it on the chopper triggered detector. For reduction of the background signal due to standing waves, an additional mirror (5) is used for tuning the output power.

2.4 Frequency Domain Magnetic Resonance

In a typical (classical) ESR experiment the sample is exposed to microwave radiation of a fixed frequency ν while the external field H is varied within the desired field range. The transmitted or reflected—depending on the experimental setup—microwave power is detected during the field-sweep and results in an ESR spectrum, $P_\nu(H)$.

While $P_H(\nu)$-spectra at a fixed field are also possible, it has turned out to be inconvenient—although not impossible—to sweep the microwave frequency instead of the field. A prominent example of a frequency domain magnetic resonance (FDMR) experiment is the spectrometer based on the electronic BWO lamps in section 2.3. While throughout this work the BWOs have been used only at fixed (though variable) frequencies in combination with the application of swept magnetic fields, the spectrometer provides also the opportunity to measure at a fixed (in particular zero) magnetic field while simultaneously sweeping the excitation frequency.

The inconvenience of this measurement concept is that the output power of a tunable source usually depends on the generated frequency. In particular, this is the case for the BWO lamps. [38] While the emitted frequency ν depends on the operation voltage U according to $\nu \propto \sqrt{U}$, the output power P is not associated with an easy relation. Actually, $P(U)$ varies in a non-predictable manner by two orders of magnitude. However, the power characteristic is highly reproducible and unique for each BWO lamp, thus allowing to easily sweep the frequency by varying U. This fact enables to determine the transmission T (or reflectivity R) and the phase shift ϕ in FDMR experiments exactly in the same way as described in section 2.3.

2.5 FIR Laser

Pulsed field ESR experiments presented in this work have been accomplished in the Laboratoire National des Champs Magnétiques Pulsés (LNCMP) in Toulouse (France) with application of an optically pumped FIR laser. The laser is based on a stable waveguide resonator (Fabry-Perot cavity) with easily interchangeable dielectric or metallic waveguides which give the system a maximum flexibility over 40 μm to 1.222 mm wavelength range (245 GHz–7.5 THz). [39] Employed are laser media such as methanol (CH_3OH), its deuterated isotopes (CH_3OD, CD_3OD, both known to be present in the interstellar medium), CH_2CF_2, CH_3CN_2 or CH_3F. Owing to the quantum transitions in the spectrum of the medium the laser is admittedly tunable only to discrete frequencies.
The FIR device is designed to be pumped by an external CO or CO_2 infra-red laser which is optically pumped. As the output power of the FIR laser is a function of the input power from the pump laser system, the CW power which can be emitted can principally reach and extend the value of 1 W between 40 and 1500 μm. The major parameters which have an effect on the laser output are thereby the pressure of the laser active gas ($\sim 100\,\mu$bar) and the length of the resonator ($< 1465 \pm 3$ mm). The amplitude stability of the output radiation is thereby as good as the CO_2 laser, if all adjustments are optimum.

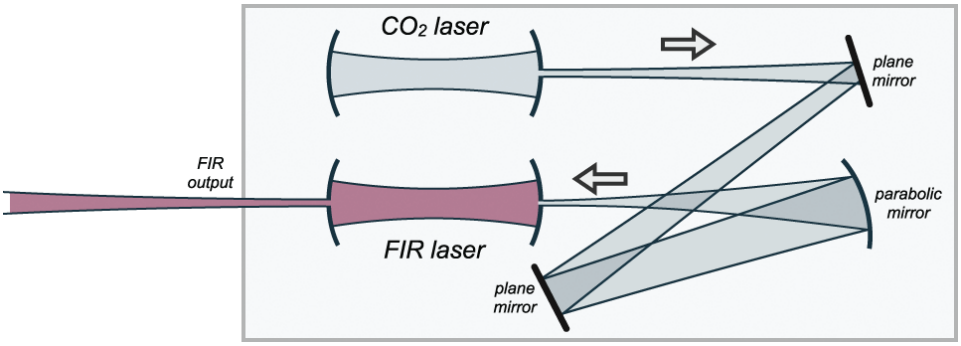

Figure 2.13: *Setup of the model 195 FIR laser (Edinburgh Instruments Ltd.). The CO_2 laser is the optical pumped source of the laser active medium in the resonator of the FIR laser.*

2.6 Special Setups and further Equipment

In the previous sections, the general experimental equipment has been introduced which was used by the author to perform ESR experiments. However, a particular "spectrometer unit" does not exist. Combinations of sources, detectors, magneto-cryostats and probeheads are possible. Nevertheless, throughout this work some special combinations were used, which are described in this section. Thereafter, remarks concerning the magnetization measurements are given.

ESR

The *MVNA* spectrometer and the *BWO* lamps are property of the IFW Dresden. Throughout this thesis both were unexceptionally used in combination with a magneto-cryostat from Oxford Instruments. The magnet provides magnetic fields of 15 T in standard mode at liquid helium temperature and 17 T if the superconducting coil is further cooled to 2 K. The cryostat provides a Variable Temperature Inset (VTI) for measurements between 1.8 and 300 K. Furthermore, the MVNA spectrometer has been used exclusively associated with the transmission probehead, shown in Fig. 2.9, while the BWO lamps were singly used with the reflection probehead which is shown in Fig. 2.12. Moreover, the radiation from the BWOs were detected by a bolometer based on the liquid helium cooled semiconductor InSb.

The *FIR* laser is a property of the pulsed field laboratory LNCMP, Toulouse. It is associated with a nitrogen cooled coil for the generation of magnetic fields up to 38 T. [40] Brass tubes and a 90° metallic mirror were used to lead the radiation to the sample which sits in the center of the coil. [41] A field pulse with a duration of 800 ms (raising time 120 ms) is generated by a discharge of a 10 kV capacitor bank on the coil. The radiation transmitted through the sample is detected by an InSb detector cooled to liquid helium temperature. The sample temperature can be varied between 4.2 and 300 K.

Magnetization

A Magnetic Properties Measurement System (MPMS) by Quantum Design based on a SQUID was used for measurements of the magnetization in static fields up to 5 T. The device allows temperature dependent measurements of the static susceptibility in the temperature range between 1.8 and 300 K.

The high-field magnetization was also measured in the pulsed field laboratory LNCMP in Toulouse. Measurements of the static magnetization have been performed in pulsed magnetic fields up to 55 T with a pulse duration of 250 ms (raising time 40 ms) by an inductive technique. A system of two concentric pick-up coils in opposition to each other equipped with additional compensation coils was utilized. The measured signal M/H was integrated numerically. The sample temperature can be varied between 1.4 K and 300 K. Since the technique does not allow for the determination of absolute values of the magnetization, the resulting data were calibrated with the absolute magnetic moment measured with the MPMS.

2.7 Errors

All stated measurands in this thesis are subject to errors. While the errors are not explicitly stated, they are mostly considered for direct reading by the number of denoted digits: Only the last digit is subject to errors. Exceptions are temperatures and frequencies.
For the measurement of the temperature in static field ESR, a Cernox sensor was used which was placed close to the sample (see Fig. 2.9). Measurements have been carried out at equilibrium temperature only. Therefore, the temperature error is limited mainly by the error of the calibration. The sensor was calibrated in a PPMS (Quantum Design) by comparison with the internal temperature sensor at equilibrium temperature. The PPMS has a temperature accuracy of $< 1\,\%$ [42].
The frequencies used in the ESR experiments are determined by the microwave counter which is exact up to 10 kHz [43]. This yields a frequency uncertainty of $< 10^{-4}\,\%$ in the range of the applied YiG oscillators (8-18 GHz). Due to the method of frequency multiplication this value is also the upper limit for the hole spectrum up to 500 GHz.
Magnetic moments measured by the MPMS are dominated by the uncertainty of the mass of the measured substance. Here, the error ranges at a maximum of 2%.

3 Single-Molecule Clusters

Though the term single-molecule magnetism leads back no more than 15–20 years, the more general research field of molecular magnetism is significantly older. Thus, before the scientific results on several molecular cluster are presented, the chapter starts with a classification of the topic into the history. Most of the information can be found in recent reviews which are marked in the text. Also, the coverage is far from complete, but should provide a path from the conventional to the single-molecule magnetism.

3.1 Overview

Applications of Magnetism

The history of magnetism starts with the discovery of magnetic lodestone, magnetite (Fe_3O_4), by the Chinese in the 4th century B.C. [44]. The mineral was found to align in the earth magnetic field and, therefore, was subsequently used most notably in compasses. They allowed for navigation at sea becoming more independent on the sun and the stars. The next big step in the evolution of applied magnetism resulted from Faraday's invention of the electric generator in the 1830s which evidently strongly influenced the subsequent industrial revolution. The following systematic exploitation of magnets and magnetism in particular in the 20th century brought tremendous benefits to mankind. Today a huge variety of different magnets with a manifold of different properties penetrate the everyday life by means of such a huge number of applications that one is frequently not fully aware of their ubiquity. Few examples are electrical motors and generators, acoustic devices, magnetic resonance imaging instruments, magnetic shielding materials, magnetomechanical applications and of course information technology.

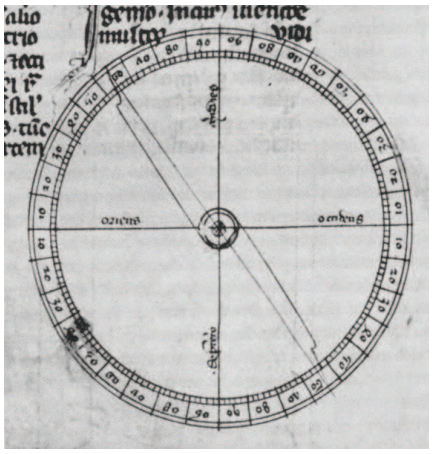

Figure 3.1: *Pivoting compass needle in a 14th century copy of* Epistola de magnete *of Peter Peregrinus (1269). Source: Wikipedia*

Based on transition metals and rare earth elements traditional magnets are produced mainly by energy intensive high temperature metallurgical processes, i.e., they are engineered physically by the composition of different metals, metal oxides or alloys. The origin of magnetism in these substances mainly arises from the spins of unpaired electrons which may interact among themselves via direct or by RKKY exchange. Typically, the magnetic properties can be tuned in a broad range by means of the composition process. For instance, magnetic compounds can be produced as non-permanent or permanent ("soft" and "hard" associated with low or high coercive fields, respectively) depending on the destined application. In fact, nowadays there is a strong desire for magnetic materials exhibiting attributes associated rather with organic or non-metallic compounds, like electrical insulation, light transparency, mechanical flexibility, low density or nano-size. Imaginable is also the possibility of magnetism switched by light, temperature, pressure or other physical interactions. Soluble magnets would disclose new areas of application. Biocompatible magnetic contrast media would be tissue selective in medical imaging.

Actually, the rethinking of the creation process for obtaining magnetic materials is not new, but dates back already to the 1950s. The term *Molecular Magnetism* is thereby associated with the mergence of the activities of the magnetism-related branches in physics and chemistry. The new interdisciplinary field is characterized in particular by the common objectives of physicists and chemists of design, synthesis and characterization of the magnetic properties of molecule based magnets. The basis for that cooperation was the field of *Magnetochemistry* which created novel options for measurements of magnetic properties and also promoted new methods for their interpretation. For example new equipment like magnetometers and magnetic resonance spectrometers were developed and also the theoretical modeling based on the works of Curie et al. was drastically enhanced by application of quantum theory and statistical physics. In particular the introduction of Hamiltonians describing the spin-spin, spin-orbit, and spin-ligand interactions and the Van Vleck formula provided experimentalists with powerful tools to compute the energy levels of the quantum states and hence to analyze the magnetic properties of the measured data [45].

A very common example to motivate the research of new magnetic materials is information technology. Not only the designers of microprocessors have to face the physical limitations of miniaturization (of transistors in integrated circuits) to a greater extent the more they approach the quantum limit. The same is true for magnetic data storage. A "bit" cell on the platter of a conventional state of the art hard disc drive comprises a number of $\sim$50–100 magnetic single domain grains in order to keep the grain boundary between unequally polarized adjacent bit cells distinctive enough for reliable data detection [46]. For an increase of the information density, the bit cells are shrunk and so are the grains in order to keep the grain-per-cell ratio constant. But there is a lower limit of this shrinking: If the

grains become too small they will loose their ferromagnetic nature and become superparamagnetic. This phase is characterized by the loss of the remanence of the grain which renders the medium inoperative in terms of data storage.
Compared to the ferromagnetic order in grains this problem does not arise for magnetic molecules, because their intra-molecular spin configuration is determined by the chemical bonding of the spin carriers and thus independent on achieving certain critical sizes or certain amounts of magnetic atoms [47]. This difficult situation may be solved by magnetic media which employ single magnetic molecules as bits instead of many grains.
Since such molecules *are* superparamagnetic they need certain prerequisites to become practicable for data storage. Basically, they should behave like an atom with a giant spin S, i.e., comprise a high-spin ground state and, moreover, in order to address bit states like "0" and "1", this ground state has to be bistable with a large blocking temperature which prevents thermally assisted depolarization of this molecular unit. The latter attribute demands for a high (negative axial) magnetic anisotropy favoring the highest multiplicity spin states with $m_S = \pm S$.

Molecular Magnetism

While the previous example calls already explicitly for the more recently discovered zero-dimensional single-molecule magnets (see below), a general approach to obtain novel magnetic materials is indeed the synthesis based on magnetic *molecules*.

Indeed, in many cases magnetic molecules include a finite number of transition metal or rare-earth centers classifying them as *metal-organic*. However, there are *purely organic* species as well which comprise free-radicals as spin carriers whose magnetism is based on unpaired electrons in s- and p-orbitals [48]. Since radicals are very reactive, one challenge in this field is to achieve stable compounds. In fact, for long range ordering of the corresponding spins in ≥ 2 dimensions, these materials may even exhibit ferromagnetic behavior. The first organic-based ferromagnet *p*-nitrophenyl nitronyl nitroxide (p-NPNN) was reported in 1991 by Kinoshita et al. [49] The β-phase crystal of this quasi-1D ferromagnet exhibits nearest neighbour coupling of $\sim -4.3\,\mathrm{K}$ [50] and undergoes an FM transition at $T_\mathrm{c} = 0.60\,\mathrm{K}$ with an estimated interchain coupling of about $-0.1\,\mathrm{K}$ [51]. In the following a variety of other organic ferromagnets were discovered. Thereby, the main objective in the development was certainly to increase the ordering temperature. The highest T_c found so far in organic based ferromagnets (35.5 K) is observed in the 1996 discovered dithiadiazolyl radical *p*-NCC_6F_4CNSSN [52].

The previous example of purely organic magnetic materials indicates the diversity in physical attributes of molecule based magnets induced by the crystal structure. Besides the already mentioned isolated molecules (0D) and 3D networks, also layers (2D) and chains (1D) are known [53] where the latter are interesting in

particular as realization of low dimensional systems which can be used to prove theoretical models.

Single-Molecule Magnets

Today, an important branch of basic research is the synthesis and study of nanomagnets. One approach in order to achieve nanoscale magnets is the synthesis of metal-organic molecular clusters comprising a finite number of paramagnetic centers. The centers are strongly interacting via superexchange by means of organic bridge ligands. Molecules with large effective spins have been realized in the past [54]: A recent record is given by the FM coupled Mn_{19} cluster with a spin of $S = {}^{83}/_{2}$ in the ground state [55]. An important attribute of these molecules is that they often can be synthesized as single crystals which comprise a macroscopic number of identical clusters. The zero-dimensionality—which renders them interesting for magnetic data storage—is achieved by an organic shell which to a large extend suppresses the inter-molecular coupling between adjacent clusters.
The most prominent representatives of this species are the compounds usually abbreviated with $Mn_{12}Ac$[1] and Fe_8[2]. Owing to their magnetic properties, these molecules are called *single-molecule magnets* (SMM) [56] and $Mn_{12}Ac$ and Fe_8 in particular are commonly referred to as the prototypes of this species [57]. $Mn_{12}Ac$ was first synthesized by Lis [58] in 1980. The structure of the disc shaped magnetic core is depicted in Fig. 3.2a. The magnetic properties of the cluster are mainly due to the four inner Mn^{IV} ($S = {}^{3}/_{2}$) and the eight outer Mn^{III}

[1] $Mn_{12}Ac$: $[Mn_{12}O_{12}(MeCO_2)_{16}(H_2O)_4] \cdot 2MeCO_2H \cdot 4H_2O$
[2] Fe_8: $\{[(tacn)_6Fe_8O_2(OH)_{12}]^{8+}$

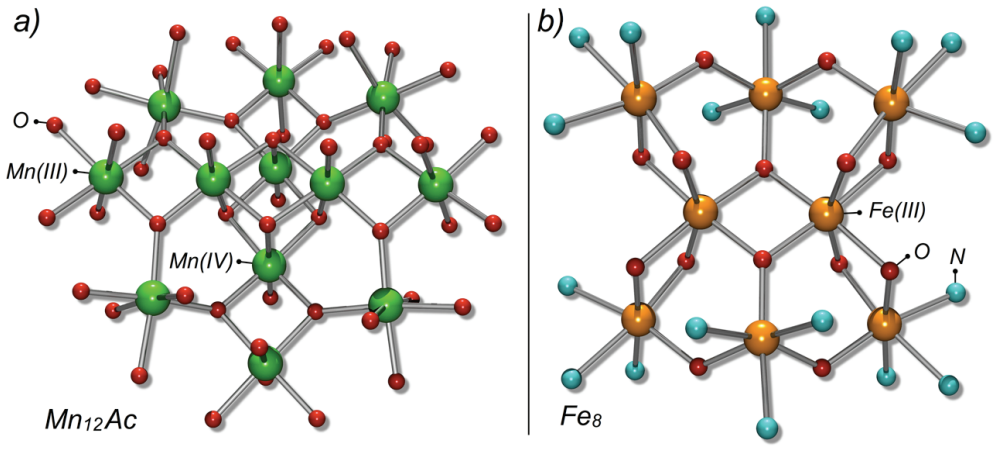

Figure 3.2: *Reduced representation of the core structure of $Mn_{12}Ac$ (a) and Fe_8 (b). The magnetic metal ions are represented as green ($Mn_{12}Ac$) and orange (Fe_8) spheres, respectively.*

($S = 2$) ions which are coupled by superexchange and form a high-spin ground state with $S = 10$. The effective spin of the cluster has been evidenced from high field magnetization studies [59] which later have been confirmed by different experimental techniques, such as high-field EPR [60], high field magnetic torque measurements [61] or neutron scattering [62, 63]. The Fe_8 cluster [64], depicted in Fig. 3.2b, has also the $S = 10$ ground state. In both clusters the negative axial single ion anisotropy ($D_{Mn_{12}} = -0.72\,K$ and $D_{Fe_8} = -0.27\,K$) removes the $2S+1$-fold degeneracy of the ground state multiplet: The $S = 10$ state is split into the $m_S = \pm 10, \pm 9, \pm 8, ..., \pm 1, 0$ levels. The $m_S = 10$ state can be viewed as the "spin up" state and the $m_S = -10$ state as the "spin down" state, see Fig. 3.3a (compare also Fig. 1.9). Since the states with $m_S = \pm 10$ have the same energy, this ground state is bistable which is characteristical for SMMs. Consequently, the two lowest quantum states are separated by the energy barrier,

$$U = |D| \left(S_{z,\max}^2 - S_{z,\min}^2 \right), \tag{3.1}$$

which strongly influences the low temperature behavior of the cluster if polarized: For temperatures $T \sim U/k_B$ the relaxation time τ of the magnetization depends on the height of the barrier according to the Arrhenius equation

$$\tau = \tau_0 \exp^{\frac{U}{k_B T}}, \tag{3.2}$$

where τ_0 is the preexponential factor. Therefore, the relaxation slows down with an increasing ratio $U/k_B T$ which yields an hysteretic behavior of the magnetization. The term SMM is due to the fact that the origin of this hysteresis is purely molecular. The characteristic measure of the blocking effect by means of the potential well (3.2) is the so-called blocking temperature: It corresponds to the temperature at which the relaxation time of the magnetization equals the characteristic time of the experiment, e.g. $(2\pi\nu)^{-1}$ in an AC susceptibility measurements. [22] See A.6 for a list of recent single-molecule magnets and their potential barrier.

Thermal activation is not the only mechanism which causes the relaxation of the magnetization. In 1996 unusual steps have been found in the hysteresis loop of Mn_{12}Ac which were observed at regular magnetic field intervals. [65, 66] If the field was tuned to a step, a substantial increase of the magnetic relaxation rate has been observed. The mechanism of this additional relaxation pathway is denoted as quantum mechanical tunneling of the direction of magnetization, or short, *quantum tunneling of magnetization* (QTM), owing to the fact that the magnetization vector rotates "through" the potential maximum which corresponds to the $m_S = 0$ quantum state. Different tunneling regimes are distinguished depending on the temperature and presence of an external field (see Fig. 3.3a–d for examples). QTM is not yet fully understood. However, the symmetry of the crystal field plays an important role. In-plane (rhombic) and higher order anisotropy may yield an admixture of isoenergetic quantum states on both sides

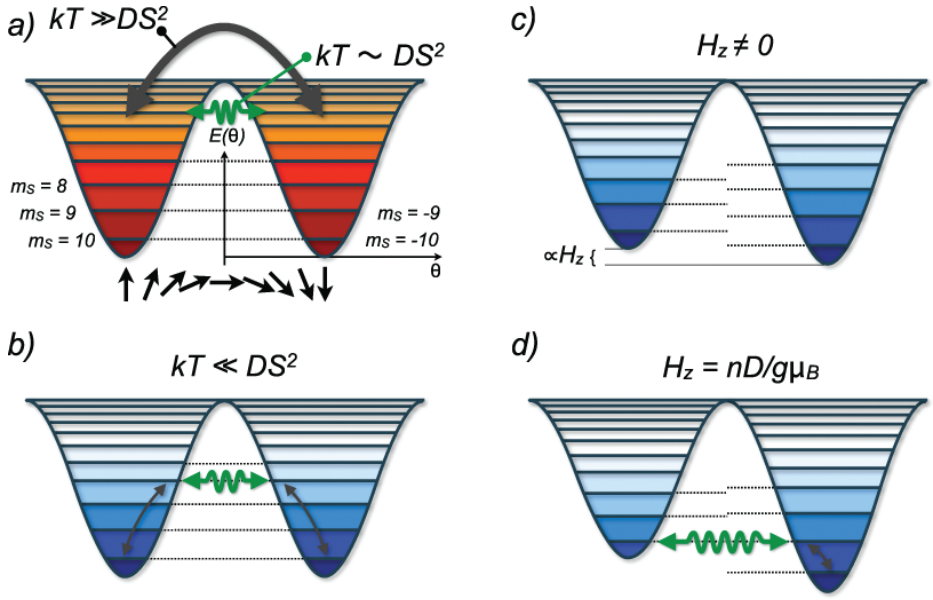

Figure 3.3: *Quantum tunneling of the magnetization. Different regimes of relaxation are shown. a) At high temperature, $k_BT \gg DS^2$, thermal activation exceeds the tunneling processes. For thermal energies of order $k_BT \sim DS^2$, tunneling in the upper paths effectively reduces the height of the barrier (thermal activated tunneling). b)–d) At low temperature, $k_BT \ll DS^2$, tunneling processes may determine the relaxation rate more significantly. Intermediate paths are tunneled with thermal assisance in (b). An external field can suppress (c) or support (d) resonant tunneling.*

of the potential barrier, see, e.g., Fig. 3.3d. While the tunneling effect is indeed an important prerequisite for quantum computing, it is limiting the usability of SMMs as components for data storage, since it results in a decrease of the effective potential barrier.

Macroscopic quantum effects like hysteresis of the magnetization and QTM are closely related to the magnetism in single molecules. These novel quantum phenomena as well as the resulting prospects of future applications in quantum computing and data storage have attracted much interest to the interdisciplinary field of molecular magnetism (for recent reviews see, e.g., Refs. [53, 67–70]). The important objectives in synthesizing molecular nanomagnets is to increase the spin multiplicity S of the ground state of the molecular clusters as well as the (negative axial) magnetic anisotropy D in order to enhance the capabilities for magnetic data storage. In doing so, the potential barrier between the states with the largest corresponding magnetic moments, i.e. $m_S = \pm S$, is steadily increased in order to create the technical relevance for molecule based data storage. In the following sections several molecular clusters are investigated in terms of possible SMM behavior.

3.2 2-leg Spin Ladder Ni-Oxalate

Introduction

In recent years, spin ladder systems have attracted a large interest as well in theoretical as in experimental condensed matter research since a variety of fascinating properties were found. For example, the doped spin ladder subunits of $(Sr,Ca)_{14}Cu_{24}O_{41}$ become superconducting upon application of hydrostatic pressure [71]. In the same type of compounds, heat transport measurements have detected large magnon contribution to the thermal conductivity. Spin ladders even seem to be related to high temperature superconductivity: It has been shown recently that the spin excitations in the doped layered high T_c cuprates resemble those of coupled one-dimensional (1D) spin ladders [72].
In cuprates the magnetic exchange is usually large ($\sim 10^3$ K), so that related ladder systems, e.g. Sr_2CuO_3, can not be studied in fields of relevant energy. Thus, model magnetic systems are of great theoretical interest, not only for cuprates. In 1D systems like the ladders, quantum effects are much more pronounced than in higher dimensions. Theoretically, subtle effects of the topology and the spin quantum number have been studied and different models have been suggested. Increasing the spin is expected to suppress quantum fluctuations. Testing these models, however, is hampered by a shortage of real examples of spin ladders. One candidate for such a model system is $Na_2TM_2(C_2O_4)_3(H_2O)_2$, with TM=Ni,Co,Fe,Mn a transition metal ion [72]. Here, 2-leg ladders are realized where magnetic ions with adjustable spin are coupled via oxalate $(C_2O_4)_2$-anions. These compounds allow a systematic study of a spin ladder system with increasing spin ($S = 1, 3/2, 2, 5/2$) [73–75]. This section is about the magnetic properties of the structural 2-leg spin ladder with TM=Ni, Ni-Oxalate. Before studying the crystal structure of this 2-leg ladder with $S = 1$, a few remarks are made concerning some closely related 1D spin systems.

A straightforward access to the subject is given by the example of an ideal $S = 1/2$ Heisenberg chain, see Fig. 3.4a. In presence of the uniform isotropic AFM nearest neighbor exchange interaction J_1 between the magnetic centers of the chain, the excitation spectrum is gapless with a power-law correlation function. [1, 76, 77] Introducing an additional interchain magnetic exchange coupling between adjacent spin chains, the so-called n-leg spin-ladders are formed. These have been discussed very intensively for the $S = 1/2$ case since they exhibit completely different ground state properties. [71, 78] In particular for even-leg ladders a non-magnetic spin-liquid ground state with a finite energy gap is found [79], see, e.g., Fig. 3.4b for a 2-leg spin-ladder with $S = 1/2$. For $S = 1$ already for a single AFM chain the ground state is a non-magnetic spin-liquid with a finite energy gap

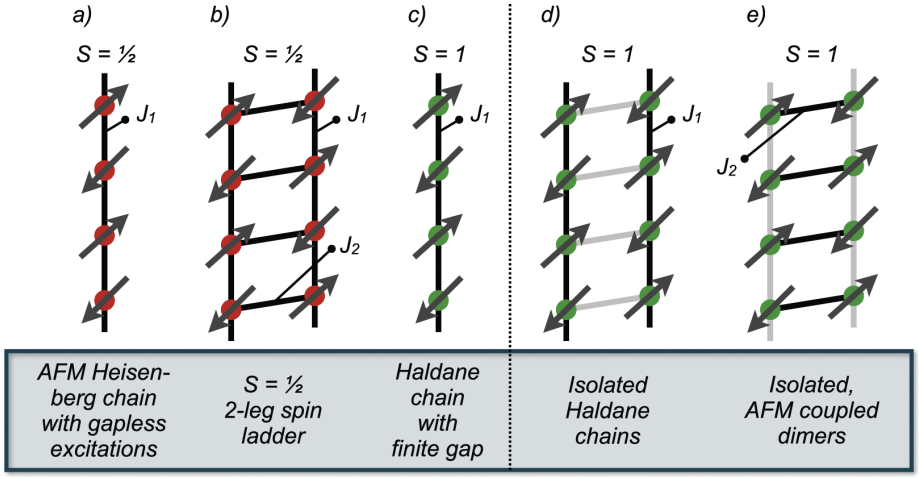

Figure 3.4: *Chain and ladder systems with different spins and exchange couplings. a)–c) Different 1D systems. d) & e): Limiting cases of the structural 2-leg ladder with AFM exchange couplings J_1 and J_2. d) $|J_1| \gg |J_2|$: For a negligible rung coupling J_2 two Haldane chains result in a spin liquid phase for the ground state. e) $|J_2| \gg |J_1|$: For a negligible coupling J_1 along the legs, isolated dimers cause a localized ground state. For details see text.*

as proposed by Haldane [3], see Fig. 3.4c for illustration. Several experimental realizations are known [80, 81]. Only very little is known about the ground state and excitations of an $S = 1$ 2-leg spin ladder. From bosonization studies [82–84] and quantum Monte Carlo simulations [85] a continuous crossover from the delocalized Haldane spin gap state to the case of localized AFM dimers, which also shows a spin excitation gap, is predicted, see Fig. 3.4d) & e) for the limiting cases. Experimentally the situation is complicated by the fact that most $S = 1$ systems (usually based on high-spin Ni^{II} transition metal ions) show a strong axial crystal field anisotropy D which modifies the ground state of the spin system. [86] To the knowledge of the author no realizations of an $S = 1$ spin ladder have been reported so far.

Structure

$Na_2Ni_2(C_2O_4)_3(H_2O)_2$ crystallizes in the monoclinic space group $P2_1/c$ with $a = 5.8144(2)$, $b = 15.6474(5)$, and $c = 6.8357(3)$ Å as determined by XRD [87] on a single crystal. All Ni^{2+} ions are crystallographically equivalent and, therefore, each of them is six-fold coordinated by a distorted octahedron of ligands in the same manner, as shown in Fig. 3.5b. The coordinated oxygens are associated with two crystallographically independent oxalate $(C_2O_4)^{2-}$ dianions (I, II) and an additional mono-dentate oxalate oxygen atom (III). The remaining site (IV) is filled by a water molecule. Ni-O bond lengths range from 2.020(1)-2.114(1) Å and opposite pairs of oxygen have similar Ni-O lengths. The network of $[Ni_2(C_2O_4)_3]_n^{2n-}$ anions forms a 1D spin-ladder. In this topology, the vertices

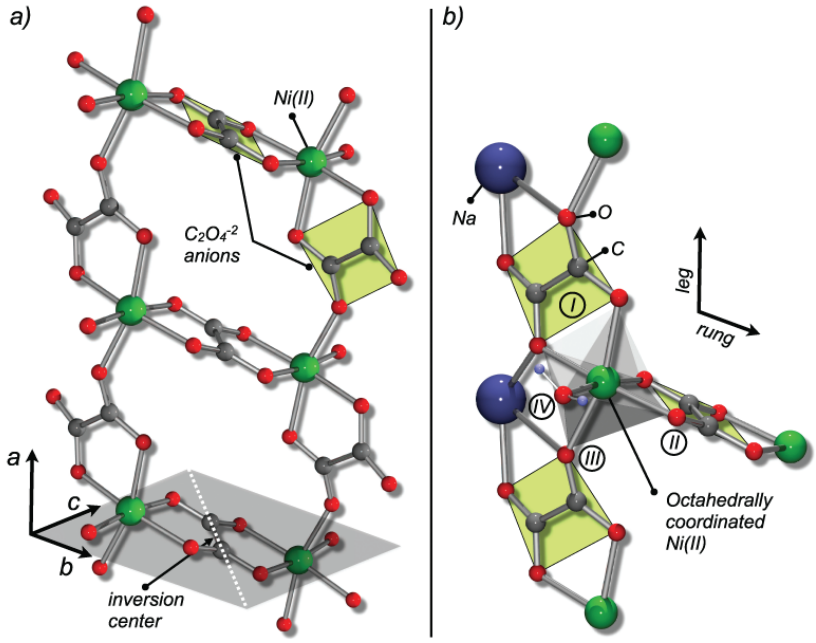

Figure 3.5: *a) Ladder structure of NiOx. b) Six-fold coordination of the Ni-ions (green) by oxalate ligands (I,II,III). The site at IV is filled with a water molecule.*

are given by the metal ions, and the bonds are represented by the oxalate bridges, see Fig. 3.5a. Although the latter form the legs as well as the rungs of the ladder, their function for the bridging of the Ni ions is different. The rung is given by a symmetric *bis*-chelating bridging mode (oxalate II in Fig. 3.5b) where the C-C centroid of the oxalate is a crystallographic inversion center. This coordination provides two superexchange paths for the magnetic interaction of the Ni ions on the rung where the bond length between the Ni is $d_{\text{rung}} = 5.294(1)$ Å. The metal centers on the legs have distances of $d_{\text{leg}} = 5.810(1)$ Å and are unsymmetrically coordinated by a second oxalate. This anion is chelating to one Ni ion and forming a mono-dentate coordination to a second Ni ion with a 1,3-*syn anti*-geometry providing only one path for superexchange. These structural linkages are likely to provide the only pathways for magnetic exchange between the metal centers.

Static Susceptibility

The static susceptibility of an oriented single crystal of NiOx was obtained by measuring the sample in an external field of $H = 2$ T between 2 and 300 K using an MPMS (section 2.6). Therefore, the fragile crystal was prepared in a small paper bag in order to ensure a durable orientation of the crystal during the measurement process while keeping the error due to the magnetic properties of the sample holder at the minimum. Fig. 3.6 shows the susceptibility versus temperature plots of the single crystal measurements where the external field is aligned parallel with respect to the a, b, and c-axis of the crystal. Depending on the orientation, the

curves exhibit pronounced maxima between 39 and 47 K. For decreasing temperature, the susceptibility strongly turns to zero indicating a non-magnetic ground state. The upturn for $T < 5\,\mathrm{K}$ is a result of paramagnetic centers in small concentrations (approx. 1 %). The corresponding Curie tails are not identical for all directions, since the entire concentrations of the observed impurities do not solely arise from the sample, but depend also on the properties of different sample holders.
For $T > 100\,\mathrm{K}$, a Curie-Weiss fit was applied to the susceptibility data of each orientation. It results in different effective moments for the different axes, shown in Tab. 3.1. The variability of the magnetic moments can be assigned to an anisotropic g-value which is not unusual for Ni. This behavior is generally expected as well for a two-leg spin ladder as for the two limiting cases, an isolated $S = 1$ Haldane chain or a system of AFM coupled dimers. [3, 79, 82, 83, 85]

$H \parallel$	$T_{\max}(\mathrm{K})$	$\mu_{\mathrm{eff}}(\mu_{\mathrm{B}})$
a	39	5.04
b	47	4.61
c	45	5.11

Table 3.1: *Characteristics of the static susceptibility for different directions. For details see text.*

Taking into account the two different exchange pathway topologies which suggest a stronger magnetic exchange interaction along the rungs than along the legs of the ladder and considering the result of the foregoing susceptibility analysis this leads to an isolated dimer model. Thereby, the dimers are formed by two $S = 1$ spins on the rung of the ladder where the coupling is assumed to be AFM in order to account for the spin-singlet in the ground state. Indeed, it turned out that the description of the measurements are nicely reproduced within the framework of an effective spin Hamiltonian comprising a Heisenberg interaction energy term and the Zeeman energy. Additionally, a single anisotropy energy term was added to consider at least the predominant uniaxial distortion of the octahedral environment of the Ni ions,

$$\mathcal{H}_{\mathrm{eff}} \;=\; J_1\,\mathbf{S}_1 \cdot \mathbf{S}_2 \;+\; \mu_{\mathrm{B}}\mathbf{H} \cdot g(\gamma) \cdot \mathbf{S} \;+\; \sum_{k=1,2} \mathbf{S}_k \cdot \mathbf{D}'(\gamma) \cdot \mathbf{S}_k. \tag{3.3}$$

In (3.3) both the g-factor and the anisotropy tensor $\mathbf{D}'$ depend on the angle γ,

$$g(\gamma)^2 \;=\; g_\perp^2 \cos^2\gamma \;+\; g_\parallel^2 \sin^2\gamma \tag{3.4}$$

$$\mathbf{D}'(\gamma) \;=\; U(\gamma)^\dagger \cdot \mathbf{D} \cdot U(\gamma), \tag{3.5}$$

which describes a rotation of the crystal about an axis perpendicular to the crystallographic z-axis and, therefore, considers different principal axis systems for the crystal. It should be remarked that $\mathbf{D}$ in (3.5) has a simple structure because it is diagonal for pure axial anisotropies as discussed in section 1.9 and, therefore, depends only on D.
The isolated dimer approximation may be improved by introducing an effective exchange interaction J_2 along the legs treated in mean field approximation in the

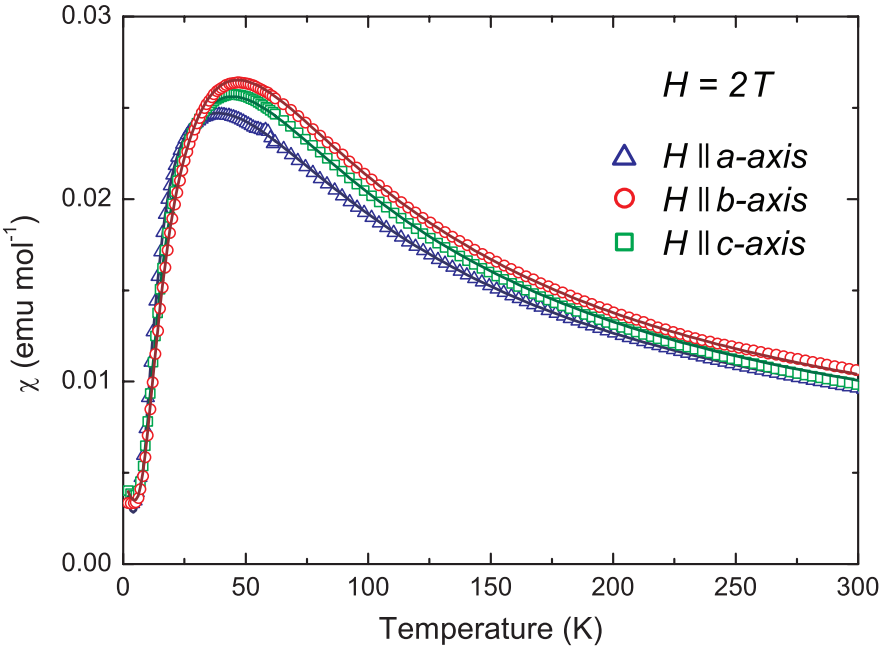

Figure 3.6: *Single crystal susceptibility data of NiOx for the principal directions a, b, and c of the unit cell. Slightly different temperature dependences of the curves indicate the presence of magnetic anisotropy. The susceptibility strongly decreases at low T indicating a non-magnetic ground state. For temperatures exceeding approximately 100 K the behavior can be described by a Curie-Weiss law. Fits are included by the solid lines.*

calculation of the magnetic susceptibility χ using

$$\chi_{\text{ladder}} = \frac{\chi_{\text{dimer}}}{1 + J_2\,\chi_{\text{dimer}}}. \tag{3.6}$$

For the analysis of the magnetization data, Hamiltonian (3.3) is numerically diagonalized for a particular orientation γ of the external magnetic field. The magnetization and finally the susceptibility χ is then calculated from the free energy by variation of the parameters of the spin Hamiltonian in an iterative process where the mean square functional of the model and experimental data points is simultaneously minimized for directions a, b, and c. Thereby, the specific Hamiltonians for all three directions share a common exchange coupling constant J_1, and the fixed absolute value of the axial anisotropy $|D|$ which is anticipated here to be 11.5 K resulting from the ESR experiment described in the next paragraph. The total susceptibility χ thereby consists of the main contribution (3.6) and also a temperature independent term $\chi_0 = \chi_{\text{dia}} + \chi_{\text{VV}}$ which includes the diamagnetic contribution χ_{dia} and the Van Vleck paramagnetic susceptibility χ_{VV} of Ni^{II} as well as a Curie contribution C_{imp}/T with a Curie constant C_{imp} owing to paramagnetic impurities,

$$\chi = \chi_{\text{ladder}} + \frac{C_{\text{imp}}}{T} + \chi_0. \tag{3.7}$$

In addition, an orientation dependent g-factor $g(\gamma)$ as well as the angle γ itself have been used as fit parameters for the different orientations, since the orientation of the principal axis of the magnetic anisotropy tensor is not known.

The fit results for the measurements at $H = 2\,\mathrm{T}$ are shown in Fig. 3.6 as solid lines. The magnetic susceptibility is very well described in the framework of the model. The calculation yields an AFM rung exchange J_1 of $\sim 43\,\mathrm{K}$, while the inter-dimer exchange J_2 results to zero. The principal values of the g-tensor are slightly anisotropic with $g_{\parallel} = 2.20$ and $g_{\perp} = 2.29$ where the perpendicular direction is defined as the b-axis which lies in the plane perpendicular to the ladder legs, see Fig. 3.5a. For details of the fit, performed by Mennerich, refer to [87].

The relative energies of the spin states of NiOx, which were calculated in the framework of the Hamiltonian (3.3), are plotted in Fig. 3.7. In this example, the energy levels have been calculated for a magnetic field oriented perpendicular to the axis of the anisotropy tensor $\mathbf{D}$. In Fig. 3.7 the spin singlet ground state is well separated from the $S = 1$ triplet and the $S = 2$ quintuplet states. The separation energy between singlet and triplet thereby corresponds to the coupling constant $E_{0,1} = J_1 = 43\,\mathrm{K}$, whereas the singlet-quintuplet gap accords to $E_{0,2} = 3E_{0,1}$. In

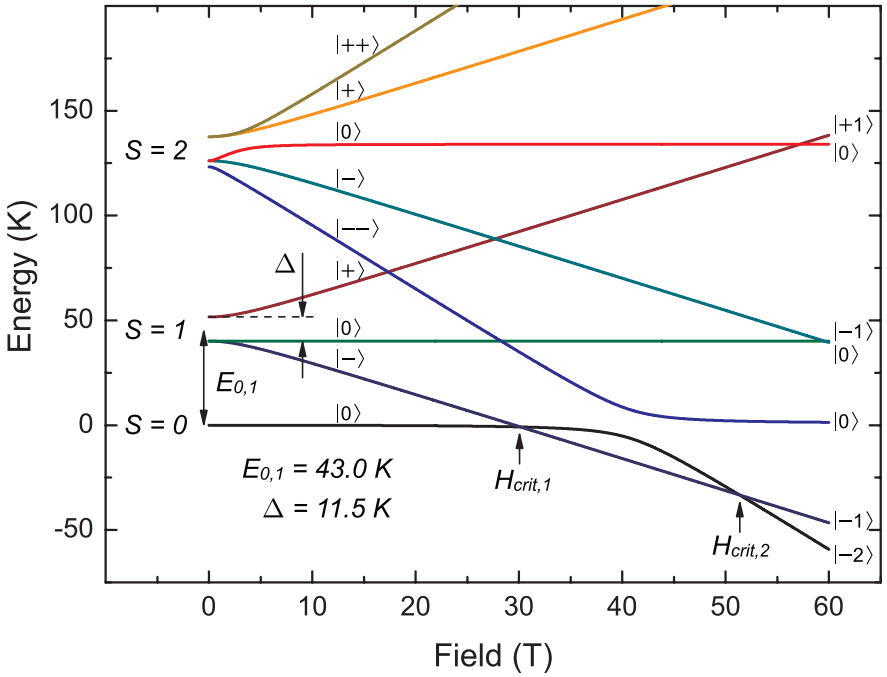

Figure 3.7: *Relative spin state energies calculated for the magnetic field applied perpendicular to the z-axis of the uniaxial anisotropy tensor: the triplet $S = 1$ and the quintuplet $S = 2$ are well separated from the $S = 0$ ground state by an activation energy of roughly $E_{0,1} = 43\,K$ and $E_{0,2} = 3E_{0,1}$, respectively. Both multiplets exhibit a zero field splitting due to crystal field anisotropy. Note the ground state spin-level crossings at approximately $H_{crit,1} = 30\,T$ and $H_{crit,2} = 52\,T$, respectively. For details see text.*

zero magnetic field the splitting of the states within the excited $S = 1$ and $S = 2$ multiplets is induced by the uniaxial magnetic anisotropy, D. Both triplet and quintuplet levels split with increasing magnetic field due to the Zeeman effect. In higher fields the singlet is crossed by the lowest triplet state $|S = 1, -\rangle$ at the field of $H_{\mathrm{crit},1} = 30\,\mathrm{T}$. A second level-crossing occurs at $H_{\mathrm{crit},2} = 52\,\mathrm{T}$. These critical fields are thereby obviously an effect of the size of the exchange J_1 and the anisotropy parameter D. In the next paragraphs these level-crossings are evidenced by tHF ESR and pulse field magnetization measurements.

High-Field ESR

ESR measurements in static magnetic fields have been performed with an MVNA (described in section 2.2). Experiments in pulsed magnetic fields up to 40 T have been carried out with an FIR laser as radiation source (refer to section 2.5). For the measurements a poly-crystalline sample of NiOx was used.[3] The powder was prepared as a pressed pellet with a small amount of a diphenyl-picryl-hydrazyl (DPPH) marker attached for calibration of the magnetic field strength.
At a base temperature of 4.2 K no ESR signals were found which could be associated with the resonance of bulk Ni^{II} spins in the sample. However, with increasing temperature, it was possible to assign four modes to the bulk ESR spectrum of NiOx, see Fig. 3.8. These modes are numbered from 1 to 4 in order of their appearance in ascending magnetic field and marked by arrows in Fig. 3.9 and in the inset of Fig. 3.8. The position of the modes in the magnetic field H depends on the excitation frequency as would be expected for magnetic resonance. Respective resonance branches versus H_i^{res} are plotted in the main panel of Fig. 3.8. In the ESR experiment mode 1 is the strongest in intensity in static magnetic fields at 550 GHz, whereas modes 2, 3, and 4 appear as weak satellites on the non-linear background. At a fixed excitation frequency $\nu = 300\,\mathrm{GHz}$ the intensity I of mode 1 has been studied as a function of temperature. The result is shown in Fig. 3.10. $I(T)$ exhibits an activation temperature dependence similar to that of the static magnetization $M(T)$ in Fig. 3.6. Since the ESR intensity is determined by the static susceptibility χ of the spins participating in the resonance the common temperature behavior of $I(T)$ and $M(T) = \chi(T)H$ gives evidence that in the ESR experiment the same spins are probed which contribute to the static magnetic susceptibilities. Mode 1 has a maximum intensity at $\mathrm{T} \sim 30$–$35\,\mathrm{K}$ which roughly corresponds to the energy separation between the singlet ground state and the first $S = 1$ excited state, see Fig. 3.7. This allows to unambiguously assign this mode to a resonance excitation within the $S = 1$ multiplet. Owing to the weakness of modes 2, 3, and 4 they can be detected only in a limited temperature range $30 - 60\,\mathrm{K}$. At smaller temperatures they are not visible due to

[3] The 2.04 mg single-crystal which has been used for the susceptibility measurements was too small to give sufficient ESR absorption. The mass of the powder sample has been one order of magnitude larger.

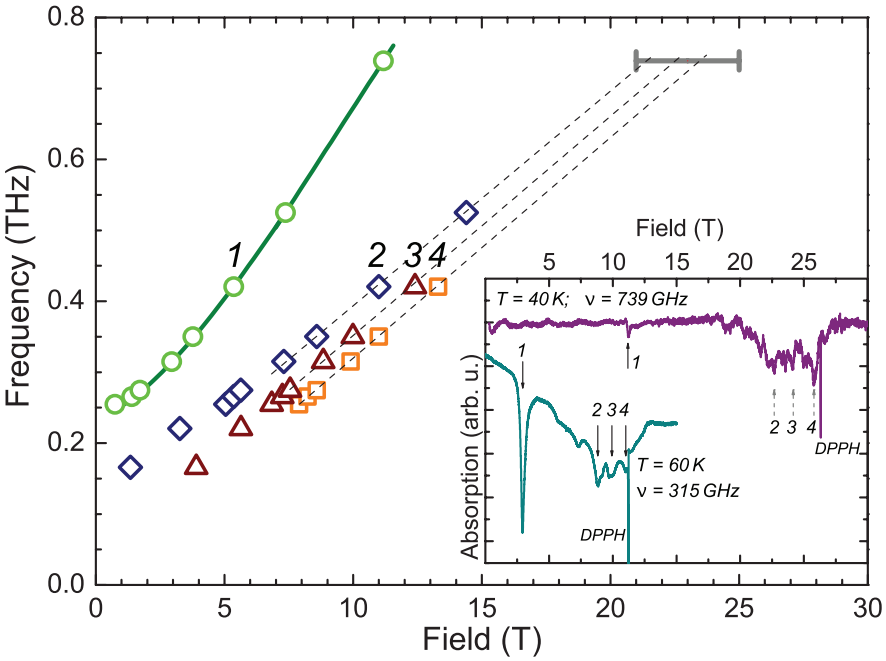

Figure 3.8: *Main panel: Relationship ν versus B_i^{res} for the ESR modes $i = 1, \ldots, 4$. Solid line is a theoretical fit of the data. Dashed lines are a linear approximation of branches 2, 3, and 4 to high fields. Gray error bar indicates a field region where a broad absorption mode is observed in the pulsed field ESR measurement. Inset: ESR spectrum in a static (bottom curve) and pulsed magnetic field ESR experiment (top curve). Sharp lines are due to the DPPH field marker. Resonance modes associated with a bulk ESR spectrum of NiOx are indicated by black arrows and numbered. The anticipated positions of modes 2, 3, and 4 at high magnetic fields are marked by gray dashed arrows. For details see text.*

the strong decrease of their amplitude, whereas at higher temperatures they also broaden. Nevertheless, their occurrence in the temperature window where the static susceptibility is strongest, see Fig. 3.6, allows to assign them to the bulk ESR response of the NiOx sample, too.

A remarkable feature of the frequency/field diagram in Fig. 3.8 is the intercept of the strongest ESR branch 1 with the frequency axis at $\nu_0 \approx 239\,\mathrm{GHz}$. This implies a finite energy gap $\Delta = \nu_0 h/k_\mathrm{B} \approx 11.5\,\mathrm{K}$ for this resonance excitation. This zero field gap can be straightforwardly identified with the zero field splitting of the first excited triplet in Fig. 3.7. Numerical solution of the Hamiltonian (3.3) yields $\Delta = |D|$. Therefore, from the ESR data an accurate estimate of the absolute value of the single ion anisotropy parameter $|D| = 11.5\,\mathrm{K}$ is obtained which is essential for the understanding of the static magnetic properties of NiOx, as discussed in the previous paragraph.

ESR measurements of a poly-crystalline sample imply the averaging of all possible orientations of the micro-crystallites in a powder with respect to the applied magnetic field H. As a result the orientations perpendicular to the z-axis of the

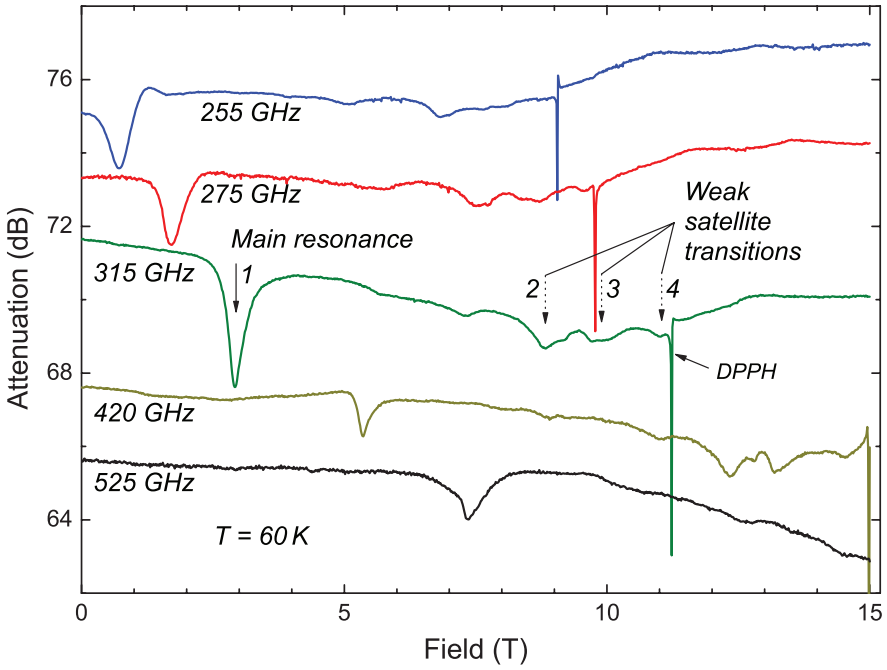

Figure 3.9: *Selected ESR spectra measured at 60 K between 255 and 525 GHz. The main ESR line and three weak satellites are marked by arrows. DPPH has been used as a field marker.*

uniaxial anisotropy tensor will dominate in the spectrum, whereas other directions may form a broad non-linear background. Thus for a qualitative understanding of the field dependence of the resonance modes it is sufficient to consider the energy diagram for $H \perp z$, shown in Fig. 3.7. The field dependence of branch 1 (solid line in Fig. 3.8) can be very well reproduced assuming that the resonance transition occurs between the $|-\rangle$ and $|+\rangle$ states of the excited triplet in Fig. 3.7. In fact, this usually forbidden transition has the strongest intensity in the spectrum for 550 GHz. This is due to the strong anisotropy of the crystal field yielding a large zero field gap Δ and mixing strongly the pure spin states $|-1\rangle$, $|0\rangle$, and $|+1\rangle$ into the $|-\rangle$ and $|+\rangle$ states for $H \perp z$ in the field regime $g\mu_B H < \Delta$. Indeed, in a pulsed field ESR experiment the relative intensity of this mode becomes appreciably smaller (see Fig. 3.8, inset). For the excitation frequency of 739 GHz the resonance field amounts to $H_1^{\mathrm{res}} = 11.2\,\mathrm{T}$. For this field strength not the crystal field, but the magnetic field direction determines the quantization axis. Thus the mixed $|-\rangle$ and $|+\rangle$ states transform into almost pure $|-1\rangle$ and $|+1\rangle$ states which do not fulfill the ESR selection rules, equation (1.5). In contrast to mode 1, the exact assignment of modes 2, 3, and 4 is difficult owing to their small intensity. The relationship ν versus H_1^{res} has a steep slope because both energy levels, $|-1\rangle$ and $|+1\rangle$, depend on magnetic field diverging from each other with increasing H. The much smaller slope of branches 2, 3, and 4 suggests that resonance transitions within the neighboring pairs of states, like, e.g., $|-\rangle \leftrightarrow |0\rangle$, $|0\rangle \leftrightarrow |+\rangle$, etc., of the multiplets $S = 1$ and $S = 2$ should be involved. Branch 2 has a much

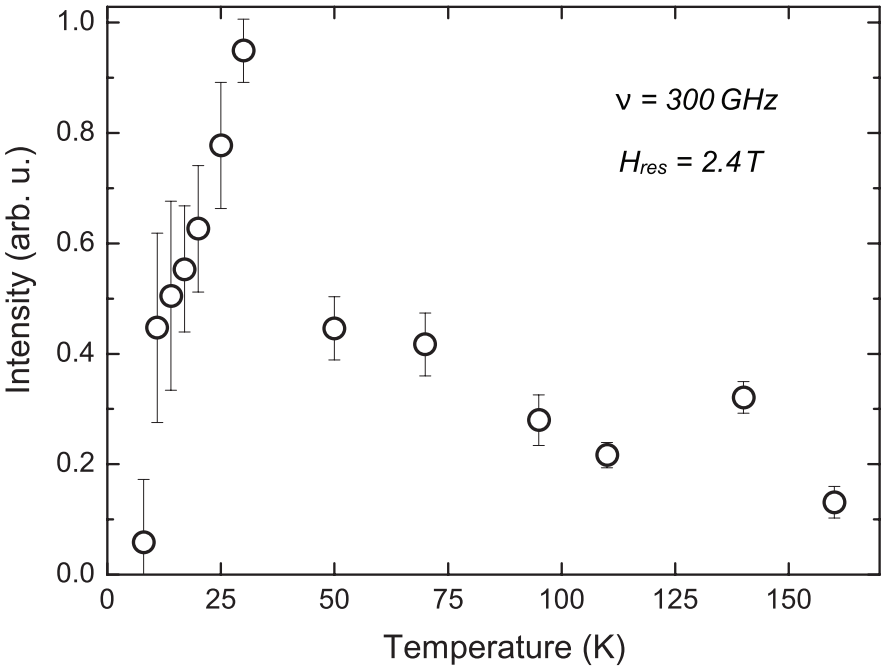

Figure 3.10: *Intensity of the strongest ESR mode 1 as a function of temperature. The activation behavior is similar to the static susceptibility $\chi(T)$, compare with Fig. 3.6.*

smaller frequency offset as compared to Δ and can be associated with the transition $|{-}{-}\rangle \leftrightarrow |{-}\rangle$ in the quintuplet $S = 2$. Branches 3 and 4 might be gapless which is the case for transitions $|{-}\rangle \leftrightarrow |0\rangle$ in the triplet as well as in the quintuplet. Unfortunately, it was not possible to achieve a better resolution of modes 2, 3, and 4 in the pulsed field measurements. Only a broad absorption mode is observed in the field region where resonances 2, 3, and 4 are anticipated, see Fig. 3.8.

High-Field Magnetization

The high-field magnetization measurements have been carried out at the pulsed field facility at the LNCMP, Toulouse, as well (see section 2.6). As can be seen from the energy diagram of the spin states of NiOx, shown in Fig. 3.7, the splitting of the states in a magnetic field yields a level-crossing of the ground state with the lowest triplet state $|{-}1\rangle$ at a field $H_{\mathrm{crit},1}$ and a second level-crossing of the $|{-}1\rangle$ state with the $|{-}2\rangle$ quintuplet state at field $H_{\mathrm{crit},2}$ with $H_{\mathrm{crit},1} < H_{\mathrm{crit},2}$. This leads to a step-like behavior in high-field magnetization measurements. For fields applied along the z-axis, the critical field $H_{\mathrm{crit},1}$ can be estimated using the equation $H_{\mathrm{crit},1} = (J_1 - D/3)/(g\mu_{\mathrm{B}}/k_{\mathrm{B}})$ strongly depending on the sign of D. For fields perpendicular to the local anisotropy axis, a negative D (leading to higher critical values for $H \parallel z$) pushes the critical field to lower values and vice versa for a positive D. Since in powder measurements the perpendicular situation

dominates the spectrum of the spin states, the field-dependent magnetization, among others, allows to determine the sign of the anisotropy D.

The critical field strengths H_{ci} depend on the magnetic exchange J_1 and an exchange energy of 43 K corresponds to roughly 30 T for $H_{\mathrm{crit},1}$. Therefore, high magnetic fields are needed to observe the magnetization steps. We performed measurements at several temperatures (1.47 K, 4.2 K, 10 K, and 26 K) on a powder sample with a mass of 23.2 mg in magnetic fields up to 55 T. The results are shown in Fig. 3.11. In the low temperature experiments the first magnetization step is clearly seen, whereas it smoothes at higher temperatures due to the thermal averaging process. The critical field $H_{\mathrm{crit},1}$ can be obtained from the derivation of the magnetization $\partial M/\partial H$ which is shown in Fig. 3.12 for 1.47 K and 4.2 K. At both temperatures a sharp peak is observed at 29 T. Additionally, a second increase of the magnetization at much higher fields of about 50 T can be anticipated. This step, though strongly broadened, is also observed in the 10 K measurement. At 26 K an almost linear field dependence of the magnetization is observed.

The solid lines in Figs. 3.11 and 3.12 describe simulations using the dimer model with the calculated g-values $g_{\parallel}$ (see above) and $g_{\perp} = g_b$ in a powder average $M = (M_{\parallel} + 2M_{\perp})/3$. For a good description of the high-field magnetization a coupling constant of $J_1 = 44$ K has been used. In particular the differential magnetization is very well reproduced by the simulation, describing both the width and the center position of the peak. A small deviation is found in the field range of 30–33 T in the measurement at 1.47 K which may originate from a little

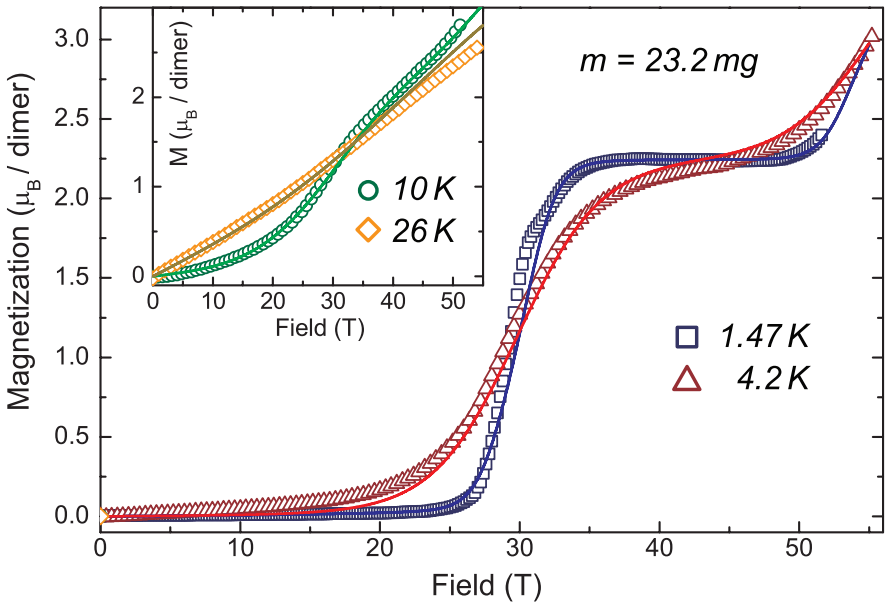

Figure 3.11: *High-field magnetization of the NiOx powder sample. The main panel shows magnetization curves at 1.47 and 4.2 K with clear step-like characteristics. Inset: Magnetization at 10 and 26 K. The solid lines represent simulation data.*

shift of the sample induced by the external field.
The simulation for a negative D of $-11.5\,\mathrm{K}$ yields no reasonable description of the data, regardless on the adjustments of the value of J_1. In this case the first magnetization step is consistent with $J_1 = 43\,\mathrm{K}$, whereas the second step is predicted at too low a field.
From Fig. 3.12, the critical field $H_{\mathrm{crit},1}$ of the powder sample is determined to $H_{\mathrm{crit},1} = 29\,\mathrm{T}$. In the simulations $H_{\mathrm{crit},1}$ results to 27.7 T and 30.7 T for the directions parallel and perpendicular to the magnetic anisotropy axis, respectively. The latter values add nicely to $H_{\mathrm{crit},1} = 29\,\mathrm{T}$ in the powder average shown in Fig. 3.11 and Fig. 3.12. Remarkably, the powder averaging leads to a broadening of the magnetization steps. For the second step, this effect is even more significant: the values 67.1 T and 51.3 T are found by the simulations for the parallel and perpendicular directions for $H_{\mathrm{crit},2}$, respectively. In a powder average this leads to a continuous double-sigmoid-like increase of the magnetization in the field range of 50–70 T where only the first increase is observed in the measurement at 1.47 K in Fig. 3.12.

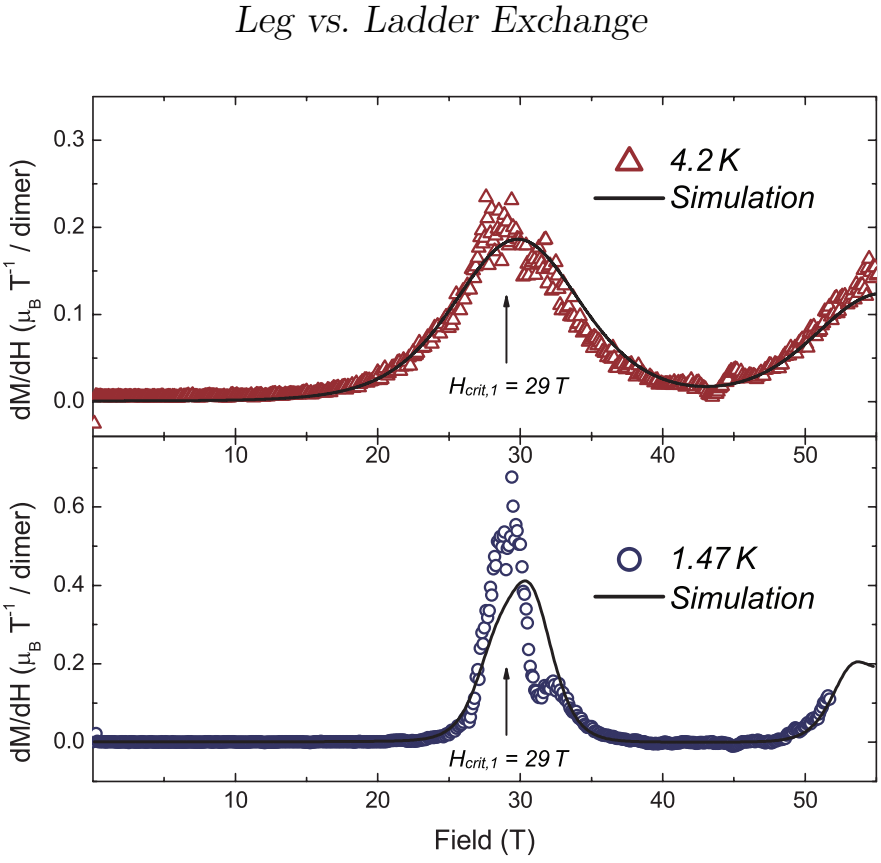

Figure 3.12: *Derivations $\partial M/\partial H$ of the magnetization curves at 1.47 and 4.2 K, (see main panel of Fig. 3.11). Solid lines represent simulation data [87]. See text for details.*

An important result of the study of NiOx is the large difference between the strengths of the magnetic exchange interactions along the rungs ($J_1 = 43\,\mathrm{K}$) compared to the leg exchange ($|J_2| < 2\,\mathrm{K}$) which is virtually not present (the boundary for J_2 is the result of Quantum Monte Carlo (QMC) calculations [87].) This is qualitatively understood considering the different coordination and superexchange angles of the oxalate molecules mediating the exchange.
On the rungs the oxalate forms a $\mu_4 - 1, 2, 3, 4$ bridge[4] between two Ni ions. This bridge provides two symmetric superexchange pathways. On each path the Ni $3d_{x^2-y^2}$ orbitals feature an enhanced electron probability density extending directly towards the corresponding oxygen ions. There is a direct overlap of the Ni $3d_{x^2-y^2}$ and the O 2p wave functions forming σ bonds. The polarized 2p orbitals themselves are strongly overlapping. Therefore, the intermediate carbon atom is not involved in the superexchange mechanism resulting in a strong AFM superexchange interaction, as shown in Fig. 3.13a. In the literature several $\mu_4 - 1, 2, 3, 4$ oxalate-bridged Ni^{II} dimer and chain systems are reported [89, 90] with exchange values (J_1) in the range of 20–42 K. The value of 43 K in NiOx is at the upper limit of the reported range.
For the oxalate bridge along the legs of the spin ladder the situation is completely different. In this case a $\mu_3 - 1, 2, 3$ oxalate bridge is formed. As shown in Fig. 3.13b one Ni ion forms two covalent bonds with the oxalate molecule (with the $x^2 - y^2$ and the $3z^2 - r^2$ orbital, respectively), whereas in the second Ni ion

[4] The prefix μ is given in the International Union of Pure and Applied Chemistry (IUPAC) nomenclature for a bridging ligand. For details of the nomenclature refer to [88]

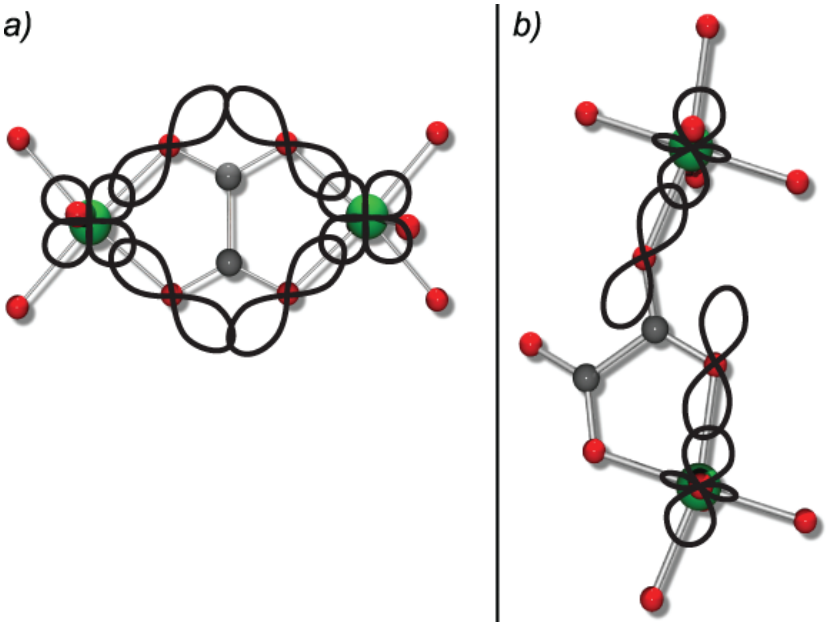

Figure 3.13: *Ni-(ox)-Ni coordination and proposed magnetic exchange pathways on the rungs (a) and on the legs (b) of the spin ladder. The involved Ni 3d and oxygen 2p orbitals are shown in black.*

only the $3z^2 - r^2$ orbital forms a covalent bond. The O 2p orbitals involved in the Ni-O bonds are not overlapping with each other and, therefore, either the carbon atoms or orthogonal O 2p orbitals are involved resulting in a strongly suppressed strength of the superexchange mechanism and maybe even leading to weak FM exchange. Similar $\mu_3 - 1, 2, 3$ oxalate bridges are reported for Cu^{II} systems with magnetic exchange strengths of -0.2 to $0.3\,K$ [91, 92] consistent with the estimate of $|J_2| < 2\,K$ for NiOx.

Conclusion

In this section synthesis, crystal structure, and magnetic properties of the structurally well defined $S = 1$ spin ladder compound NiOx were analyzed. Magnetic susceptibility and pulse field magnetization measurements have been performed to examine the thermodynamic properties of the spin system. The magnetic excitations have been examined with tHF ESR.
Although from the structural point of view NiOx is a 2-leg spin-ladder, a model for isolated dimers formed by the Ni^{II} pairs on the rungs of the ladder yields a very good description of the observations. The analysis of the temperature dependent susceptibility data leads to a singlet ground state: The quantitative analysis results in an intra-dimer AFM exchange constant of $J_1 = 43\,K$, while the estimate for the leg-exchange amounts to $|J_2| < 2\,K$. Moreover, the principal axis of the axial anisotropy tensor could be deduced from a detailed analysis of the single crystal susceptibility data for different orientations. The analysis of the ESR temperature dependence of a poly-crystalline sample of NiOx evidences an activation behavior of the signal intensity of the first excited multiplet which is qualitatively in agreement with the susceptibility data. A strong axial magnetic anisotropy of Ni appreciably admixes pure spin states of the $S = 1$ multiplet in low magnetic fields. Therefore, the anisotropy gives rise to a half-field ESR signal which is owing to the transition $|-\rangle \leftrightarrow |+\rangle$.
By measurement of the ESR frequency dependence of the associated ν/H_ν^{res} resonance branch, it was possible to directly determine the zero-field gap Δ. Numerical analysis of the relevant spin Hamiltonian enabled to assign this gap to the parameter D of the axial component of single ion anisotropy, $\Delta = |D| = 11.5\,K$.
Measurement of the magnetization of NiOx in high magnetic fields yields a step at $H_{crit,1} = 29\,T$. This step could be assigned to the level-crossing of the $|-\rangle$ state in the first excited multiplet $S = 1$ with the spin-singlet. Since the step position $H_{crit,1}$ depends on the intradimer exchange as well as on D, simulations of the magnetization could be used to determine the sign of this parameter to be positive.
The strong anisotropy of the magnetic exchange concerning rung and leg interactions was found to be due to different superexchange pathways on the oxalate molecules. Due to the weak inter-dimer exchange, the compound NiOx represents an excellent example of an $S = 0$ dimer. Its intra-dimer exchange of $43\,K$ enables

to “tune” the ground state by magnetic fields achievable in the laboratory. Finally, this tunability enabled detection of the sign of the axial magnetic anisotropy determined by ESR. So this compound is also an example which documents the power of combining complementary measurement techniques like macroscopic and local magnetic properties.

3.3 Ni_4-Cluster with Tunable Ground State

Introduction

From the magnetic point of view the structural $S = 1$ 2-leg spin ladder compound NiOx, presented in the previous section, behaves like an $S = 0$ dimer. In this compound the AFM intra-dimer coupling on the rung is strong compared to the negligible inter-dimer exchange along the leg of the ladder. This fact yields a hierarchy of the coupling parameters. The following sections will turn from this magnetic homobinuclear to a series of tetranuclear clusters which have been studied in a similar manner [41, 93–95]. Again, the paramagnetic species which has been utilized in the synthesis is Ni, in order to benefit from the commonly observed significant single ion anisotropy [96, 97]. Regarding the ligands for linking the Ni^{II} centers, instead of the oxalate anions, carboxylate and N_3 azide ions are preferred where the latter is known for its ability to mediate different types of strong magnetic couplings depending on its coordination mode [98]. Therefore, the structural flexibility of the bridging azides brings about diverse molecular structures with different geometries of Ni_4 arrays and yields significant variations in magnetic properties.

In this section high-field ESR and static magnetization results on a quadruple-Ni^{II} complex of type $[L_2Ni_4(N_3)(O_2CAda)_4](ClO_4)$ are presented [41]. This compound is a representative of a novel class of tetranuclear Ni^{II} complexes that feature a genuine $\mu_4 - 1, 1, 3, 3$ azide coordination which has been recently communicated [93, 94]. Owing to the complexity of the spectrum of the spin states, arising from the exchange coupling within the molecule, a comprehensive understanding of the magnetism requires application of both bulk and local magnetic

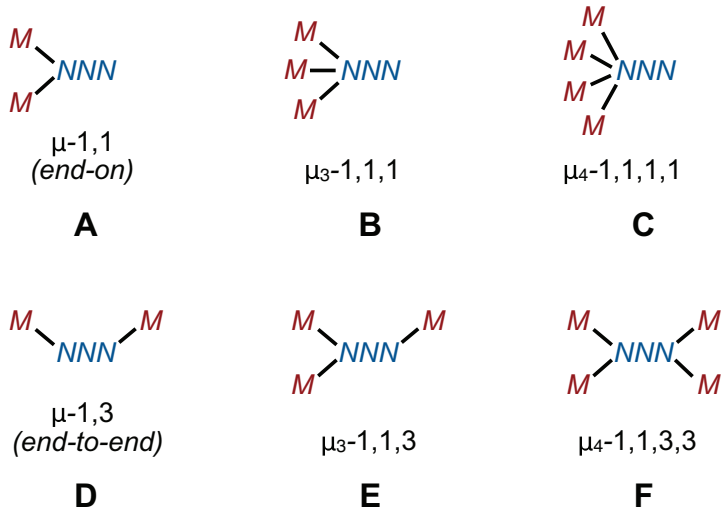

Figure 3.14: *Overview of azide binding modes (taken from Ref. [94]). The compound NiAz utilizes an unprecedented F-type configuration.*

probes such as magnetization measurements and ESR. In particular, tunable millimeter- and submillimeter-wave ESR spectroscopy in strong magnetic fields turned out to be essential for an accurate characterization of the ground state properties and low-lying magnetic excitations of the tetranuclear Ni-Azide complex. The data reveal a non-magnetic ground state of the complex which turns into a magnetic one in strong magnetic fields above $H_{\mathrm{crit},1} \sim 25\,\mathrm{T}$ due to a spin-level crossing. A significant magnetic anisotropy gap of $\sim 7\,\mathrm{K}$ has been observed in the first excited spin multiplet $S = 1$. A semi-quantitative analysis in the framework of a minimal effective spin Hamiltonian yields a good description of the experimental data.

The next section will then turn to a variety of similar Ni_4 complexes with a unique topology in which two of the azide ligands adopt an unusual $\mu_3 - 1,1,3$ bridging mode resulting in FM and AFM exchange interactions that give rise to an overall $S_{\mathrm{tot}} = 0$ ground state. The results of $M(H)$ and ESR measurements on these complexes allow for the important conclusion that increasing the number of the azide bridging ligands strongly enhances the AFM intra-molecular coupling between the Ni spins resulting in the stabilization of the diamagnetic ground state of the complexes. Even though the exchange exceeds the energy range of the applied high magnetic fields and, therefore, prohibit the tuning of the ground state in the range of applied magnetic fields ($< 52\,\mathrm{T}$), the ESR parameters g and D have been successfully probed by thermally exciting the first excited multiplet and inducing spin transitions.

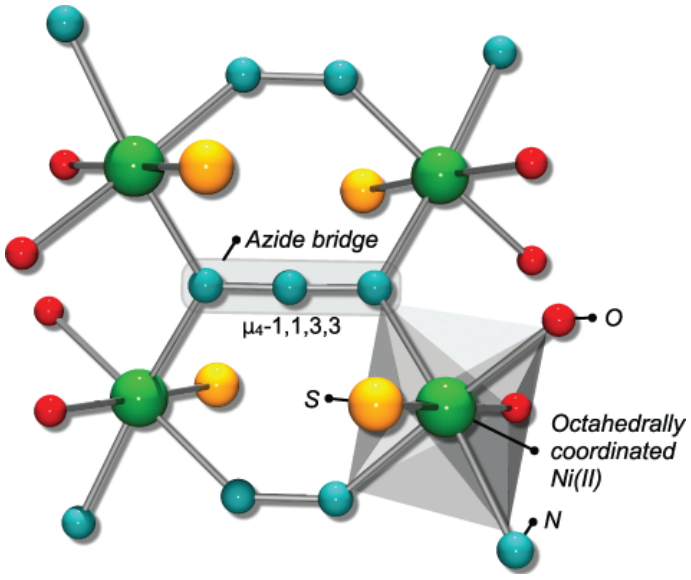

Figure 3.15: *Reduced representation of the molecular structure of the Ni_4-complex $[L_2Ni_4(N_3)(O_2CAda)_4](ClO_4)$, NiAz. The four Ni^{II} ions are connected by the central azide, pyrazolate, and carboxylate bridges (only the F-type $\mu_4 - 1,1,3,3$ azide bridge is shown). Refer to [93] for details.*

Structure

The compound $[L_2Ni_4(N_3)(O_2CAda)_4](ClO_4)$, NiAz, as well as the other clusters from the series published in Ref. [94] basically comprise a network of four Ni^{II} ions in a single molecule featuring an unprecedented central μ_4-1,1,3,3 azide bridging ligand which is symmetric. This novel bridging unit is characterized by a high structural flexibility in terms of binding angles and torsion resulting, together with the individual geometric details of the Ni_4 arrays, in significant differences in the magnetic coupling strengths. While the two major binding modes of the azide ligand are given by *end-on* and *end-to-end* configurations (as shown in Fig. 3.14 A and D) which usually exhibit FM (A) and AFM (D) coupling behavior, only very few examples for the $\mu_3 - 1,1,1$ (B) and the $\mu_3 - 1,1,3$ (E) mode are known where the latter might exhibit AFM and FM exchange. The more unusual binding modes B, C, E and F are only recently reported and should be suited for the linkage of high nuclearity clusters as well as 2D and 3D networks of paramagnetic metal centers [94].

For the synthesis of NiAz two pyrazolate-based dinuclear building blocks are assembled to give a tetranuclear network which is spanned by a central μ_4-azide. Therefore, in particular in order to get crystalline material, four adamantyl carboxylates have been used as additional bridging ligands for holding together the two dinuclear building units.
The molecule crystallizes in the monoclinic space group $P2_1$ (no.14) with $a = 16.391(2)$, $b = 16.515(2)$, $c = 18,416(2)$ Å, and $\beta = 103.902(3)^\circ$ as determined by XRD. The molar mass is $2048.88\,\mathrm{g\,mol^{-1}}$. Details of the synthesis and characterization of the compound under study can be found in [94]. Its molecular structure is shown in Fig. 3.15.

Experimental

For ESR measurements in static magnetic fields we used the MVNA to generate and detect the millimeter-waves, as is described in (section 2.2). In particular, the transmission probehead was used, shown in Fig. 2.9. ESR experiments in pulsed magnetic fields up to 40 T have been performed at the LNCMP Toulouse with the FIR laser described in section 2.5. Complementary measurements of the static magnetization have been performed in pulsed magnetic fields up to 55 T (section 2.6).
For the ESR measurements, a powder sample of NiAz has been pressed into a pellet. A diphenyl-picryl-hydrazyl (DPPH) marker attached to the sample has been used for field calibration.

ESR in Static Fields

At temperatures below 5 K no ESR signals have been detected which can be attributed to the resonance of Ni^{II} in the static field measurements in fields $H < 15$ T. However, a well-defined ESR spectrum develops with increasing temperature. In Fig. 3.16a a few representative spectra are shown between 10 and 130 K at a fixed excitation frequency of 332 GHz. Four resonances were observed by sweeping the magnetic field up to 15 T, numbered from 1 to 4 in the order of their appearance in increasing field direction. The intensity of an ESR signal is proportional to the static susceptibility of the resonating spins [12]. In Fig. 3.16b the temperature dependence of the individual resonance intensities, $I_i(T)$, i.e., the areas under the respective absorption lines, and of the total intensity $I_{\mathrm{tot}}(T) = \sum_i I_i$ are shown. Both $I_i(T)$ and $I_{\mathrm{tot}}(T)$ exhibit an activated temperature behavior. In particular the total intensity $I_{\mathrm{tot}}(T)$ reveals a T dependence similar to the static susceptibility χ_{stat} results (see Ref. [94] and Fig. 3.22): when lowering the temperature from 300 K it shows a Curie-like paramagnetic increase, followed by a maximum at about 50 K. At lower temperatures, $I_{\mathrm{tot}}(T)$ goes to zero indicating a non-magnetic ground state. Examination of the temperature dependence of the intensities $I_i(T)$ of the individual resonances yields important additional information. Peaks 1, 2 and 4 follow a common activation behavior with maxima at about 30 K, whereas resonance 3 shows a broad maximum at roughly 150 K, as can be seen from Fig. 3.16. This observation suggests

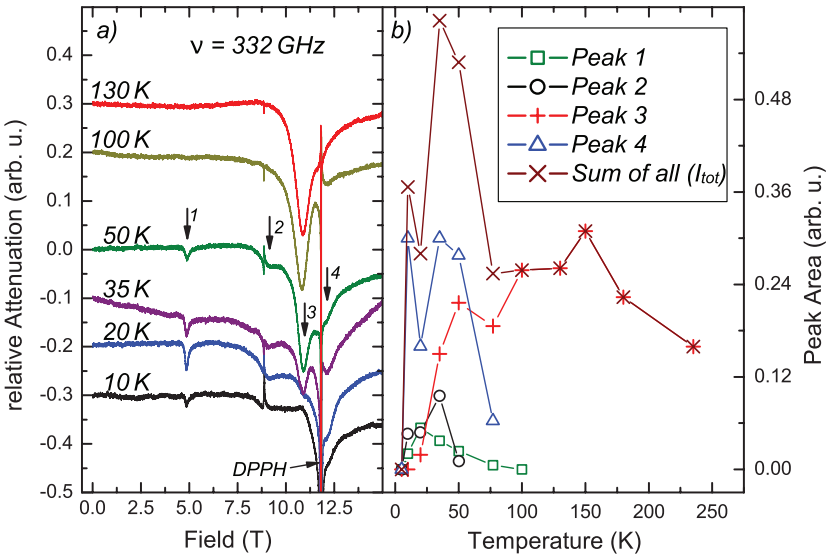

Figure 3.16: *Left panel: ESR spectra of NiAz at $\nu = 332$ GHz for different selected temperatures. Four thermally activated resonance peaks are indicated by the arrows and numbered from 1 to 4, respectively. A sharp resonance signal at 11.8 T is due to the DPPH field marker. Right panel: Temperature dependence of the areas I_i under the resonance peaks $i = 1$ to 4 and the total area I_{tot}, respectively.*

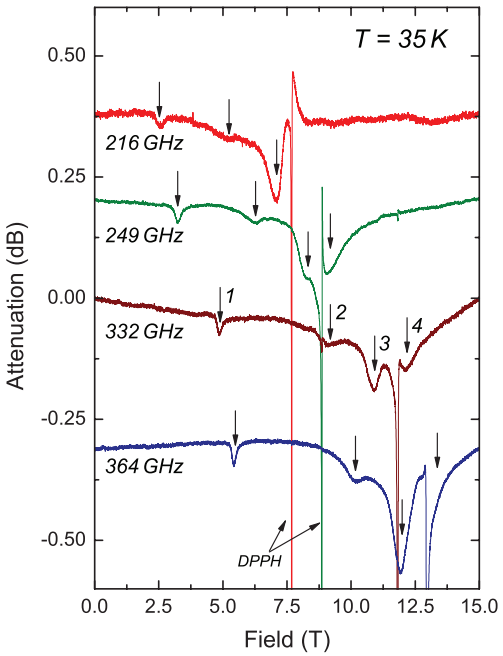

Figure 3.17: *ESR spectra of NiAz at $T = 35\,K$ at different selected excitation frequencies ν. Four resonance modes are indicated by the arrows. Sharp lines are DPPH signals.*

that resonances 1, 2, and 4 belong to resonance transitions in the same (first) excited spin state, whereas peak 3 is due to spin resonance in a higher lying energy state.

At the selected temperature of 35 K where all four resonance modes are clearly seen the ESR spectrum has been measured at different excitation frequencies ν. As can be seen in Fig. 3.17 where several typical spectra are plotted, the positions of the peaks in magnetic field H_i^{res} depends on ν which ensures their character as magnetic resonances. The relation between ν and H_i^{res} is shown in Fig. 3.18. The data fall into four well defined resonance branches labeled from 1 to 4 according to the numbering of the detected resonance modes. Remarkably, extrapolation of the branches 1 and 2 to zero magnetic field reveals them to intercept the frequency axis at $\nu_0 = 139\,\mathrm{GHz}$, i.e., there is a finite energy gap $\Delta_1 = \nu_0 h/k_{\mathrm{B}} = 6.7\,\mathrm{K}$ for resonance excitations 1 and 2. On the other hand, branches 3 and 4 can be extrapolated to almost zero frequency at zero field indicating resonances 3 and 4 to be gapless within the experimental resolution.

ESR in Pulsed Magnetic Fields

Measurements of ESR at an excitation frequency $\nu = 739\,\mathrm{GHz}$ in pulsed magnetic fields confirm the static field data for smaller ν. Representative ESR spectra are shown in Fig. 3.19a. No signals are detected at $T = 4.2\,\mathrm{K}$, whereas three thermally activated resonances appear at $T \geq 25\,\mathrm{K}$. They can be straightforwardly

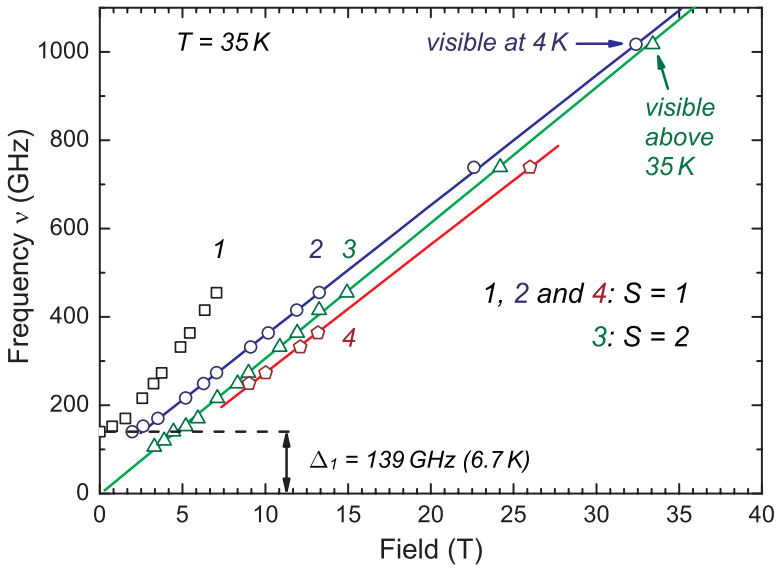

Figure 3.18: *Resonance branches at $T = 35\,K$ [including pulsed field ESR at 739 GHz (35 K) and 1017 GHz (4.2 K)]. Branches 1 and 2 have a finite frequency offset Δ_1, whereas branches 3 and 4 can be extrapolated to zero frequency at zero magnetic field. Note that resonance 2 at 1017 GHz is visible at 4.2 K owing to the spin-level crossing. Solid lines are guides for the eye.*

assigned to the resonance modes 2, 3, and 4, respectively, as they nicely fall into the respective ν vs H_i^{res} resonance branches in Fig. 3.18. However, measurements of ESR at an excitation frequency $\nu = 1017\,\mathrm{GHz}$ yield a new feature in the spectrum: At a low temperature of 4.2 K a strong absorption mode develops at $H > 25\,\mathrm{T}$ whose intensity decreases with increasing T. At even higher temperatures another thermally activated resonance arises in the spectrum, as can be seen from Fig. 3.19b. The peak position H_i^{res} of the former corresponds to branch 2, whereas the peak position of the latter can be assigned to branch 3 in Fig. 3.18.

Magnetic Field Dependence of the Magnetization

The occurrence of the ESR resonance mode 2 already at a low temperature of 4.2 K for $H > 25\,\mathrm{T}$ should be related to changes in the static magnetic properties of the sample. We hence performed magnetization studies $M(H)$ at 4.2 and 1.45 K in pulsed fields up to 55 T in order to directly probe these changes. The $M(H)$ dependences at both temperatures are very similar and, indeed, the data yield a broad step-like increase of $M(H)$ centered at a field $H_{\mathrm{crit}} \sim 25\,\mathrm{T}$, as shown in Fig. 3.20. The magnetization curves are reversible, i.e., no hysteresis between the up- and down field sweeps can be observed within the experimental accuracy. Remarkably, there is a finite slope of the magnetization at $H < H_{\mathrm{crit}}$ of the order $\partial M/\partial H = \chi_< = 6.78 \times 10^{-3}\,\mathrm{emu\,mol^{-1}\,Ni}$ which is almost doubled for $H > H_{\mathrm{crit}}$ reaching a value $\chi_> = 1.24 \times 10^{-2}\,\mathrm{emu\,mol^{-1}\,Ni}$, where $\chi_{\lessgtr}$ is χ at $H \lessgtr H_{\mathrm{crit}}$.

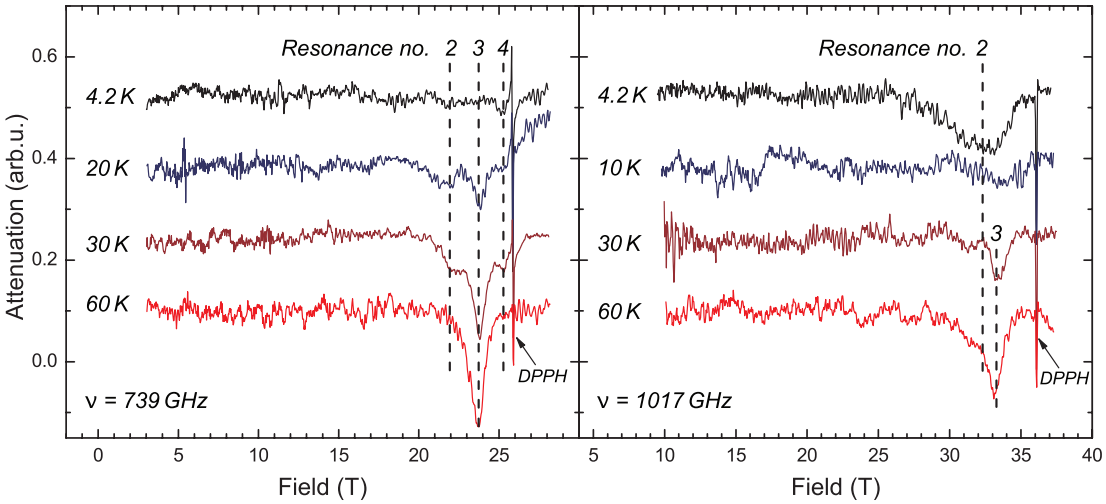

Figure 3.19: *ESR spectra of NiAz in pulsed magnetic field at 739 and 1017 GHz, respectively. a) Resonance modes 2, 3, and 4 indicated by thin lines are visible at elevated temperatures only. b) Note that at 4.2 K a new broad line with a peak at about 32 T appears in the spectrum.*

To summarize the experimental section, the central result of our measurements in pulsed magnetic fields concerns the fact that high frequency ESR reveals an additional strong absorption mode at 4.2 K in high magnetic fields above 25 T. Concomitantly, the pulsed field magnetization exhibits a broad step-like increase of $M(H)$, at low temperatures, centered at a field $H_{\mathrm{crit}} \sim 25\,\mathrm{T}$. Both features signal drastic changes of the magnetic ground state tuned by the magnetic field which is discussed in detail in the following section. Additionally, the experimental results provide the diagram of the excitation frequency of the ESR modes versus resonance magnetic field. In the next section we will attribute these features to specific spin transitions and, in particular, deduce important parameters such as the g-factor and the zero field splitting (ZFS) gap. It is noteworthy to emphasize the necessity of the experimental determination of these quantities for a comprehensive understanding of the spectrum of the spin states of NiAz, specifically the occurrence of the magnetic field driven transition to a new magnetic state in strong fields.

The Effective Spin Hamiltonian: Minimal Model

In order to address the magnetic properties of NiAz, in the following a minimal model is discussed which describes the magnetic field dependence of the spin levels. In NiAz, the Ni_4 cores of each molecule are well separated in the solid phase. Hence, it is reasonable to assume the inter-molecular magnetic interactions to be much weaker than the intra-molecular ones. The latter couplings are mediated via the central azide bridge which connects the four Ni centers with some contribution from the pyrazolate and carboxylate bridges, see Fig. 3.15. The

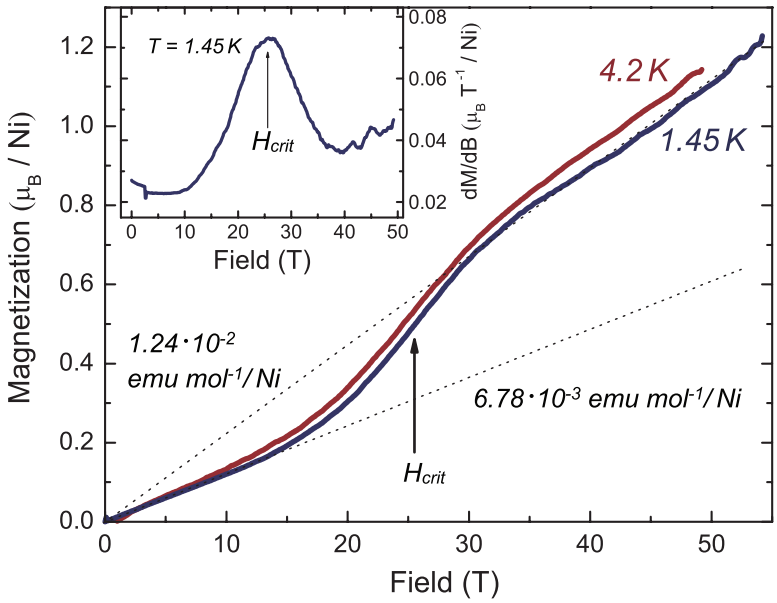

Figure 3.20: *Field dependence of the static magnetization $M(H)$ in pulsed magnetic field. Note a step-like increase of M at $\sim 25\,T$ and a linear background indicated by dot lines in the field range 0–15 T and 30–50 T, respectively. The field derivative of the magnetization $\partial M/\partial H$ at 1.45 K is shown in the inset.*

minimal effective spin Hamiltonian to describe the magnetism of the Ni_4 complex should, therefore, contain the magnetic exchange interactions between the four Ni spins $S_{\mathrm{Ni}} = 1$. Additionally, the magnetic energy is determined by the single ion anisotropy caused by the crystal field (CF) and the spin-orbit coupling as well as the Zeeman energy:

$$\begin{aligned}
\mathcal{H} = \quad & J_1(\mathbf{S}_1 \cdot \mathbf{S}_2 + \mathbf{S}_3 \cdot \mathbf{S}_4) \\
& + J_2(\mathbf{S}_1 \cdot \mathbf{S}_3 + \mathbf{S}_2 \cdot \mathbf{S}_4) \qquad (3.8) \\
& + J_3(\mathbf{S}_1 \cdot \mathbf{S}_4 + \mathbf{S}_2 \cdot \mathbf{S}_3) \\
& + D \sum_{i=1\cdots4} \left[S_{iz}^2 - \frac{1}{3} S_{\mathrm{Ni}}(S_{\mathrm{Ni}} + 1) \right] \qquad (3.9) \\
& + g\mu_{\mathrm{B}} \mathbf{H} \cdot \sum_{i=1\cdots4} \mathbf{S}_i. \qquad (3.10)
\end{aligned}$$

The first term (3.8) of the Hamiltonian represents the isotropic exchange between the Ni ions. The topology of the Ni_4 core suggests three different exchange paths which are described by the exchange parameters $J_{1,2,3}$ and shown in the coupling scheme in Fig. 3.21. Here, $J_i > 0$ denotes an AFM coupling. The effect of the CF on the Ni spins is accounted for by term (3.9) in the spin Hamiltonian. In NiAz each Ni is surrounded by a distorted octahedron comprising three nitrogen, two oxygen, and one sulfur ligand, see Fig. 3.15. Assuming that the ligand CF is dominated by its axial component the interaction with the CF can be described by a single parameter D, yielding term (3.9) in the Hamiltonian. The magnitude of D

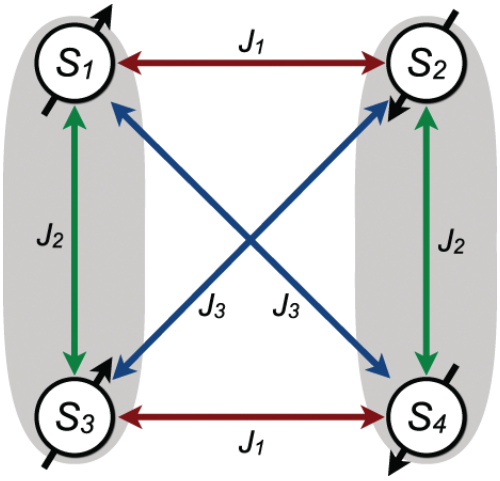

Figure 3.21: *Proposed exchange paths between Ni spin centers in NiAz. The resulting spin singlet can be understood by consideration of a hierarchy of coupling parameters. Due to the predominant coupling J_2 two FM dimers (S_1,S_3) and (S_2,S_4) are formed which are coupled AFM by J_1 and J_3.*

is determined by the average energy splitting between the 3d-orbital sets of the t_{2g} and e_g symmetry, respectively, $\Delta \sim 1$–$2\,\mathrm{eV}$, the splitting within the t_{2g} set, $\delta \ll \Delta$, and the spin-orbit coupling $\lambda \approx -40\,\mathrm{meV}$, $D \approx 4\lambda^2(\delta/\Delta^2)$ [12]. According to section 1.9 the energy of a particular spin state depends on its magnetic quantum number S_z even in zero magnetic field in the case of $D \neq 0$. This yields a ZFS gap with a magnitude proportional to D. The third contribution to the Hamiltonian (3.10) describes the Zeeman interaction of the spins with the external magnetic field H. In the case of uniaxial anisotropy, the g-factor reads $g_\parallel = 2 - 8\lambda/\Delta$ and $g_\perp = 2 - 8\lambda/(\Delta + \delta)$ for H parallel and perpendicular to the uniaxial z-axis, respectively (ref. [12] and (1.52) in section 1.9). In particular, the spin-orbit coupling results in deviations of the g-factor from the spin-only value $g_e \sim 2$ and in a small anisotropy of g.

Numerically solving the Hamiltonian (3.8)–(3.10) provides the relative energies of the spin states of the Ni_4 cluster as a function of the external magnetic field. Using the experimentally determined values for the g-factor (2.11) and the ZFC gap $\Delta_1 = 6.7\,\mathrm{K}$ a reanalysis of the magnetic susceptibility data $\chi(T)$ has been performed using the spin Hamiltonian described above. This is in particular necessary since the D value reported in Ref. [94] for this compound was unrealistically large ($D = -50.4\,\mathrm{K}$). As shown in Fig. 3.22, the fit of the susceptibility according to Hamiltonian (3.8)–(3.10) under consideration of an additional impurity term is in excellent agreement with the measured data. The present combined analysis of $\chi(T)$ and the ESR data results in magnetic exchange constants $J_1 = 37.3\,\mathrm{K}$ (AFM coupling), $J_2 = -57.8\,\mathrm{K}$ (FM), a diagonal exchange of $J_3 = 37.1\,\mathrm{K}$ (AFM), and yields a realistic value of the single-ion anisotropy parameter $D = -4.8\,\mathrm{K}$.

The coupling of four spins $S_{Ni} = 1$ in the cluster yields an extensive spectrum of $(2S_{Ni} + 1)^4 = 81$ individual spin state energies. For simplicity only the states of lowest energy are shown in Fig. 3.23. The ground state of the quadrumer is rendered a spin singlet $S = 0$ which is well separated from the $S = 1$ triplet and the $S = 2$ quintuplet. The separation energy $E_{0,i}$ amounts to $E_{0,1} \simeq 37\,\mathrm{K}$ in the case of the singlet-triplet gap, and $E_{0,2} \simeq 3E_{0,1}$ for the singlet-quintuplet gap,

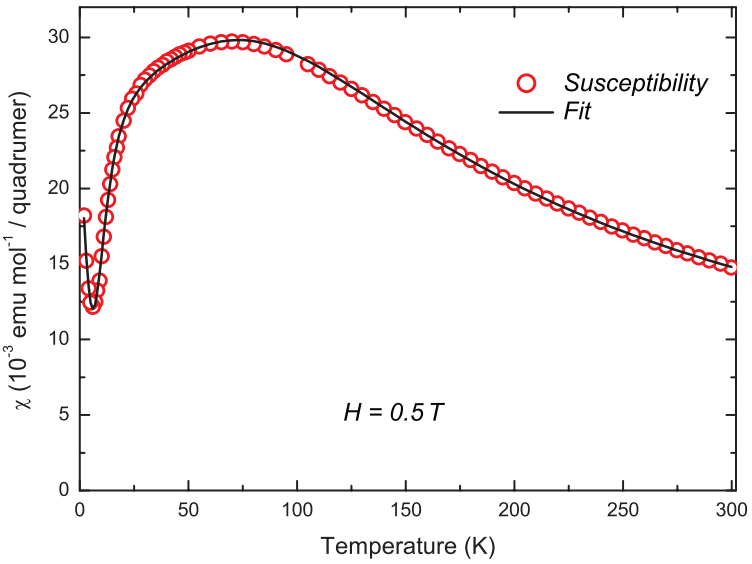

Figure 3.22: *Magnetic susceptibility χ of NiAz [94] measured in an external field of 0.5 T (open circles). The solid line represents a numerical fit using the Hamiltonian (3.8)–(3.10). This fit includes a temperature independent contribution $\chi_0 = 8.08 \times 10^{-4}$ emu mol^{-1} as well as a Curie-like impurity contribution corresponding to $\sim 2\%$ of "defect" Ni^{II} paramagnetic sites which is responsible for a Curie tail below 20 K.*

respectively. Remarkably, the ground state is a spin singlet state although the net exchange is negative, $J = 2\sum i = 1, 2, 3 J_i = 33.2\,\mathrm{K}$, i.e., ferromagnetic. In the framework of our minimal model this can be understood by considering the hierarchy of the coupling parameters, i.e., by assuming two FM dimers, formed due to J_2, for instance, pairs of ions (1,3) and (2,4) in Fig. 3.21 which are coupled AFM through J_1 and J_3.

Assignment of ESR Modes

It is straightforward to assign the observed resonance modes in the ESR spectrum to the spin-flip transitions between different energy states of the Ni_4 complex introduced in the previous section. While comparing the experimental results (Fig. 3.18) with the numerical results in Fig. 3.23 powder averaging effects should be taken into account. In particular, most spectral weight is caused by the particles with the uniaxial CF axis close to the perpendicular direction to the external magnetic field due to the averaging of the different orientations of micro-crystallites in a powder spectrum. This yields the field dependence of the spin state energies shown in Fig. 3.23. The absence of the ESR signals associated with bulk Ni spins at low temperatures for excitation frequencies $\nu \leq 739\,\mathrm{GHz}$ and the occurrence of four modes in the spectrum at elevated temperatures suggests all resonances in this frequency domain are due to the transitions within thermally populated spin multiplets. The comparison with the numerical results

suggests the resonance branches 1, 2, and 4 depicted in Fig. 3.18 are due to excitations within the $S = 1$ multiplet shown in Fig. 3.23, whereas peak 3 is due to spin resonance in the $S = 2$ quintuplet, lying higher in energy than the triplet. Resonance 1 is a so-called forbidden transition between levels labeled as $|-\rangle$ and $|+\rangle$ in Fig. 3.23 which in small magnetic fields are the mixture of $|-1\rangle$ and $|+1\rangle$ spin states due to the CF effect and the spin-orbit coupling [12]. Therefore, the resonance transition between these levels may have an appreciable intensity. Since both $|-\rangle$ and $|+\rangle$ states change their energy approximately as $-g\mu_B H$ and $+g\mu_B H$, respectively, branch 1 in the ν/H^{res} diagram in Fig. 3.18 has a much stronger slope as compared to other branches.

There is a finite energy gap Δ_1 in zero magnetic field between the doublet $|+\rangle$, $|0\rangle$ and the singlet $|-\rangle$ states of the triplet (see Fig. 3.23) which is caused by the uniaxial CF anisotropy and the spin-orbit coupling. It can be directly derived from the intercept of the $\nu(H_1^{res})$ dependence with the frequency axis. From the numerical solution of the Hamiltonian (3.8)–(3.10) the single-ion anisotropy parameter $D \simeq -0.72\Delta_1 = -4.8\,\mathrm{K}$ is obtained. Branch 2 having the same frequency offset by the extrapolation to zero magnetic field has an appreciably weaker field dependence which allows to identify it as a transition between the $|0\rangle$ and $|-\rangle$ states within the $S = 1$ multiplet (also Fig. 3.23). From the slope of the $\nu(H_2^{res})$ dependence the g-factor $g = 2.11 \pm 0.01$ is obtained which is within the typical range of Ni g-factors [12]. In contrast to branches 1 and 2, no frequency

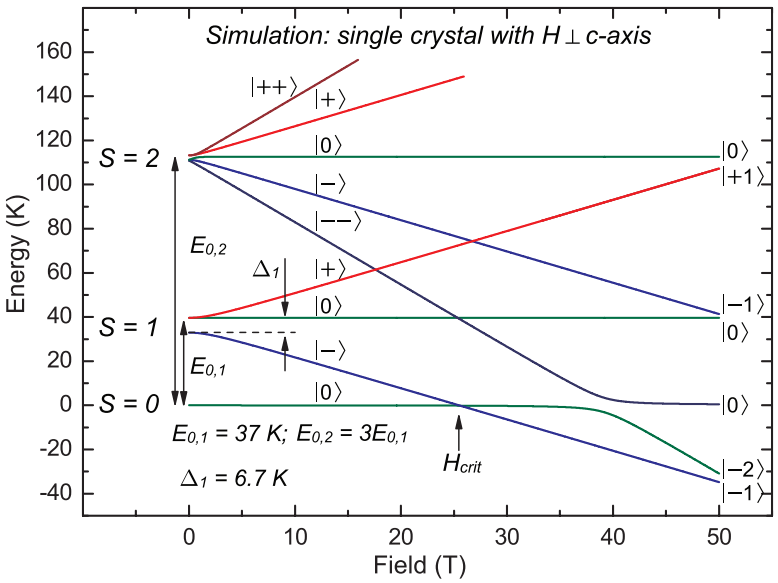

Figure 3.23: *Low lying energy levels calculated for a single crystal with the magnetic field perpendicular to the z-axis: the triplet $S = 1$ and the quintuplet $S = 2$ are well separated from the $S = 0$ ground state by an activation energy of $E_{0,1} = 37\,K$ and $E_{0,2} \simeq 3E_{0,1}$, respectively. Both multiplets exhibit a zero field splitting due to the anisotropic CF. Note the level-crossing at zero energy at 25 T which yields the change of the ground state.*

offset can be found within experimental error for branch 4 which allows to assign it to a transition between $|0\rangle$ and $|+\rangle$ states. The slope of the $\nu(H_4^{\mathrm{res}})$ dependence yields $g = 2.08 \pm 0.01$, similar to the results for branch 2.
In contrast to peaks 1, 2, and 4, which follow a common activation behavior with maxima at about 30 K, resonance peak 3 shows a broad maximum at roughly 150 K, see Fig. 3.16b. This observation implies peak 3 to be due to spin resonance at higher energies, i.e., in the $S = 2$ multiplet. Remarkably, no frequency offset can be revealed in the dependence $\nu(H_3^{\mathrm{res}})$ in agreement with the solution of Hamiltonian (3.8)–(3.10) which yields a much smaller zero field splitting of the spin states within the $S = 2$ multiplet as compared with the $S = 1$ multiplet, compare Fig. 3.18. [27] In the $S = 2$ case the strongest resonance transitions $|{-}{-}\rangle \leftrightarrow |{-}\rangle$, $|{-}\rangle \leftrightarrow |0\rangle$, $|0\rangle \leftrightarrow |+\rangle$, and $|+\rangle \leftrightarrow |{+}{+}\rangle$ occur at a fixed excitation frequency at almost the same value of the resonance field for all transitions. Surprisingly a somewhat larger g-factor amounting to $g = 2.18 \pm 0.01$ has been estimated from the $\nu(H_3^{\mathrm{res}})$ slope which is not expected in the framework of Hamiltonian (3.8)–(3.10). A possible reason for the discrepancy could be a small experimentally unresolvable zero field splitting of the spin states which, however, might affect the lineshape of the total signal from the $S = 2$ multiplet and cause an error in the determination of the resonance field.

Ground State in Strong Magnetic Fields

The calculation of the H dependence of the spin state energies from Hamiltonian (3.8)–(3.10) with the experimentally determined set of parameters suggests the energy of the mixed $|-\rangle$ state of the $S = 1$ multiplet dropping below the ground state singlet $S = 0$ at a field of ~ 25 T, as can be seen from Fig. 3.23. In fact, in such strong fields the quantization axis is defined not by the crystal field anymore, but is given by the direction of the magnetic field [12]. Therefore, the mixed $|-\rangle$ state transforms into the $|{-}1\rangle$ state characterized by a single spin quantum number $S_z = -1$. Such a level-crossing should turn the Ni_4 complex to a new magnetic ground state. Compelling evidence for this peculiar phenomenon comes from the observation of a strong signal within branch 2 at low temperatures in a pulsed field ESR experiment with the highest excitation frequency of 1017 GHz, see Figs. 3.19b and 3.18. As it follows from the $\nu(H_3^{\mathrm{res}})$ dependence, for $\nu = 1017$ GHz the resonance field H_2^{res} exceeds the level-crossing point. Therefore, the resonance excitation occurs from the new magnetic ground state which explains its observation at a low temperature of 4.2 K and the decrease of its intensity with increasing T. Still, a thermally activated resonance within the $S = 2$ multiplet can be observed (branch 3) at elevated temperatures, whereas resonances 1 and 2 are not visible anymore. The former is completely forbidden in strong magnetic fields which turn the mixed $|-\rangle$ and $|+\rangle$ states into the pure spin states $|{-}1\rangle$ and $|{+}1\rangle$, respectively. The latter having a much smaller intensity as compared to resonance 3 cannot be resolved probably due to a limited sensitivity of the equipment at such high frequencies.

The observation of the strong change of the static magnetization about $H_{\rm crit} \sim 25\,\mathrm{T}$ vigorously supports the level-crossing scenario suggested by the ESR data. The $M(H)$ data give evidence for a strongly magnetic state above 25 T which is characterized by a large value of the magnetic susceptibility of the order of $10^{-2}\,\mathrm{emu\,mol^{-1}/Ni}$. Surprisingly, an appreciable linear increase of M not only above $H_{\rm crit}$, but also in the low field regime has been found, see Fig. 3.20. Such a linear contribution to M visible in a field range up to 20 T cannot be explained by paramagnetic impurities. Furthermore, magnetic coupling between the NiAz molecules in the solid phase is obviously much smaller than the intra-molecular exchange. Thus strong long-range AFM correlations between Ni spins in different clusters which could yield the linear increase of $M(H)$ at $H < H_{\rm crit}$ are very improbable. In fact, such a linear behavior of the magnetization is reminiscent of the Van Vleck polarization paramagnetism which is due to the quantum mechanical mixing of different spin states by the magnetic field. However, the experimentally found values of the linear contribution to $M(H)$ are appreciably larger as compared with the typical Van Vleck susceptibilities which are of the order of $10^{-4}\,\mathrm{emu\,mol^{-1}}$. [99] Therefore, one has to think of a different mechanism which can provide a significant admixture of the high energy magnetic multiplets to a ground state singlet in a magnetic field. As a possible candidate one may suggest the anisotropic magnetic exchange between the Ni centers, e.g., the Dzyaloshinsky-Moriya (DM) interaction [29, 100] which is, in principle, allowed by symmetry in NiAz. Indeed, recent theoretical calculations reveal an important role of the DM term for the microscopic description of the magnetization of paramagnetic molecular clusters. [101] To examine the relevance of the DM interaction to the case of NiAz theoretical modeling beyond the framework of Hamiltonian (3.8)–(3.10) is highly desirable. In particular, in the presence of an anisotropic interaction one may expect the occurrence of an anti-crossing energy gap between the $S = 0$ singlet state and the $|-1\rangle$ state of the $S = 1$ triplet near the level-crossing point at $H_{\rm crit}$. [101] Experimentally such a gap yields a hysteresis behavior of the static magnetization owing to non-equilibrium processes in the spin system which depends on the sweep rate of the magnetic field $\partial H/\partial t$ (see, e.g., Refs. [102] and [103]). In our pulsed field magnetization experiment the rates $\partial H/\partial t$ are very high and different for the ascending and descending fields, of the order of 5000 and 500 T/min, respectively. In this regime we find no hysteresis between the up and down sweeps, the observation which calls for a theoretical modeling of the spin-relaxation processes in NiAz near the critical level-crossing points. The opening of an anti-crossing gap at about $H_{\rm crit}$, e.g., owing to the DM interaction, should broaden the spin state transition.[101] This may explain a large width of 10 T of the magnetization step of NiAz at $H_{\rm crit} \sim 25\,\mathrm{T}$, compare Fig. 3.20. The energy diagram in Fig. 3.23 predicts the second level-crossing at a field of about 53 T. Though the increase of the derivative magnetization above $H \sim 40\,\mathrm{T}$ which gets even stronger at $H > 50\,\mathrm{T}$ (inset of Fig. 3.20) can be considered as a signature of the second crossing, no well defined step can be observed in the $M(H)$ curve. Possibly, as suggested by theoretical calculations in Ref. [101],

for particular orientations of the DM vector the width of the magnetization step may increase appreciably with increasing H_{crit}. Thus the experimentally available field range limited to 55 T might not be sufficient for the observation of the second strongly smeared out magnetization step.

Conclusion

The structurally zero-dimensional cluster denoted by NiAz includes four Ni centers which are mainly bridged by three nitrogen ions—the central so-called azide bridge in the μ_4−1,1,3,3 binding mode. The dominant AFM exchange in this molecule gives rise to a non-magnetic ground state. However, in this case three distinct intra-quadrumer exchange couplings between the Ni centers are involved. The analysis of the temperature dependence of the static magnetic susceptibility revealed a hierarchy of these coupling parameters: The dominant FM exchange ($\sim -60\,\mathrm{K}$) yields two $S = 2$ dimers which are coupled AFM via the remaining two coupling paths (each $\sim 40\,\mathrm{K}$). Four resonance modes have been detected by ESR measurements. They were studied as a function of temperature and the excitation frequency. Based on the temperature dependence, the observed resonances were assigned to dedicated spin transitions in the first and the second excited multiplet. A considerable zero-field gap Δ was directly deduced from the frequency dependence. Numerical analysis of the spin Hamiltonian and consideration of the susceptibility data yielded that the zero-field splitting is due to a negative uniaxial single ion anisotropy, $D = -4.8\,\mathrm{K}$. Remarkably, the calculated dependence of the energy spectrum on the magnetic field suggests a change of the ground state in strong magnetic fields: At the critical field of $\sim 25\,\mathrm{T}$ the non-magnetic ground state changes to a magnetic one due to a spin-level crossing. Indeed, such tuning of the ground state by application of strong magnetic fields was confirmed by additional tHF ESR and magnetization experiments: In the ESR experiment the lowest excited multiplet may give rise to a ground state excitation at low temperature. As expected, this was the case for excitation frequencies which were high enough to exhibit the dedicated resonance signal at magnetic fields beyond the critical one. A broad jump of the pulse field magnetization was recognized at the critical field, too.

3.4 Ni_4-Clusters with 3 Azide Bridging Ligands

Introduction

This section is about a series of Ni_4 complexes which is closely related to the NiAz compound (refer to section 3.3). Similar to NiAz, the polytypes of this species include the azide ligand for binding the Ni ions. However, each of the derivates, abbreviated with NiTriAz(a,b,c) in the following, incorporates *three* azide ions—instead of a single one. Two of them adopt the unusual genuine $\mu_3-1,1,3$ binding mode and the third is an $\mu-1,3$ end-to-end transmitter (refer to items E and D, respectively, in Fig. 3.14).
Information on synthesis and structure as well as susceptibility data are given in Refs. [93, 95]. For all complexes NiTriAz(a-c), $\chi(T)$ decreases rapidly when the temperature is lowered, as shown in Fig. 3.24. This is indicative of a non-magnetic ground state which is due to significant AFM exchange within the Ni_4 core. The following investigation comprises high-field studies of the magnetization and the ESR spectrum in order to characterize the ground state more precisely. Further object of the analysis is the determination of the single ion anisotropy.

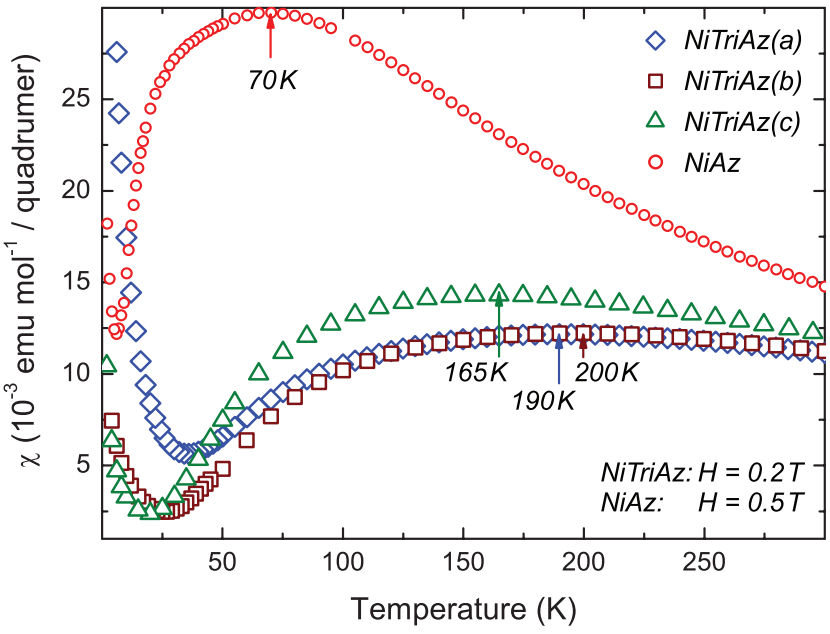

Figure 3.24: *Susceptibility data of NiTriAz [95] and NiAz [94]. The local maxima of NiTriAz are located at considerably higher temperatures (165–200 K) than for NiAz (70 K). For all complexes, the decrease of the susceptibility for lowering the temperature is indicative of a non-magnetic ground state. The upturn at even lower T is owing to Ni defects.*

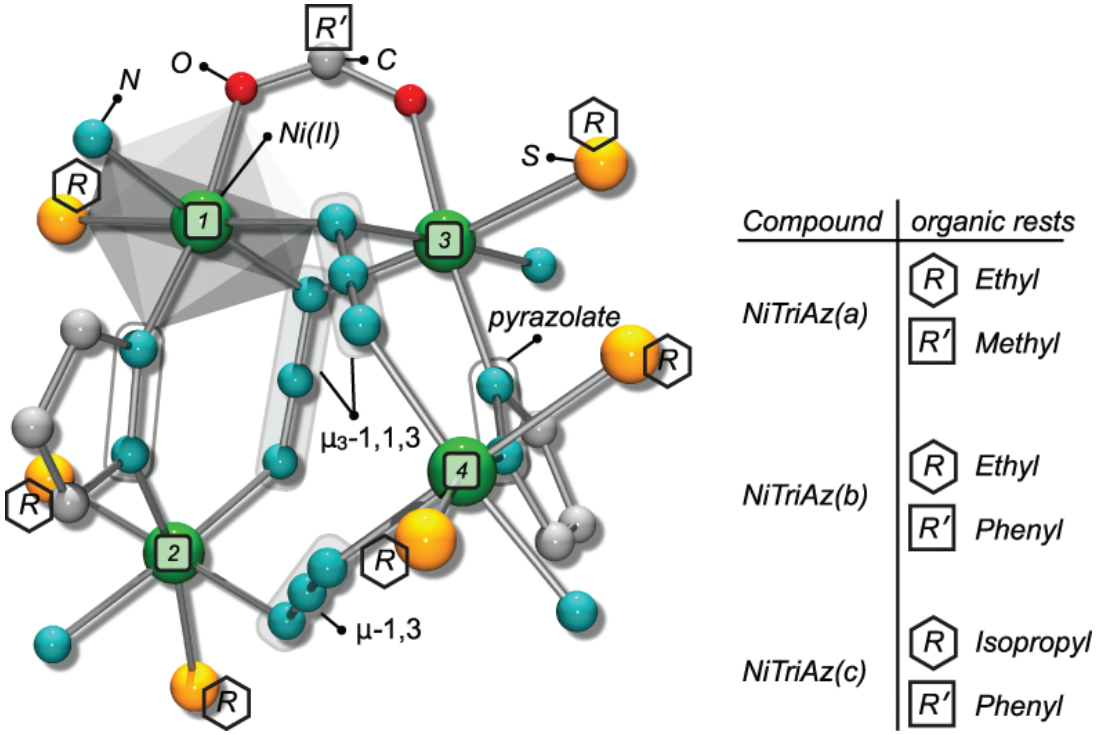

Figure 3.25: *Magnetic core of NiTriAz. Linking positions of different thioether substituents (R) and carboxylates (R′) are indicated. For details see text.*

Structure

The family of NiTriAz compounds, $[L_2Ni_4(N_3)_3(O_2CR')](ClO_4)_2$, is synthesized from pyrazolate-based ligands L with different thioether substituents[5] (L=L[1]: R=Et, L=L[2]: R=*i*Pr) where different carboxylates (R′=Me, R′=Ph) have been used in order to evaluate the scope of these systems. [95]

Fig. 3.25 shows the magnetically active core and the composition of the three studied polytypes, NiTriAz(a-c). Rather, the figure shows the core of NiTriAz(c) which is representative also for the derivatives (a) and (b), since the metric parameters for the three complexes differ only slightly. However, regarding the intra-molecular couplings, subtle differences of the organic rests have some effect on the magnetic properties of the Ni_4 core. The Ni ions are numbered from 1 to 4. The Ni triples (1,2,3) and (1,3,4) are both bridged by genuine $\mu_3 - 1, 1, 3$ azide ions, whereas an additional pyrazole ring bridges the pairs (1,2) and (3,4). The Ni pair (1,3) is bridged twice by the azide ions and by an additional methyl (a) or phenyl group, R′ (b,c). A third azide bridge in *end-to-end* binding mode connects the Ni pair (2,4) in the lower part of the figure (compare also Fig. 3.14 for explanation of the binding modes). Finally, the compounds (b) and (c) utilize the carboxylate phenyl instead of methyl (a).
The closest inter-molecular Ni-Ni distances range between 7.03 Å for polytype

[5]Refer to the appendix for commonly used abbreviations.

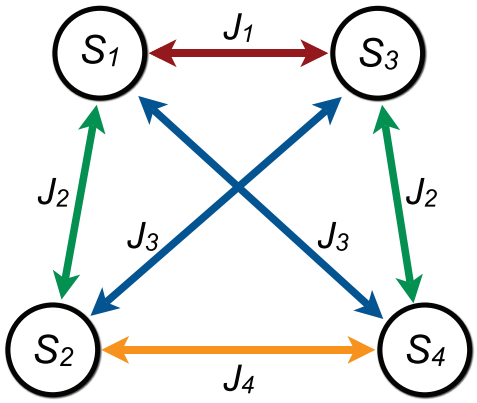

Figure 3.26: *The topology of the molecule suggests four distinct coupling parameters J_1,...,J_4.*

(a) and 8.6 Å for (c) as measured by Meyer et al. with XRD. Therefore, intermolecular exchange should be mainly suppressed. For details of the synthesis refer to [95].
The inspection of the binding situation in NiTriAz yields the intra-molecular exchange coupling scheme, as shown in Fig. 3.26. Due to the topology of the molecule the magnetic exchange between the Ni pairs (1,2) and (3,4) is equal. The same is true for the pairs (1,4), (2,3). Therefore, the number of distinct exchange parameters J is reduced from 6 to 4.

High-Field magnetization

Magnetization measurements $M(H)$ have been performed on compounds (b) and (c) in static (MPMS) and pulsed fields (refer to section 2.6 for further details). The results of these measurements are plotted in Fig. 3.27. For both compounds, the dependence of M on H is almost linear in the entire field range. The averaged slopes $\chi = M/H$ yield values of $\chi_b = 1.78 \cdot 10^{-3}\,\mathrm{emu\,mol^{-1}\,/\,Ni}$ for (b), and $\chi_c = 1.50 \cdot 10^{-3}\,\mathrm{emu\,mol^{-1}\,/\,Ni}$ for compound (c) which is ~ 4 times smaller in comparison to the single bridged Ni_4-complex NiAz for $H < H_{crit}$. This linear contribution to $M(H)$ presumably occurs owing to the admixture of the lowest excited states to the non-magnetic ground state, e.g. by DM interaction.[6] In NiTriAz the admixture is obviously less pronounced than in NiAz, indicated by the smaller susceptibilities $\chi_{b,c}$. Possible explanations include the admixture mechanism itself (weaker anisotropic coupling) as well as the energy separation of the admixed states. The separation depends basically on the isotropic exchange parameters. Susceptibility measurements in [95] indeed reveal dominating AFM couplings of the order of $\sim 100\,\mathrm{K}$ for all three polytypes of NiTriAz which is indeed larger by a factor of ~ 3–4 as compared to NiAz [41, 95]. This is also

[6] For a detailed discussion of DM interaction in NiAz refer to section 3.3.

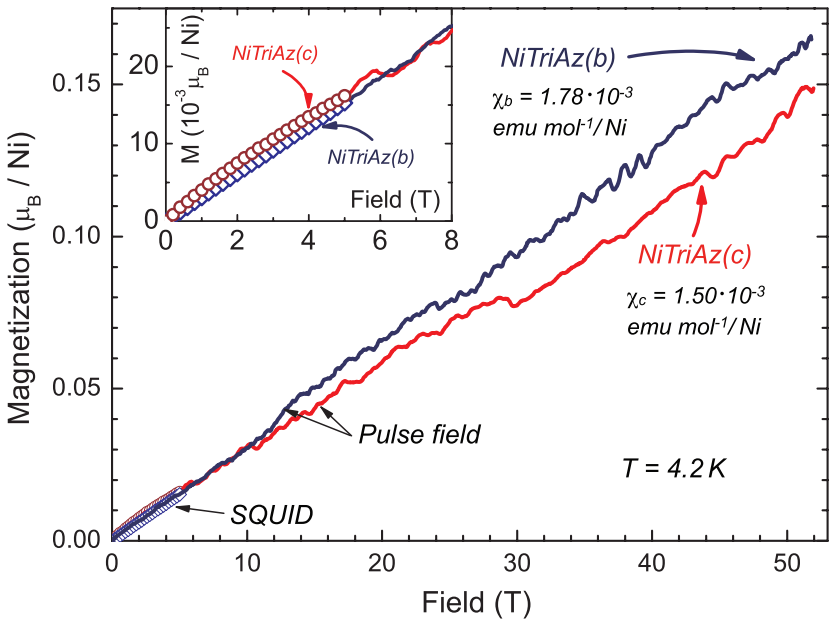

Figure 3.27: *Pulsed field magnetization at 4.2 K with $H < 52$ T on powder samples of NiTriAz(b) (blue line), and NiTriAz(c) (red line). For both samples the increase of the magnetization is almost linear within the probed field range. Inset: Calibration with data of the SQUID measurement (< 5 T).*

in agreement with the relative positions of the susceptibility maxima, shown in Fig. 3.24.
A larger separation energy is also in agreement with the absence of any step-like anomaly in $M(H)$ (in contrast to NiAz, see Fig. 3.20). Increasing the field strength on NiTriAz(b,c) does not reveal any indication of a changing ground state (non-magnetic→magnetic) by means of a spin-level crossing.

High-Field ESR

ESR measurements have been performed with the MVNA in transmission mode (section 2.2) and with pulsed fields (section 2.6) in a wide range of temperatures. In Fig. 3.28 some representative spectra of NiTriAz(a,b) at constant frequencies are shown.
Generally, the ESR signal is weak at low temperatures < 40 K, while for increasing temperature two clearly thermally activated resonance lines evolve.
In the spectra of NiTriAz(a), see Fig. 3.28a, two resonances numbered 1 and 2 are observed, whereas the stronger resonance 2 exhibits an intensity maximum at about 180 K. Both resonances are due to spin transitions in excited multiplets. Obviously, resonance 1 is caused by a "half-field" transition ($\Delta S_z = \pm 2$). The presence of this ESR line gives evidence for a CF induced single-ion anisotropy which is appreciably mixing pure spin states [12].
In contrast, for NiTriAz(b) no half-field transition is observed. Instead, both ESR lines appear in fields associated with ESR transitions of the kind $\Delta S_z = \pm 1$. The

intensities of both signals exhibit an activation behavior, as shown in Fig. 3.28b. The stronger resonance 1, e.g., exhibits its maximum intensity at $\sim 200\,K$.
The observed activation behavior of both compounds (a) and (b) corresponds nicely with the static susceptibility data [95]. As mentioned before, they suggest a non-magnetic ground state due to the dominating AFM coupling of the order of $\sim 100\,K$ for all three polytypes of NiTriAz. In comparison to the single bridged complex NiAz, the AFM couplings for NiTriAz are larger and the energies of the magnetic multiplets are thus increased. Therefore, ESR is observable only at comparatively higher temperatures (see also the ESR temperature dependence of NiAz in Fig. 3.16). Distinctive differences of (a) and (b) are found concerning the presence of magnetic anisotropy. While for compound (a) resonance 1 is clearly due to the presence of magnetic anisotropy, no such peak is found for compound (b).
The excitation frequency was varied at 100 K yielding the ν/H_ν dependence of

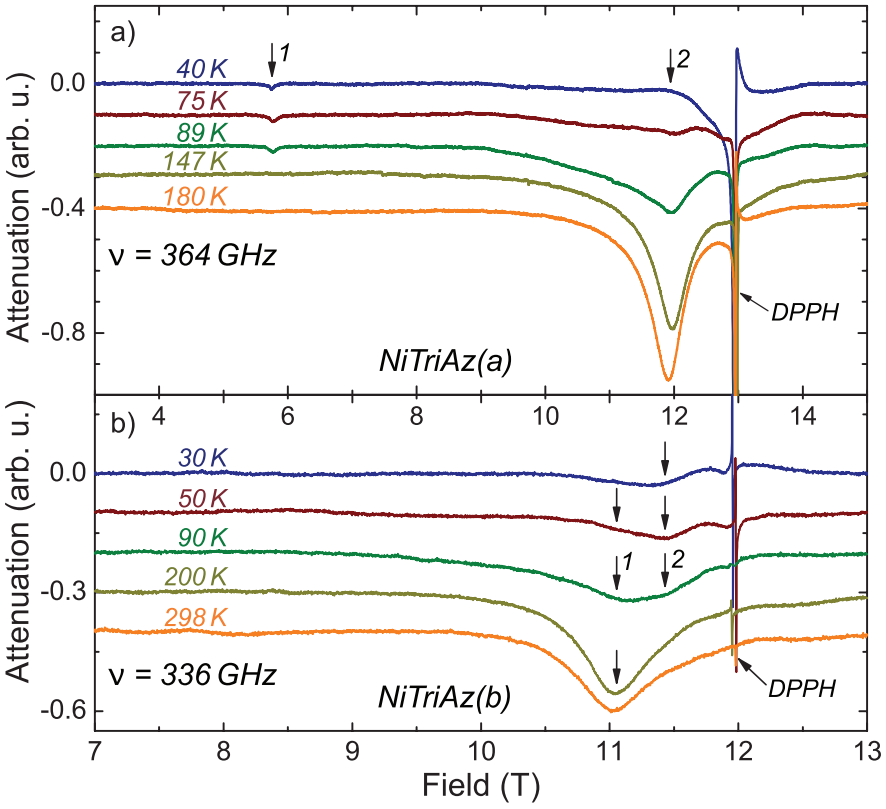

Figure 3.28: *Selected spectra of compounds NiTriAz(a) and (b) at different temperatures. a) The main peak 2 evolves at elevated temperature, while it is suppressed at low. The weak transition (peak 1) is caused by the admixture of pure spin states owing to the presence of single ion anisotropy. b) Peak 1 is thermally activated and exhibits a maximum intensity at $\sim 200\,K$. Resonance 2 shows also an activation behavior. Its temperature dependence differs from peak 1 and is shifted to lower temperature.*

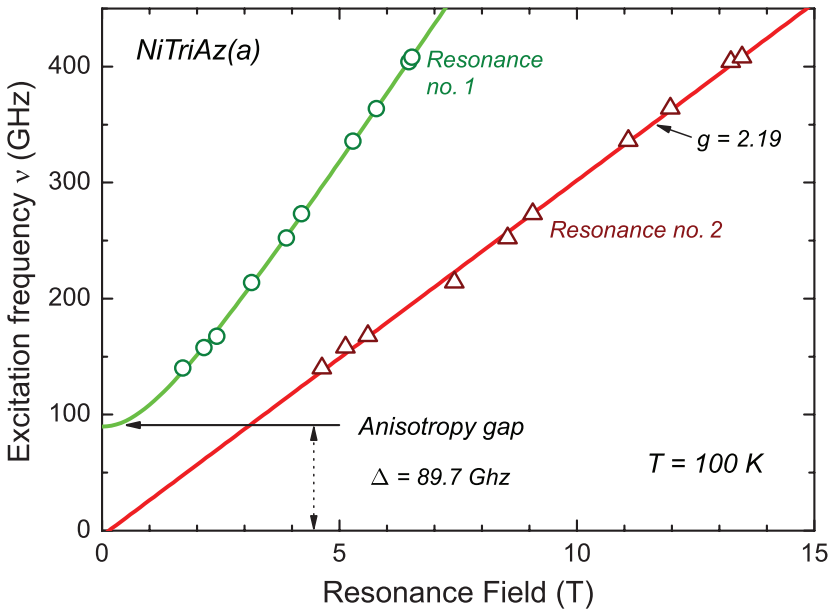

Figure 3.29: *Dependence of the excitation frequency ν on the resonance fields of peak 1 and 2 of NiTriAz(a) at 100 K. The fits suggests $g = 2.19$ and a ZFS of the order of 90 GHz (4.30 K). See text for details.*

the resonances. For compound (a) it is shown in Fig. 3.29. The g-factor have been determined from these branches for both of the studied compounds, (a) and (b). They amount to 2.19 for (a) and 2.16 for (b) and thus fall into the range of g-values which is usually found in the ESR literature [12] for Ni^{II}.
Additionally, for resonance 1 of compound (a) the dependence of the excitation frequency ν on the resonance field has been extrapolated to low fields after $h\nu = \sqrt{\Delta^2 + (g\mu_B H)^2}$ (green fitted line). The relation yields an estimation for the scale of the ZFS which amounts $\Delta_{ZFS} = 89.7\,\text{GHz}$ (4.30 K).
Furthermore, consistent with the information from the magnetization, the ESR results give no indication for a change of the ground state in the investigated field range from a non-magnetic to a magnetic one as has been found in the previous study of NiAz.

Conclusion

The polytypes of NiTriAz(a-c) are qualitatively comparable to NiAz. From susceptibility measurements as well as the temperature dependence of the ESR signal, the ground state is clearly a spin-singlet in either of the three NiTriAz compounds. Nevertheless, there are significant differences which are mainly induced by the size of the coupling parameters and the single ion anisotropy. Clear evidence is given for a stabilization of the ground state as compared to NiAz. Indicative for this fact are shifts of the maxima in $\chi_{a,b,c}(T)$ to higher temperatures, the absence of steps in $M(H)$, and the significantly smaller susceptibilities $\chi_{a,b}$

derived from the pulse field magnetization. Also the high temperature of the ESR intensity maxima support this conclusion. The energy of the excited multiplets is high enough to avoid ground state changes due to spin-level crossings for fields $< 52\,\mathrm{T}$ (in contrast to NiAz). Nevertheless, at least the first excited multiplet can be thermally occupied. This enables to determine the g-factor for (a) and (b) and the scale of the ZFS using ESR measurements. The ZFS for (a) amounts 4.3 K and is therefore smaller than for NiAz (6.7 K). For (b) no indication for a zero-field gap is given. This leads to the assumption that the influence of the ligand field in terms of the uniaxial anisotropy is smaller in the triply bridged compounds.

3.5 Ni_4-Cluster with High-Spin Ground State

Introduction

The foregoing sections 3.2, 3.3 and 3.4 demonstrate that nickel might exhibit an appreciable single ion anisotropy. The effect is due to a strong uniaxial anisotropy of the CF in conjunction with the high degree of orbital quenching for the $3d^8$ configuration of Ni^{II}. On the other hand it is obviously a challenge to get an FM coupled cluster of spins, since unpaired electrons of non-orthogonal orbitals tend to form spin-singlets rather than triplets: in NiAz a rather large AFM coupling has been observed which can be attributed to the azide bridging ligand in the $\mu_4 - 1,1,3,3$ binding mode. The AFM coupling strength grows even more by increasing the number of azide ligands, as seen in the family of NiTriAz(a-c).
In this section another tetranuclear Ni^{II} complex is presented. Actually, it utilizes two azide bridging ligands (both in the binding mode $\mu_2 - 1,3$) *and* exhibits a predominant FM intra-molecular exchange coupling.
The Ni_4 complex presented in this section realizes a system with a spin multiplicity of the ground state which could not be determined by simple measurement of the magnetization. Indeed, the measurement below 5 T proved the magnetic ground state, but the applied magnetic field was insufficient to fully polarize the spins. Therefore, a pulse field measurement has been performed to get the saturation value of the magnetization. However, the resulting number of Bohr magnetons $\mu/\mu_B \sim 3\, g_{Ni}$ for fields exceeding ~ 10 T still leaves questions about the lowest lying multiplet ($S = 3$ or $S = 4$). Additionally, tHF ESR measurements have been carried out to clarify this ambiguity. In the latter experiment it was possible to nicely resolve spin-flip transitions between different states of the low energy multiplet. The transitions manifest as a set of resonance lines in the ESR spectrum. The assignment of these peaks in the framework of the relevant spin Hamiltonian eventually yields a fully polarized magnetic state of the complex at low temperatures with a total spin of $S_{tot} = 4$. Moreover, the analysis of the frequency dependence of the resonance peaks reveals an appreciable magnetic anisotropy of the molecule, $S_z^2\,|D| \sim 5$ K. With decreasing temperature, a significant transfer of the spectral weight to the low-field part of the spectrum evidences a negative sign of the anisotropy parameter D, i.e., a magnetically bistable ground state $|S_z = \pm 4\rangle$ is realized.
Preliminary measurements of the dynamic susceptibility χ_{AC} at low temperature reveal an anomaly which clearly indicates the slowing down of the relaxation rate of the magnetization. A lower limit for the blocking temperature is estimated. Thus, the studied Ni_4-molecular complex appears to be on a promising route towards realization of bistable and highly magnetic single-molecule magnets.

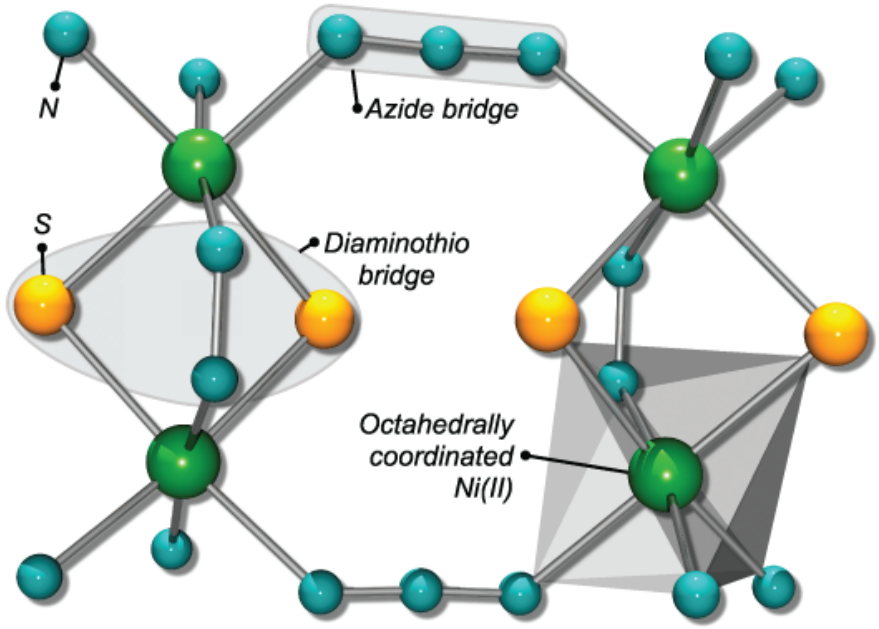

Figure 3.30: *Structure of* $[\{(L^2)Ni_2(\mu - pydz)(N_3)\}_2](BPh_4)_2$, *(NiBiAz). The vertical diaminothio-bridged binuclear building blocks are horizontally linked by* μ_2 *azide ions. Each* Ni^{II} *is sitting in the center of a pseudo octahedron of ligands. For clarity only the magnetic core is shown.*

Structure

The starting point in the synthesis of the complex is basically given by the preparation of a Ni^{II} dimer. It acts as the building block for the preparation of the polynuclear complex. Thereby, two Ni^{II} ions each with spin $S = 1$ are linked via two thiophenolate sulfur atoms and a μ-pydz ligand. This gives an $(SCN)N_2Ni(\mu\text{-}S)_2(\mu\text{-pydz})NiN_2(NCS)$ core structure with a pseudoconfacial bioctahedral geometry. [104] The final complex $[\{(L^2)Ni_2(\mu - pydz)(N_3)\}_2](BPh_4)_2$, here denoted as NiBiAz, is then composed of two of these binuclear subunits. These dimers are linked by two $\mu_2 - 1,3$ azide ions and give a rectangular array of four six-coordinate Ni^{II} ions. Fig. 3.30 shows a top-view representation of the molecular structure of NiBiAz. It is reduced for clarity, but comprises both distinct interaction pathways: the azide- and the diaminothio-bridges.

The crystals were grown by slow evaporation of the complex solved in acetonitrile. The molecule crystallizes in the monoclinic space group $P2_1/n$ (no.14) with $a = 17.695(4)$, $b = 17.647(4)$, $c = 18.081(4)$ Å, and $\beta = 101.03(3)°$ as determined by XRD (the asymmetric unit of NiBiAz·2MeCN·MeOH consists of one half of the formula unit). The molar mass is $2205.18\,g\,mol^{-1}$. This information and further details of the synthesis are given in Ref. [104].

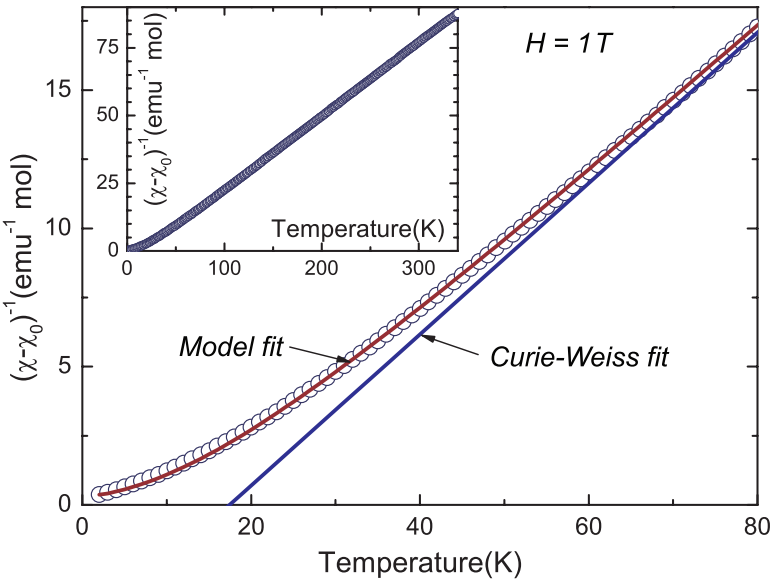

Figure 3.31: *Inverse static susceptibility, $(\chi(T)-\chi_0)^{-1}$, of NiBiAz. The inset shows the linear behavior of the data in a wide range of the measurement which adapts perfectly to a Curie-Weiss law in the high T range > 80 K. Main: Inverse susceptibility (circles), Curie law (blue line), and the fit of a 2-J model (red line) are shown. The Curie-Weiss constant of $C = 3.66\,emu\,mol^{-1}\,K$ corresponds to an effective magnetic moment of $5.4\,\mu_B$ ($S_{eff} \approx 2$). The deviation of the data from the Curie law corresponds to an increasing magnetic moment for lower temperature. The model fit gives two FM coupling parameters $J_1 = -16\,K$ and $J_2 = -8\,K$. For details see text.*

Magnetization

The static susceptibility $\chi(T)$ of NiBiAz has been measured by application of an external field of 1 T with an MPMS. In Fig. 3.31, the temperature dependent part of the inverse susceptibility $(\chi(T)-\chi_0)^{-1}$ is plotted versus temperature. The inset shows a perfectly linear behavior of the curve between 80 and 340 K. This high temperature domain has been fitted with a Curie-Weiss law. The fit yields a Curie-Weiss constant of $C = 3.66\,\mathrm{emu\,mol^{-1}}$ which gives an effective moment of $5.4\,\mu_\mathrm{B}$. This moment will corresponds to an effective spin of $S_\mathrm{eff} = 2$, if a typical g-factor of 2.2 for nickel is assumed [12]. The positive sign of the Weiss temperature $\theta_\mathrm{Weiss} \sim +17\,\mathrm{K}$ indicates an FM exchange in the cluster.
The main panel of Fig. 3.31 gives a more detailed view of the low temperature domain for $T < 80\,\mathrm{K}$. While the slope of the curve is proportional to the inverse effective magnetic moment μ^{-1} of the cluster, its deviation from the Curie-Weiss fit in this temperature region yields additional information about the low temperature properties. Thereby, with lowering the temperature a decreasing slope is observed which corresponds to an increasing magnetic moment.
The low T magnetization gives a more quantitative conclusion. $M(H)$ was measured in static fields $|H| < 5\,\mathrm{T}$ at 2 and 4.2 K, respectively. Neither of the

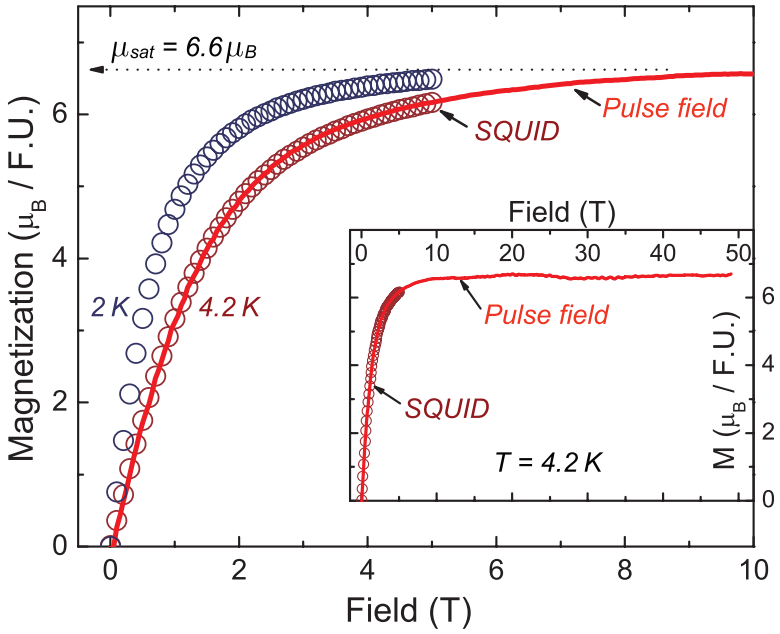

Figure 3.32: *Magnetization measurements at 2 and 4.2 K, respectively, for static fields $|H| < 5$ T (blue and red circles), and in pulsed magnetic fields with $H <$ 49 T (red curve). The magnetic moment saturates at $\mu/\mu_B = 6.6 = 3g_{Ni}$ which is apparently an increase of 50% compared to the high-T Curie-Weiss fit ($2\,g_{Ni}$), but only 75% of the expected $4\,g_{Ni}$ for an $S = 4$ ground state.*

measured curves show a hysteresis loop. In Fig. 3.32, the magnetization at both temperatures is shown for positive field values. The saturation value of $6.6\,\mu_B$ is not reached at 5 T. Therefore, additional pulse field measurements at fields < 49 T have been performed. The corresponding curve taken at 4.2 K is shown in Fig. 3.32 as a red line. For $0 < H < 5$ T the data are in good accordance with the corresponding SQUID results. The inset shows the development of the magnetization for fields > 10 T. It is similar to a Brillouin function (not shown) and flows into the saturation plateau that extends up to 49 T.
Remarkably, the observed number of Bohr magnetons p associated with the saturation moment $p = \mu/\mu_B = 3.0\,g_{Ni}$ is well below the expected value for an $S = 4$ ground state, $4\,g_{Ni}$. From this point of view the magnetization measurements do not give a direct answer on the spin multiplicity of the ground state. Actually, the analysis of the ESR experiment, described in the following paragraph, will give evidence that the lowest multiplet is indeed an $S = 4$.

High-Field ESR

High-field ESR has been performed on a poly-crystalline sample of NiBiAz. The sample has been pressed into a small compact pellet and was measured with the MVNA in transmission mode (refer to sections 2.6 for the details of the particular setup). Fig. 3.33 shows the frequency dependence of the ESR spectrum at 3 K. Between 109 and 400 GHz, as can be seen from Fig. 3.33b, each spectrum reveals a broad and asymmetric ESR signal. The resonance spans a field range of roughly 2.5 T and the spectral weight is located in the high-field part, indicated by a sharp spike.

At frequencies lower than 109 GHz the overall appearance of the spectra is basically unchanged. However, the spike is softened with lowering the frequency and an additional fine-structure appears. Fig. 3.33a shows an example spectrum at $\nu = 76$ GHz. The profiles of these low frequency spectra comprise up to eight pronounced features. They are associated with the branches *a*–*h* in Fig. 3.33a which give linear ν/H_ν dependences. The branch attributed to resonance feature *a* thereby intersects the axis of ordinate at ~ 40 GHz (1.92 K). This intersection is characterized by the highest millimeter-wave energy compared to the crossings of the rest of the branches *b*-*h* and, therefore, gives a first approximation for the ZFS Δ. As will be discussed in detail, the associated resonance *a* belongs to the lowest transition in the $S = 4$ multiplet which can be referred to as $|-4\rangle \leftrightarrow |-3\rangle$. Besides that, the *g*-factor has been determined from the mean value of slopes of the linear fits to each branch (colored lines in Fig. 3.33a) to $g = 2.17$.

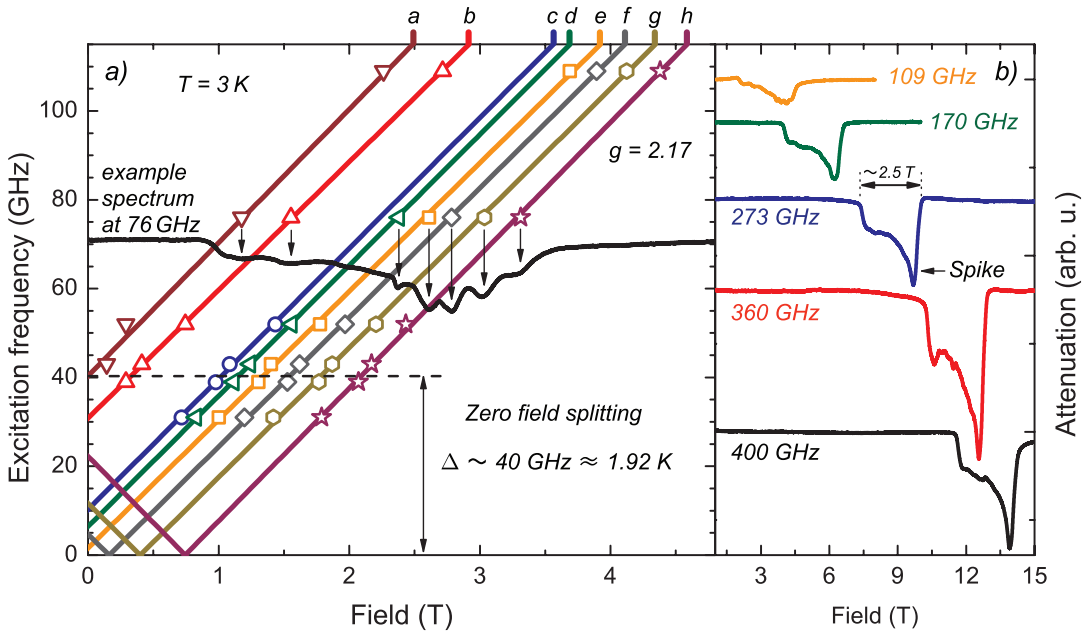

Figure 3.33: *The frequency dependence ν/H_ν of dedicated features a–h from powder spectra at 3 K. An example spectrum at 76 GHz is shown. The g-factor averages to 2.17. The zero field splitting has been determined to 40 GHz (1.92 K).*

It is noteworthy that the branches represent the ν-dependences of *some* spectrum features. Owing to the powder averaging these features a not necessarily originated by dedicated genuine resonance peaks. Therefore, the experimental accuracy of both the ZFS and the g-factor can be improved, since either values base on the fits of these branches. However, the values give a good starting point for the following analysis.

Fig. 3.34a shows the temperature dependence of the ESR spectrum at the fixed frequency of $\nu = 360\,\mathrm{GHz}$. The spectrum at 5 K basically comprises the absorption signal of a powder averaged ground state excitation. The asymmetry observed in this spectrum can be attributed to the presence of CF anisotropy of the Ni in combination with the equal distribution of the crystallite orientations in the powder sample. The resonance field of each crystallite thereby depends on the orientation with respect to the external field. With rising temperature, higher lying spin states are increasingly populated. Spin transitions between them result in the fine-structure which is observed in the spectra for $T \geq 10\,\mathrm{K}$. On further increasing the temperature, the lowest lying spin states get almost equally occupied. Therefore, the associated ESR intensities drop due to the decreasing net absorption, while the excited spin states dominate the spectrum.
Fig. 3.34c shows the same powder spectra in a different field range between 5 and

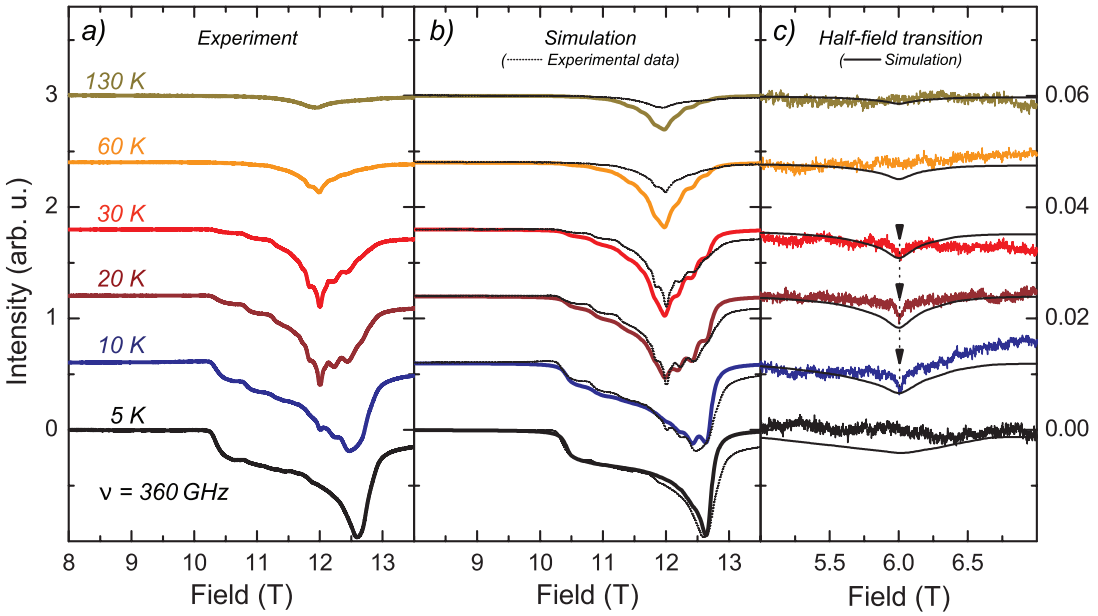

Figure 3.34: *ESR temperature dependence at 360 GHz; Experimental and simulated spectra. a) The asymmetry of the low temperature spectrum is a fingerprint of the magnetic anisotropy. With increasing temperature spin transitions between higher lying spin states contribute to the evolving fine-structure. b) Comparison of the powder simulation (colored lines) and the experimental data (dotted lines). c) Weak ESR transition detected at ∼ 6 T. For details see text.*

7 T plotted to a 50 times larger intensity scale. In the temperature range between 10 and 30 K a weak but distinct peak is observed at ∼6 T. The peak is due to a transition between spin states which are admixed[7], e.g. by influence of the CF $|-\!-\!-\!-\rangle \leftrightarrow |-\!-\rangle$. As well as the powder asymmetry, this so-called *half-field* transition is a fingerprint of the magnetic anisotropy.

Additional ESR measurements at the same frequency have been carried out on an oriented sample. The sample was prepared by putting a loose powder within a brass-ring covered with capton foil in order to preserve the mobility of the individual crystallites. By application of the magnetic field during the experiment the crystallites aligned their easy axis along the external field axis. In contrast to the powder spectra obtained from the pellet (Fig. 3.34a), the spectra of the oriented sample, shown in Fig. 3.35a, reveal up to six well resolved resonance signals. The peaks, numbered 1–6 in the figure, are almost equally spaced by $\Delta H \sim 0.43$ T and can hence be associated with dedicated spin transitions. While resonance

[7]The notation for such states is as follows: pure→admixed: $|\pm 1/2\rangle \rightarrow |\pm\rangle$, $|\pm 1\rangle \rightarrow |\pm\pm\rangle$, etc.

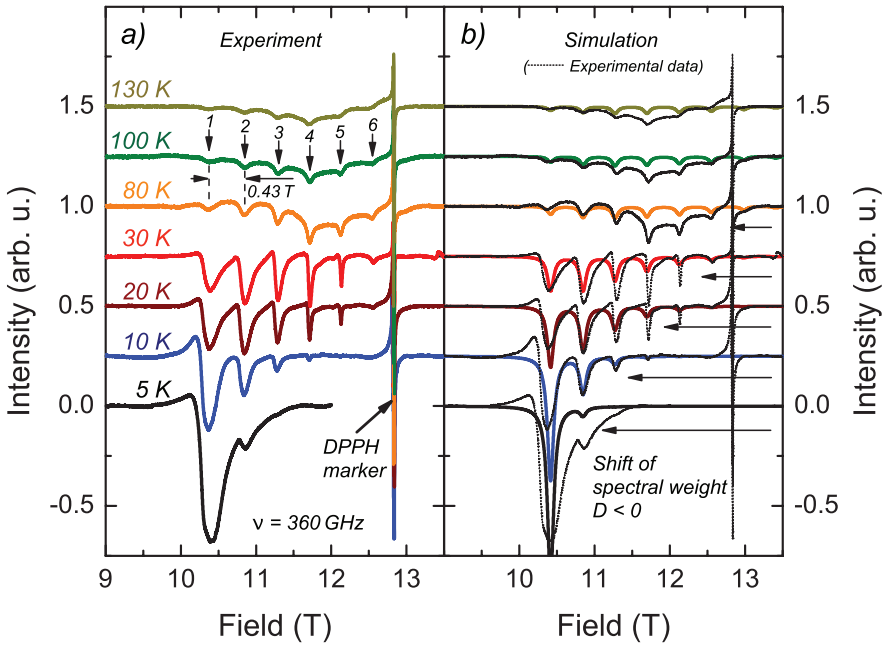

Figure 3.35: *Temperature dependence of experimental and simulated ESR spectra at 360 GHz. a) Experiment: Loosely prepared poly-crystallites of the sample are oriented by application of the external magnetic field due to their magnetic anisotropy. The spectral weight at low temperature gives evidence for a negative single ion anisotropy D. Up to six equally spaced resonances (with spacings of ∼ 0.43 T) are observed. While resonance 1 is due to the ground state excitation, resonances 2–6 are successively activated with increasing temperature. b) Simulated spectra (colored) in comparison with the experimental results (dotted lines).*

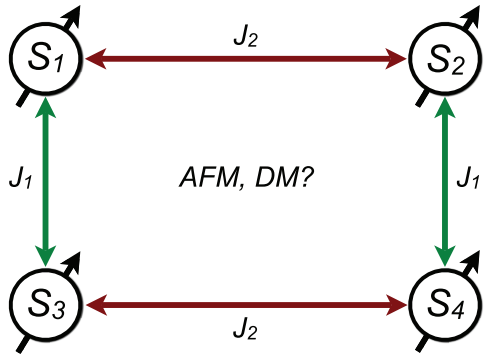

Figure 3.36: *FM coupling scheme of NiBiAz. Reduced moment due to additional interactions?*

1 is observed even at 3 K, the resonances 2–6 are successively activated with increasing temperature. This observation leads to the conclusion that resonance 1 is caused by the ground state excitation $|-4\rangle \leftrightarrow |-3\rangle$, resonance 2 to the first excited transition $|-3\rangle \leftrightarrow |-2\rangle$ etc. in the lowest lying $S = 4$ multiplet.

Modeling

The ESR data can be interpreted and well understood in the framework of the relevant spin Hamiltonian. Considering the topology of the NiBiAz core, shown in Fig. 3.30, the four Ni spins are assumed to be coupled as sketched in Fig. 3.36. The coupling between the Ni centers of the dinuclear building blocks is described by the isotropic coupling parameter J_1 and the coupling mediated by the azide ion is denoted as J_2. In addition to the Heisenberg exchange, the spin Hamiltonian comprises further terms for the energy of the magnetic anisotropy and the effect of external fields. The single ion anisotropy (SIA) is represented by D_{sia} which is usually the dominant lowest order term for tetragonal distortions of the pseudo-octahedral metal center environment due to CF effects. The magnetic energy in external magnetic fields is considered by the spin Zeeman energy. The Hamiltonian then reads

$$\begin{aligned}
\mathcal{H} = \quad & J_1(\mathbf{S}_1 \cdot \mathbf{S}_3 + \mathbf{S}_2 \cdot \mathbf{S}_4) \\
& + J_2(\mathbf{S}_1 \cdot \mathbf{S}_2 + \mathbf{S}_3 \cdot \mathbf{S}_4) && (3.11) \\
& + D_{\mathrm{sia}} \sum_{i=1\cdots4} \left[S_{iz}^2 - \frac{1}{3} S_{\mathrm{Ni}}(S_{\mathrm{Ni}} + 1) \right] && (3.12) \\
& + g\mu_{\mathrm{B}} \mathbf{H}'(\theta) \cdot \sum_{i=1\cdots4} \mathbf{S}_i. && (3.13)
\end{aligned}$$

Additionally, for the simulation of the powder averaging, the applied field in (3.13) can be rotated about the x-axis, $\mathbf{H}' = \mathbf{R}_x(\theta)\, H_z \mathbf{e}_z$. Thereby, $\theta = 0°(90°)$ corresponds to a parallel field alignment to the $z(y)$-axis. Hamiltonian (3.11–3.13) covers the complete spin space of $2(S+1)^4 = 81$ spin states. It has been used to fit the susceptibility

$$\chi = -\frac{\partial^2 \mathcal{H}(H; J_1, J_2, g, D_{\mathrm{sia}})}{\partial H^2} + \frac{C_{\mathrm{imp}}}{T} + \chi_0 \qquad (3.14)$$

for determination of the coupling parameters J_1 and J_2. The parameters $D_{\mathrm{sia}} = \Delta = -1.92\,\mathrm{K}$ and $g = 2.17$ have been used, as obtained by the frequency dependence of the powder ESR spectra, shown in Fig. 3.33. Before fitting, it has been checked that taking $\Delta = D_{\mathrm{sia}}$ indeed reproduces an energy gap of 1.92 K between the lowest lying levels in zero field (i.e. $|\pm 4\rangle$ and $|\pm 3\rangle$). The fitted curve for $J_1 \sim -16\,\mathrm{K}$ and $J_2 \sim -8\,\mathrm{K}$ is plotted in the main panel of Fig. 3.31 (red line). Except for the small deviation at about 10 K, the agreement of the model fit with the experimental data is reasonable. However, the fit requires an additional small negative temperature dependent contribution which is presumable due to an instrumental artefact of the MPMS [105] and renders the size of the determined parameters not perfectly reliable.
After all, the size of the coupling parameters J_1 and J_2 is not precisely known and a simplified model is assumed in the following. It considers only the lowest lying multiplet for the analysis of the ESR data. The following consideration may justify the multiplicity of this multiplet and support the FM nature of the coupling parameters. While two AFM couplings for J_1 and J_2 in Fig. 3.36 and even the combination FM-AFM would cause a non-magnetic ground state, the only possibility in the framework of the introduced coupling scheme is an $S = 4$ ground state. The latter is clearly the result of two FM couplings, i.e., it corresponds to negative parameters J_1 and J_2, as indicated by the fit results of the susceptibility. The Hilbert space can now be effectively truncated by modeling just the lowest lying multiplet. The new model is achieved by neglecting the Heisenberg term (3.11), while instead assuming a single giant spin $\tilde{S} = 4$,

$$\mathcal{H}(\theta) \;=\; D_{\mathrm{mol}}\,\tilde{S}_z^2 \;-\; \frac{1}{3}\,\tilde{S}\,(\tilde{S}+1) \;+\; g\,\mu_{\mathrm{B}}\,\mathbf{H}'(\theta)\;\cdot\;\tilde{\mathbf{S}}. \tag{3.15}$$

Remarkably, such a modification changes the scale of the parameter D, so that $D_{\mathrm{mol}} \neq D_{\mathrm{sia}}$. However, both parameters are related by application of ITOs (ref. section 1.9 and [12, 27]). In fact, by setting $D_{\mathrm{mol}} = D_{\mathrm{sia}}/(4^2 - 3^2)$ the analytical value of $\Delta = 7D_{\mathrm{mol}}$ yields the correct order of the ZFS from the experiment in this case.

Fig. 3.37 shows an example of the resulting spin-levels. Their field dependence is obtained from the diagonalization of Hamiltonian (3.15) for $H \parallel z$, i.e. $\theta = 0$. The anisotropy has been chosen negative. The ZFS complies to the gap Δ between the magnetic states $|\pm 4\rangle$ and $|\pm 3\rangle$. The figure shows also the simulation of an ESR spectrum for $\nu = 50\,\mathrm{GHz}$ (model temperature of 8 K). The spectrum is composed of Lorentzian lineshapes which were scaled by their relevant transition probabilities and the Boltzmann factor (for details of the simulation refer to section 1.11).
In the same way the simulated powder spectra in Fig. 3.34b and the oriented spectra in Fig. 3.35b have been calculated. Both simulations have been accomplished by numerical diagonalization of (3.15) for different field values H in the interval of $[0, 16\,\mathrm{T}]$ with a field increment of $\Delta H = 80\,\mathrm{G}$. The powder simulation is composed of single crystal spectra for different crystallite orientations, $0 < \theta < 90°$

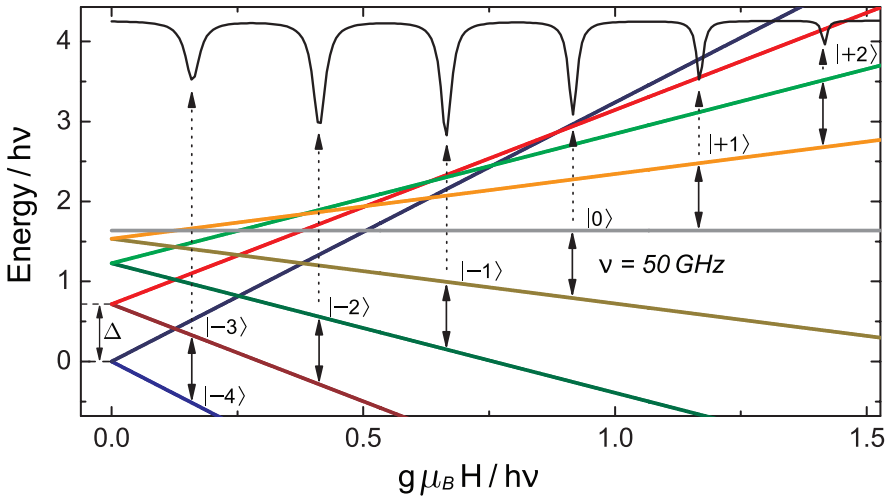

Figure 3.37: *Spin levels for $S = 4$ with a uniaxial anisotropy of $D_{mol} = -0.31\,K$ and $g = 2.16$ in an external field with $H \parallel z$. A simulated ESR spectrum is plotted as an example for the excitation frequency of 50 GHz. The ground state is bistable $|\pm 4\rangle$ in zero field and $|-4\rangle$ otherwise.*

with an increment of $\Delta\theta = 0.5°$. Since powder averaging is equivalent to an integration over the solid angle, each spectrum scales with an additional factor of $\sin\theta$. [106] For the single crystal simulation the linewidth of the Lorentzian lineshape has been set to 2000 G. For a good agreement with the experimental data the powder spectra are modeled with a linewidth of 1500 G. Since the linewidth is not part of the model it was adjusted arbitrarily.

AC Susceptibility

Due to the FM coupling scheme and the negative axial anisotropy the ground state spin levels $|\pm 4\rangle$ are obviously separated by a potential well with the magnitude of $U = |D_{\mathrm{mol}}|\tilde{S}^2 \sim 4.96\,\mathrm{K}$. Consequently, for thermal energies small compared to the barrier, $T \ll 4.96\,\mathrm{K}$, NiBiAz may exhibit a slowing down of the magnetization dynamics by means of the missing thermal activation to overcome the well. Therefore, the AC susceptibility[8] of NiBiAz has been measured at low temperature $> 35\,\mathrm{mK}$. The measurement was carried out in zero DC external field by application of a small AC field oscillating with 16 Hz. [107] Fig. 3.38 shows the response function χ_{AC}. With lowering the temperature the signal shows a pronounced maximum at $\sim 160\,\mathrm{mK}$ which is due to the magnetization oscillations getting out-of-phase compared to the exciter. The maximum is a clear indication of the relaxation of the magnetization becoming slower at this temperature. Therefore, a lower limit for the blocking temperature $T_{\mathrm{B}} > 160\,\mathrm{mK}$ has been found.

[8]For a description of AC susceptometry refer to, e.g., [22].

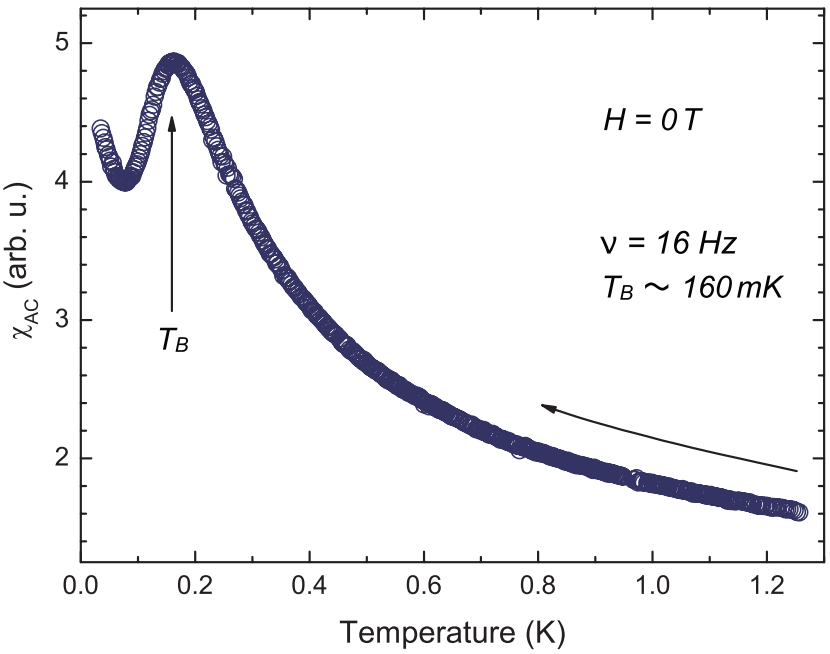

Figure 3.38: *AC susceptibility of NiBiAz in zero field. Clear resonance is seen at ∼ 160 mK despite the rather low frequency of 16 Hz.*

Results and Discussion

The experimental data and the results of the modeling of the Ni_4 cluster NiBiAz suggest that its ground state is bistable and hence magnetic. In the framework of the simplified spin Hamiltonian approach (3.15) simulations with the parameters $D_{\mathrm{mol}} = -0.31\,\mathrm{K}$ and $g = 2.16$ yield a good agreement with the experimental results. The shape and the general temperature dependence of the powder spectra in Fig. 3.34b are well reproduced by the simulation. Even the half-field transition is present in the results of the calculation, as shown in Fig. 3.34c. The spectra of the oriented sample have been calculated with the same parameter set. Also here the agreement is good, except for presumably dispersive contributions to the experimental spectrum, which yield partially asymmetric edges. Additional intrinsic effects, like different anisotropy (in particular in-plane anisotropy $\propto S_x^2 - S_y^2$) may yield the observed ESR peak asymmetry. Both effects are not in the scope of the calculation hence producing deviations between model and experiment. The remaining mismatch of the experimental and the simulated spectra (in particular for the high temperature spectra in Fig. 3.35b) can be attributed to an incomplete orientation of the sample. The remaining powder averaged fraction of single crystallites then results in a background signal.

The magnetization measurements in pulsed fields indicate a ground state which is given by a total spin of $S = 3$ or $S = 4$, respectively. The ambiguity arises from the saturation moment in pulsed fields which is too low to exclude $S = 3$. In fact, the spectrum simulations of the ESR temperature dependence supports

that the lowest lying spin states are $|\pm 4\rangle$. However, it is not clear so far whether these states form a doublet. More probably, they are further split by the effect of the CF in terms of transverse anisotropy. The multiplicity of 9 is thereby a result of the very presence of peak no. 1 in Fig. 3.35a. This resonance is due to a spin transition $|-4\rangle \leftrightarrow |-3\rangle$ as shown in Fig. 3.37. If the ground state multiplet were determined by a spin of $S = 3$, the lowest lying doublet would not exist. On the other hand the position of peak 2 in the spectrum is determined by the g-factor and the ZFS. In the $S = 3$ scenario an ESR signal at the resonance field of peak 1 requires either a significantly larger g-factor or a stronger axial anisotropy D than the measured one.
Remarkably, the preliminary results for the g-factor (2.17) and the ZFS Δ (1.92 K) from the frequency dependence of the powder ESR signal (see Fig. 3.33) yield already good approximations in comparison to the result of the more precise analysis by the model simulation ($g = 2.16, \Delta = 2.17\,\mathrm{K}$). As a final check, the field spacing between the absorption peaks in the oriented spectra is calculated using (1.13),

$$\Delta H \;=\; \frac{2|D_{\mathrm{mol}} \times 20.8\,\mathrm{GHz\,K^{-1}}|}{14\,g} \;=\; 0.426\,\mathrm{T}, \tag{3.16}$$

in a good agreement with the measured spacing of $\Delta H = 0.43\,\mathrm{T}$ (compare Fig. 3.35a).

The resulting potential well $U = 4.96\,\mathrm{K}$ leads to a slowing down of the magnetization dynamics for low temperatures. A lower limit of 160 mK for the blocking temperature T_{B} has been observed by measurement of the dynamic susceptibility.

To summarize, the experimental results are in good agreement with the description of the cluster in the framework of the giant spin Hamiltonian (3.15) by means of the effective spin and the values found for g and D_{mol}. Ambiguities remain for the interpretation of the saturation magnetization. The coupling parameters J_1 and J_2 are obviously of FM nature. However, the saturation moment of $\mu_{\mathrm{sat}} = 4g\mu_{\mathrm{B}}$ for the applied temperature (4.2 K) and field strength ($< 49\,\mathrm{T}$) is not reached in the experiment. A reduction of the effective moment could be due to several mechanisms. For example, an additional AFM exchange which magnetically couples the centers (1,4) and (2,3), respectively (i.e. along the diagonals in Fig. 3.36), could be responsible for the introduction of some frustration into the cluster. The result would be a canting of the spins and an effective reduction of the magnetic moment by means of the resulting misalignment. Similar considerations are true for the presence of Dzyaloshinsky-Moriya interaction [29, 100] (DM) which could also account for a misalignment of the spins. Unfortunately, both scenarios do not seem to be applicable. The DM interaction is only a small perturbation with respect to the isotropic interaction. Also an additional AFM interaction has to be smaller than J_1 and J_2 because otherwise it would render the ground state a spin singlet. On the other hand, the pulse field magnetization-

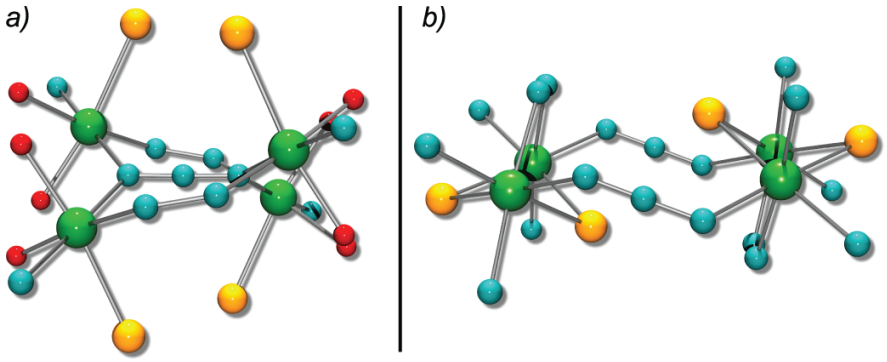

Figure 3.39: *Side-view of the molecules NiAz (a) and NiBiAz (b). The large uniaxial anisotropy of NiAz is due to the opposing sulfur (large yellow sphere) and oxygen (tiny red sphere) ligands.*

shows a clear saturation up to fields of 49 T (28 K). This would imply a rather strong effect of the AFM exchange. Further theoretical modeling beyond the simplified Hamiltonian (3.11–3.13) is highly desired.

Finally, Fig. 3.39 shows a comparison of the molecular structures of the AFM NiAz (a) (section 3.3) and the FM NiBiAz (b). While NiAz has a large axial SIA of $D = -4.8\,\mathrm{K}$, the corresponding parameter of NiBiAz is an order of magnitude smaller, $D = -0.31\,\mathrm{K}$. Since the difference is so drastic, it can be observed already in the structure of the six-coordinate Ni environment. For NiAz the axis of largest distortion responsible for the large D value is the one formed by opposing sulfur and oxygen ligands. For NiBiAz such an axis can not be identified from the view in Fig. 3.39b.

To conclude, the tetranuclear Ni cluster NiBiAz proved to have a magnetic ground state with an effective spin of $S_{\mathrm{eff}} = 4$ due to considerable FM exchange. Moreover, it has been evidenced that the Ni ions exhibit an appreciable single ion anisotropy D caused by the CF. The negative sign of D as well as the presence of the anomaly in the AC susceptibility are fingerprints of SMM behavior. So NiBiAz is on the right route to SMM.

3.6 Spin-Frustrated Mn_3Cr Star

Introduction

While the foregoing sections were about the study of magnetically homonuclear compounds, the current one makes the turn to clusters combining two different species of (paramagnetic) nuclei in a single molecule. Generally, polynuclear complexes are of increasing interest to molecular magnetism [53]. In contrast to the homonuclear, in the heterometallic systems the easier realization of strictly orthogonal magnetic orbitals supports the stabilization of the highest multiplicity spin states. Additionally, the synthesis of such complexes might be promising, as new exchange pathways can be expected by overlap of unusual sets of magnetic orbitals. [20] Finally, polynuclear complexes can have a large net spin in the ground state, despite the usually AFM next-neighbour exchange between the magnetic nuclei, as can be seen below.

An important aim in the field of molecular magnetism is to achieve systems with high-spin ground states (section 3.1). However, intra-molecular exchange usually does not tend to be FM. One route to increase the overall spin multiplicity is to make a virtue of this necessity: consequently, the objective is to polarize several high peripheral spins by means of the favored AFM interactions with a common low-spin central ion. The cluster presented in this section is one of the rare representatives of a star-shaped tetranuclear compound synthesized with this strategy in mind.
Despite the interest in the properties of heteronuclear systems, synthetic methods are yet to reach the level of efficiency attained with mononuclear complexes. [108] The strategies used so far to prepare polynuclear 3d-metal complexes are essentially based on random self-assembling methods. The disadvantage of this approach is that the final products cannot be determined a priori. One particular successful route involves the use of metalloligands, i.e., mono- or binuclear complexes with ligands already bound to one metal ion. [109] Metalloligands provide free coordination sites that are able to link to a second metal ion. The favored strategy of Khanra *et al.* [108] for the controlled synthesis of the multinuclear heterometallic complex $Mn_3^{II}Cr^{III}(PyA)_6Cl_3$, abbreviated as Mn_3Cr in the following, is the utilization of metal oximate building blocks as ligands [110–112].

High-field ESR and magnetization measurements have been performed on a powder sample of Mn_3Cr. The alignment of the transition metal ions in this molecule forms a star. Thereby, the Mn^{II} ions with $S = 5/2$ build a regular triangle, and the Cr^{III} ion with $S = 3/2$ is placed on the three-fold symmetry axis through its center. As will be shown in the following, the investigation of the magnetization data reveals an effective spin of $S_{\text{eff}} = 6$ which can be attributed to the presence

of a dominant AFM Mn-Cr exchange. However, an additional reduction of the effective spin in low fields can not be explained by this sole exchange coupling. A careful analysis of the pulse field magnetization in the framework of the relevant spin Hamiltonian indeed supports an additional Mn-Mn coupling and gives the coupling strengths of $J_{\text{Mn-Cr}} \sim 12\,\text{K}$ and $J_{\text{Mn-Mn}} \sim 3\,\text{K}$. These values are supported by ESR measurements: The excitation frequency of 210 GHz (10 K), which is of the order of $J_{\text{Mn-Cr}}$, represents a boundary at which the ESR spectrum exhibits radical changes. Finally, the low frequency analysis suggests the presence of a single ion anisotropy which manifests by a ZFS of the order of 1 K (20 GHz).

Structure

The crystal structure of Mn_3Cr has been determined by single-crystal XRD [108] at 100 K. In the cluster three pseudo-octahedral Mn^{II}-polyhedra act as ligands for the central Cr^{III}. They are bound through the oximato-oxygen ions resulting in a CrO_6 unit. The space group of Mn_3Cr is $R\bar{3}$ (no. 148) with $a = b = 18.222(2)$, $c = 32.411(5)\,\text{Å}$, and $\gamma = 120°$. The lattice is built of discrete tetranuclear molecules. Fig. 3.40 shows the trigonal core with the central Cr and the three Mn ions at the apices of an equilateral triangle. Due to the presence of the three-fold axis, the three Mn^{II} ions are strictly coplanar.

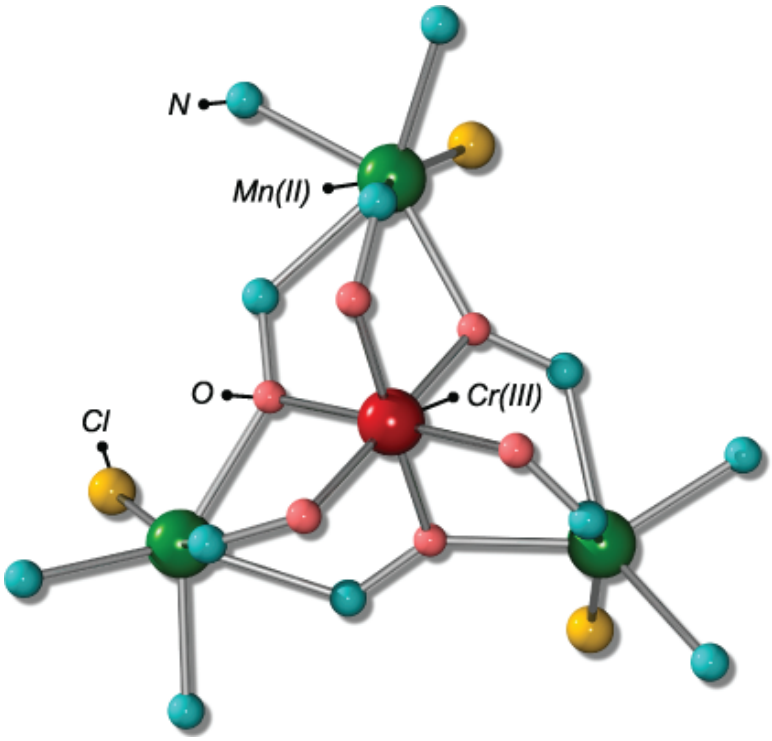

Figure 3.40: *Trigonal core of Mn_3Cr with a Cr^{III} in the center and three Mn^{II} at the apices of the equilateral triangle.*

The central Cr is enclosed by an almost perfect octahedron of six oximato oxygen atoms forming the highly symmetric CrO_6 unit. In contrast, the six-fold coordinated Mn centers form a substantially distorted $MnOClN_4$ core. Thereby, each peripheral Mn^{II} ion is linked to the central Cr^{III} through two oximate (N−O) bridges and a μ_2-O_{ox} connection. The Mn-Cr bonds are expected to give the major contribution to the magnetic exchange, but also the Mn-Mn bonds inside one single cluster might interact with each other by means of their common oximate μ_2−N−O group. However, they are separated by a relatively large distance of 5.49 Å.
The molecules in the crystal are well separated from each other. The shortest Mn-Mn and Mn-Cr distances between neighboring clusters amount 7.8 and 8.8 Å, respectively. The molar mass is 1049.89 g mol^{-1}. Further details of the synthesis and the structure are given in Ref. [108].

Fig. 3.41 shows the expected coupling scheme. It comprises only two different exchange couplings ($J_{\text{Mn-Cr}}$ and $J_{\text{Mn-Mn}}$) due to the three-fold symmetry of the cluster. The exchange $J_{\text{Mn-Cr}}$ couples each corner Mn to the central Cr, while $J_{\text{Mn-Mn}}$ couples pairs of Mn centers. For $J_{\text{Mn-Mn}} = 0$ the ground state is basically determined by the sign of $J_{\text{Mn-Cr}}$. For an FM exchange $J_{\text{Mn-Cr}}$ all the spins are aligned thus yielding the maximum available spin value of $S_{\text{tot,FM}} = 3 \cdot {}^5/_2 + {}^3/_2 = 9$. If the coupling is AFM as expected, the spin of the ground state will be reduced to $S_{\text{tot,AFM}} = 3 \cdot {}^5/_2 - {}^3/_2 = 6$ due to the antiparallel Cr spin with respect to the Mn. In this case the strength of $J_{\text{Mn-Cr}}$ is principally probable by a magnetization experiment at low temperature: For instance, if the g-factors of Cr and Mn are both assumed equal to 2 the moment will show a magnetization plateau at 12 μ_B

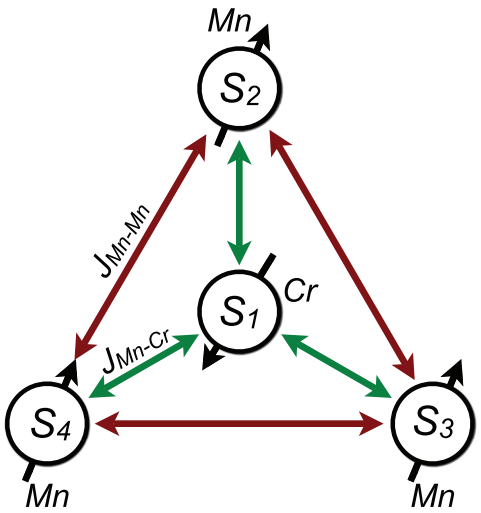

Figure 3.41: *Symmetric coupling scheme: Mn-Cr bonds are shorter than the Mn-Mn bonds. Therefore, $J_{Mn\text{-}Cr}$ is expected to be the dominating exchange coupling. An FM nature of $J_{Mn\text{-}Mn}$ stabilizes the ground state while AFM exchange introduces frustration.*

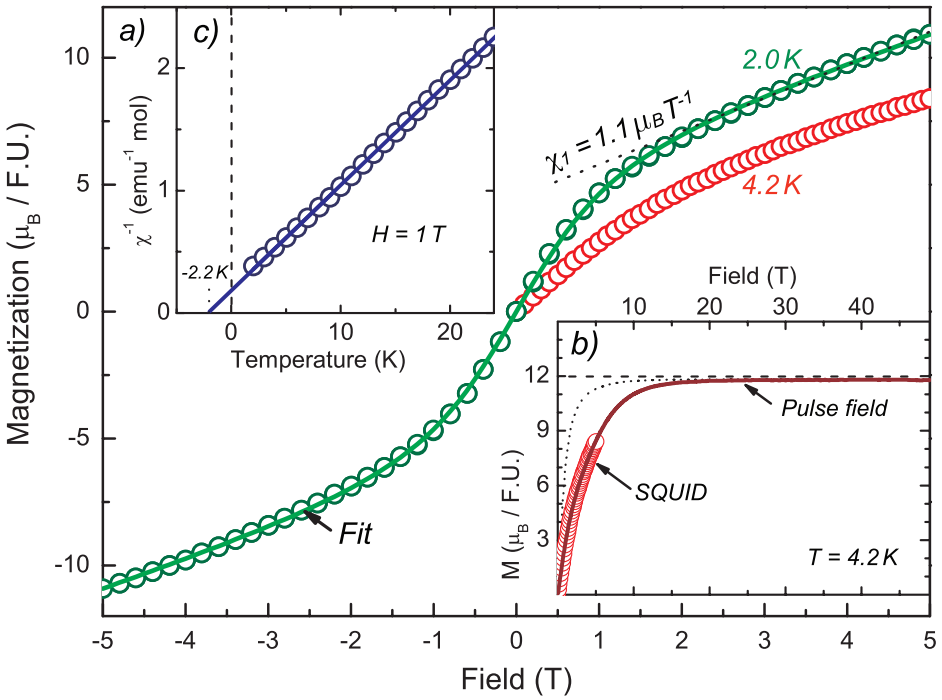

Figure 3.42: *Main panel a): Field dependence of the magnetization at 2 (dark green circles) and at 4.2 K (red circles). The data taken at 2 K can be represented using $M_{Brillouin}(H)+\chi_1 H$ (green line). Inset b): Pulse field magnetization (dark red line) at 4.2 K. The black dotted line corresponds to a Brillouin function $M_{Brillouin}(H; S = 6, g = 1.97)$. Inset c): Inverse static susceptibility χ^{-1} (circles) at 1 T and a Curie-Weiss fit (line).*

starting at field regimes compensating the thermal depolarization. For fields high enough to exceed the AFM exchange energy, the cluster will be eventually completely polarized with $\mu_{\mathrm{sat}} = 18\,\mu_{\mathrm{B}}$.
If we now introduce a small coupling $J_{\text{Mn-Mn}}$, $0 < |J_{\text{Mn-Mn}}| < |J_{\text{Mn-Cr}}|$, it will either, if FM, stabilize the particular ground state, or, if AFM, cant the Mn spins. The latter case will introduce some frustration and may effectively reduce the observed magnetic moment for low external fields. A present single ion anisotropy may lift the degeneracy of the multiple degenerate ground states.

Magnetization

Magnetization measurements of the Mn_3Cr-star have been performed with an MPMS and in pulsed fields (section 2.6). Fig. 3.42a shows the magnetization $M(H)$ of the powder sample measured at 2 and at 4.2 K. The curve at 2 K was measured in the field range $|H| < 5$ T and shows neither hysteresis, nor saturation. In fact, the slope of the curve at 5 T corresponds to a linear increase of $\chi_1 \sim 1.1\,\mu_{\mathrm{B}}\mathrm{T}^{-1}$ (see [9]).

[9]The value of the slope χ_1 was obtained by fitting the composition of a Brillouin function and

$M(H)$ at 4.2 K was measured for calibration of the pulse field magnetization data which are shown in Fig. 3.42b. In high magnetic fields the magnetization saturates at a level of $\sim 12\,\mu_B$ per Mn_3Cr-cluster. This result gives clear evidence of an AFM nature for the Mn-Cr exchange $J_{\text{Mn-Cr}}$. The coupling strength of $J_{\text{Mn-Cr}}$ is considerable, since even at 49 T it prevents the Cr spin from aligning with the Mn spins. A more quantitative analysis will be given in the modeling section below. Moreover, the effect of an additional exchange interaction is observed in the pulse field data: in fields below 20 T the measured magnetization is distinctly smaller than the one calculated by using a Brillouin function[10] (black dotted line in Fig. 3.42b). This behavior can be attributed to an AFM exchange along the Mn-Mn bonds.

Additionally, the susceptibility $\chi(T)$ was measured at 1 T in a broad temperature range between 2 and 385 K. Fig. 3.42c shows $\chi^{-1}(T)$ for low temperature together with an applied Curie-Weiss fit. Except for a small upturn of χ^{-1} at low temperature, the fit is in very well agreement with the data over the complete temperature range. It yields a small Weiss temperature of $\theta = -2.2$ K and an effective moment of $\mu_{\text{eff}}/\mu_B = 9.65$. This value corresponds to an effective spin of $S_{\text{eff}} = 4$ or $S_{\text{eff}} = 5$ (depending on the g-factor) which—when compared

an additional term $\chi_1 H$ to the experimental curve (green line in Fig. 3.42a).

[10] The Brillouin functions in the Figs. 3.42 a) and b) are different: The first one was only used to determine the slope of $M(H)$ at 5 T, while the second one well describes the low field behavior ($H < 20$ T) of a cluster with $J_{\text{Mn-Mn}} = 0$.

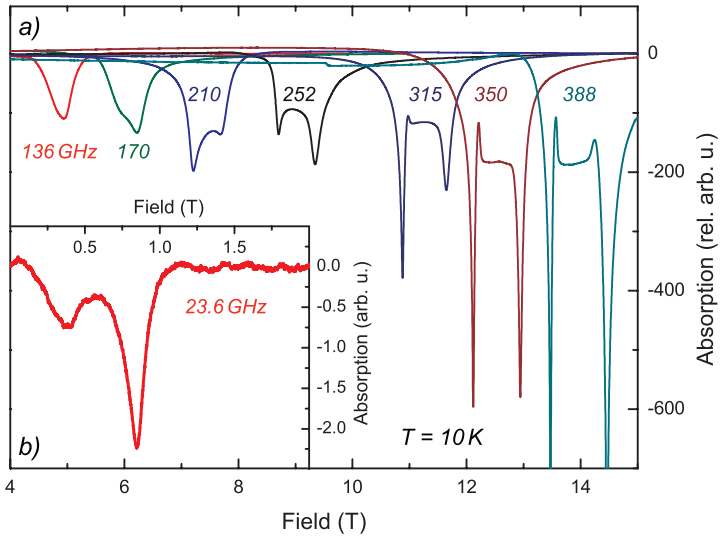

Figure 3.43: *Selected HF ESR spectra measured for different excitation frequencies at $T = 10$ K. No signals are detected at 20 GHz. A well defined spectrum comprising the main peak and a weak satellite is detected at 23.6 GHz (inset). For $\nu > 170$ GHz two sharp resonance lines on a broad dome-shaped background evolve in the spectrum. Compare also Fig. 3.45.*

to $S_{\text{eff}} = 6$ from the pulse field experiment—nicely reflects the deficiency in the magnetic moment at low fields.

High-Field ESR

Further magnetic characterization of Mn_3Cr was obtained by tHF ESR on the powder sample. ESR experiments have been carried out with the MVNA in the transmission geometry (section 2.2). A set of ESR spectra has been collected at a temperature of 10 K, in magnetic fields up to 15 T and in a frequency range between 19 and 388 GHz. The evolution of the spectrum with increasing the excitation frequency is shown in Fig. 3.43.
Below 20 GHz no ESR signals have been observed which indicates the occurrence of the gap for resonance excitations $\Delta \sim 20$ GHz. It can be related to the magnetic anisotropy gap of the molecular complex which arises owing to the ZFS of the spin states. Thus, the gap suggests a respective energy scale for magnetic anisotropy of the order of 1 K in agreement with the estimate of the ZFS parameter D from the static magnetic measurements found in [108].

An ESR spectrum comprising the main absorption peak and a weak satellite has been detected at 23.6 GHz (inset of Fig. 3.43). The intensity of the main peak strongly increases with increasing frequency, whereas the satellite peak rapidly vanishes. The latter peak can be presumably attributed to a "forbidden" ($\Delta S_z = \pm 2$) resonance transition whose probability strongly decreases with increasing the magnetic field strength. The resonance field H_{res} of the strong

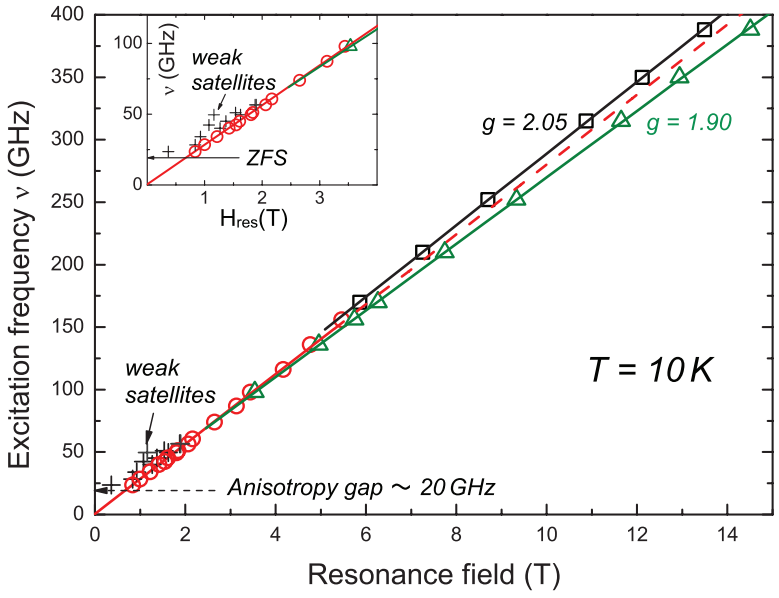

Figure 3.44: *ν vs. H_{res} diagram: Circles and crosses correspond to the main peak and a weak one, respectively.*

absorption line scales linearly with ν, as shown in Fig. 3.44. From the slope of the ν vs. H_{res} dependence below 170 GHz one obtains a g-factor of 2.00 which is expected for both the Cr^{III} and the Mn^{II} [13, 113].

For excitation frequencies exceeding 170 GHz, the ESR signal splits into two separate lines on the top of the broad dome-shaped background (Fig. 3.43 and Fig. 3.45). The signal can be well fitted as a sum of three Lorentzian lines. An example spectrum at $\nu = 350$ GHz and the corresponding fits are shown in Fig. 3.45. Two sharp peaks are well reproduced by narrow Lorentzian profiles, whereas a third much broader Lorentzian line is required to model the broad background. From the fit, the resonance fields of the two sharp lines are obtained. They give the branches which are plotted in Fig. 3.44. The data points are located symmetrically with respect to the anticipated position of the low frequency single peak indicated by the dashed line in this figure. It is tempting to assign these two absorption lines to the individual resonances of Cr^{III} and Mn^{II} which may become resolved owing to the increase of the spectroscopic resolution with increasing magnetic field. The analysis of the static magnetic data, presented below, yields an exchange coupling between the paramagnetic ions of the order of 12 K as shown in the next paragraph. This result is consistent with the ESR observations, because in this case one may expect that in associated magnetic fields starting below $\sim$10 K the spins of Cr and Mn will precess independently. For slightly different g-factors, the ESR signals of Cr and Mn separate with increasing the magnetic field. From the slopes of their ν vs. H_{res} dependences, one obtains the g-factors of 1.90 and 2.05, shown in Fig. 3.44. The latter value is somewhat

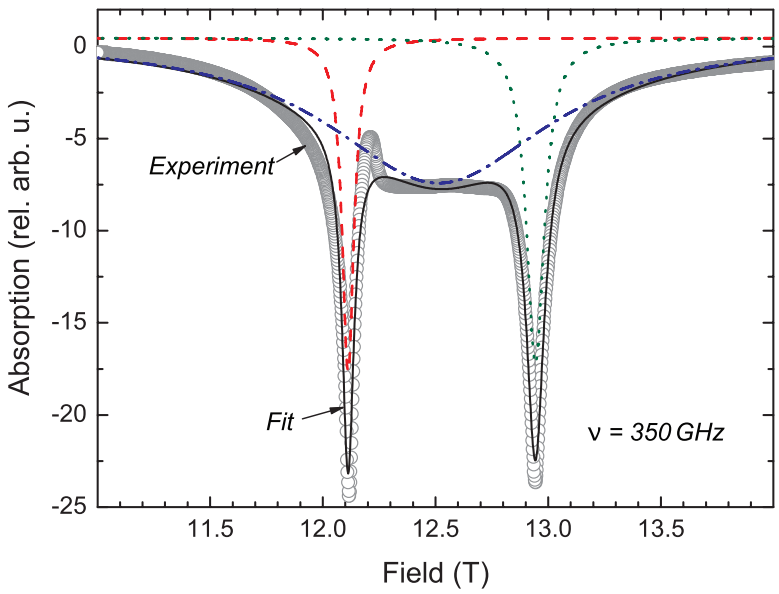

Figure 3.45: *Example fit of a 10 K spectrum at 350 GHz (circles) with three Lorentzian line profiles (dashed, dash-dotted and dotted line, respectively) and their sum (solid line) yielding the resulting fit. For details see text.*

surprising because for Cr^{III} and Mn^{II} a g-factor $\leq g_e$ is expected (compare to equation (1.30) and [12]).

In any case at present it is difficult to unambiguously conclude which of the two sharp resonances belong to Cr^{III} and Mn^{II}, respectively. It is noteworthy that owing to the ZFS both Cr^{III} and Mn^{II} may exhibit ESR spectra with a fine-structure. This structure depends on the direction of the magnetic field with respect to the principal axes of the metal ion-ligand cluster [13]. Thus, the shape of the powder ESR spectrum being an average of the spectra of randomly oriented individual micro-crystallites will depend on such parameters as the ZFC parameters D_{Cr}, and D_{Mn} and g-factors. Preliminary results of the modeling of the spectra indeed clearly indicate that the resulting powder spectrum comprises two sharp peaks associated with Mn and Cr centers, respectively, while the broad background is a powder averaging effect and thus is likely caused by both the Cr^{III} and Mn^{II} ions.

Modeling

The effort for analysis of the Mn_3Cr system is remarkable owing to the large number of parameters (due to the heteronuclearity) as well as the high dimension of the Hilbert space of the appropriate spin Hamiltonian. Thereby, the Heisenberg exchange is formed by a 2-J model complying to the coupling scheme in Fig. 3.41: The dominant AFM coupling $J_{\text{Mn-Cr}}$ aligns the Mn spins parallel to each other and antiparallel with respect to the Cr spin. The exchange between the Mn centers is given by $J_{\text{Mn-Mn}}$. The magnetic energy is included in terms of the axial components of the magnetic anisotropy and the Zeeman energy. The spin Hamiltonian then reads

$$\begin{aligned}
\mathcal{H} = \quad & J_{\text{Mn-Cr}}(\mathbf{S}_1 \cdot \mathbf{S}_2 + \mathbf{S}_1 \cdot \mathbf{S}_3 + \mathbf{S}_1 \cdot \mathbf{S}_4) \\
& + J_{\text{Mn-Mn}}(\mathbf{S}_2 \cdot \mathbf{S}_3 + \mathbf{S}_3 \cdot \mathbf{S}_4 + \mathbf{S}_4 \cdot \mathbf{S}_2) && (3.17) \\
& + D_{\text{Cr}} \left[S_{1z}^2 - \frac{1}{3} S_{\text{Cr}}(S_{\text{Cr}} + 1) \right] && (3.18) \\
& + D_{\text{Mn}} \sum_{i=2\cdots4} \left[S_{iz}^2 - \frac{1}{3} S_{\text{Mn}}(S_{\text{Mn}} + 1) \right] && (3.19) \\
& + \mu_{\text{B}} \mathbf{H}'(\theta) \left[g_{\text{Cr}} \mathbf{S}_1 + g_{\text{Mn}} \sum_{i=2\cdots4} \mathbf{S}_i \right]. && (3.20)
\end{aligned}$$

The angle θ allows to rotate the external field about an axis perpendicular to the symmetry axis of the magnetic anisotropy.[11] Powder spectra of the magnetization are calculated in the following by using the powder average according to $M = (M_\parallel + 2M_\perp)/3$. For the reduction of the numbers of parameters D_{Cr} and D_{Mn} were set identical to $-0.5\,\text{K}$ which is of the order of the results from the ESR experiment. A justification of the dedicated value is discussed below.

[11] An example for $H'(\theta)$ is given in equation (3.13).

The dimension of the Hilbert space is $(2S_{\mathrm{Cr}} + 1)(2S_{\mathrm{Mn}} + 1)^3 = 864$ which is already quite large for a tetranuclear system.[12] However, in order to estimate the couplings J the modeling of the high-field magnetization is necessary. It requires the modeling of the full set of energy states owing to the large range of the magnetic energy scale involved.

Fortunately, the model of the magnetization $M(H) = -\partial\mathcal{H}/\partial H$ turns out to be quite sensitive to both exchange coupling parameters. This fact, combined with the large field interval of the data, enables to determine values for $J_{\text{Mn-Cr}}$ and $J_{\text{Mn-Mn}}$ which are restricted to narrow confines, as shown in the following. In a first approach, the magnetic Mn-Mn exchange is assumed to be much weaker than the one between Mn and Cr, $|J_{\text{Mn-Mn}}| \ll |J_{\text{Mn-Cr}}|$. The parameter $J_{\text{Mn-Cr}}$, if AFM, basically describes the field range of the plateau $M(H)$, as shown in Fig. 3.46a. For external fields H which are strong enough to break the AFM Mn-Cr coupling $J_{\text{Mn-Cr}}$, the Cr spin will finally align parallel with respect to

[12] 1296 is the maximum for 3d ions, e.g. for Mn_4 with $S_{\mathrm{Mn}} = 5/2$.

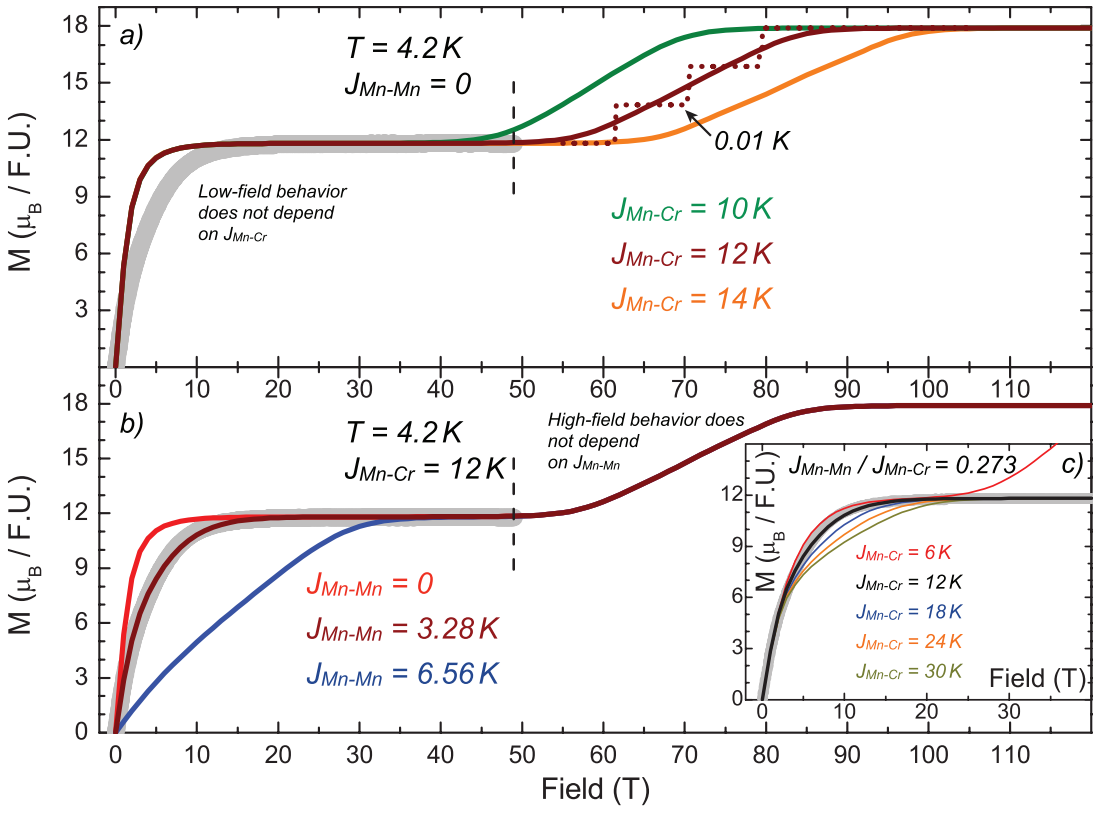

Figure 3.46: *Simulation of the pulse field magnetization. Thick grey line is the experimental curve. a) For $J_{\text{Mn-Mn}} = 0$ the Mn-Cr coupling $J_{\text{Mn-Cr}}$ tunes the step position in high fields at 4.2 K. Dotted points show the successive Cr spin alignment at 0.01 K. b) For $J_1 = 12$ K the Mn-Mn exchange affects basically the low field slope of the magnetization. c) Both exchange parameters $J_{\text{Mn-Cr}}$ and $J_{\text{Mn-Mn}}$ are varied while keeping their ratio constant.*

the Mn spins which will lead to a further increase and a second plateau, as can be seen in Fig. 3.46a. For different values of $J_{\text{Mn-Cr}}$, $M(H)$ is calculated with $J_{\text{Mn-Mn}} = 0$. When comparing the resulting curves to the experimental one it turns out, that a lower limit of $\sim 12\,\text{K}$ for $J_{\text{Mn-Cr}}$ preserves a good agreement with the experimental curve. Thereby, proper $J_{\text{Mn-Cr}}$ values yield magnetization curves without any indication for the softened step $12\,\mu_\text{B} \leftrightarrow 15\,\mu_\text{B}$ below 49 T, just like in the experimental data. This is the case for $J_{\text{Mn-Cr}} \geq 12\,\text{K}$, as observed in Fig. 3.46a. Actually, the broad step in high fields is due to the successive alignment of the Cr spin in three sub-steps as shown for $J_{\text{Mn-Cr}} = 12\,\text{K}$ at 0.01 K (dotted line in Fig. 3.46a).
Remarkably, for values $J_{\text{Mn-Cr}}$ of the order of 10 K, the low-field behavior of $M(H)$ does not depend on the choice of $J_{\text{Mn-Cr}}$. Of course, for very small values of $J_{\text{Mn-Cr}}$ (e.g. <1 K) the first step will vanish completely.
Fig. 3.46b shows the calculated magnetization for different values of $J_{\text{Mn-Mn}}$ with $J_{\text{Mn-Cr}} = 12\,\text{K}$. It turns out that here the high-field behavior, i.e. the step position, is not influenced by the Mn-Mn exchange as long as it is not of the order of the Mn-Cr exchange. However, in low fields the calculated magnetization strongly depends on the introduction of AFM Mn-Mn exchange, as expected. Tuning the parameter $J_{\text{Mn-Mn}}$ yields the best low-field behavior in terms of the slope $\chi = \partial M/\partial H$ for a value of 3.28 K.
By fixing the ratio $J_{\text{Mn-Mn}}/J_{\text{Mn-Cr}}$ to $3.28/12 \approx 0.273$ the exchange was further tuned to optimize the agreement in the range between 5 and 15 T. The inset of Fig. 3.46b shows simulations with different values for $J_{\text{Mn-Cr}}$. Leaving the ratio $J_{\text{Mn-Mn}}/J_{\text{Mn-Cr}}$ constant preserves the slope $\chi(H)$ in the vicinity of zero external fields. Obviously, the best results are achieved for $6\,\text{K} \leq J_{\text{Mn-Cr}} \leq 12\,\text{K}$, while for larger values of $J_{\text{Mn-Cr}}$ the achievement of the plateau is softened too much. On the other hand 12 K represents already the lower limit for $J_{\text{Mn-Cr}}$ in order to describe the high-field part well. Therefore, the values $(J_{\text{Mn-Cr}}, J_{\text{Mn-Mn}}) = (12.0\,\text{K}, 3.28\,\text{K})$ yield obviously the best results from the calculation of $M(H)$.

The number of Bohr magnetons which are associated with the saturation level of the plateau is not exactly equal to 12, but with $p = 11.8$ slightly below. In order to give reasonable calculation results for the plateau level, the g-factors of Mn and Cr have to fulfill the condition

$$\frac{15}{2} g_{\text{Mn}} - \frac{3}{2} g_{\text{Cr}} = 11.8. \tag{3.21}$$

Minimizing the least square functional

$$F(g_{\text{Mn}}) = \left[\left(\left\{ 5 g_{\text{Mn}} - \frac{3}{2} 11.8 \right\} - g_1 \right)^2 + (g_{\text{Mn}} - g_2)^2 \right]^{\frac{1}{2}} \tag{3.22}$$

with g_1, g_2 the values 2.05 and 1.90 from the ESR experiment yields $g_{\text{Cr}} = 2.03$ and $g_{\text{Mn}} = 1.98$. Although the absolute agreement of the calculated and the

experimental g-values is still not perfect, at least the tendency $g_{\mathrm{Cr}} > g_{\mathrm{Mn}}$ was a useful result for the further analysis. For that reason these values have been used for the simulation.
For a final optimization the axial anisotropy D has been varied within the margin given by the ESR experiment. Although small changes of D in the range of $\pm 1\,\mathrm{K}$ have a rather small effect on the shape of $M(H)$, the best result was obtained with $D_{\mathrm{Cr}} = D_{\mathrm{Mn}} = -0.5\,\mathrm{K}$.

Remarkably, all $M(H)$ calculations are simulations rather than fits and they may give good starting values for the reduction of a least square functional comprising the experimental data. A fit of has not been performed due to the massive time consumption such a calculation would cost. While the number of parameters for optimization ($J_{\text{Mn-Cr}}, J_{\text{Mn-Mn}}, D$) has been reduced to an economically justifiable amount, the existence of the different regions for optimization (low field increase, arriving at the plateau, high-field behavior) demands for a high number of fitting points. The difficulties further increase due to the necessary powder averaging approach.

Conclusion

The star-shaped molecule Mn_3Cr with a small central spin belongs to a class of tetranuclear complexes which are expected to yield high-spin molecules [114, 115], because of their molecular spin topology. In fact, the synthesis of high-spin molecules is here due to the polarization of high peripheral spins owing to AFM interactions with a small central spin. Since the Mn-Cr interaction is expected AFM, the ground state of Mn_3Cr would be characterized by the spin $S_{\mathrm{tot}} = 3S_{\mathrm{Mn}} - S_{\mathrm{Cr}} = 6$ which is a comparatively high spin in spite of dominating AFM interaction in the cluster. Magnetization measurements indeed exhibit a plateau in $M(H)$ at a level of $11.8\,\mu_{\mathrm{B}}$ which is due to a considerable AFM Mn-Cr exchange. The low-field behavior of the magnetization indicates an additional AFM exchange which is due to the Mn-Mn exchange. Within a 2-J-model the magnetization $M(H)$ has been reproduced with AFM exchange couplings for Mn-Cr ($J_{\text{Mn-Cr}} \sim 12\,\mathrm{K}$) and also Mn-Mn ($J_{\text{Mn-Mn}} \sim 3.28\,\mathrm{K}$) up to 49 T. The model predicts further steps in the magnetization curve at 61.5, 70.5 and 79.5 T due to the successive alignment of the Cr spin with respect to the Mn spins.
The ESR spectra exhibit three resonance signals with different g-factors of 1.90, 2.00, and 2.05 in fields exceeding $\sim 8\,\mathrm{T}$. The absence of ESR signals at frequencies below 20 GHz indicates a gap due to ZFS of the order of 1 K. In the model system for the magnetization the ZFS parameter $D = D_{\mathrm{Mn}} = D_{\mathrm{Cr}}$ has been found to reproduce the experimental data best for a value of $-0.5\,\mathrm{K}$.
As a further result, the model suggests an association of the g-factors to the peaks in the ESR spectra where the sharp low-field signal is due to the Cr, while the high-field peak is caused by the Mn centers, i.e., $g_{\mathrm{Mn}} < g_{\mathrm{Cr}}$.

3.7 Fe_2Cu_2-Complex with Butterfly Motif

Introduction

A particular variety of zero-dimensional spin clusters is given by the family of molecular complexes forming the so called butterfly motif. These complexes are tetranuclear objects with five metal-metal interaction pathways, as shown in Fig. 3.47. The topology comprises metal centers for the body (M1, M1′) and the wing-tips (M2, M2′) of the butterfly. Since the latter are well separated, they can not interact with each other while the body centers do. Additionally, each wing-tip interacts with the body. The example introduced in the following utilizes Cu^{II} for the body and Fe^{III} as wing-tips and thus belongs to the multinuclear butterfly species. In section 3.6 it was already argued that studies on heterometallic complexes might be more informative in terms of unusual exchange paths in comparison to their homonuclear counterparts. However, in the past mainly tetra-manganese butterfly complexes have emerged [116–120], while only few studies of heterometallic butterfly complexes exist. [121–123]

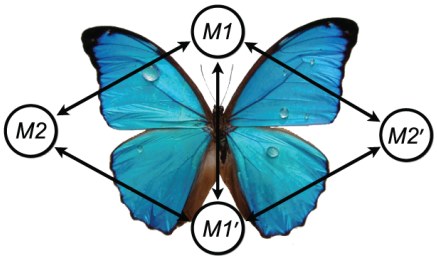

Figure 3.47: *Butterfly motif.*

A reduced core representation of Fe_2Cu_2 is shown in Fig. 3.48. Similar to the star-shaped Mn_3Cr cluster from the previous section, one strategy in the utilization of different metal centers is to gain a high-spin ground state by the polarization of high spins due to AFM coupling with low-spin centers. In Fe_2Cu_2 peripheral high-spin Fe^{III} ($S = 5/2$) centers are polarized by AFM interaction with (two) common $S = 1/2$ Cu^{II} centers. Additionally, a competition of the spin interactions at the body sites is expected which is induced by the topology of the magnetic core, see Fig. 3.47.

Structure

The strategy for the synthesis of Fe_2Cu_2 has been to compose the cluster from mononuclear metal complexes which serve as building blocks for the polynuclear one. The compound $[(Me_3\,Tacn)Fe_2(dapdo)_2Cu_2(O...H...O)(\mu_2\text{-}Cl)](ClO_4)_2$ (abbreviated as Fe_2Cu_2 in the following) is thereby the product of the mononuclear complex $[Cu(dapdoH_2)_2](ClO_4)_2$ which has been reacted with $[Me_3Tacn\,Fe]^{3+}$ in the presence of triethylamine. More details of the synthesis can be found in [124]. The pathways for the magnetic exchange within the Fe_2Cu_2 core are shown in Fig. 3.48. The wings are associated with the body by hydroxo- (OH) and oximato- (N-O) bridges on one hand or by a sole oximato bridge on the other. In the first case, the dominant exchange is expected to be mediated by the oxo-

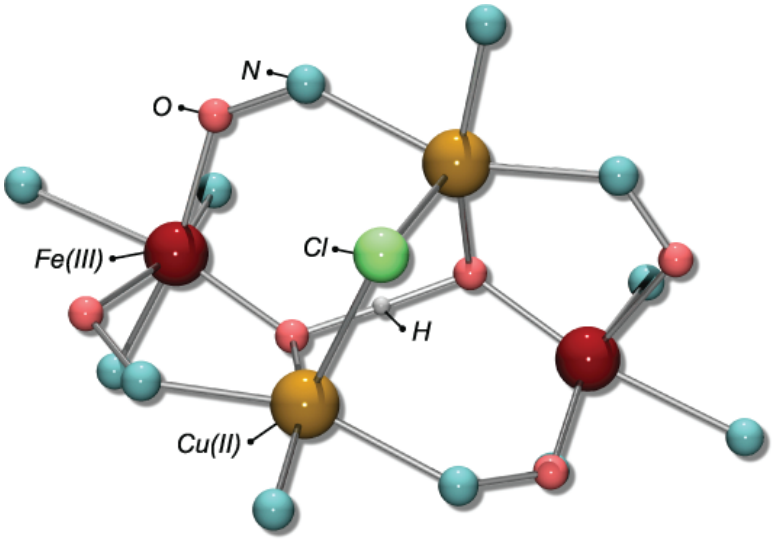

Figure 3.48: *Core structure of the butterfly molecule Fe_2Cu_2. Fe-Cu exchange is mediated by hydroxo- and oximato-bridges. The two Cu centers interact over the Chlorine.*

transmitter. [124] The third pathway refers to the copper-chlorine-copper interaction. While principally five exchange paths are present in the butterfly types, in Fe_2Cu_2 the number of distinct exchange paths is reduced to three, which is due to the core's topology.

Magnetization

Temperature and field dependent magnetization measurements have been performed with the MPMS. The pulse field magnetization experiment was carried out at the LNCMP (Toulouse). Refer to section 2.6 for detailed information. For the measurements, a powder sample of Fe_2Cu_2 was wrapped into a teflon strip. The inverse of the static susceptibility at 1 T exhibits a perfectly linear behavior over a broad temperature range between $\sim$50 and 320 K. In this domain a Curie-Weiss fit yields a Weiss temperature of $\theta_{\mathrm{Weiss}} = +5.8\,\mathrm{K}$ and an effective moment of $\mu_{\mathrm{eff}} = 6.81\,\mu_{\mathrm{B}}$. A rough estimation (with g-values for both Cu and Fe assumed equal to 2) results in an effective spin of $S_{\mathrm{eff}} = 3$. The inset of Fig. 3.49 shows the temperature dependent part of the inverse susceptibility $(\chi - \chi_0)^{-1}$ in the low temperature range where a significant deviation from the Curie-Weiss law is observed: starting from $\sim$45 K the magnetic moment increases continuously, while cooling the sample further. More information concerning the ground state of Fe_2Cu_2 is given by magnetization data at 4.2 K, shown in the main panel of Fig. 3.49. While in static fields (SQUID) the saturation level is not reached, supplementary measurement in the pulse field exhibits a broad plateau starting at about $\sim$10 T and extending to the maximum applied field of 50 T. The magnetic moment of the plateau level amounts $8\,\mu_{\mathrm{B}}$ which corresponds to an effective spin

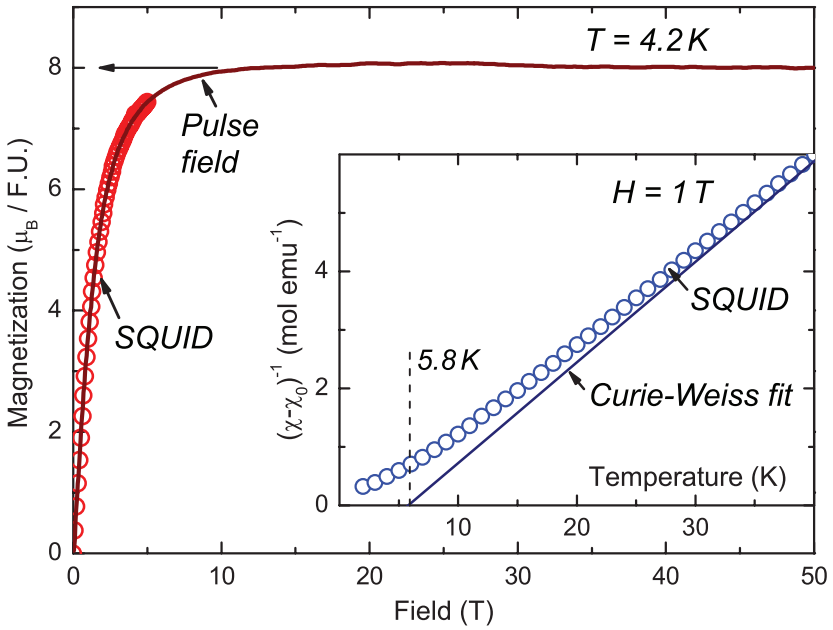

Figure 3.49: *a): Magnetization measurements at $T = 4.2\,K$ in static $H < 5\,T$ (red circles) and pulse field $H < 50\,T$ (dark red curve). b) Low temperature inverse static susceptibility $(\chi(T) - \chi_0)^{-1}$ at 1 T.*

of $S_{\text{eff}} = 4$ of the ground state for $g = 2$. This observation corresponds to a parallel alignment of the Fe spins which are antiparallel with respect to both Cu spins.

High-Field ESR

ESR has been measured on a powder sample of Fe_2Cu_2 in both static and pulsed magnetic fields. For the measurement in static fields, BWO lamps were utilized for the generation of the millimeter-waves (section 2.3). The spectra were achieved utilizing the reflection geometry probehead (shown in Fig. 2.12) and a bolometer for the detection. For pulse field ESR an FIR laser (section 2.5) was utilized as radiation source (see section 2.6 for further details).

The temperature dependence of the ESR signal exhibits a complex behavior. Selected spectra of measurements at 354 GHz (BWO) and 739 GHz (FIR) are shown in Fig. 3.50. For either frequency, the lowest temperature spectra (2 and 4.2 K, respectively) show a broad absorption signal with significant sharp edges. The very presence of this signal indicates a magnetic ground state in agreement with the results of the magnetization measurements. However, the unprecedented shape of this low-T signal indicates that this spectrum of Fe_2Cu_2 is not an ordinary powder average of a resonant ground state excitation.
Usually, the following is expected. For an excitation energy of, e.g., $\nu = 354\,\text{GHz}$, resonant spin-levels are separated by an energy of $h\nu\, k_{\text{B}}^{-1} \sim 18\,\text{K}$. If the system is

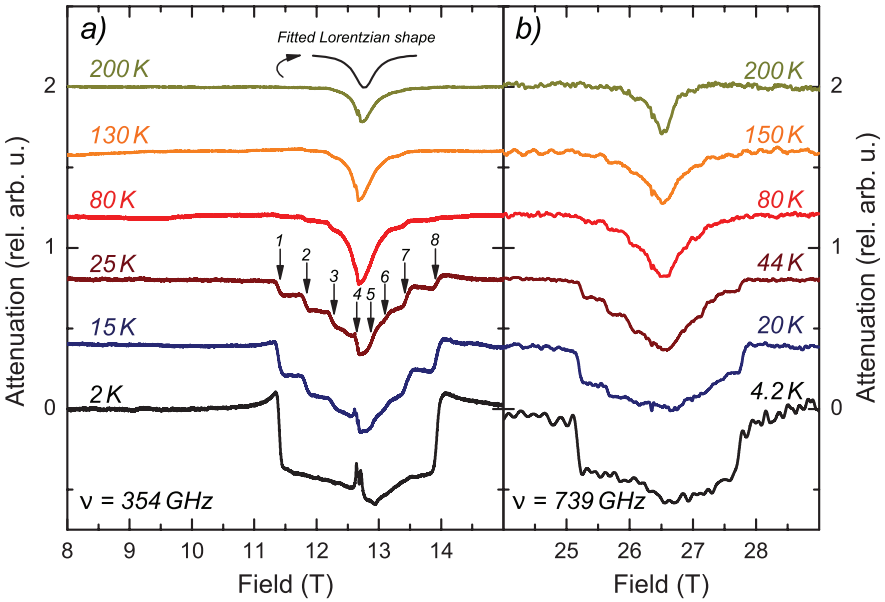

Figure 3.50: *a) Selected spectra at 354 GHz at different temperatures. At 2 K only the ground state excitation causes the spectrum resulting in a broad symmetric spectrum with unusual steep shoulders. With increasing the temperature higher spin states contribute to the spectrum and manifest in a pronounced step-like structure which is nearly symmetric. At high temperature the steps disappear due to decreasing intensity, and instead a smooth ESR line evolves which has Lorentzian shape. b) Pulse field spectra at 739 GHz at similar temperatures. The signal width and overall shape is well reproduced, when compared to a).*

at 2 K, the lowest lying multiplet will be strongly polarized by means of the thermal occupation after Boltzmann.[13] Consequently, the associated ESR spectrum is dominated by a sole resonance transition, i.e. the transition between the lowest spin states, $|-4\rangle \leftrightarrow |-3\rangle$. In this case, an additional finite ZFS in combination with the powder averaging effect can easily account for the large linewidth of the observed ESR signal: Due to the orientation dependence of the magnetically anisotropic crystallites, the resonance peaks of distinct crystallites are spread over an appreciable field range. The linewidth of the detected ESR signal in the powder spectrum is then basically proportional to the size of the anisotropy parameter D. However, the resulting spectrum would be strongly asymmetric (similar to the low-T spectrum of NiBiAz in Fig. 3.34b, section 3.5).
The contrary is observed for Fe_2Cu_2—the spectrum is rather symmetric. On the other hand, for an isotropic spin cluster (without ZFS) the ESR spectrum would be indeed symmetric, though with a different shape and a much smaller linewidth than is observed in Fig. 3.50a. After all, the frequency dependence of Fe_2Cu_2 gives evidence of an appreciable ZFS of $\Delta = 35$ GHz, as described below.
With increasing temperature a pronounced step-like structure develops in the

[13] The same argument holds true for the low temperature spectrum at 739 GHz in Fig. 3.50b.

spectrum. Eight of these approximately equally spaced steps are observed at 25 K in Fig. 3.50a, numbered in the order of their appearance. This fine-structure is clearly due to transitions between thermally activated spin states, e.g. $|-3\rangle \leftrightarrow |-2\rangle$, $|-2\rangle \leftrightarrow |-1\rangle$ and so forth. At 130 K the structure is still present, though its intensity becomes already negligible when compared to the appearing additional Lorentzian shaped feature. The latter is also clearly thermally activated and hence not present at low temperature. Instead, it is observed at 25 K, reaches an intensity maximum at ~ 80 K and then gets weak with further ascending temperature.

Fig. 3.50b shows supplementary spectra measured in the pulse field at 739 GHz. While the overall temperature behavior is very similar to the one observed at 354 GHz, the excellent reproducibility of the feature-rich spectra is noteworthy.

The temperature dependence in Fig. 3.50 reveals that the fine-structure is most pronounced at 30 K. So for best recognition of the steps, the ESR frequency dependence has been measured at this intermediate temperature. The frequency ν was varied within a broad range between 150 and 983 GHz. In Fig. 3.51 it is plotted versus the positions of the steps with respect to the magnetic field H_ν yielding the ν/H_ν branches. Linear interpolation functions have been fitted to each branch in order to determine the relevant ESR parameters.

The g-values (proportional to the slope) range at 1.99. An estimation of the ZFS

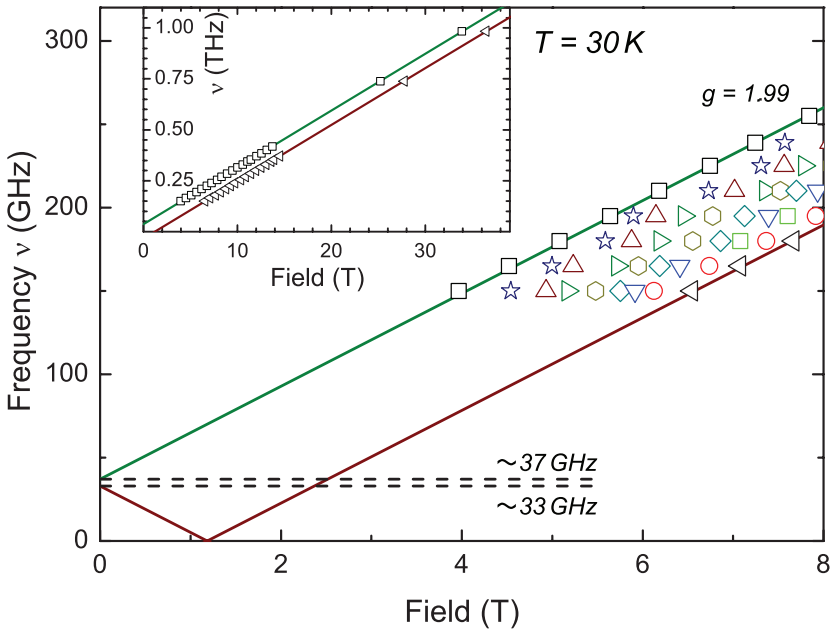

Figure 3.51: *Branches ν/H_ν of the step dependences on the field. The linear fits exhibit a slope corresponding to $g = 1.99$. The branch fits represented by the dark green and dark red lines exhibit a ZFS of 1.6–1.8 K. Inset: Pulse field measurements at 738.92 GHz and 983.61 GHz exhibit only two shoulders which are in good agreement with the fit results.*

was obtained by extrapolation of the linear fits to $H = 0$. The resulting lines associated with the outermost steps in the spectrum are shown in the main panel of Fig. 3.51. The respective excitation frequencies range at ~ 33 and ~ 37 GHz, respectively, which corresponds to a zero-field gap of the order of 1.6–1.8 K.

Modeling

The magnetization at 4.2 K saturates at $\mu_{\mathrm{sat}} = 8\,\mu_{\mathrm{B}} = 4g_{\mathrm{avg}}\,\mu_{\mathrm{B}}$.[14] Since the full polarization of the spins would yield a moment of $6g_{\mathrm{avg}}\,\mu_{\mathrm{B}}$, the experimental result strongly indicates the presence of AFM interaction within the spin cluster. Fig. 3.52 shows a possible coupling scenario which can well account for the measured value of μ_{sat} by means of three different coupling constants J_1, J_2 and J_3. The first, J_1, describes the magnetic exchange between the oximato-bridged Fe-Cu pairs (1,2) and (3,4). J_2 denotes the Fe-Cu bonding (1,4) and (3,2) where the oximato *and* the hydroxo-bonds transmit the exchange interaction. The remaining coupling parameter J_3 denotes the Cu-Cu exchange (2,4) which is mediated by the central chlorine ion.
Regarding dinuclear $Fe^{III}Cu^{II}$ clusters which are simultaneously bridged by oxo- and hydroxo-ligands, strong AFM exchange is reported in literature for a large series of compounds. [125–131] On the other hand, the second wing-body interaction in Fe_2Cu_2 (which is represented by the sole N-O bridge) is reported and hence expected to be weakly AFM. [132, 133] Due to the literature on chloro-bridged Cu_2^{II}-complexes, the third exchange pathway in Fe_2Cu_2 is expected to give only small or no exchange at all. [134–137]
Assuming a small value of J_3, and significantly different strengths of J_1 and J_2, a hierarchy of the coupling parameters is introduced: $|J_2| > |J_1| > |J_3|$. Solely by

[14] The nomenclature g_{avg} is formal to reduce the description. A value of about 2 is assumed in the following.

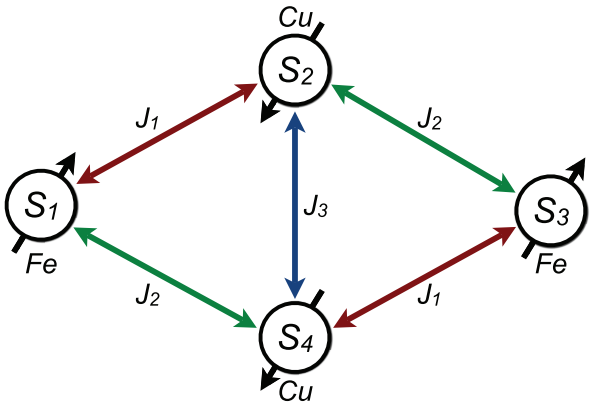

Figure 3.52: *Competing spin interactions: For dominating AFM couplings J_1 and J_2, both Fe align parallel to each other and antiparallel with respect to the Cu.*

consideration of this ranking, it is already clear that the nature of both J_1 and J_2 is AFM in order to account for the reduced total effective spin of $S_{\mathrm{tot}} = 4$.[15] This coupling scheme results in a parallel arrangement of the two Fe spins ($S_{\mathrm{Fe}} = 5/2$), while both Cu spins ($S_{\mathrm{Cu}} = 1/2$) align antiparallel with respect to the iron centers. The additional weak coupling J_3 may slightly stabilize or destabilize this configuration depending on whether its nature is FM or AFM.

On the basis of these considerations, the magnetization data of Fe_2Cu_2 have been analyzed in the framework of a 3-J model. It contains the relevant magnetic exchange reflected by $J_{1,2,3}$ and the magnetic energy. Noteworthy, in this compound the magnetic anisotropy is solely caused by Fe. This is because Cu with $S_{\mathrm{Cu}} = 1/2$ can not show a ZFS due to the Kramers theorem of spin parity [23]. This theorem states that the ground state of an ion with half-integer spin is at least doubly degenerate, which does not depend on the presence of spin-orbit coupling and the degree of the CF.
The analysis of $\chi(T)$ is based on the spin Hamiltonian

$$\begin{aligned}
\mathcal{H} = \quad & J_1(\mathbf{S}_1 \cdot \mathbf{S}_2 + \mathbf{S}_3 \cdot \mathbf{S}_4) \\
& + J_2(\mathbf{S}_2 \cdot \mathbf{S}_3 + \mathbf{S}_4 \cdot \mathbf{S}_1) && (3.23)\\
& + J_3\, \mathbf{S}_2 \cdot \mathbf{S}_4 && (3.24)\\
& + D_{\mathrm{Fe}} \sum_{i=1,3} \left[S_{iz}^2 - \frac{1}{3} S_{\mathrm{Fe}}(S_{\mathrm{Fe}} + 1) \right] && (3.25)\\
& + \mu_{\mathrm{B}} \mathbf{H}'(\theta) \left[g_{\mathrm{Fe}} \sum_{i=1,3} \mathbf{S}_i + g_{\mathrm{Cu}} \sum_{i=2,4} \mathbf{S}_i \right]. && (3.26)
\end{aligned}$$

Unfortunately, it gives some odd results for the coupling parameters which is due to the convergence behavior of the fit procedure owing to the number of parameters. Nevertheless, reasonable fit results can be obtained by neglecting J_3, i.e. setting it to zero and effectively applying the 2-J approach. The fit then yields a strong AFM coupling for J_2 (363 K) and a weak one for J_1 (6 K). [138] The single ion anisotropy from the fit results in $D_{\mathrm{Fe}} = +2.15$ K where this value has to be taken with care since the effect of D on the calculated magnetization is only slight. The g-factors for Fe and Cu amount both to 2.04. [138]

After all the magnetization data of Fe_2Cu_2 are conclusive in terms of the spin multiplicity of the ground state. The exact coupling constants of the intra-molecular exchange are not perfectly determined. However, the particular coupling scheme gives a reasonable starting point for the ESR analysis.
The low temperature spectra in Fig. 3.50 have an almost symmetric shape, which is—as argued before—unusual for magnetically anisotropic compounds with an appreciable ZFS. In such compounds one expects an asymmetric ESR spectrum

[15] Otherwise, the effective spin will be either 6 (J_1 and J_2 FM) or identical to zero (J_1 AFM and J_2 FM or vice versa).

which is shown by the simulation below.

The Hilbert space of Hamiltonian (3.23)–(3.26) has the dimension of 144. ESR simulations based on this Hamiltonian would not only require the knowledge of the complete set of coupling parameters $J_{1,2,3}$, but would result also in critically large calculation times. So in the following, a simplified spin Hamiltonian is assumed. As argued before, at low temperature the lowest lying $S = 4$ multiplet is dominant. To get a low temperature approximation of (3.23)–(3.26), the Heisenberg term (3.11) is excluded in the following. Additionally, the effective spin operator $\tilde{\mathbf{S}}$ with $\tilde{S} = 4$ is used instead of S_{Fe} and S_{Cu}. This approach yields a reduced 9-dimensional Hilbert space which basically restricts the description to the lowest $S = 4$ multiplet.
For the assumed predominant axial symmetry of the CF, the ESR Hamiltonian is then identical to the one given in (3.15):

$$\mathcal{H}(\theta) \;=\; D_{\mathrm{mol}}\,\tilde{S}_z^2 \;-\; \frac{1}{3}\,\tilde{S}\,(\tilde{S}+1) \;+\; g\,\mu_{\mathrm{B}}\,\mathbf{H}'(\theta)\,\cdot\,\tilde{\mathbf{S}}. \tag{3.27}$$

For the calculation of the powder spectra, Hamiltonian (3.27) has been diagonalized for different angles θ with an increment of $\Delta\theta = 0.2$, and the resulting spectra were properly combined.[16] As a result of the approximation, the single ion anisotropy D_{mol} in (3.27) differs from the parameter D_{Fe}. A starting value for D_{mol} has been calculated with the resulting ZFS determined from the ESR frequency dependence: In Fig. 3.51 Δ was determined to a value of the order of 35 GHz (~ 1.68 K). The largest splitting from ESR transitions within the $S = 4$ multiplet is observed for the lowest lying $|{-4}\rangle \leftrightarrow |{-3}\rangle$. This yields $|D_{\mathrm{mol}}| = \Delta/(4^2 - 3^2) = 0.24$ K. For refinement of $|D_{\mathrm{mol}}|$, the parameter was then varied to yield a good agreement of experimental and calculated spectra.

The best result for the simulation with $T = 25$ K and $g = 1.99$ is shown in Fig. 3.53. For a negative anisotropy parameter $D_{\mathrm{mol}} = -0.25$ K the step positions in the low field part of the experimental spectrum (< 12.67 T) are well reproduced. It is noteworthy, that a Gaussian lineshape (linewidth: 1000 G) was assumed for the individual resonances, while a Lorentzian did not yield the steps. As expected, the high-field part of the simulation yields the dominant contribution of the spectral weight, which results in a strong asymmetry of the spectrum. The situation will change to the inverse (good reproduction of the steps in the high-field domain, dominant spectral weight at lower fields), if the sign of D_{mol} is flipped to $D_{\mathrm{mol}} = 0.25$ K (not shown in Fig. 3.53). The apparent discrepancy between the calculation and the experimental results can not be resolved in the framework of Hamiltonian (3.27).

[16] For details of the powder averaging refer to sections 1.11 and 3.5.

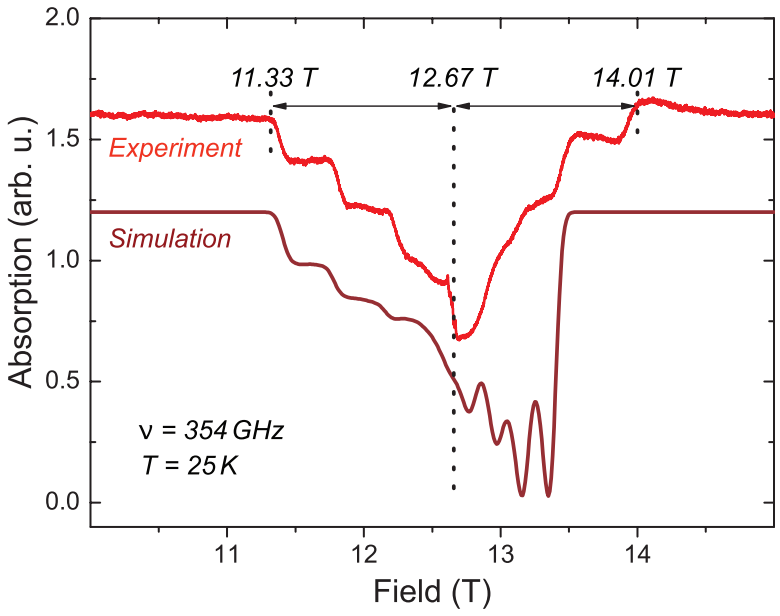

Figure 3.53: *Comparison of experimental and simulated data of Fe_2Cu_2 at $T = 25\,K$. The experimental spectrum shows a symmetry with respect to the resonance field associated with the g-factor of 1.99 (12.67 T). The simulation with $D_{mol} = -0.25\,K$ on the other hand does not account for the symmetry. However, the steps in the low field range between 11.33 and 12.67 T are reproduced.*

Conclusion

The investigated Fe_2Cu_2 cluster is a rare representative of hetero-tetranuclear single-molecule clusters with the butterfly motif. Although an interpretation of the magnetization and the ESR spectra is difficult in the framework of the introduced spin Hamiltonians some substantial results can be extracted from the study.

First of all, the Fe centers on the wing tips of the butterfly are successfully polarized by means of AFM exchange interaction with the low-spin Cu ions of the body. ESR spectra at low temperature leave no doubt of a magnetic ground state, and measurement of the magnetization at high field proved the size of the saturation moment which is due to a low lying $S = 4$ multiplet.

Furthermore, the considerable ESR linewidth at low temperature and the presence of the fine-structure at increased temperature indicates a zero-field gap Δ. By measurement of the ESR frequency dependence, an estimation of Δ yields the size of $\sim$1.68 K. The ESR simulations with $\Delta = 1.75$ ($|D_{\mathrm{mol}}| = 0.25\,\mathrm{K}$) give a good agreement concerning the observed fine-structure. The sign of the single ion anisotropy D, however, remains unknown owing to the intriguing and unprecedented symmetry of the absorption signal. While usually the asymmetric spectral weight is a fingerprint of its nature, the present data give no indication for D being positive or negative. For the further study the investigation of an oriented sample of Fe_2Cu_2 promises more insights on the kind of the ZFS and

the origin of symmetry in the ESR absorption signal. Also, an improvement of the theoretical model is desired. To summarize, the strategy of synthesizing high-spin molecules polarized by AFM exchange in heteronuclear spin clusters is a promising approach to get SMM behavior.

Summary

In this work, low dimensional iron group clusters have been studied by application of high magnetic fields. The magnetization has been probed with an MPMS as function of temperature and field. The combination with pulse field measurements up to 52 T allowed to determine the magnetic exchange coupling parameters, and to probe the effective spin of the ground state. The main focus was on tunable high-field/high-frequency (tHF) ESR in static fields < 17 T and pulse field ESR up to 36 T. This magnetic resonance method has been used for the characterization of the local magnetic properties: The detailed analysis of the field dependence of dedicated spin states allowed to determine the magnetic anisotropy and g-factors. The results were analyzed in the framework of the appropriate effective spin Hamiltonians in terms of magnetization fits and ESR spectrum simulations.

The investigated systems included weakly coupled spin clusters with a finite number of iron group ions. The intra-molecular coupling between these spins is mediated via superexchange by a variety of diamagnetic bridging ligands. The latter affect the local crystal field of the spin carriers which is responsible for the desired single ion anisotropy. Hence, the ligands are crucial components with significant influence on the ground state properties. For example the susceptibility of the system denoted as NiOx—a Ni^{II}-based 2-leg spin ladder with oxalate bridging ligands—proved a singlet ground state for the compound. The oxalate anions transfer the magnetic exchange between the $S = 1$ Ni centers either on the rungs and on the legs of the ladder. However, strong anisotropy of the exchange has been found to be due to different superexchange pathways on the oxalate molecules. Owing to the very weak leg exchange, the rungs of the ladder represent virtually isolated dimers which are AFM coupled by an exchange strength of 43 K and result in the singlet ground state. The ESR study of the magnetic excitations yielded the local picture: The frequency dependence of the ESR spectrum includes a half-field transition which is the fingerprint of single-ion anisotropy by means of the chemical environment of the Ni centers. The measurement of the zero-field splitting and its analysis in the framework of the relevant spin Hamiltonian gave a considerable amount of axial single ion anisotropy, $|D| = 11.5$ K. In further pulse field magnetization measurements it was possible to polarize the dimer by applying fields which were strong enough to break the AFM intra-dimer coupling: A step in the magnetization at 29 T and the sign of a second step at ~ 50 K have been addressed to the successive alignment of the Ni spins. These steps were well reproduced by simulation of the magnetization for a positive sign of the anisotropy D.

A structurally 0D compound denoted as NiAz includes four Ni centers which are mainly bridged by three nitrogen ions—the central so-called azide bridge in the μ_4−1,1,3,3 binding mode. Also in this compound dominant AFM exchange gives rise to a non-magnetic ground state. However, in this case three distinct intra-quadrumer exchange couplings between the Ni centers are involved. The analysis of the susceptibility revealed a hierarchy of these coupling parameters: The dominant FM exchange ($\sim -60\,\mathrm{K}$) yields two $S = 2$ dimers which are coupled AFM via the remaining two coupling paths (each $\sim 40\,\mathrm{K}$). Four resonance modes have been detected by ESR measurements. They were studied as a function of temperature and the excitation frequency. Based on the temperature dependence, the observed resonances were assigned to dedicated spin transitions in the first and the second excited multiplet. A considerable zero-field splitting Δ was directly deduced from the frequency dependence. Numerical analysis of the spin Hamiltonian and consideration of the susceptibility data yielded that the zero-field splitting is due to a negative uniaxial single ion anisotropy, $D = -4.8\,\mathrm{K}$. Also in this compound the ground state could be tuned in strong magnetic fields: At the critical field of $\sim 25\,\mathrm{T}$ the non-magnetic ground state changed to a magnetic one due to a spin-level crossing. Indeed, such tuning was confirmed by additional tHF ESR and magnetization experiments. By introduction of additional azide ligands into the Ni_4 core—as in the system shortened with NiTriAz—the non-magnetic ground state is stabilized. Three polytypes of NiTriAz have been studied. The substances have very similar Ni_4 cores, since they were synthesized just with different carboxylates and thioether substituents. However, the binding situation of the four Ni centers is more comprehensive compared to NiAz: Here, three azide ligands occur in two different binding modes. The result is overall stronger AFM exchange. This has been observed by the study of the susceptibility maximum which shifts to considerably higher temperatures. Also, no jumps have been detected in the magnetization which could have been assigned to a change of the ground state to a magnetic one. Furthermore, the temperature dependence of the ESR spectra exhibited maximal intensity of the discovered resonance signals at significantly higher temperatures. However, by ESR a zero-field splitting of $\Delta = 4.3\,\mathrm{K}$ has been determined for one polytype of NiTriAz.

Besides AFM exchange, azide ions can also transfer FM interaction. The cluster denoted as NiBiAz combines 4 Ni ions in a single molecule which interact via two azides and two diaminothio bridges. Combined magnetization measurements in static and pulsed magnetic fields indicated the FM ground state. However, the observed saturation of the magnetization moment is significantly below the expected value for an effective spin of 4. Finally, this magnetic state has been determined by ESR to be due to an $S = 4$ multiplet: The position of the ESR resonances measured on an oriented sample evidenced a full polarization of the Ni_4 core. Furthermore, the distribution of the ESR spectral weight in combination with the analysis of simulated spectra left no doubt of a negative axial

component of the single ion anisotropy D, which amounts to $\sim -0.3\,\mathrm{K}$. Thanks to these properties, the lowest $S = 4$ multiplet of NiBiAz is not multiply degenerate, but only the spin states $|\pm 4\rangle$ are lying lowest. This is an important prerequisite for single molecular magnetism. The resulting energy barrier due to the uniaxial anisotropy should slow down the relaxation of the magnetization in single-molecule magnets. In order to evidence this SMM property, the AC susceptibility was measured at 16 Hz and, indeed, a lower limit of the blocking temperature of 160 mK has been found. A more detailed analysis at different frequencies is still outstanding.

While FM exchange is advantageous in order to yield a magnetic ground state, it is by no means necessary. AFM exchange between different species of iron group ions can also yield polarization. An example is the star-shaped molecule abbreviated with Mn_3Cr. In the core, three Mn^{II} ions on the apices of a regular triangle enclose the central Cr^{III} center which resides on the three-fold axis of the cluster. The ground state has an effective spin of 6 as was evidenced by measurement of the magnetic moment in high magnetic fields. The moment is the result of parallel aligned Mn spins which is due to the AFM coupling of each Mn with the common central Cr spin. Though the dominant intra-molecular exchange is the one between Mn and Cr, also a small AFM Mn-Mn exchange exists which constricts the parallel alignment of the Mn in low magnetic fields. Within a 2-J-model the magnetization $M(H)$ has been reproduced with AFM exchange couplings for Mn-Cr ($\sim 12\,\mathrm{K}$) and Mn-Mn ($\sim 3.3\,\mathrm{K}$) up to 49 T. The model predicts further steps of the magnetization curve at 61.5, 70.5 and 79.5 T due to the successive alignment of the Cr with respect to the Mn spins. The absence of ESR signals at low frequencies indicated a zero-field splitting which was estimated to 1 K. ESR spectra yielded three resonance signals with different g-factors of 1.90, 2.00, and 2.05 in fields exceeding $\sim 8\,\mathrm{T}$. The latter value is surprising, since both Mn^{II} and Cr^{III} are expected to exhibit $g \leq 2$ due to their electron configuration. In this case, the applied spin Hamiltonian approach returns excellent results for the reproduction of the macroscopic properties. However, the local properties have yet to be considered in the framework of an improved model.

The second hetero-tetranuclear cluster which has been studied includes an Fe_2Cu_2 core which forms the butterfly motif. Magnetization measurements on this cluster exhibited a magnetic ground state due to dominant AFM intra-molecular exchange couplings: The Fe^{III} centers on the wing tips of the butterfly are aligned parallel. This is the case owing to their AFM exchange with the low-spin Cu^{II} ions of the body. The result is that the lowest lying multiplet has a spin of $S = 4$. Also ESR at low temperature left no doubt of this magnetic ground state. However, a complex spectrum with some unusual aspects has been observed: A considerable ESR linewidth at low temperature and the presence of the fine-structure at increased temperature indicated a zero-field splitting Δ. By measurement of the ESR frequency dependence, an estimation of Δ yielded the

size of $\sim$1.7 K. ESR simulations with $\Delta = 1.75\,\mathrm{K}$ ($|D_{\mathrm{mol}}| = 0.25\,\mathrm{K}$) resulted in some agreement concerning the observed fine-structure. However, the sign of the single ion anisotropy D remained unknown owing to the intriguing and unprecedented symmetry of the absorption signal. While usually in powder spectra the asymmetric distribution of the spectral weight is a fingerprint of its sign, the present data gave no indication for D being positive or negative. For the further study the investigation of an oriented sample of Fe_2Cu_2 promises more insights on the kind of the ZFS and the origin of symmetry in the ESR absorption signal.

The results of this thesis have clearly shown that ESR and magnetization measurements are essential tools for the investigation of magnetic molecular clusters. Regarding magnetization measurements the application of pulsed magnetic fields provided the required probing energy for partially or full polarization. Concerning ESR, the application of high excitation frequencies enabled the determination of large zero-field gaps up to 11.5 K (239 GHz). Also the gain of the spectroscopic resolution in high magnetic fields (for Mn_3Cr) and the broad field range of the ESR spectra (Ni ESR) have been the essential capabilities to achieve meaningful spectra. However, the thesis documents also, that the interpretation of local properties makes demands to the model system and is not always straightforward.

Appendix

A.1 Physical Units and Abbreviations

Abbr.	Meaning
α	Sommerfeld fine-structure constant
χ	Static susceptibility
χ_{VV}	Van Vleck susceptibility
χ_0	Diamagnetic susceptibility
D	Axial single ion anisotropy
E	Transverse single ion anisotropy
g	Gyromagnetic factor
g_{e}	Free electron value of g
$\mathcal{H}$	Hamiltonian
$\mathcal{H}_0$	Many electron Hamiltonian
$\mathcal{H}_{\mathrm{CF}}$	Hamiltonian of the crystal field
$\mathcal{H}_{\mathrm{LS}}$	Russel-Saunders Hamiltonian
$\mathcal{H}_{\mathrm{Z}}$	Zeeman Hamiltonian
H	Magnetic field
J_α	Direct exchange
ν	ESR excitation frequency
μ_{eff}	Effective magnetic moment
μ_{sat}	Saturation magnetic moment
$m_{L,S}$	Magnetic quantum number of orbital/spin moment
S	Spin quantum number
$\mathbf{S}$	Spin operator
T	Temperature

A.2 Chemical Abbreviations

Abbr.	Meaning
Et	Ethyl group, C_2H_5
L, L^α	Ligand
*i*Pr	Isopropyl, C_3H_7
Me	Methyl group, CH_3
Ph	Phenyl group, C_6H_5
R, R′	Organic rest

A.3 General Abbreviations

Abbr.	Meaning
AC	Alternating current
AFM	Antiferromagnetic
BWO	Backward wave oscillator
CF	Crystal (electric) field
CW	Continuous wave
DC	Direct current, Directional coupler (depending on the context)
DPPH	Field marker diphenyl-picryl hydrazyl, $g = 2.0036$
EPR	Electron paramagnetic resonance
ESR	Electron spin resonance
FDMR	Frequency domain magnetic resonance
FIR	Far infra-red
FM	Ferromagnetic
HF	High frequency
HG	Harmonic generator
HM	Harmonic mixer
IF	Intermediate frequency
ITO	Irreducable tensor operator
LO	Local oscillator
mm/sub-mm	Millimeter/sub-millimeter
MVNA	Millimeterwave vector network analyzer
MU	Multiharmonic mixer
PLL	Phase locked loop
QTM	Quantum Tunneling of the Magnetization
RF	Radio frequency
SIA	Single ion anisotropy
SMM	Single molecule magnetism
SQUID	Superconducting quantum interference device
tHF ESR	Tunable high field/high frequency ESR
TIP	Temperature independent paramagnetism
TM	Transition metal
VTI	Variable temperature insert
YIG	Yttrium iron garnet
XRD	X-ray diffraction
ZFS	Zero field splitting

A.4 Constants and Conversion

	SI	cgs (emu)	unit
l	$1\,\mathrm{m}$	$10^2\,\mathrm{cm}$	length
E	$1\,\mathrm{J}$	$10^7\,\mathrm{erg}$	energy
B	$1\,\mathrm{T}$	$10^4\,\mathrm{G}$	magnetic flux
H	$1\,\mathrm{A\,m^{-1}} = 4\pi\,10^{-7}\,\mathrm{T}$	$4\pi \cdot 10^{-3}\,\mathrm{Oe}$	magnetic field
μ	$1\,\mathrm{J\,T^{-1}}$	$10^3\,\mathrm{emu}$	magnetic moment
c	$2.997\,924\,58{\cdot}10^8\,\mathrm{ms^{-1}}$	$2.997\,924\,58{\cdot}10^{10}\,\mathrm{cm\,s^{-1}}$	speed of light
h	$6.626\,068\,96\,(33){\cdot}10^{-34}\,\mathrm{J\,s}$	$6.626\,068\,96\,(33){\cdot}10^{-27}\,\mathrm{erg\,s}$	Planck constant
k_B	$1.380\,6504\,(24){\cdot}10^{-23}\,\mathrm{J\,K^{-1}}$	$1.380\,6504\,(24){\cdot}10^{-16}\,\mathrm{erg\,K^{-1}}$	Boltzmann constant
μ_0	$4\pi \cdot 10^{-7}\,\mathrm{V\,s\,A^{-1}m^{-1}}$	1	magnetic constant
μ_B	$9.274\,009\,15\,(23){\cdot}10^{-24}\,\mathrm{J\,T^{-1}}$	$9.274\,009\,15(23){\cdot}10^{-21}\,\mathrm{emu}$	Bohr magneton
g_e	$2.002\,319\,304\,3622\,(15)$		electronic g-value
N_A	$6.022\,141\,79\,(30){\cdot}10^{23}\,\mathrm{mol^{-1}}$		Avogadro number

A.5 Tesseral Harmonics

The spherical harmonics for the d-states [18] are defined by

$$Y_2^0 \;=\; \frac{1}{4}\sqrt{\frac{5}{\pi}}\,(3\,\cos^2\theta\;-\;1) \;=\; \frac{1}{4}\sqrt{\frac{5}{\pi}}\,\frac{3z^2-r^2}{r^2} \tag{A.1}$$

$$Y_2^{\pm 1} \;=\; \mp\frac{1}{4}\sqrt{\frac{30}{\pi}}\,\sin\theta\,\cos\theta\,\mathrm{e}^{\pm i\phi} \;=\; \mp\frac{1}{4}\sqrt{\frac{30}{\pi}}\,\frac{z(x\pm iy)}{r^2} \tag{A.2}$$

$$Y_2^{\pm 2} \;=\; \frac{1}{8}\sqrt{\frac{30}{\pi}}\,\sin^2\theta\,\mathrm{e}^{\pm 2i\phi} \;=\; \frac{1}{8}\sqrt{\frac{30}{\pi}}\,\frac{x\pm iy}{r^2}. \tag{A.3}$$

Thereby, spherical coordinates have been applied on the right side of (A.1)–(A.3),

$$x \;=\; r\,\sin\theta\,\cos\phi \tag{A.4}$$

$$y \;=\; r\,\sin\theta\,\sin\phi \tag{A.5}$$

$$z \;=\; r\,\cos\theta. \tag{A.6}$$

By introduction of the linear combinations, $Y_2^{m_L} \pm Y_2^{-m_L}$, the following real wavefunctions are defined:

$$|d_{xy}\rangle \;\propto\; Y_2^2 \;-\; Y_2^{-2} \tag{A.7}$$

$$|d_{xz}\rangle \;\propto\; Y_2^1 \;-\; Y_2^{-1} \tag{A.8}$$

$$|d_{yz}\rangle \;\propto\; Y_2^1 \;+\; Y_2^{-1} \tag{A.9}$$

$$|d_{x^2-y^2}\rangle \;\propto\; Y_2^2 \;+\; Y_2^{-2} \tag{A.10}$$

$$|d_{3z^2-r^2}\rangle \;\propto\; Y_2^0 \tag{A.11}$$

A.6 Oxo-Bridged Magnetic Cluster

Examples of single molecule magnets (taken from [139]).

SMM	S	D(K)	U_{eff}(K)	Ref.
$[Mn_{12}O_{12}(CH_2BrCO_2)_{16}(H_2O)_4]$	10		81	[140]
$[Mn_{12}O_{12}(CHCl_2CO_2)_8(Bu^tCH_2CO_2)_8(H_2O)_4]$	10	-0.65	72	[141]
$[Mn_{12}O_{12}(CHCl_2CO_2)_8(EtCO_2)_8(H_2O)_4]$	10	-0.60	70	[141]
$[Mn_{12}O_{12}(MeCHCHCO_2)_{16}(H_2O)_4]$	10	-0.63	65	[142]
$[Mn_{12}O_{12}(p\text{-}PhC_6H_4CO_2)_{16}(H_2O)_4]$	10	-0.63	65	[142]
$[Mn_{12}O_{12}(p\text{-}MeC_6H_4CO_2)_{16}(H_2O)_4]$	10		63	[143]
$[Mn_{12}O_{12}(MeCO_2)_{16}(H_2O)_4]$	10	-0.72	60	[57, 59, 144]
$[Mn_{12}O_{12}(MeCO_2)_8(Ph_2PO_2)_8(H_2O)_4]$	10	-0.59	60	[145]
$[Mn_{12}O_{12}(PhCO_2)_{16}(H_2O)_4]^{1-}$	$^{19}/_2$	-0.63	58	[146]
$[Mn_{30}O_{24}(OH)_8(Bu^tCH_2CO_2)_{32}(H_2O)_2(MeNO_2)_4]$	7	-1.14	56	[147]
$[Mn_{12}O_{12}(CHCl_2CO_2)_{16}(H_2O)_4]^{2-}$	10	-0.39	39	[148]
$[Mn_{12}O_{12}(p\text{-}MeC_6H_4CO_2)_{16}(H_2O)_4]$	10		37	[143]
$[Mn_{12}O_8Cl_4(PhCO_2)_8(hmp)_6]$	7	-0.86	30	[149]
$[Mn_9O_7(MeCO_2)_{11}(thme)(py)_3(H_2O)_2]$	$^{17}/_2$	-0.42	27	[150]
$[Fe_8O_2(OH)_{12}(tacn)_6]^{8+}$	10	-0.27	22	[151]
$[V_4O_2(EtCO_2)_7(bpy)_2]^{1+}$	3	-1.5	20	[152]
$[Mn_4(MeCO_2)_2(pdmH)_6]^{2+}$	8	-0.35	17	[153]
$[Mn_4O_3(p\text{-}MeC_6H_4CO_2)_4(dbm)_3]$	$^9/_2$	-0.89	17	[154]
$[Mn_4(hmp)_6Br_2(H_2O)_2]^{2+}$	9	-0.50	16	[155]
$[(Me_3tacn)_6MnMo_6(CN)_{18}]^{2+}$	$^{13}/_2$	-0.47	14	[156]
$[Fe_{19}O_6(OH)_{14}(metheidi)_{10}(H_2O)_{12}]^{1+}$	$^{33}/_2$	-0.050	13.7	[157]
$[Mn_4O_2(MeO)_3(PhCO_2)_2L_2(MeOH)]^{2+}$	$^7/_2$	-1.11	13.7	[158]
$[Mn_4O_3Br(MeCO_2)_3(dbm)_3]$	$^9/_2$	-0.72	11.9	[159]
$[Mn_4O_3Cl(MeCO_2)_3(dbm)_3]$	$^9/_2$	-0.76	11.8	[160]
$[Ni_{12}(chp)_{12}(MeCO_2)_{12}(H_2O)_6(THF)_6]$	12	-0.068	10	[161]
$[Mn_{10}O_4(biphen)_4Br_{12}]^{4-}$	12	-0.053	7.0	[162]
$[(tetren)_6Ni_6Cr(CN)_6]^{9+}$	$^{15}/_2$		6.0	[163]
$[Fe_{10}Na_2O_6(OH)_4(PhCO_2)_{10}(chp)_6(H_2O)_2(MeCO_2)_2]$	11		5.3	[164]
$[Ni_4(MeO)_4(sal)_4(MeOH)_4]$	4		5.3	[165]
$[Mn_9(O_2CEt)_{12}(pdm)_2(pdmH)_2(C_{14}H_{16}N_2O_4)_2]$	$^{11}/_2$	-0.16	4.5	[166]
$[Ni_{21}(OH)_{10}(cit)_{12}(H_2O)_{10}]^{16-}$	3		4.2	[167]
$[Fe_4(MeO)_6(dpm)_6]$	5	-0.3	3.5	[168]
$[Fe_2F_9]^{3-}$	5	-0.22	2.2	[169]

Bibliography

[1] M. Takahashi. Thermodynamics of One-Dimensional Solvable Models. *Cambridge University Press, Cambridge, 1999*, 1999.

[2] B. Barbara, L. Thomas, F. Lionti, I. Chiorescu, and A. Sulpice. Macroscopic Quantum Tunneling in Molecular Magnets. *J. Magn. Magn. Mater.* **200**, *167–181*, 1999.

[3] F. D. M. Haldane. Nonlinear Field Theory of Large-Spin Heisenberg Antiferromagnets: Semiclassically Quantized Solitons of the One-Dimensional Easy-Axis Néel State. *Phys. Rev. Lett.* **50**, *1153–1156*, 1983.

[4] G. Otter and R. Honecker. Atome-Moleküle-Kerne, Band I: Atomphysik. *Teubner Stuttgart*, 1993.

[5] P. Zeeman. Over den Invloed eener Magnetisatie op den Aard van het Door een Stof uitgezonden Licht (On the Influence of Magnetism on the Nature of the Light Emitted by a Substance). *Versl. Kon. Ak. Wet* **5**, *181 (1896); Phyl. Mag.* **43**, *226 (1897).*

[6] G. E. Uhlenbeck and S. Goudsmit. *Die Naturwissenschaften, Nov. 20*, 1925.

[7] B. Friedrich and D. Herschbach. Stern and Gerlach: How a Bad Cigar Helped Reorient Atomic Physics. *Physics Today,* **56**, *12, 53–59*, 2003.

[8] W. Heisenberg. Über den Anschaulichen Inhalt der Quantentheoretischen Kinematik und Mechanik. *Z. Phys.* **43**, *172–198*, 1927.

[9] F. Bloch. Nuclear Induction. *Phys. Rev.* **70**, *460*, 1946.

[10] C. J. Gorter. Paramagnetic Relaxation. *Elsevier, Amsterdam*, 1947.

[11] G. Jeschke. Einführung in die ESR. *Mainz, online*, 1998.

[12] A. Abragam and B. Bleaney. Electron Paramagnetic Resonance of Transition Ions. *(Oxford University Press, London*, 1970.

[13] J. R. Pilbrow. Transition Ion Electron Paramagnetic Resonance. *Clarendon Press, Oxford*, 1990.

[14] F. Schwabl. Quantenmeckanik. *Springer*, 1993.

[15] K. Kopitzki. Einführung in die Festkörperphysik. *Teubner*, 1993.

[16] M. Tinkham. Group Theory and Quantum Mechanics. *MacGraw-Hill Book Co., New York*, 1964.

[17] H. F. Jones. Groups, Representations and Physics. *Adam Hilger, Bristol and New York*, 1990.

[18] P. Fazekas. Lecture Notes on Electron Correlation and Magnetism. *World Scientific*, 1999.

[19] F. Hund. Zur Deutung Verwickelter Spektren, Insbesondere der Elemente Scandium bis Nickel. *Z. Phy.* **33**, *345–371*, 1925.

[20] O. Kahn. Molecular Magnetism. *John Wiley & Sons*, 1993.

[21] J. A. Weil and J. R. Bolton et al. Electron Paramagnetic Resonance. *Wiley-Interscience*, 1994.

[22] D. Gatteschi and R. Sessoli. Molecular Nanomagnets. *Oxford*, 2006.

[23] H. A. Kramers. *Proc. Acad. Sci. Amsterdam* **33**, *959*, 1930.

[24] B. Bleaney and K.W.H. Stevens. Paramagnetic Resonance. *Rep. Progr. Phys.* **16** *108*, 1953.

[25] J. S. Griffith. The theory of transition metal ions. *Cambridge University Press*, 1961.

[26] J. S. Griffith. The Irreducible Tensor Method for Molecular Symmetry Groups. *Englewood Cliffs, N.J.: Prentice-Hall*, 1962.

[27] A. Bencini and D. Gatteschi. EPR of Exchange Coupled Systems. *Springer*, 1990.

[28] L. Sorace, C. Golze, D. Gatteschi, A. Bencini, H.-W. Roesky, J. Chai, and A. Stückl. Low-Valent Low-Coordinated Manganese(I) Ion Dimer: A Temperature Dependent W-Band EPR Study. *Inorg. Chem.* **45**, *395–400*, 2006.

[29] T. Moriya. Anisotropic Superexchange Interaction and Weak Ferromagnetism. *Phys. Rev.* **120** *91–98*, 1960.

[30] W. Heisenberg. Mehrkörperproblem und Resonanz in der Quantenmechanik. *Z. Phys.* **38**, *411*, 1926.

[31] Wolfram Research. *http://www.wolfram.com*, 2007.

[32] C. Dahl, P. Goy, and J. P. Kotthaus. Millimeter and Submillimeter Wave Spectroscopy of Solids, edited by G. Grüner. *Springer-Verlag, Berlin, Heidelberg), Topics in Applied Physics, Vol.* **74**, *p. 221–282*, 1998.

[33] H. Bohlen and H. Döring. Klystron-Technik in "Handbuch der Vakuumtechnik". *Herausg. Eichmeier/Heynisch, Verlag Oldenburg, 167–191*, 1989.

[34] B. Friedrich and D. Herschbach. Naturwissenschaft und Technik. Elektronik. *Zweiburgen Verlag. Weinheim*, 1992.

[35] J. Slater. Microwave Electronics. *Rev. Mod. Phys.* **18**, *441*, 1992.

[36] Millimeter-Submillimeter Wave Quasioptical Spectrometer, Users Manual. 2004.

[37] P. Goy, J. Mallat, J. Tuovinen, A. Maestrini, G. Annino, M. Fittipaldi, and M. Martinelli. Millimeter-Submillimeter Vector Measurements in Free Space, and in Resonant Structures. *Proc. of Mat. Res. Soc.*, Spring 2000 Meeting, April 24–28.

[38] G. Kozlov and A. Volkov. "Coherent Source Submillimeter Wave Spectroscopy" in Millimeter and Submillimeter Wave Spectroscopy of Solids, edited by G. Grüner. *Springer-Verlag, Berlin, Heidelberg), Topics in Applied Physics, Vol.* **74**, *p. 51–109*, 1998.

[39] Edinburgh Instruments Ltd. Instruction Manual for Model 195 FIR Laser. *Issue 2*, 1982.

[40] O. Portugall, F. Lecouturier, J. Marquez, D. Givord, and S. Askenazy. Pulsed Magnetic Fields in Toulouse - Past, Present and Future. *Physica B* **294–295**, *579*, 2001.

[41] C. Golze, A. Alfonsov, R. Klingeler, B. Büchner, V. Kataev, C. Mennerich, H.-H. Klauss, M. Goiran, J.-M. Broto, H. Rakoto, S. Demeshko, G. Leibeling, and F. Meyer. Tuning the Magnetic Ground State of a Tetranuclear Nickel(II) Molecular Complex by High Magnetic Fields. *Phys. Rev. B* **73**, *224403*, 2006.

[42] Operation Manual, Physical Properties Measurement System (PPMS), Quantum Design.

[43] Models 575B & 578B, Source Locking CW Microwave Frequency Counters, Operation Manual.

[44] L. Shu-hua. Origine de la Boussole 11. Aimant et Boussole. *Isis* **45**, *2, 175*, 1954.

[45] J. H. van Vleck. The Theory of Electric and Magnetic Susceptibility. *Oxford University Press, Oxford*, 1932.

[46] Hitachi Global Storage Technologies. Patterned Magnetic Media. *http://www.hitachigst.com/hdd/research/storage/pm/index.html*, 2004.

[47] A. V. Postnikov, J. Kortus, and M. R. Pederson. Density Functional Studies of Molecular Magnets. *Phys. Stat. Sol. (b)* **243**, *2533–2572*, 2006.

[48] O. Kahn. Chemistry and Physics of Supramolecular Magnetic Materials. *Acc. Chem. Res.* **33**, *647–657*, 2000.

[49] M. Tamura, Y. Nakazawa, D. Shiomi, K. Nozawa, Y. Hosokoshi, M. Ishikawa, M. Takahashi, and M. Kinoshita. Bulk Ferromagnetism in the β-Phase Crystal of the *p*-Nitrophenyl Nitronyl Nitroxide Radical. *Chem. Phys. Lett.* **186**, *401–404*, 1991.

[50] M. Takahashi, P. Turek, Y. Nakazawa, M. Tamura, K. Nozawa, D. Shiomi, M. Ishikawa, and M. Kinoshita. Discovery of a Quasi-1D Organic Ferromagnet, p-NPNN. *Phys. Rev. Lett.* **67**, *746–748*, 1991.

[51] Y. Nakazawa, M. Tamura, N. Shirakawa, D. Shiomi, M. Takahashi, M. Kinoshita, and M. Ishikawa. Low-temperature Magnetic Properties of the Ferromagnetic Organic Radical, p-Nitrophenyl Nitronyl Nitroxide. *Phys. Rev. B* **4**, *8906–8914*, 1992.

[52] A. J. Banister, N. Bricklebank, I. Lavender, J. M. Rawson, C. I. Gregory, B. K. Tanner, W. Clegg, M. R. J. Elsegood, and F. Palacio. Spontaneous Magnetization in a Sulfur-Nitrogen Radical at 36 K. *Angew. Chem. Int. Ed. Engl.* **35**, *(21) 2533–2535*, 1996.

[53] Special Issue of MRS Bull. **25**, No. 11, 21 (2000), edited by guest editors J. S. Miller and A. J. Epstein.

[54] D. Gatteschi, A. Caneschi, L. Pardi, and R. Sessoli. Large Clusters of Metal Ions: The Transition from Molecular to Bulk Magnets. *Science* **265**, *1054*, 1994.

[55] A. M. Ako, I. J. Hewitt, V. Mereacre, R. Clérac, W. Wernsdorfer, C. E. Anson, and A. K. Powell. A Ferromagnetically Coupled Mn_{19} Aggregate with a Record $s = {}^{83}/_{2}$ Ground Spin State. *Angew. Chem. Int. Ed.,* **45**, *4296–4299; Angew. Chem.,* **118**, *5048–5051*, 2006.

[56] S. M. J. Aubin, M. W. Wemple, D. M. Adams, H.-L. Tsai, G. Christou, and D. N. Hendrickson. Distorted $Mn^{IV}Mn^{III}_3$ Cubane Complexes as Single-Molecule Magnets. *J. Am. Chem. Soc.* **118** *(33), 7746–7754*, 1996.

[57] R. Sessoli, H. L. Tsai, A. R. Schake, S. Wang, J. B. Vincent, K. Folting, D. Gatteschi, G. Christou, and D. N. Hendrickson. High-Spin Molecules: $[Mn_{12}O_{12}(O_2CR)_{16}(H_2O)_4]$. *J. Am. Chem. Soc.* **115**, *1804–1816*, 1993.

[58] T. Lis. *Acta Crystallogr.* **B36**, *2042–2046*, 1980.

[59] A. Caneschi, D. Gatteschi, R. Sessoli, A. L. Barra, L. C. Brunel, and M. Guillot. Alternating Current Susceptibility, High Field Magnetization, and Millimeter Band EPR Evidence for a Ground $S = 10$ State in $[Mn_{12}O_{12}(CH_3COO)_{16}(H_2O)_4]\cdot 2CH_3COOH\cdot 4H_2O$. *J. Am. Chem. Soc.* **113** *(1991) 5873–5874*, 1991.

[60] A. L. Barra, D. Gatteschi, and R. Sessoli. High-Frequency EPR Spectra of a Molecular Nanomagnet: Understanding Quantum Tunneling of the Magnetization. *Phys. Rev. B* **56***, 8192*, 1997.

[61] A. Cornia, M. Affronte, A. G. M. Jansen, D. Gatteschi, A. Caneschi, and R. Sessoli. Magnetic Anisotropy of Mn_{12}-Acetate Nanomagnets from High-Field Torque Magnetometry. *Chem. Phys. Lett.* **322***, 477*, 2000.

[62] I. Mirebeau, M. Hennion, H. Casalta, H. Andres, H. U. Güdel, A. V. Irodova, and A. Caneschi. Low-Energy Magnetic Excitations of the Mn_{12}-Acetate Spin Cluster Observed by Neutron Scattering. *Phys. Rev. Lett.* **83***, 628*, 1999.

[63] R. A. Robinson, P. J. Brown, D. N. Argyriou, D. N. Hendrickson, and S. M. J. Aubin. Internal Magnetic Structure of Mn_{12} Acetate by Polarized Neutron Diffraction. *J. Phys.: Condens. Matter* **12***, 2805*, 2000.

[64] K. Wieghardt, K. Phol, I. Jibril, and G. Huttner. Hydrolyseprodukte des Monomeren Aminkomplexes $(C_6H_{15}N_3)FeCl_3$: Die Struktur des Octameren Eisen(III)-Kations von $[(C_6H_{15}N_3)_6Fe_8(m_3{-}O)_2(m_2{-}OH)_{12}]Br_7(H_2O)Br\cdot 8H_2O$. *Angew. Chem. Int. Ed. Engl.* **23***, 77*, 1984.

[65] J. R. Friedman, M. P. Sarachik, J. Tejada, and R. Ziolo. Macroscopic Measurement of Resonant Magnetization Tunneling in High-Spin Molecules. *Phys. Rev. Lett.* **76***(20), 3830*, 1996.

[66] L. Thomas, F. Lionti, R. Ballou, D. Gatteschi, R. Sessoli, and B. Barbara. Macroscopic Quantum Tunnelling of Magnetization in a Single Crystal of Nanomagnets. *Nature (London),* **383***, 145*, 1996.

[67] B. Barbara and L. Gunther. Magnets, Molecules and Quantum Mechanics. *Physics World* **12***, 35*, 1999.

[68] M. Verdaguer. *Polyhedron* **20***, 115*, 2001.

[69] D. Gatteschi and R. Sessoli. Quantum Tunneling of Magnetization and Related Phenomena in Molecular Materials. *Angew. Chemie Int. Ed.* **42***, 3, 268–297*, 2003.

[70] O. Waldmann. Supramolekulare Nanomagnete: Quantenphysik im mesoskopischen Grenzbereich. *Habilitation*, 2003.

[71] E. Dagotto. Experiments on Ladders Reveal a Complex Interplay Between a Spin-Gapped Normal State and Superconductivity. *Rep. Prog. Phys.* **62**, *1525–1571*, 1999.

[72] J. M.Tranquada, H. Woo, T. G. Perring, H. Goka, G. D. Gu, G. Xu, M. Fujita, and K. Yamada. Quantum Magnetic Excitations from Stripes in Copper-Oxide Superconductors. *Nature* **429**, *534*, 2004.

[73] D. J. Price, A. K. Powell, and P. T. Wood. Hydrothermal Synthesis, Structure, Stability and Magnetism of $Na_2Co_2(C_2O_4)_3(H_2O)_2$: A New Metal Oxalate Ladder. *J. Chem. Soc., Dalton Trans., 3566–3569*, 2000.

[74] D. J. Price, A. K. Powell, and P. T. Wood. A New Series of Layered Transition Metal Oxalates: Hydrothermal Synthesis, Structural and Magnetic Properties. *J. Chem. Soc., Dalton Trans., 2478–2482*, 2003.

[75] J. Kreitlow, D. Baabe, A. U. B. Wolter, S. Süllow, F. J. Litterst, D. J. Price, and H.-H. Klauss. Mössbauer Studies on the Fe^{III} Oxalate Spin Ladder $Na_2Fe_2(C_2O_4)_3(H_2O)_2$. *J. Magn. Magn. Mater.* **272**, *152–153*, 2004.

[76] A. Klümper and D. C. Johnston. *Phys. Rev. Lett.* **84**, *4701*, 2000.

[77] F. D. M. Haldane. *Phys. Lett. A* **93**, *469*, 1983.

[78] E. Dagotto and T. M. Rice. *Science* **271**, *618*, 1996.

[79] E. Dagotto, J. Riera, and D. Scalapino. *Phys. Rev. B* **45**, *5744*, 1992.

[80] T. Takeuchi, M. Ono, H. Hori, T. Yosida, A. Yamagishi, and M. Date. *J. Phys. Soc. Jpn.* **61**, *3255*, 1998.

[81] T. Sakai. *Phys. Rev. B* **62**, *R9240*, 2000.

[82] D. Allen and D. Sénéchal. *Phys. Rev. B* **61**, *12134*, 2000.

[83] D. Sénéchal. *Phys. Rev. B* **52**, *15319*, 1995.

[84] M. Sato. Low-Energy Properties of Two-Leg Spin-1 Antiferromagnetic Ladders with Commensurate External Felds and their Extensions. *Phys. Rev. B* **71**, *024402*, 2005.

[85] S. Todo, M. Matsumoto, C. Yasuda, and H. Takayama. *Phys. Rev. B* **64**, *224412*, 2001.

[86] W. Chen, K. Hida, and B. C. Sanctuary. *Phys. Rev. B* **67**, *104401*, 2003.

[87] C. Mennerich, H.-H. Klauss, M. Broekelmann, F. J. Litterst, C. Golze, R. Klingeler, V. Kataev, B. Büchner, S.-N. Grossjohann, W. Brenig, M. Goiran, H. Rakoto, J.-M. Broto, O. Kataeva, and D.-J. Price. Antiferromagnetic Dimers of Ni(II) in the $S = 1$ Spin-Ladder $Na_2Ni_2(C_2O_4)_3(H_2O)_2$. *Phys. Rev. B* **73**, *174415*, 2006.

[88] A. Salzer. Nomenclature of Organometallic Compounds of the Transition Elements. *Pure Appl. Chem.* **71**, *8, 1557–1585*, 1999.

[89] A. Escuer, R. Vicente, M. S. El Fallah, and J. Jaud. Magnetic Studies on the μ-oxalato Nickel(II) Dimers with an $[NiN_4O_2]$ Environment. Crystal Structure of (μ-ox)-$[Ni(323\text{-tet})]_2(ClO_4)_2{\cdot}2H_2O$ (323-tet=N,N′-bis(3-aminopropyl)-1,2-ethanediamine). *Inorg. Chim. Acta* **232**, *151–156*, 1995.

[90] P. Román, C. Guzmán-Miralles, A. Luque, J. I. Beitia, J. Cano, F. Lloret, M. Julve, and S. Alvarez. *Inorg. Chem.* **35**, *3741*, 1996.

[91] H. Núnez, J.-J. Timor, J. Server-Carrió, L. Soto, and E. Escrivà. *Inorg. Chim. Acta* **318**, *8*, 2001.

[92] O. Castillo, A. Luque, S. Iglesias, C. Guzmán-Miralles, and P. Román. *Inorg. Chem. Commun.* **4**, *640*, 2001.

[93] F. Meyer, P. Kircher, and H. Pritzkow. *Chem. Commun., 774* **44**, *519*, 2003.

[94] S. Demeshko, G. Leibeling, W. Maringgele, F. Meyer, C. Mennerich, H.-H. Klauss, and H. Pritzkow. Structural Variety and Magnetic Properties of Tetranuclear Nickel(II) Complexes with a Central μ_4-azide. *Inorg. Chem.* **44**, *519*, 2005.

[95] F. Meyer, S. Demeshko, G. Leibeling, B. Kersting, E. Kaifer, and H. Pritzkow. Structures and Magnetic Properties of Tetranuclear Nickel Complexes with Unusual μ_3-1,1,3 Azido Bridges. *Chem. Eur. J.* **11**, *1518–1526*, 2005.

[96] R. S. Edwards, S. Maccagnano, E.-C. Yang, S. Hill, W. Wernsdorfer, D. Hendrickson, and G. Christou. *J. Apl. Phys.* **93**, *7807*, 2003.

[97] E. del Barco, A. D. Kent, E.-C. Yang, and D. N. Hendrickson. *Phys. Rev. Lett.* **93**, *157202*, 2004.

[98] J. Ribas, A. Escuer, M. Monfort, R. Vicente, R. Cortés, L. Lezama, and T. Rojo. *Coord. Chem. Rev.* **193–195**, *1027*, 1999.

[99] R. Carlin and A. J. van Duyneveldt. Magnetic Properties of Transition Metal Compounds. *Springer Verlag, New York*, 1977.

[100] I. Dzyaloshinsky. Anisotropic Superexchange Interaction and Weak Ferromagnetism. *Phys. Cem. Solids* **4** *241*, 1958.

[101] N.P. Konstantinidis and D. Coffey. Magnetic Anisotropy in the Molecular Complex V_{15}. *Phys. Rev. B* **66** *174426*, 2002.

[102] I. Chiorescu, W. Wernsdorfer, A. Müller, H. Bögge, and B. Barbara. *Phys. Rev. Lett.* **84** *3454*, 2000.

[103] O. Waldmann, R. Koch, S. Schromm., P. Müller, I. Bernt, and R. W. Saalfrank. *Phys. Rev. Lett* **89** *246401*, 2002.

[104] B. Kersting, G. Steinfeld, and D. Siebert. Binuclear Complexes as Building Blocks for Polynuclear Complexes with High-Spin Ground States: Synthesis and Structure of a Tetranuclear Nickel Complex with an $S = 4$ Ground State. *Chem. Eur. J.* **7***, No. 19, 4253–4258*, 2001.

[105] V. Kataev. private communication.

[106] M. Edèn. Computer Simulations in Solid-State NMR. III. Powder Averaging. *Wiley Periodicals, Inc., Concepts in Magnetic Resonance, Part A,* **18A***, 1, 24–55*, 2003.

[107] O. Ignatchik. Preliminary results.

[108] S. Khanra, B. Biswas, C. Golze, B. Büchner, V. Kataev, T. Weyhermüller, and P. Chaudhuri. A Spin-Frustrated Star-Shaped Heterotetranuclear $Cr^{III}Mn^{II}_3$ Species and its Magnetic and HF-EPR Measurements. *Dalton Trans. 481–487*, 2007.

[109] Refer to [108] for citations on examples of metalloligands.

[110] P. Chaudhuri. Salicylaldoxime: An Old Ligand with New Faces. *Proc. Indian Acad. Sci. (Chem. Sci.)* **111***, 397–412*, 1999.

[111] P. Chaudhuri. Homo- and Hetero-Polymetallic Exchange Coupled Metal-Oximates. *Coord. Chem. Rev.* **243***, 143–190*, 2003.

[112] S. Khanra, T. Weyhermüller, E. Bill, and P. Chaudhuri. Deliberate Synthesis for Magnetostructural Study of Linear Tetranuclear Complexes $B^{III}Mn^{II}Mn^{II}B^{III}$, $Mn^{III}Mn^{II}Mn^{II}Mn^{III}$, $Mn^{IV}Mn^{II}Mn^{II}Mn^{IV}$, $Fe^{III}Mn^{II}Mn^{II}Fe^{III}$, and $Cr^{III}Mn^{II}Mn^{II}Cr^{III}$. Influence of Terminal Ions on the Exchange Coupling. *Inorg. Chem.* **45***, 5911–5923*, 2006.

[113] F. E. Mabbs and D. Collison. Electron Paramagnetic Resonance of d Transition Metal Compounds. *Elsevier, Amsterdam*, 1992.

[114] Y. Pei, Y. Journaux, and O. Kahn. *Inorg. Chem.* **28***, 100*, 1989.

[115] F. Lloret, Y. Journaux, and M. Julve. *Inorg. Chem.* **29**, *3967*, 1990.

[116] M. W. Wempel, D. K. Coggin, J. B. Vincent, J. M. McCusker, W. E. Streib, J. C. Huffman, D. N. Hendrickson, and G. Christou. *J. Chem. Soc., Dalton Trans., 719*, 1998.

[117] J. B. Vincent, C. Christmas, H.-R. Chang, Q. Li, P. D. Boyd, J. C. Huffman, D. N. Hendrickson, and G. Christou. *J. Am. Chem. Soc.,* **111**, *2086*, 1989.

[118] E. Libby, J. M. McCusker, E. A. Schmitt, K. Folting, D. N. Hendrickson, and G. Christou. *Inorg. Chem.,* **30**, *3486*, 1991.

[119] E. Bouwman, M. A. Bolcar, E. Libby, J. C. Huffman, K. Folting, and G. Christou. *Inorg. Chem.,* **31**, *5185*, 1992.

[120] M. W. Wempel, H.-L. Tsai, S. Wang, J. B. Claude, W. E. Streib, J. C. Huffman, D. N. Hendrickson, and G. Christou. *Inorg. Chem.,* **35**, *6437*, 1996.

[121] P. Chaudhuri, F. Birkelbach, M. Winter, P. Fleischhauer, W. Hasse, U. Flörke, and H.-J. Haupt. *J. Chem. Soc., Chem. Commun., 566*, 1993.

[122] P. Chaudhuri, F. Birkelbach, M. Winter, V. Staemmler, P. Fleischhauer, W. Hasse, U. Flörke, and H.-J. Haupt. *J. Chem. Soc., Dalton Trans., 2313*, 1994.

[123] P. Chaudhuri, E. Rentschler, F. Birkelbach, K. Krebs, E. Bill, T. Weyhermüller, and U. Flörke. *Eur. J. Inorg. Chem., 541*, 2003.

[124] S. Khanra. Designed Synthesis of Exchange-Coupled Oximate-Based Polynuclear Complexes. *Dissertation, Max-Planck-Institut für Bioanorganische Chemie, Mülheim*, 2005.

[125] E. Kim, E. E. Chufan, K. Kamraj, and K. D. Karlin. *Chem. Rev.* **104**, 2004.

[126] S. Fox, A. Nanthakumar, M. Wikstrom, K. D. Karlin, and N. J. Blackburn. *J. Am. Chem. Soc.* **118, 24**, 1996.

[127] K. D. Karlin, A. Nanthakumar, S. Fox, N. N. Murthy, N. Ravi, B. H. Huynh, R. D. Orosz, and E. P. Day. *J. Am. Chem. Soc.* **116**, *4753*, 1994.

[128] M. J. Scot, H. H. Zhang, S. C. Lee, B. Hedman, K. O. Hodgson, and R. H. Holm. *J. Am. Chem. Soc.* **117**, *568*, 1995.

[129] S. C. Lee and R. H. Holm. *J. Am. Chem. Soc.* **115**, *11789*, 1996.

[130] K. E. Kaufmann, C. A. Goddard, Y. Zang, R. H. Holm, and E. Münck. *Inorg. Chem.* **36***, 985*, 1997.

[131] H. V. Obias, G. P. F. Van Strijdonk, D.-H. Lee, M. Ralle, N. J. Blackburn, and K. D. Karlin. *J. Am. Chem. Soc.* **120***, 9696*, 1998.

[132] S. Ross, T. Weyhermüller, E. Bill, K. Wieghardt, and P. Chaudhuri. *Inorg. Chem.* **40***, 6656*, 2001.

[133] S. Ross, T. Weyhermüller, E. Bill, E. Bothe, U. Flörke, K. Wieghardt, and P. Chaudhuri. *Eur. J. Inorg. Chem., 984*, 2004.

[134] S. K. Hoffmann, D. K. Towle, W. E. Hatfield, P. Chaudhuri, and K. Wieghardt. *Inorg. Chem.* **24***, 1307*, 1985.

[135] R. F. Drake, V. H. Crawford, N. W. Laney, and W. E. Hatfield. *Inorg. Chem.* **13***, 1246*, 1974.

[136] M. Du, Y. Guo, X. Bu, J. Ribas, and M. Monfort. *New J. Chem.* **26***, 939*, 2002.

[137] F. Bentiss, M. Lagrenée, O. Mentre, P. Conflant, H. Vezin, J. P. Wignacourt, and E. M. Holt. *Inorg. Chem.* **43***, 1865*, 2004.

[138] S. Khanra, C. Golze, B. Biswas, T. Weyhermüller, E. Bill, V. Kataev, and P. Chaudhuri. A Heterotetranuclear $Fe_2^{III}Cu_2^{II}(\mu_4{-}OHO)$ Butterfly Core with an $S_t = 4$ Ground State. A Magnetostructural and High-Field EPR Study. *in preparation*, 2007.

[139] J. R. Long. Molecular Cluster Magnets in "Chemistry of Nanostructured Materials", edited by P. Yang. *World Scientific, Hong Kong* **B36***, 291–315*, 2003.

[140] H.-L. Tsai, D.-M. Chen, C.-I. Yang, T.-Y. Jwo, C.-S. Wur, G.-H. Lee, and Y. Wang. A Single-Molecular Magnet: $[Mn_{12}O_{12}(O_2CCH_2Br)_{16}(H_2O)_4]$. *Inorg. Chem. Commun.* **4** *511–514*, 2001.

[141] M. Soler, P. Artus, K. Folting, J. C. Huffman, D. N. Hendrickson, and G. Christou. Single-Molecule Magnets: Preparation and Properties of Mixed-Carboxylate Complexes $[Mn_{12}O_{12}(O_2CR)_8(O_2CR')_8(H_2O)_4]$. *Inorg. Chem.* **40** *4902–4912*, 2001.

[142] D. Ruiz-Molina, P. Gerbier, E. Rumberger, D. B. Amabilino, I. A. Guzei, K. Folting, J.-C. Huffman, A. Rheingold, G. Christou, J. Veciana, and D. N. Hendrickson. Characterization of Nanoscopic $[Mn_{12}O_{12}(O_2CR)_{16}(H_2O)_4]$ Single-Molecule Magnets: Physicochemical Properties and LDI- and MALDI-TOF Mass Spectrometry. *J. Mater. Chem.* **12** *1152–1161*, 2002.

[143] S. M. J. Aubin, Z. Sun, H. J. Eppley, E. M. Rumberger, I. A. Guzei, K. Folting, P. K. Gantzel, A. L. Rheingold, G. Christou, and D. N. Hendrickson. Single-Molecule Magnets: Jahn-Teller Isomerism and the Origin of Two Magnetization Relaxation Processes in Mn_{12} Complexes. *Inorg. Chem.* **40** *2127–2146*, 2001.

[144] R. Sessoli, D. Gatteschi, A. Caneschi, and M.-A. Novak. Magnetic Bistability in a Metal-Ion Cluster. *Nature* **365***, 141–143*, 1993.

[145] C. Boskovic, M. Pink, J. C. Huffman, D. N. Hendrickson, and G. Christou. Single-Molecule Magnets: Ligand-Induced Core Distortion and Multiple Jahn-Teller Isomerism in $[Mn_{12}O_{12}(O_2CMe)_8(O_2PPh_2)_8(H_2O)_4]$. *J. Am. Chem. Soc.* **123** *9914–9915*, 2001.

[146] S. M. J. Aubin, Z. Sun, L. Pardi, J. Krzystek, K. Folting, L.-C. Brunel, A. L. Rheingold, D. N. Hendrickson, and G. Christou. Reduced Anionic Mn_{12} Molecules with Half-Integer Ground States as Single-Molecule Magnets. *Inorg. Chem.* **38** *5329–5340*, 1999.

[147] M. Soler, E. Rumberger, K. Folting, D. N. Hendrickson, and G. Christou. Synthesis, Characterization and Magnetic Properties of $[Mn_{30}O_{24}(OH)_8(O_2CCH_2\text{-}C(CH_3)_3)_{32}(H_2O)_2(CH_3NO_2)_4]$: The Largest Manganese Carboxylate Cluster. *Polyhedron* **20** *1365–1369*, 2001.

[148] M. Soler, S. K. Chandra, D. Ruiz, E. R. Davidson, D. N. Hendrickson, and G. Christou. A third Isolated Oxidation State for the Mn_{12} Family of Single-Molecule Magnets. *Chem. Commun. 2417–2418*, 2000.

[149] C. Boskovic, E. K. Brechin, W. E. Streib, K. Folting, J. C. Bollinger, D. N. Hendrickson, and G. Christou. Single-Molecule Magnets: A New Family of Mn_{12} Clusters of Formula $[Mn_{12}O_8X_4(O_2CPh)_8L_6]$. *J. Am. Chem. Soc.* **124** *3725–3736*, 2002.

[150] E. K. Brechin, M. Soler, J. Davidson, D. N. Hendrickson, S. Parsons, and G. Christou. A New Class of Single-Molecule Magnets: $[Mn_9O_7(OAc)_{11}(thme)(py)_3(H_2O)_2]$ with an $S = {}^{17}/_2$ Ground State. *Chem. Commun. 2252–2253*, 2002.

[151] A.-L. Barra, P. Debrunner, D. Gatteschi, C. E. Schulz, and R. Sessoli. Superparamagnetic-Like Behavior in an Octanuclear Iron Cluster. *Europhys. Lett.* **35** *133–138*, 1996.

[152] S. L. Castro, Z. Sun, C. M. Grant, J. C. Bollinger, D. N. Hendrickson, and G. Christou. Single-Molecule Magnets: Tetranuclear Vanadium(III) Complexes with a Butterfly Structure and an $S = 3$ Ground State. *J. Am. Chem. Soc.* **120** *2365–2375*, 1998.

[153] J. Yoo, E. K. Brechin, A. Yamaguchi, M. Makano, J. C. Huffman, A. L. Maniero, L.-C. Brunel, K. Awage, H. Ishimoto, G. Christou, and D. N. Hendrickson. Single-Molecule Magnets: A New Class of Tetranuclear Manganese Magnets. *Inorg. Chem.* **39** *3615–3623*, 2000.

[154] N. Aliaga, K. Folting, D. N. Hendrickson, and G. Christou. Preparation and Magnetic Properties of Low Symmetry $[Mn_4O_3]$ Complexes with $S = 9/2$. *Polyhedron* **20** *1273–1277*, 2001.

[155] J. Yoo, A. Yamaguchi, M. Nakano, J. Krzystek, W. E. Streib, L.-C. Brunel, H. Ishimoto, G. Christou, and D. N. Hendrickson. Mixed-Valence Tetranuclear Manganese Single-Molecule Magnets. *Inorg. Chem.* **40** *4604–4616*, 2001.

[156] J. J. Sokol, A. G. Hee, and J. R. Long. A Cyano-Bridged Single-Molecule Magnet: Slow Magnetic Relaxation in a Trigonal Prismatic $MnMo_6(CN)_{18}$ Cluster. *J. Am. Chem. Soc.* **124** *7656–7657*, 2002.

[157] J. C. Goodwin, R. Sessoli, D. Gatteschi, W. Wernsdorfer, A. K. Powell, and S. L. Heath. Towards Nanostructured Arrays of Single Molecule Magnets: New Fe_{19} Oxyhydroxide Clusters Displaying High Ground State Spins and Hysteresis. *J. Chem. Soc., Dalton Trans. 1835–1840*, 2000.

[158] E. C. Sañudo, V. A. Grillo, M. J. Knapp, J. C. Bollinger, J. C. Huffman, D. N. Hendrickson, and G. Christou. Tetranuclear Manganese Complexes with Dimer-of-Dimer and Ladder Structures from the Use of a Bis-Bipyridyl Ligand. *Inorg. Chem.* **41** *2441–2450*, 2002.

[159] H. Andres, R. Basler, H.-U. Güdel, G. Aromí, G. Christou, H. Büttner, and B. Rufflé. Inelastic Neutron Scattering and Magnetic Susceptibilities of the Single-Molecule Magnets $[Mn_4O_3X(OAc)_3(dbm)_3]$ (X=Br, Cl, OAc, and F): Variation of the Anisotropy along the Series. *J. Am. Chem. Soc.,* **122***, 50, 12469–12477*, 2000.

[160] S. M. J. Aubin, N. R. Dilley, L. Pardi, J. Krzystek, M. W. Wemple, L.-C. Brunel, M. B. Maple, G. Christou, and D. N. Hendrickson. Resonant Magnetization Tunneling in the Trigonal Pyramidal $Mn^{IV}Mn^{III}_3$ Complex $[Mn_4O_3Cl(O_2CCH_3)_3(dbm)_3]$. *J. Am. Chem. Soc.* **120** *4991–5004*, 1998.

[161] C. Cadiou, M. Murrie, C. Paulsen, V. Villar, W. Wernsdorfer, and R. E. P. Winpenny. Studies of a Nickel-Based Single Molecule Magnet: Resonant Quantum Tunneling in an $S = 12$ Molecule. *Chem. Commun. 2666–2667*, 2001.

[162] A. L. Barra, A. Caneschi, D. P. Goldberg, and R. Sessoli. Slow Magnetic Relaxation of $[Et_3NH][Mn(CH_3CN)(H_2O)_2][Mn_{10}O_4(biphen)_4Br_{12}]$ (biphen = 2,2′-Biphenoxide) at Very Low Temperature. *J. Solid State Chem.* **145** *484–487*, 1999.

[163] N. Vernier, G. Bellesa, T. Mallah, and M. Verdaguer. Nonlinear Magnetic Susceptibility of Molecular Nanomagnets: Tunneling of High-Spin Molecules. *Phys. Rev. B* **56** *75–78*, 1997.

[164] C. Benelli, J. Cano, Y. Journaux, R. Sessoli, G. A. Solan, and R. E. P Winpenny. A Decanuclear Iron(III) Single Molecule Magnet: Use of Monte Carlo Methodology to Model the Magnetic Properties. *Inorg. Chem.* **40** *188–189*, 2001.

[165] M. Nakano, G.-E. Matsubayashi, T. Muramatsu, T. C. Kobayashi, K. Amaya, J. Yoo, G. Christou, and D. N. Hendrickson. Slow Magnetization Reversal in $[Ni_4(OMe)_4(sal)_4(MeOH)_4]$. *Mol. Cryst. Liq. Cryst.* **376** *405–410*, 2002.

[166] C. Boskovic, W. Wernsdorfer, K. Folting, J. C. Huffman, D. N. Hendrickson, and G. Christou. Single-Molecule Magnets: Novel Mn_8 and Mn_9 Carboxylate Clusters Containing an Unusual Pentadentate Ligand Derived from Pyridine-2,6-Dimethanol. *Inorg. Chem.* **41** *5107–5118*, 2002.

[167] S. T. Ochsenbein, M. Murrie, E. Rusanov, H. Stoeckli-Evans, C. Sekine, and H. U. Güdel. Synthesis, Structure, and Magnetic Properties of the Single-Molecule Magnet $[Ni_{21}(cit)_{12}(OH)_{10}(H_2O)_{10}]^{16-}$. *Inorg. Chem.* **41** *ASAP*, 2002.

[168] A. L. Barra, A. Caneschi, A. Cornia, F. Fabrizi de Biani, D. Gatteschi, C. Sangregorio, R. Sessoli, and L. Sorace. Single-Molecule Magnet Behavior of a Tetranuclear Iron(III) Complex. The Origin of Slow Magnetic Relaxation in Iron(III) Clusters. *J. Am. Chem. Soc.* **121** *5302–5310*, 1999.

[169] R. Schenker, M. N. Leuenberger, G. Chaboussant, H. U. Güdel, and D. Loss. Butterfly Hysteresis and Slow Relaxation of the Magnetization in $(Et_4N)_3Fe_2F_9$: Manifestations of a Single-Molecule Magnet. *Chem. Phys. Lett.* **358** *413–418*, 2002.

[170] C. Baumann. *Dissertation*, 2005.

Publication List

1. *Low-Valent Low-Coordinated Manganese(I) Ion Dimer: A Temperature Dependent W-Band EPR Study.*
   L. Sorace, C. Golze, D. Gatteschi A. Bencini H.-W. Roesky, J. Chai and A. Stückl, *Inorg. Chem.* **45**, *395–400*, (2006)

2. *Tuning the Magnetic Ground State of a Tetranuclear Nickel(II) Molecular Complex by High Magnetic Fields.*
   C. Golze, A. Alfonsov, R. Klingeler, B. Büchner, V. Kataev, C. Mennerich, H.-H. Klauss, M. Goiran, J.-M. Broto, H. Rakoto, S. Demeshko, G. Leibeling and F. Meyer, *Phys. Rev. B* **73**, *224403*, (2006)

3. *AFM Dimers of Ni(II) in the $S = 1$ Spin-Ladder $Na_2Ni_2(C_2O_4)_3(H_2O)_2$.*
   C. Mennerich, H.-H. Klauss, M. Broekelmann, F. J. Litterst, C. Golze, R. Klingeler, V. Kataev, B. Büchner, S.-N. Grossjohann W. Brenig, M. Goiran, H. Rakoto, J.-M. Broto, O. Kataeva and D.-J. Price, *Phys. Rev. B* **73**, *174415*, (2006)

4. *Magnetism of a Novel Tetranuclear Nickel(II) Cluster in Strong Magnetic Fields.*
   V. Kataev, C. Golze, A. Alfonsov, R. Klingeler, B. Büchner, M. Goiran, J.-M. Broto, H. Rakoto, C. Mennerich, H.-H. Klauss, S. Demeshko, G. Leibeling and F. Meyer, *Jour. Phys.: Conf. Ser.* **51**, *351–354*, (2006)

5. *A Spin-Frustrated Star-Shaped Heterotetranuclear $Cr^{III}Mn^{II}_3$ Species and its Magnetic and HF-EPR Measurements.*
   S. Khanra, B. Biswas, C. Golze, B. Büchner, V. Kataev, T. Weyhermüller and P. Chaudhuri, *Dalton Trans. 481–487*, (2007)

6. *High Field Level Crossing Studies on Spin Dimers in the Low Dimensional Quantum Spin System $Na_2Ni_2(C_2O_4)_3$ $(H_2O)_2$ with T=Ni, Co, Fe, Mn.*
   C. Mennerich, H.-H. Klauss, A. U. B. Wolter, S. Süllow, F. J. Litterst, C. Golze, R. Klingeler, V. Kataev, B. Büchner, M. Goiran, H. Rakoto, J.-M. Broto, O. Kataeva and D.-J. Price, *arXiv:cond-mat/0701575v1*, 2007

7. *A Heterotetranuclear $Fe(III)_2Cu(II)_2(\mu_4-OHO)$ Butterfly Core with an $S_t = 4$ Ground State. A Magnetostructural and High-Field EPR Study.*
   S. Khanra, C. Golze, B. Biswas, T. Weyhermüller, E. Bill, V. Kataev and P. Chaudhuri, *in preparation*, 2007

Acknowledgement

In the first place I want to thank my "Doktorvater" Prof. Dr. Bernd Büchner. This work would not exist without his confidence and commitment. In particular I have to thank him for giving me the opportunity not only to work with excellent colleagues and state-of-the-art ESR equipment in Dresden. In the early stage of graduation, he also enabled my stay in Florence and established the contact to one of the most famous groups of molecular magnetism. Finally, I thank him for giving me numerous possibilities to broaden my mind during stays in the pulse field lab in Toulouse.

Special thanks go to Dr. Vladik Kataev. As group leader of the ESR "cluster" in the IFW Dresden, he introduced me not only to magnetic resonance and cryophysics. Since I was a novice to the subject and, furthermore, the very first (under-graduate) member of the group, a large benefit was it to share the office with him for some time: Although I cannot remember a period he was not downright busy, he was always willing to suspend for listening to my questions.

A really large help was provided by the members of the ESR group. A special thanks goes to Dr. Ferenc Murányi whose excellent knowledge concerning high frequency components helped a lot in understanding the working principle of the MVNA. I also convey my thank to Uwe Schaufuß who spent considerable amount of time in improving the user interface of the measurement software and optimizing probeheads. It was, moreover, pleasent to work together with Yulieth Arango, Mohammed Elbahrawy and Alexei Alfonsov.

Dr. Rüdiger Klingeler was always ready for discussion and provided many helpful suggestions regarding everything associated with magnetization measurements. Also, the fruitful Dredsen-Toulouse network was established by him. Some special thanks go also to the "Braunschweig connection", to-be Professor Dr. H.-H. Klauß and Christopher Mennerich. We had very productive discussions and a good time on several meetings. The same is true for Prof. Dr. J. Schnack from the University of Bielefeld. Prof. Dr. Schnack, Prof. Dr. Klauß and Prof. Dr. Büchner deserve big compliments for their speedy preparation of the thesis reports. Without their efforts the completion of my PhD would not have been possible in 2007.

I also enjoyed the time with my officemate Dr. Hajo Grafe. We had much fun despite frequently panting for air. I convey my thank also to Dr. Christoph a.k.a.

Tiffel Baumann. Thanks to his sociable nature, it was never difficult to turn recreational time into time calling for recreation (compare [170]). I appreciate Dr. Sven Kiele as critical proofreader of the script of this thesis. Dr. Torben Hänke acted as style-police, thanks also for that.

To my parents I offer a great big "Thanks!" for supporting my scientific career all along with their love—and their money. Last but not least I want to thank my wife Daria. She suffered my complaints about writing the thesis all the time and never became desperate.